THE UNIVERSITY *of* EDINBURGH

Numerical methods for modelling the viscous effects on the interactions between multiple wave energy converters

Peter D. McCallum

Doctor of Philosophy

THE UNIVERSITY OF EDINBURGH

2017

Abstract

The vast and rich body of literature covering the numerical modelling of hydrodynamic floating body systems has demonstrated their great power and versatility when applied to offshore marine energy systems. It is possible to model almost any type of physical phenomenon which could be expected within such a system, however, limitations of computing power continue to restrict the usage of the most comprehensive models to very narrow and focused design applications. Despite the continued evolution of parallel computing, one major issue that users of computational tools invariably face is how to simplify their modelled systems in order to achieve practically the necessary computations, whilst capturing enough of the pertinent physics, with great enough 'resolution', to give robust results. The challenge is, in particular, to accurately deliver a complete spectrum of results, that account for all of the anticipated sea conditions and allow for the optimisation of different control scenarios.

This thesis examines the uncertainty associated with the effects of viscosity and nonlinear behaviour on a small scale model of an oscillating system. There are a wide range of Computational Fluid Dynamics (CFD) methods which capture viscous effects. In general however, the oscillating, six degree-of-freedom floating body problem is best approached using a linear potential flow based Boundary Element Method (BEM), as the time taken to process an equivalent model will differ by several orders of magnitude. For modelling control scenarios and investigating the effects of different sea states, CFD is highly impractical. As potential flows are inviscid by definition, it is therefore important to know how much of an impact viscosity has on the solution, particularly when different scales are of interest during device development.

The first aim was to develop verified and validated solutions for a generic type decaying system. The arrangement studied was adapted from an array tank test experiment which was undertaken in 2013 by an external consortium (Stratigaki *et al.*, 2014). Solutions were delivered for various configurations and gave relatively close approximations of the experimental measurements, with the modelling uncertainties attributed to transient nonlinear effects and to dissipative effects. It was not possible however to discern the independent damping processes.

A set of CFD models was then developed in order to investigate the above discrepancies, by numerically capturing the nonlinear effects, and the effects of viscosity. The uncontrolled mechanical effects of the experiment could then be deduced by elimination, using known response patterns from the measurements and derived results from the CFD simulations. The numerical uncertainty however posed a significant challenge, with the outcomes supported by verification evidence, and detailed discussions relating to the model configuration.

Finally, the impact of viscous and nonlinear effects were examined for two different interacting

systems – for two neighbouring devices, and an in-line array of five devices. The importance of interaction behaviour was tested by considering the transfer of radiation forces between the model wave energy converters, due to the widely accepted notion that array effects can impact on energy production yields. As there are only very limited examples of multi-body interaction analysis of wave energy devices using CFD, the results with this work provide important evidence to substantiate the use of CFD for power production evaluations of wave energy arrays.

An effective methodology has been outlined in this thesis for delivering specific tests to examine the effects of viscosity and nonlinear processes on a particular shape of floating device. By evaluating both the inviscid and viscous solutions using a nonlinear model, the extraction of systematic mechanical effects from experimental measurements can be achieved. As these uncontrolled frictional effects can be related to the device motion in a relatively straightforward manner, they can be accommodated within efficient potential flow model, even if it transpires that they are nonlinear. The viscous effects are more complex; however, by decomposing into shear and pressure components, it may in some situations be possible to capture partially the dynamics as a further damping term in the efficient time-domain type solver. This is an area of further work.

Acknowledgements

I am indebted to a great number of people for their support during the preparation of this thesis. First and foremost, I must thank my academic supervisors Dr Venki Venugopal and Dr David Forehand for their invaluable care and support whilst undertaking this work. Their knowledge and experience provided me with both the platform to undertake the present work, and the inspiration to deliver work which I could not have done otherwise. I will forever be grateful for the time they have spent nurturing my technical knowledge and academic skills. My two industrial supervisors, Dr Rebecca Sykes and Peter Davies of Lloyd's Register, played a huge role in the developing the present work, and also provided me with vital support on many occasions. Their insight from both industrial and academic perspectives helped in many ways during this research, for which I am sincerely grateful.

I am extremely thankful for the opportunity I was granted to work on the HYDRALAB IV WECwakes project. This provided me with the invaluable data upon which this thesis is heavily reliant, whilst also giving me extremely useful hands on experience of conducting wave tank experiments. The group of researchers behind this work have provided me with a great deal of inspiration. A big thank you is extended in particular to Dr Vicky Stratigaki of Ghent University. I must also thank Dr Tim Stallard of the University of Manchester for the input and comments he has provided at various times.

Having facilitated this work in a number of ways, I am very grateful for the support I have received from Lloyd's Register. Alongside my industrial supervisors, I received invaluable support from a number of others within the organisation. I would like to thank in particular Chris Craddock, Stewart Whitworth and Alex Caldas who shared great insight into the application of CFD in the marine industry. Furthermore, Lloyd's Register provided funding for this research, through a shared grant with the Engineering and Physical Sciences Research Council (EPSRC).

Closer to home, the journey would not have been the same without the support and friendship from those in IES. A big thanks goes out to Cameron McNatt, Istvan Gyongy, Susan Tully, Mark McAllister, George Lavidas, Duncan Sutherland and many others from Alrick 124 and beyond, who have provided a constant source of encouragement and inspiration.

Last and definitely not least, I cannot thank my wife Ali enough for her endless patience and support. I feel very lucky to have you and little Joe, and can't thank you enough for your trust, allowing me the freedom to work on my studies. I must also thank both my family and my wife's family for their ongoing encouragement and support, and in particular to John for his input and enthusiasm.

Declaration

I declare that this thesis was composed by myself, that the work contained herein is my own except where explicitly stated otherwise in the text, and that this work has not been submitted for any other degree or professional qualification except as specified.

Peter D. McCallum

Contents

Figures and Tables

Figures

Tables

Nomenclature

Latin

A	Wave amplitude
$\mathcal{A}$	State matrix (state-space)
$A_{ij}(\omega)$	Added mass coefficient relating modes i, j (= 1 to 6): finite frequencies
$A_{ij}(\infty)$	Added mass coefficient relating modes i, j (= 1 to 6): infinite frequency
$\mathbf{A}(\omega)$	Added mass matrix
$\mathcal{B}$	Input matrix (state-space)
$B_{ij}(\omega)$	Added damping coefficient relating modes i, j (= 1 to 6)
B^E_{ij}	Coefficient of externally applied damping loads (modes i, j = 1 to 6)
$\mathbf{B}(\omega)$	Added damping matrix
$\mathcal{C}$	Output matrix (state-space)
$\bar{C}, \bar{C}_g$	Phase velocity, group velocity of free surface waves (mild-slope)
$C_{1\varepsilon}, C_{2\varepsilon}$	Turbulence model constant (k-ε)
C_f	Skin friction coefficient
C_{ij}	Hydrostatic stiffness coefficient relating modes i, j (= 1 to 6)
C^E_{ij}	Coefficient of externally applied spring loads (modes i, j = 1 to 6)
$\mathbf{C}$	Stiffness matrix
D	Body diameter (at water plane)
$\mathcal{D}$	Feedthrough matrix (state-space)
$E(\kappa)$	Spectral energy (turbulent flow)
F_{ij}	Force, interaction between modes i and j (= 1 to 6)
F^R_{ij}	Force due to wave radiation, between modes i and j (= 1 to 6)
F^D_i	Force resulting from the diffracted wavefield, in mode i (= 1 to 6)
F_j	Force (j = 1 to 6)
F_s	Factor of safety (grid convergence)
$F_{3,P}$	Pressure force in heave
$F_{3,\tau}$	Shear force in heave
$F_{3,p(Euler)}$	Pressure force in heave, inviscid
$F_{3,p(RANS)}$	Pressure force in heave, viscous
$F_{3,p(visc)}$	Pressure force in heave, due to viscous effect
$\mathbf{F}^D$	The force from the diffracted wave field, acting on a surface
$\mathbf{F}^E$	The forces due to external effects
$\mathbf{F}^H$	The hydrostatic force
$\mathbf{F}^I$	Inertial force for a moving body

$\mathbf{F}^R$	The forces due to radiated waves
$G(\mathbf{x};\boldsymbol{\xi})$	Green's function
G_f	Grid flux (due to mesh motion, finite volume method)
H	Water depth
$H(\omega)$	Transfer function (frequency-domain)
J_0	Bessel function of zero order
K	Infinite depth wavenumber
$K_j(t)$	Impulse response function for the free surface elevation
$\mathbf{K}$	Radiation impedance matrix
L	Scaling factor (L=1 throughout)
$L_{ij}(t)$	Radiation impulse response function, relating modes i, j (= 1 to 6)
M	Free body modes per device
M_{ij}^E	Externally applied mass ($i, j = 1$ to 6)
M_{ij}	Body mass per mode ($i, j = 1$ to 6)
$\mathbf{M}$	Body mass matrix
N	Number of bodies
N_b	Number of panels used to define the discretised body
N_{cor}	Number of components, imposed motion function
N_{int}	Number of panels used to define the interior plane
N_{it}	Number of inner iterations (finite volume method)
$P(\omega)$	Total power for the dynamic floating body system
P_0	Power from an isolated device
P_i	Power from device i, within an array
P_j	Power from mode j (= 1 to 6)
$P_k(\omega)$	Instantaneous power due to the kinematics of the system
$P_p(\omega)$	Instantaneous power due to potential energy sources
$P_R(\omega)$	Dissipated power
R	Radial distance
R_j	Damping resistance
S	Surface area
S_b	Wetted surface of the floating body
S_{ij}	Rate of deformation of fluid element (directions $i, j = 1$ to 3)
S_w	Cross sectional water plane area
S_ϕ	Source term for the generic property ϕ (finite volume method)
T	Period of oscillation
T_0	Natural period of oscillation
$\mathcal{T}$	Time period of interest (decay sequence)
$U(\omega)$	Input vector (frequency-domain)
U, V, W	Mean velocities in x, y, z (RANS)

$\mathbf{U}$	Mean velocity vector (RANS)
$\forall$	Volume
X_i	Excitation force, resulting from mode i (= 1 to 6)
X_j	Reactance associated with mode j (= 1 to 6)
$Y(\omega)$	Output vector (frequency-domain)
Z_j	Complex impedance associated with mode j (= 1 to 6)
$\mathbf{a}_f$	Face area vector (finite volume method)
a	Device frontage (length)
c	Row spacing dimension
d	Device spacing dimension
$\mathbf{f}(t)$	Excitation force vector
f^{extr}	Extrapolated (theoretical) numerical results due to numerical convergence
f_0	Natural frequency (fundamental), Hz
f_1, f_2, f_3	Numerical solutions (grid convergence)
g	Acceleration due to gravity (9.80665m/s^2)
h	Wave height
$h(t)$	Generic impulse response function
$h_{s,max}$	Significant wave height
h_{wdc}	Wave disturbance coefficient
i	Imaginary unit, $\sqrt{-1}$
i, j, k	Indices (various, defined in text)
$\mathbf{k}$	Radiation impulse response matrix
k	Turbulence kinetic energy
l	Characteristic length of submerged body
l_{abs}	Absorption length
m	Mass
m_{ij}	Component of mass i, j (= 1 to 6)
n	Unit normal
n_1, n_2, n_3	Unit normal in translation modes ($\mathbf{n}$)
n_4, n_5, n_6	Unit normal in rotation modes ($\mathbf{x} \times \mathbf{n}$)
p	Pressure
p_f	Formal order of accuracy of a numerical solution (grid convergence)
p_o	Observed order of accuracy (grid convergence)
q	Array interaction factor
r	Ratio of mesh refinement (grid convergence)
s	Scaling factor
s_k	Surface of the k-th panel
Δt	Time step (CFD)

t	Time
$\mathbf{u}$	Velocity vector
u', v', w'	Turbulent velocity fluctuations in x, y, z (RANS)
$u(t)$	Input vector (state-space)
u_∞	Free stream velocity
u_τ	Shear velocity
u_{max}	Maximum velocity during oscillation
$\Delta x, \Delta y, \Delta z_i$	Grid size (CFD); Δz_i (vertical) is governed by the mesh region index i
$\mathbf{x}$	Position vector of point of interest
$\mathbf{x}(t)$	State variables (state-space)
x, y, z	Position coordinates of point of interest
$y(t)$	Output vector (state-space)
y^+	Dimensionless distance to the wall of smallest cell
y_p	Distance to nearest wall (CFD)

Greek

α	Turbulence spectrum constant
$\alpha_i, \beta_i, \gamma_i, \theta_i, \vartheta_i, \zeta$	Imposed motion function coefficients
α_a, α_w	Volume fraction of air and water (VOF)
β	Wave heading angle
$\beta_1, \beta_2, \beta^*, \gamma_2$	Turbulence model constants (k-ω SST)
δ	Overall system damping coefficient
δ_{ij}	Kronecker delta function
ε	Rate of energy dissipation (turbulent flow)
η	Free surface elevation
Γ	General diffusion coefficient (finite volume method)
κ	Finite depth wavenumber
κ_C	Wavenumber of turbulent fluctuations
λ_0	Wavelength of fundamental frequency component
μ	Dispersion (Boussinesq)
μ_a	Dynamic viscosity of air (1.855×10^{-5}Pa·s)
μ_t	Eddie viscosity
μ_w	Dynamic viscosity of water (1.108×10^{-3}Pa·s)
ν	Kinematic viscosity
ω	Angular frequency
ω	Turbulence frequency (RANS)
ω_0	Natural frequency (fundamental)
ω_d	Damped natural frequency
Φ	Scalar velocity potential

ϕ	Generic property (finite volume method)
φ	Complex velocity potential
φ_0	Complex velocity potential for incident wave conditions
φ_D	The diffraction potential ($\varphi_0 + \varphi_S$)
φ_R	Complex velocity potential for radiation
φ_S	Complex velocity potential for scattering
ψ_i	Artificial function of the i^{th} mode (used in nonlinear BEMs)
ρ	Density of water (998.78kg/m^3)
$\sigma_\varepsilon, \sigma_k, \sigma_{\omega 1}, \sigma_{\omega 2}$	Turbulence model constants
τ	Convolution time parameter
τ_{ij}	Reynolds stresses
τ_w	Wall shear stress
θ_j	Phase difference (impedance)
ξ_0	Initial displacement during tests
ξ_j	Displacement, mode j (= 1 to 6)
$\hat{\xi}_j$	Complex excursion amplitude, mode j (= 1 to 6)
$\Delta\xi_n$	Residual changes in displacement per oscillation
ξ_x, ξ_y, ξ_z	Position coordinates of point source
$\boldsymbol{\xi}$	Position vector of point source

Overmarks, superscripts and subscripts

$'$	Relating to fluctuating (turbulent) parameter components (RANS)
$\bar{}$	Nondimensional parameter
$\dot{}$	First derivative with respect to time
$\ddot{}$	Second derivative with respect to time
$\hat{}$	Complex amplitude
$_{EULER}$	Relating to inviscid CFD results (Euler)
$_{EXP}$	Relating to experimental results (WECwakes)
$_{MOD}$	Relating (generally) to numerical model results
$_{RANS}$	Relating to viscous CFD results (RANS)
$_{TD}$	Relating to time-domain results
$_{int}$	Relating to non-physical interior region of floating body (BEM)

Acronyms

API	Application Program Interface
BEM	Boundary Element Method
CFD	Computational Fluid Dynamics
DFBI	Dynamic Floating Body Interaction
DHI	Danish Hydraulic Institute
DM	Direct Matrix
DOF	Degrees Of Freedom
EERA	Eurpoean Energy Research Alliance
EIA	Environmental Impact Assessment
EMEC	European Marine Energy Centre
EPSRC	Engineering and Physical Sciences Research Council
FFT	Fast Fourier Transform
FRF	Frequency Response Function
FSI	Fluid-Structure Interaction
FV	Finite Volume
GA	Genetic Algorithm
GCI	Grid Convergence Index
HEM	Hybrid Element Method
HPC	High Performance Computing
HRIC	High Resolution Interface Capturing
IRF	Impulse Response Function
ITTC	International Towing Tank Conference
LCOE	Levelised Cost of Energy
MS	Multiple Scattering
ORE	Offshore Renewable Energy
OWC	Oscillating Water Column
PA	Point Absorber
PI	Parabolic Intersection
PTO	Power Take-off
PV	Photovoltaic
PW	Plane Wave
RANS	Reynolds-Averaged Navier-Stokes
RAO	Response Amplitude Operator
RTF	Rational Transfer Function

SPH	Smoothed Particle Hydrodynamics
SST	Shear-Stress Transport
STFT	Short-Time Fourier Transform
TRL	Technology Readiness Level
VOF	Volume Of Fluid
WEC	Wave Energy Converter
WES	Wave Energy Scotland

Chapter 1

Introduction

1.1 Background

One of the great challenges of the present day is the de-carbonisation of energy supplies across the globe. There is no doubt that two centuries of industrialisation have changed the chemical composition of the atmosphere and oceans of the planet. What emerged from a number of pivotal international conventions on the subject was that industrial activity could be linked directly to drastic changes to both large scale and global climate patterns. While these claims faced stiff opposition for decades, in recent years the mounting evidence has given weight to political decisions that prioritise the development of sustainable technologies.

With an increasingly industrialised world, the urgency of evasive action cannot be overstated. Energy consumption in historically wealthy countries has remained high, despite seeing declines in industrial activity. In the more recently developed regions which now supply much of the global needs for raw materials and manufactured goods, vast new markets have expanded rapidly, along with energy needs which match the old industrial nations. By contrast, living conditions in large parts of the world remain, to date, sub-standard, with over 1 billion people lacking access to electricity, and 2.9 billion without access to clean forms of cooking (REN21, 2015). The international community must embrace new energy models to meet the needs of the changing nature of demand, playing a crucial role in climate change mitigation, universal energy access, and energy security. Irrespective of where industry is geographically based at present and in the future, these above implications are global concerns, for which we need technological advancement in terms of energy production, and in terms of consumption.

Changes to the atmosphere and climate represent just part of the problem. Going forward, our means to generate energy must evolve to lessen our dependency on finite fuel supplies. Renewable energy systems provide the most sustainable alternative for energy production. The range of technologies for renewable energy generation must be diverse if we are to extract from the variety of natural resources that exist, in varying abundance, across the globe. Wind, photovoltaics (PV) and hydro form the largest contributions at present (REN21, 2015), with a range of other technologies including biomass / waste gas, geothermal and solar heating. Wave and tidal renewable energy systems have received a great deal of attention in recent

years, particularly in Western Europe, the Americas, Australia and the coastal states of Asia. However at present, the technology lacks maturity, and many challenges still lie ahead.

1.1.1 Wave energy

The present work is focused solely on wave energy. The theoretical capacity of such installations is significant, with the an estimated figure of 95TWh/yr for the UK alone (Carbon Trust, 2012), while RenewableUK (2012) puts the global figure, for economically accessible wave energy, at 500TWh/yr. Figure 1.1 shows a representation provided by Gunn and Stock-Williams (2012) of wave energy distribution worldwide. Despite the fact that early developments in wave energy emerged from the northern hemisphere, for example in Europe, Japan and USA, the largest untapped resources are found between the latitudes of 40° and 60° South, and in general, the opportunities for deployment are widespread.

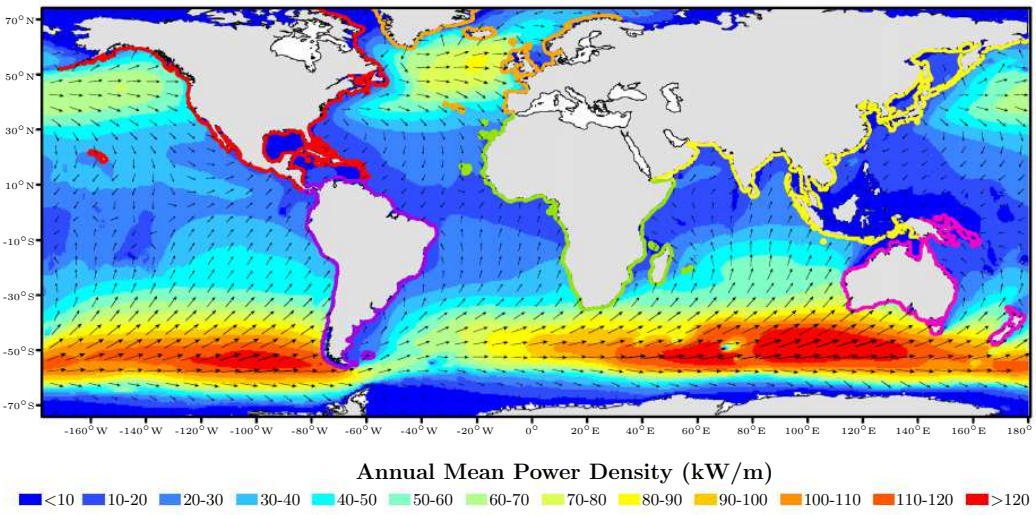

Figure 1.1: Global wave resource map (Gunn and Stock-Williams, 2012)

In Europe, the renewed interest in wave energy dates back to the early 1990s when the European Commission incorporated wave energy into its R&D program on renewable energy. In the two decades that followed, a broad range of academic research output has emerged, covering topics that include control, nonlinear systems, computational methods and experimental testing. The foundation of all modern research however remains in the 1970s and 80s with the pioneering work by Salter, Budal, Falnes, Evans, Newman, Mei, Jefferys, Count and others. There are a number of fascinating accounts of the historical developments of wave energy extraction included in Salter (1989), Clément *et al.* (2002), Falnes (2007), Drew *et al.* (2009), Falcão (2010), Langhamer *et al.* (2010), Lindroth and Leijon (2011) and Moriarty and Honnery (2012). These articles cover a range of review subjects in the context of wave energy conversion. Other notable publications include Newman (1977), Mei (1983), Falnes (2002), Holthuijsen (2007), which are widely regarded as standard theoretical texts on the subject.

1.1.2 The UK energy model

In the UK, the Department of Energy and Climate Change (2013) publishes national statistics on energy consumption and fuel and energy production from which simplified representations can be drawn, such as Figure 1.2. One of the clear observations from this is that the UK is a net importer of energy. The proportion of energy generated using indigenous fuels is at its lowest level since 1976, with this figure standing at only 57% in 2012 and with total imports also at a record high. Around 46.8Mtoe (million tonnes of oil equivalent) of coal for example was consumed in 2012, only 15.0Mtoe of which was sourced in the UK. With regard to fuels used specifically for electricity generation (not shown explicitly in Figure 1.2), 34.1Mtoe of coal was consumed, with a further 18.2Mtoe of natural gas, and 15.9Mtoe generated by nuclear. The renewable energy contribution to electrical demand was just 2.2Mtoe in 2012, which suggests that much more must be done to exploit these resources. The balance must consider base loading, peak demand and the low load factors associated with renewables; however, larger renewable energy contributions will be necessary if the UK is to meet its onerous CO_2 reduction targets.

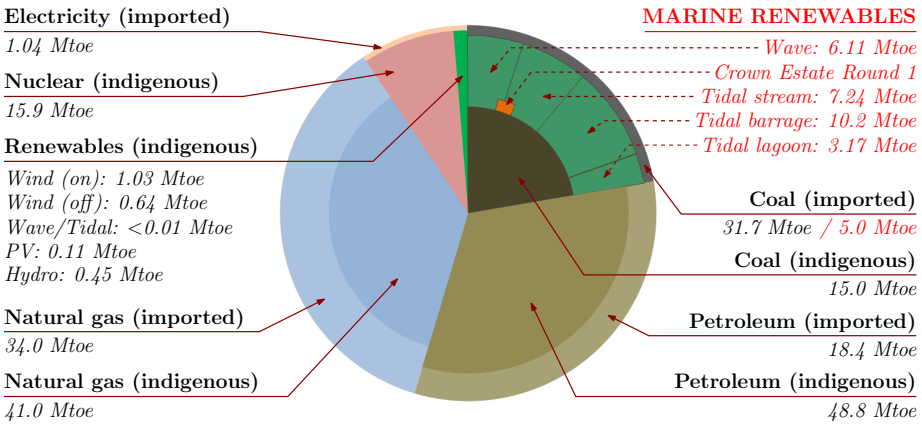

Figure 1.2: Theoretical contributions of marine renewable energy sources (The Crown Estate, 2012) imposed onto the UK energy consumption in 2012, excluding transport. The additional contributions (detailed in red) represent maximum values assuming a uniform load factor of 30%. These are shown notionally to displace imported coal.

Figure 1.2 also shows the theoretical maximum wave and tidal energy output of the UK (The Crown Estate, 2012), overlaid onto the UK energy consumption in 2012. It is not expected that electricity generation at this scale will be realised for the foreseeable future, but the opportunities that these resources present are significant. The leasing of offshore zones, specifically for the purpose of energy extraction, has reflected this potential. The orange segment in Figure 1.2 represents the potential capacity of the first leasing round in 2010, as established by The Crown Estate. These zones are spread throughout UK waters although a large concentration of wave sites are found in the far North and West of the UK, as seen in Figure 1.3.

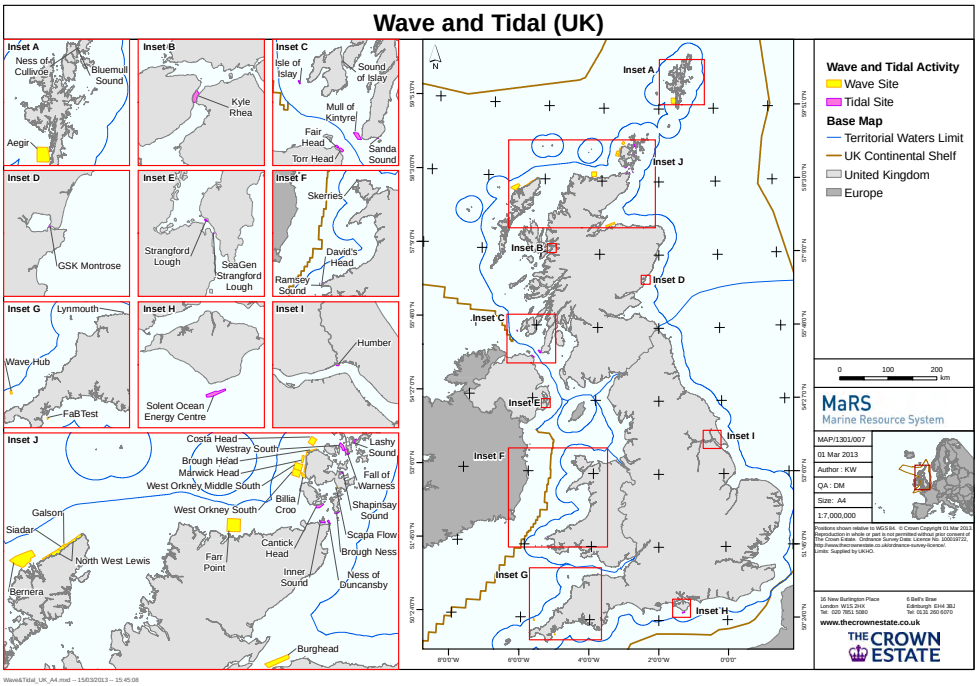

Figure 1.3: The Crown Estate (2012), leasing round 1 for wave and tidal energy (UK).

1.1.3 The state of the industry

There have been a number of notable projects to date in which the principles of wave energy extraction have been tested at full scale, in many cases with the involvement of large utility companies. The UK's Crown Estate has played an influential role by leasing offshore sites specifically for this purpose. Other organisations have taken equally important steps, including Marine Scotland, who have established Environmental Impact Assessment (EIA) procedures for the emerging wave and tidal industries. International Standards are also in development, consolidating experience from research and industry. The IEC Technical Committee 114 has presented draft technical specifications on resource characterisation, design requirements and moorings, with plans to cover a diverse range of other topics *.

However, there are still huge technical difficulties to overcome in the development of reliable wave energy extraction systems. A lack of suitable component systems for the highly specialised technology has caused significant issues for some of the large scale prototypes tested over the last number of years. On limited resources and budgets, developers have been forced to design novel working systems for the demanding marine environment, for hydraulics, electrical systems, power take-off mechanisms and so on. With respect to non-technical barriers, planning and ecological issues, changes in government policy, access rights over other industries and the military, and economics are just a few of the other difficulties facing the immature technology.

*http://www.iec.ch

The uncertainty over provision of new high voltage cables connecting Shetland and Lewis to the UK grid [†] has been cited as such an example.

There is also significant uncertainty in the Levelised Cost of Energy (LCOE) for wave power, which can adversely affect the investment climate for the industry. Long range forecasts published by DECC for example increased by more than 20% between consecutive reports (Department of Energy and Climate Change, 2012, 2013). While there were spells in which the level of venture capitalist investment was very positive, at present a number of large companies have withdrawn their involvement due to the commercial risks associated with the extremely demanding technical challenges. A number of the prevalent companies that developed the pioneering technology, such as Pelamis Wave Power and Aquamarine Power, have since been forced into administration.

There have been some more positive developments within the UK context however in the last two years. In light of the technical difficulties mentioned above, two organisations have been established, both of which are aimed at reducing the technology risks - the Offshore Renewable Energy (ORE) Catapult and Wave Energy Scotland (WES). Along with the well established Carbon Trust, these organisations have assumed important roles in orchestrating collaborative research between industry and academia, and importantly, between the developers and the wider marine technology industry. With respect to earlier collaborative mechanisms, greater emphasis has been placed on component level development, to strengthen the supply chain and reduce the operating risks for developers with established designs, and with new concepts. In marked contrast to earlier accelerator incentives such as the Saltire Prize, a strong focus on open collaboration has been considered crucial to the future of the industry.

1.1.4 Prototype projects

There have been a wide range of wave energy converter (WEC) concepts proposed, many of which have been tested at large scale. The different devices extract energy through various modes of motion, with each designed to operate in a particular water depth and in particular wave conditions. Examples of projects active in the last 5 years include those shown in Figure 1.4. There are many other examples from around this period, and earlier, which utilised very large prototype machines to demonstrate proof of concept for the different designs.

Figure 1.4a shows one of two Pelamis P2 devices deployed over different spells between 2010 and 2014 at the EMEC test site in Orkney, UK. These measured approximately 180m in length, around 60m longer than the first generation device. The design is categorised as an attenuator, generating energy though pitch, yaw and heave motions. This device was designed to operate in water depths of around 50m, and to capture energy from sea-states with relatively long wavelengths , which is reflected in the choice of physical dimension. Both prototype

[†] http://www.scotland.gov.uk/Resource/Doc/295194/0124652.pdf

(a) Pelamis Wave Power

(b) WaveStar A/S

(c) Aquamarine Power Ltd.

(d) Ocean Power Technologies

Figure 1.4: Large scale prototype projects operational in the last 5 years.

P2 devices were owned and operated by commercial utility companies, which was the first such example for the industry. Four first generation WECs were operational at different times between 2004 and 2008, and represented the first grid connected floating wave energy converter system (EMEC) , and the first grid connected array (Aguçadoura, Portugal).

An example of a point absorber type device for shallower water depths is shown in Figure 1.4b, the 1:2 scale prototype WEC installed at Roshage (Hanstholm, Denmark), developed by Wave Star A/S. The test system was designed to operate in a water depth of 5 to 8m, with the full scale proposed design aimed at depths of 10 to 20m. The installation was completed in 2010, and Wave Star have continued to develop advanced Power Take-off (PTO) control systems for this test device, to actively target beneficial interaction effects between the two floats. The full scale concept systems is proposed to have 20 floats, measuring around 80m in length (Wave Star A/S, 2013).

Aquamarine Power Ltd. developed a terminator type WEC concept, producing two large-scale grid-connected prototype devices. The completed second generation machine is shown in Figure 1.4c, prior to deployment at the European Marine Energy Centre (EMEC) test site. During operation, the buoyant flap was designed to pivot under the surging motion of waves, with the top of the flap protruding just above the water surface. Delivery of electrical power was achieved using onshore plant, with all offshore transmission via a hydraulic system. The

device measured 26m in width, and was installed in a water depth of around 13m.

Ocean Power Technologies (OPT) developed a heaving point absorber WEC, which generates power through the relative motion of two independent bodies. Figure 1.4d shows the 44m spar, which is orientated vertically when installed, and protrudes around 9m above the water surface. The motion of the spar is restrained through use of a rigidly fixed heave plate, whereas the float structure (right hand side of the image) is free to move in heave, in response to passing waves. This system was designed to be moored, and to operate in water depths of 45 to 500m.

From the above examples, there are no plans unfortunately to continue the development of the Pelamis or Aquamarine designs, with both developers recently entering administration. Development of the Wave Star and OPT devices is ongoing, along with similar scale projects from a number of other developers, including Carnegie Wave Energy. The Australian based company is currently developing its sixth generation prototype design, Ceto 6, of a sub-surface six degree of freedom point absorber type WEC. A deployment of three Ceto 5 units was tested in 2015 to demonstrate array operation of the devices, as seen in Figure 1.5. Each unit had a maximum power rating of 240kW, measuring 11m in diameter. Small scale tank testing of the Ceto 6 unit took place in 2014, with plans for the full scale device to be significantly larger than Ceto 5, at around 20m diameter, with a maximum power rating at up to 1MW. Other developments include a redesign of the power take-off system, allowing the new device to be deployed further from shore, in depths of up to 35m.

1.1.5 Academic research

There are a large number of universities and research laboratories actively involved with wave energy projects, across Europe, The Americas, Asia and Australasia. Interaction between the many institutes has been enhanced through collaborative mechanisms and a wide range of joint research projects, with many project consortia also spanning industry and academia. There are also many examples of international partnerships between universities and broader strategic alliances that encompass groups of organisations, to ensure that research themes are coordinated in order to give the greatest impact in industry. An example of this is the European Energy Research Alliance (EERA) for Ocean Energy, which has members from across eight European states.

The SuperGen Marine Energy Research Consortium has had a particularly significant impact within the UK, which is in its third phase and has incorporated fifteen universities. Academic training has also been carefully coordinated to enhance the diversity and impact of output from postgraduate level researchers, both within SuperGen and other frameworks like the completed Wavetrain project. Doctoral training centres have been established across multiple institutes, including the Industrial Doctoral Training Centre for Offshore Renewable Energy (IDCORE) and Doctoral Training in Renewable Energy Marine Structures (REMS).

(a) The three installed devices, in operational positions (submerged)

(b) One of the Ceto 5 units

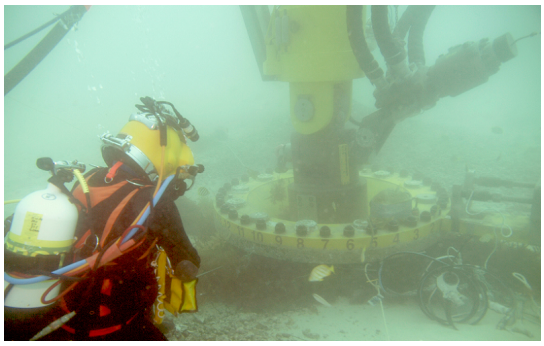

(c) Sea bed coupling link

Figure 1.5: Carnegie Wave Energy Ceto 5 demonstrator array, off Garden Island Western Australia.

1.1.6 The context of this research

Observations from industry and academia show that research themes can be broadly grouped into the following subjects:

1. Local hydrodynamics and dynamic loading;
2. Wider domain hydrodynamics (resource modelling and wave climate modification);
3. Power take-off, control and electrical system design;
4. Environmental and marine biology impacts;
5. Mooring and subsea systems;
6. Policy and economics modelling;
7. Materials engineering;
8. Energy storage.

The present work concerns the first of these subjects only. Before describing the main objectives and specific motivation for the research presented in this thesis, a general methodology for device design is provided in Section 1.2. This methodology has, more specifically, been taken from the perspective of designing the hydrodynamic system, i.e. studying the direct effects of the body on the fluid, and vice versa. This is a particularly interesting subject, in part because it is central to the design of a wave energy converter, but also because of the complexity of

the challenges present when attempting to assess and optimise float geometries and dynamic responses to incident waves. These challenges include:

1. Identifying relationships between the design parameters that describe the system, and the performance of the system (through use of numerical models);
2. Verifying the fidelity of the numerical models, with respect to the applied scientific principles;
3. Designing of reduced scale physical test systems to validate the numerical models;
4. Identifying linear, or weakly nonlinear relationships for the response parameters of the tested systems, to the physical scale of the test specimens;
5. Extrapolating the response parameters, to give indicative results for future large-scale tests, and for the proposed full-scale commercial device;
6. Preparation of the device design for the next development stage (i.e. at a larger physical scale).

When designing a WEC, the above challenges are, in general, addressed sequentially in the order given here. Most of these steps will also be revisited as the small-scale test systems progress to larger scale, and again at the next development stage, and so on. The motivation for the present work, with respect to these challenges, is discussed in Section 1.3, following the design methodology presented in Section 1.2.

No specific treatment of Items 5 and 6 is given in this thesis, as these issues will be highly specific to any given device under development, and the target wave environment. The approach taken here is to use a generic floating body design, to outline a detailed procedure for the development of validated numerical models for a WEC (Items 1 to 4). The procedures described herein consider the appropriate application of both linear and nonlinear models, as well as inviscid and viscous solvers. The application of this procedure is extended in Chapter 7 of this thesis to study interactions between small arrays of devices.

1.2 Device development and testing

1.2.1 Design methodology

By designing in conjunction with numerical methods one can study in great detail the relationships between design parameters such as the shape of the immersed body or nature of any external forces, and the performance of the device. Iterations of design variables can be processed, in a variety of configurations, in order to achieve some degree of optimisation. The extent of such studies will ultimately be limited by the computing resources and time available, particularly if this requires computational fluid dynamics (CFD). This may infer that only a few permutations of design variables is practical. Potential flow based methods on the other hand can allow comprehensive tuning of design parameters, provided that the implied

assumptions are reasonable. In any case, when developing a numerical model it is imperative that an appropriate procedure is followed and the uncertainties are quantified.

It is not possible to scale faithfully a physical hydrodynamic system in terms of both inertial and viscous forces[‡], which suggests that the numerical and physical models are mutually reliant, and complementary. The role of CFD is important within this framework, given its capacity to model nonlinear rotational flow and shear forces within the fluid and at boundary interfaces, resolving any additional damping effects this might have on the body motion. The role of inviscid solvers and/or frequency-domain solutions can also be explored, using for example a potential flow based boundary element method (BEM) to extrapolate efficiently to any scale. The overlapping applications of these methods is examined in this thesis.

In general, nonlinear models can be applied to the generic problem using an overall modelling framework. This is shown in Figure 1.6, which illustrates a methodology for developing a new device design. This proposes that two concurrent numerical models, *(a)* and *(b)*, should be progressed through early, intermediate and advanced project stages. Model *(a)* should provide an indication of how the commercial device should perform; however, without a validated numerical model, the predictions from model *(a)* will be associated with significant uncertainty. This implies the use, first, of a secondary model, *(b)*, which can be validated using a physical tank test model, *(c)*. Once a formal verification and validation procedure has been completed, the extrapolated performance can be delivered, using model *(a)*.

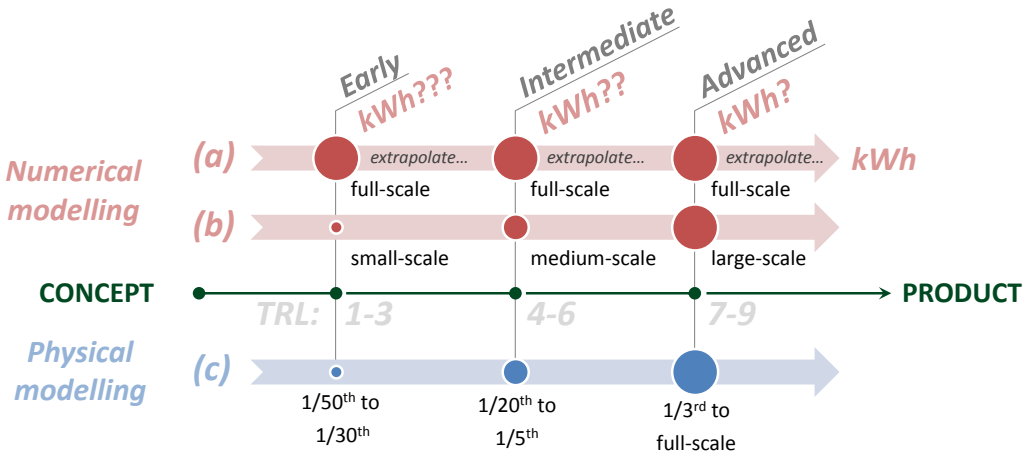

Figure 1.6: General schematic overview of modelling procedures for performance evaluations at various stages of the design process. Model (a) should provide extrapolated energy yields at each stage. Models (b) and (c) develop together to advance the design of the system. Scaling factors and Technology Readiness Levels (TRLs) are indicative.

[‡]Without altering the properties of the fluid, one cannot scale and retain both the same Reynolds and Froude numbers

1.2.2 Numerical modelling

For a wave energy system in the research and design phase, numerical modelling plays a wide range of roles throughout the development programme, from the early concept design stages, right through to pre-commercial testing. At each stage, the specific purpose of a numerical model will vary considerably. Early concept design exercises may involve investigations of a variety of notional ideas, whereas the detailed design of an established scheme is likely to focus on optimising specific design parameters. The models themselves will be very different; however, all modelling work will serve the same overall purpose which is to reduce the uncertainty and risk associated with the project.

In order to use a numerical model as a design tool the results should be validated for each new configuration. In some instances this can be achieved using well understood numerical methods. This may for example be the only practical solution, such as when modelling very large geographical areas with limited buoy data, a reliable model such as WAVEWATCH III might be used. Reduced scale physical testing however should provide the validation data required for near-field hydrodynamic models. And while there is a reliance upon scale tests for the diligent application of numerical methods, the same can be said of the opposite. In order to extrapolate performance results from a small-scale tank test to a full-scale deployment, the nonlinear relationships between the performance and physical scale should be well understood.

1.2.3 Physical modelling

The purpose of the physical tests must of course be stressed. Implementing engineering solutions directly from a purely theoretical basis brings significant risk and uncertainty to a project. Generally speaking for a large industrial system, small and medium-scale physical testing is a crucial step towards the development of a product that should ultimately enter service with a strong case for commercial success. For the case of wave energy conversion, this should be demonstrated in terms of the effective power output, the survivability, and the operability of the systems. These factors constitute the product value, and if evidence is lacking on any part it is not likely that investment will be forthcoming.

As has been the norm through wave energy developments in academia and industry, small and medium-scale testing becomes an involved process that provides both quantitative and qualitative results. The test subjects can range from fairly rudimentary models to highly complex arrangements incorporating active power output systems. And while vast quantities of data can be produced using many different types of sensors, the practical and operational aspects of testing are also hugely beneficial, particularly if this involves open water. When testing is carried out in the controlled environment of a wave tank, highly repeatable experiments are possible, which is instrumental for numerical model validation. Working with smaller test specimens in a safe environment also allows design changes to be implemented quickly, and relatively small costs can be maintained.

The nature of wave energy conversion means that it is crucial to have a sound understanding of the hydrodynamic behaviour of the system. The structures involved can be very different from other marine systems, which otherwise rely on many decades of comprehensive research and in-service experience, along with industry standard design codes. Furthermore, as energetic sea-states and harmonics are targeted for wave energy systems, the hullforms required for active components of the device should be carefully optimised to exploit the predominant conditions. Physical tests at small, medium and then large prototype scale will allow the design to evolve, alongside a comprehensive hydrodynamic numerical modelling programme. As the devices become progressively larger at each stage, coordination with the electrical and structural systems becomes fully integrated, and other important experience begins to develop in terms of fabrication, economics and the ecological impact of the design.

1.2.4 Validation & verification

The hydrodynamic numerical models referred to above are extremely important design tools for the given context. As is the case with all aspects of design in engineering, however, a numerical or mathematical model is only an indicative reproduction of the physical system of interest, which will feature a range of numerical uncertainties and modelling uncertainties. While it must be accepted that the system cannot be modelled perfectly, the pragmatic approach is to follow formal procedures for *verification* and *validation*.

As with many other engineering systems, the hydrodynamic problem is also characterised by a degree of randomness, which adds great complexity and results in very computationally onerous evaluations. To achieve any quantity of useful results, assumptions must be made in a way that preserves the general integrity of the method. Or, if appropriate, a computationally efficient method may be used instead if its capabilities suit that of the specific problem. The discretisation in time and/or space will also introduce uncertainty, along with machine precision, choice of numerical schemes and iterative procedures. These particular elements relate to numerical uncertainty (requiring *verification*), whereas the suitability of the theoretical method relates to modelling uncertainty (requiring *validation*). Ultimately, the nature of hydrodynamic modelling means that results that are not verified and validated should be treated with the utmost caution.

1.3 The present research objectives

The remainder of this chapter is devoted to the explanation and justification for the research undertaken during the preparation of this thesis. Given the brevity of the above introduction to wave energy converter modelling, the explicit questions posed here are followed by some specific considerations which aim to justify the direction taken throughout this work. The reader is also referred to the literature review presented in Chapter 2, to clarify the context of this work within the broader research.

1.3.1 Research questions

The work presented in this thesis serves to answer pertinent and specific questions relating to the usage of CFD for WEC array interaction modelling. The limited availability of validated WEC array models using CFD has been highlighted in particular as a gap in the existing literature. The questions posed in this work are as follows:

1. How important are viscous and nonlinear effects in relation to the WEC array interaction problem?
2. How should small-scale experimental effects be treated in a numerical model of a WEC array?
3. What measures are required to construct a valid finite volume, CFD model of a floating WEC array?

Whilst some aspects of the subject matter highlighted in these questions are not new, their application to the WEC array problem is a novel subject. The work presented in this thesis provides validated evidence to support the application of CFD for modelling WECs operating under normal conditions. The research motivation behind this is discussed in the below (Section 1.3.2).

1.3.2 Research motivation

Causes of uncertainty in the industry

The commercial and technological barriers that are currently impeding developments in wave energy conversion are all closely linked to uncertainty and risk. By recognising a clear distinction between technology which is immature and technology which is characteristically expensive, the approach to research and development can be carefully considered and the correct risks can be identified at an early stage. If, for example, there was certainty over the LCOE for wave energy, and this was still considerably higher than for more conventional energy sources, it would be possible to structure governmental support mechanisms and private investment plans to help the industry develop gradually into niche markets. Security of invested capital and of jobs would then be assured, and the technology could mature progressively through deployment in specialist applications. Strategies for lowering the LCOE and increasing

installed capacity would then be given more robust grounding, and the impact of the technology would be greatly increased when the broader energy landscape changes, as has happened in the last decade with wind energy. The case of solar energy is equally applicable, as the technology progressed over the course of many decades, from laboratories to large scale power stations, via applications like satellites, military systems, remote/portable communications systems and consumer electronics. By 2015, an estimated 7-8% of the annual energy demand in Italy, Greece and Germany was generated using photovoltaics (REN21, 2015).

The role of numerical models in reducing uncertainty

There is however significant uncertainty in the LCOE, as highlighted in Section 1.1.3, which makes the economic and political climate for wave energy very volatile. The obvious concern with unproven technology is that it is difficult to manage expectations of investors, both prospective and engaged. Providing reliable projections of the expected performance is notoriously difficult. Aside from the economic considerations in the evaluation of the LCOE, a huge range of technical assumptions are necessary to give yields in kWh from individual devices. The notion of interaction effects in WEC arrays (i.e. the q-factor) can also be a consideration, although these are highly sensitive to a number of factors. One of these factors, which is not well documented in any research, is the effects of nonlinear hydrodynamic behaviour and of viscosity on the q-factor. These concerns are described in more detail in Section 3.1 in response to Question 1 (from Section 1.3.1), and are assessed in Chapters 6 and 7 by studying the nonlinear hydrodynamic processes and viscous effects on body forces. Evaluations of power output as a result of incident wave conditions were beyond the scope of this work, as such, no direct correlation is made to the q-factor.

Despite the fact that viscous effects are not expected to play a *dominant* role in the floating body dynamics of a full scale device, potential for compounded effects from both ends of the interaction processes should be assessed for a WEC array, before they are dismissed. An intriguing characteristic of viscosity is that when a small-scale model of a device is tested, the effects of viscosity are disproportionate. This suggests then that, if viscous effects are relevant for a small-scale tank test, the relationship between performance and physical scale may be complex and nonlinear. The specific behaviour of this added dissipation should be captured using an appropriate numerical model, to ensure that more accurate evaluations of the full scale device can be delivered. Other nonlinear hydrodynamic behaviour can also exist, which may or may not extrapolate predictably with scale. These aspects of testing small scale physical models should be carefully considered.

Figure 1.7 outlines the general approach, whereby a combination of linear/inviscid modelling and nonlinear/viscous modelling is carried out. This fits with the outline framework depicted in Figure 1.6. The necessary decisions at the different stages in Figure 1.7 will require fairly involved input from the designers.

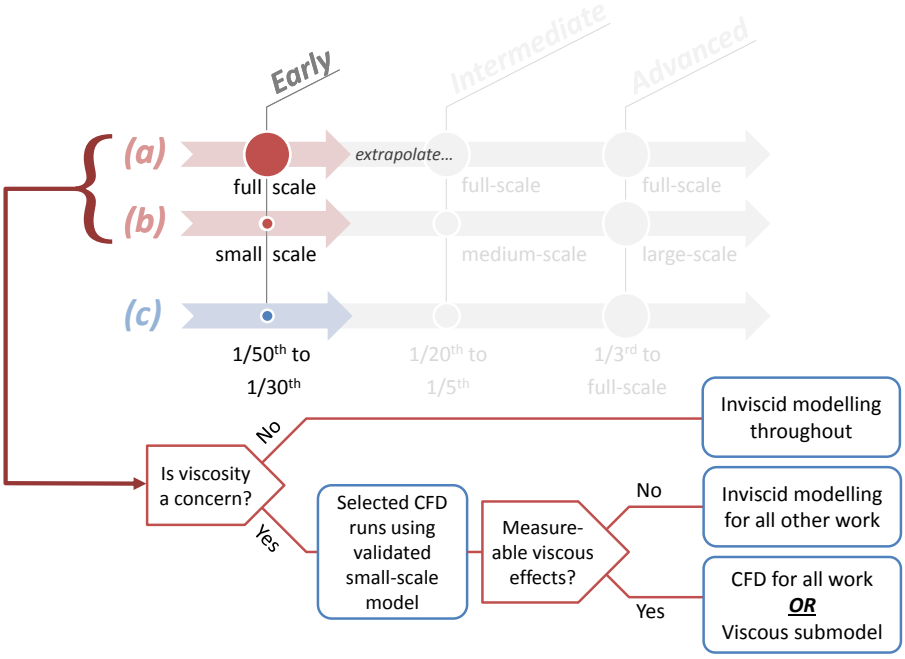

Figure 1.7: Methodology for considering viscous effects during prototype WEC development.

Modelling of experimental effects

In relation to the important consideration of physical model testing for the production of validation data, as discussed in Section 1.2, a wide range of specific implications also exist for small-scale model tests. The practical aspects of this subject are well documented in terms of the design and execution of experiments, including the following references: EquiMar (2009, 2010a,b, 2011); EMEC (2009); ITTC (1999, 2005, 2011b,c); Payne (2008); McCombes *et al.* (2012); IEA (2010a,b); DTI (2007). Due to the Froude scaling associated with power in particular, the characteristics of dissipative power losses must be accounted for the small-scale numerical models. This does not only include any power take-off mechanisms; the uncontrolled damping effects will likely have a significant bearing on the measured output from experiments. In the present work, this is carried out using a series of evaluations using both a linear BEM / time-domain based model, and CFD. It was possible therefore to deduce discrete components of the experimental effects: damping caused by mechanical dissipation through bearings, sensors, etc.; and damping caused by viscosity, which again, is disproportionate at small scale. This is examined in later chapters, in response to Question 2 (Section 1.3.1).

General applicability of CFD to WEC power evaluations

Descriptions are provided in the literature review (see Section 2.2 in particular) regarding the use of semi-analytical methods, boundary element methods (BEMs) and computational fluid dynamics (CFD), in order to study the precise hydrodynamic behaviour of a system. The semi-analytical methods generally require highly-specific knowledge and experience of the particular case studied; as such these are often confined to academia. Commercial companies which develop devices will also, of course, be equally well-equipped to deliver high quality results from semi-analytical models. The problem in industry, however, is that highly-specific semi-analytical models can potentially be difficult to scrutinise and compare when third party due diligence is carried out. This is an important consideration because both verifiers (providers of assurance, guidance and contributors to policy) and potential investors are well versed in more conventional methods, as used for the traditional marine industries.

The widely validated BEM and CFD methods can, in theory, be applied generically to any system, and, due to the availability of commercial codes and the large community of users and experience in the wider workforce, companies are generally better positioned to apply these methods. Even so, more needs done to validate CFD for the highly-specific WEC array problem.

The use of CFD for wave energy systems is a very active area of research; however, much of the current work being carried out is focused on modelling of impact loads and survivability during extreme wave events. These, of course, are very important considerations which still pose a wide range of challenges. Furthermore, the use of CFD for this application is not disputed. Literature on the use of CFD for power evaluations in more benign sea conditions, as studied here, is relatively sparse, and the production of further evidence has been identified here as an area for development. Where it was stated above that, CFD can *in theory* be applied generically to any marine system, this hides a plethora of complications which burden designers when demonstrating WEC array interactions using CFD. As a primary consideration of this work, CFD is examined in a relatively innovative application. This was raised by Question 3 (Section 1.3.1).

It is common for the propagation of waves in free surface CFD models to suffer from adverse effects, which may be dissipative or cause other non-physical disruption to the flow. These issues, along with more general numerical instability issues, require careful consideration when verifying the CFD model, which in practice can be an extremely onerous task.

A number of CFD methodologies are currently being used to study wave energy systems, in particular, those suited to free surface wave propagation and floating body motions. These include the Volume Of Fluid (VOF) method and Smoothed Particle Hydrodynamics (SPH). The former is adopted in this work, partly due to the extent of validation evidence for marine applications in both academia and industry for more traditional marine applications. Detailed

guidance is provided from number of sources regarding acceptable meshing criteria and model configurations for accurate free surface capturing. The suitability and practicality of these criteria are examined in this thesis. Furthermore, despite current developments relating to wave energy using the VOF method, validation of the array interaction problem is still limited.

Summary

From the starting point of reducing uncertainty in the power prediction calculations, it is imperative that all hydrodynamic behaviour is captured accurately in the numerical models, and that a careful exercise is conducted to scale the validated small-scale numerical models to full-scale. Concerns are discussed in this work regarding the effects of viscosity at both 'source and sink ends' of the energy transport processes from radiated waves, which produce the interaction effects described above (encapsulated by the q-factor). Again, the importance of nonlinear effects require special consideration. In circumstances where viscosity and nonlinear effects have a significant bearing on the solution, CFD should form an important part of the numerical modelling process.

1.3.3 Scope and research outcomes

The background context and motives of this work are as described in Sections 1.1.6 and 1.3.2. The scope of this research is discussed here to interpret how the results may be applied to future work, and to clarify the limitations.

This work should provide the reader with:

1. A framework for developing a floating type wave energy converter using numerical models and scaled physical tests;
2. Assurance that computational fluid dynamics can adequately describe the floating body, free surface problem, for individual devices and for small arrays;
3. A detailed description of specific difficulties when modelling fluid structure interaction problems, using computational fluid dynamics.

The reader should be aware that the following considerations are not within the scope of this work:

1. Detailed device design;
2. Detailed modelling of control methodologies and power take-off design;
3. Hull optimisation studies;
4. Resource modelling at prospective wave farm sites;
5. Design of experiments or model construction for tank tests (this work only involved participation in an external project);
6. Full scale design appraisals for offshore wave farm deployments.

As stated in item 5 from the above limitations, experiments were neither designed nor carried out independently as part of this PhD work. A short period was however spent participating in a larger external project, 'WECwakes' [§], which had involvement from a consortium of nine different institutions. Details and descriptions of that array experiment are provided in Chapter 4.

1.3.4 Publications

The publications presented during the course of this research are as follows:

1. "On the performance of an array of floating wave energy converters for different water depths (OMAE2014-24094)," P. McCallum, V. Venugopal, D. Forehand, and R. Sykes, Proc. of the ASME 33th International Conference on Ocean, Offshore and Arctic Engineering.
2. "Evaluation of viscous effects on the decay motion of a heaving wave energy converter," P. Mccallum, V. Venugopal, D. Forehand, R. Sykes, V. Stratigaki and T. Stallard, prepared for Renewable Energy (not published at time of writing).
3. Tank testing procedures for small scale wave and tidal energy converter models, Lloyd's Register (internal report).
4. Guidance note on CFD Analysis of Interacting Floating Structures, Lloyd's Register (internal report).

It is noted here that this work was carried out with the support of Lloyd's Register EMEA, with the outline remit and scope based on providing technical assurance to support the developing industry, and to inform stakeholders and prospective investors. Items 3 and 4 above were carried out during the course of this research. Item 3 was prepared alongside the results associated with Question 2, as outlined in Section 1.3.1. Similarly, Item 4 was prepared alongside the work carried out for Question 3.

[§] www.ugent.be/ea/civil-engineering/en/research/coastal-bridges-roads/news-events/wecwakes-project.htm

Chapter 2

Literature Review

A review of the existing literature is presented in this chapter. The numerical modelling methods discussed are divided into two groups. Potential flow based techniques (semi-analytical, boundary element method, etc.) and computational fluid dynamics (CFD) codes are considered well suited to evaluating the hydrodynamic characteristics of a wave energy converter (WEC), as well as addressing the device interactions within an array of WECs. The wave propagation models on the other hand address far-field effects due to the presence of an array of WECs. These include the phase-resolving Boussinesq and mild-slope methods and phase-averaged spectral wave techniques. An outline understanding of these methods is necessary in order to give the main work of this thesis some context. Furthermore, it is important that engineers and designers of wave energy systems have some all-round knowledge of the various numerical methods, in order to make best use of the vast research material on the subject.

A general summary of the numerical methods is introduced in the first section of this chapter. Section 2.2 discusses the various methods for assessing the detailed interactions between a moving body and the surrounding fluid, and for interactions between bodies for array configurations. The subsection devoted to literature on CFD is extended due to the particular relevance to the main work in this thesis. Section 2.3 goes on to discuss the far-field numerical methods, with some examples of hybrid models. In the final two sections of this chapter, some discussions are provided on current activities, and the context of this work within the existing literature.

2.1 Background

2.1.1 General approach

Modelling of hydrodynamic interactions between floating, fixed and constrained rigid bodies with ocean waves has been the focus of many studies in the field of marine engineering. This has traditionally been carried out for the design of ships and military vessels, but also applies to oil storage and production platforms, harbours and coastal defence systems, and more recently, WECs. Conceptual models of these systems often start from the assumption that the sea surface can be decomposed into a spectrum of waves of different frequency and amplitude. Phase

characteristics of these components can either be retained or neglected, and nonlinearities can be included if desired. Navier-Stokes-based solvers are capable of modelling viscous effects, air entrainment, compressibility, green water and extreme wave loads. Although use of CFD codes are becoming increasingly feasible, more traditional numerical approximating methods are still widely used, and can provide very efficient assessments that are, in many cases, more appropriate than the equivalent CFD models.

The need for a diverse set of modelling methods for wave energy conversion can be illustrated by considering the range of technical engineering challenges involved. For large, simple oscillating structures in relatively calm sea-states, the body motions, wave diffraction and wave radiation characteristics can be effectively modelled using an inviscid solver, evaluated entirely in the frequency-domain. This can extend to interactions between devices, if configured in an array. An example of a simple system is provided in Figure 2.1, showing the six degrees of freedom (DOF) which are treated as independent modes when evaluated using a frequency-domain solver.

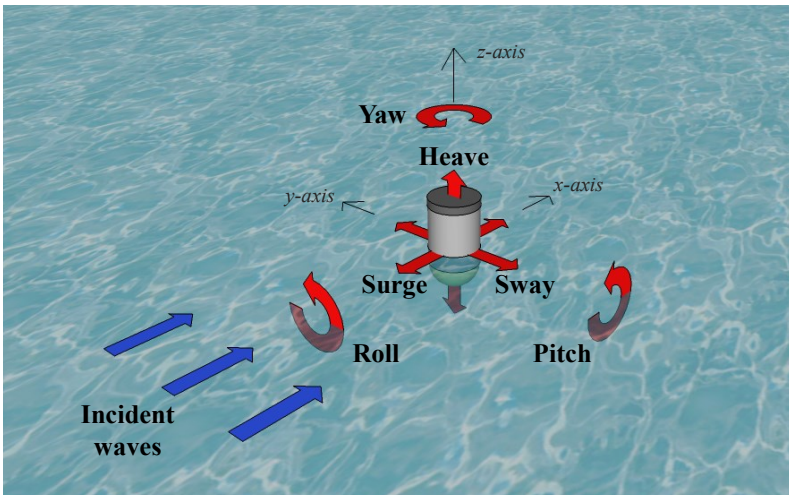

Figure 2.1: The independent modes, or degrees of freedom, of a simple floating system.

On a much more localised scale, the behaviour of water around, say, a coupling link in a complex multi-body device implies the need for a fully nonlinear solver that can capture the complex motion. There are many instances where viscosity can be ignored; however, careful consideration must be given to the effects of assumptions on the accuracy of a model. Some methods can account for viscosity and nonlinear effects; however, opting to resolve these more complex characteristics of a system will result in significant penalty with regard to processing time.

One of the pertinent considerations in the design of WECs is the degree of interaction between neighbouring devices in an array. It has long been understood that wave diffraction and radiation of surface piercing WECs can affect the response of other devices within the same array.

Within the array as a whole, these interactions can, in theory, result in a net negative or positive change to the array performance in terms of power capture. This effect is expressed using the array interaction factor, or *q-factor*, and as this widely used indicator of array performance appears throughout the literature, it is defined here, as:

$$q(\kappa,\beta) = \sum_{i=1}^{N} \frac{P_i(\kappa,\beta)}{N \times P_0(\kappa,\beta)}\,. \tag{2.1}$$

The power capture of a given WEC is denoted P_i, for the N WECs in the array. The power P_0 is the power capture of a single WEC in isolation, which will depend on the incoming wave condition, in terms of wavenumber κ, and on the wave heading, β. As the *q-factor* is strongly linked to the layout of the array, there will be a dependency on β even if the isolated WEC case is β-independent. The *q-factor* is generally used to assess the optimal design configurations for the array layout and for Power Take-off (PTO) control methodologies, which enforce some degree of controllability to the independent device motions. Where results indicate that $q > 1$, a net positive interaction effect is expected from that particular configuration.

2.1.2 Summary of the methods

A number of review papers have been published which summarise the applications of the various numerical methods. Folley *et al.* (2012) provide a review of hydrodynamic modelling of WEC arrays, giving benefits of each method by evaluating three characteristics: fundamental modelling ability, computational processing requirements and usability. This highlights issues such as code availability, stability and processing time. The authors also score the key numerical methods against their suitability to various types of study, showing relative merits. Another important review is that of Li and Yu (2012), who also consider the numerical methods available, specifically for modelling point absorber arrays.

A summary of hydrodynamic modelling methods is provided in Figure 2.2. Two distinct groups are apparent, the first including potential flow based codes (semi analytical, boundary element method) and CFD solvers, both of which are well suited to addressing the device interaction problem. Diffraction and radiation can be accurately modelled, giving realistic device responses within the scattered and radiated wave fields. Various assumptions can be made in order to give simplified representative models that are extremely efficient. Various extension can be incorporated into these models starting with the inclusion of basic time-dependent processes and external conditions, which necessitates translation to the time-domain. From this standpoint, it is possible to generate highly complex, yet relatively efficient computational models.

For situations which require more detailed treatment of highly nonlinear systems, it becomes appropriate to consider CFD. The computational expense however will always limit the scope of these methods, and whilst the various commercial packages are relatively accessible as

design tools, specific model cases should be scrutinised carefully to verify that the implementation is appropriate. One of the main aims of this thesis, is to examine this thought process. In later chapters, relatively intensive methods are used to assess a weakly nonlinear system, which could be argued as excessive. This would certainly be the case if CFD was used universally for all numerical modelling. Once again, however, it is proposed here that a limited and careful selection of CFD simulations are used to examine the nonlinear processes in some detail (including viscosity). It is possible that this information could be used to enhance time-domain derived results using nonlinear external loading. This has been highlighted in Chapter 8 as an important area for future work.

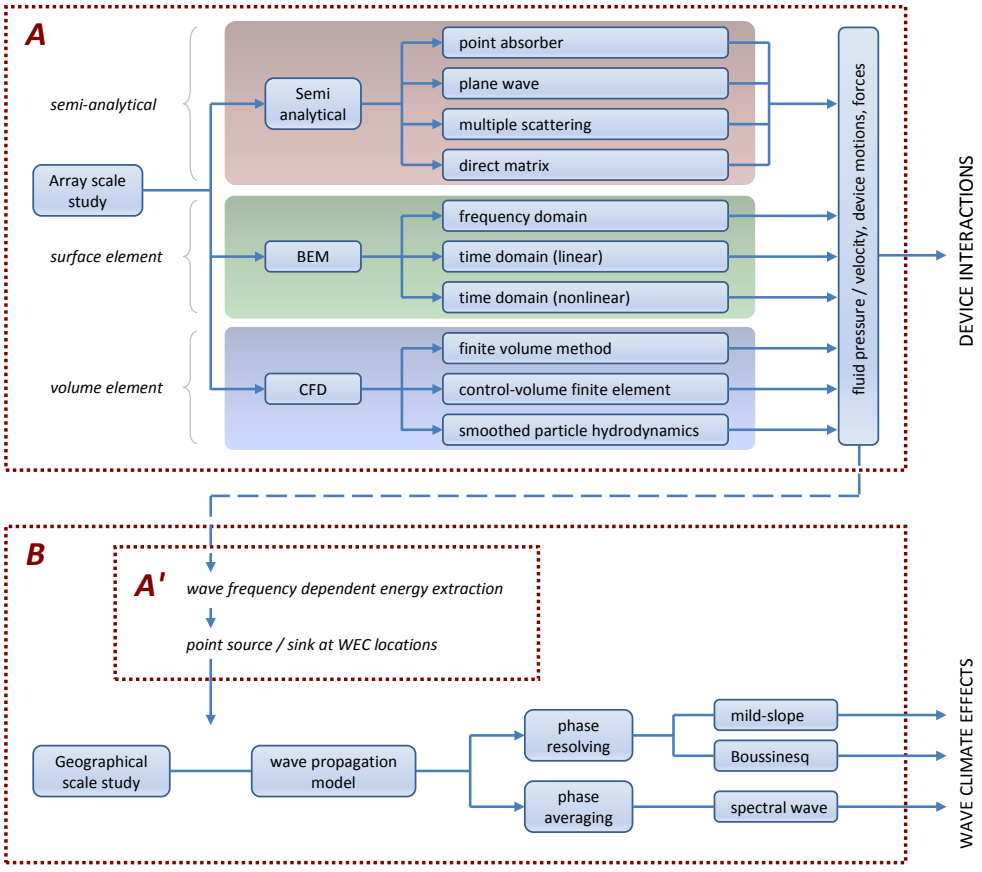

Figure 2.2: Schematic showing the available numerical methods for WEC hydrodynamic design.

The second group of methods highlighted in Figure 2.2 include those used for evaluating the far-field effects due to the presence of an array of WECs. These codes model wave propagation through a larger geographical scale domain, approximating the effects of energy extraction for a real ocean site, with capacity to model ecological and morphological changes around a WEC

array. These can be phase-resolving or phase-averaging techniques, and can capture the various coastal processes that are observed on a medium to large scale. Examples in literature of the applications of these methods are described in Section 2.3.

2.2 Array-scale hydrodynamic modelling methods

To evaluate the interactions between multiple moving bodies and the surrounding fluid, designers can employ either a potential flow method or CFD method. The potential flow methods include the Point Absorber (PA, see Table 2.1), Plane Wave (PW, see Table 2.2), Multiple Scattering (MS, see Table 2.3), Direct Matrix (DM, see Table 2.4) and Boundary Element Methods (BEMs, see Tables 2.5, 2.6 and 2.7). A wide range of CFD methods are available, including the widely-used Finite Volume (FV) method.

The above potential flow methods are considered semi-analytical (with the exception of BEM) in that assumptions may be assessed objectively to construct a bespoke numerical model for the specific problem posed. The semi-analytical methods generally require highly-specific knowledge and experience of the particular case studied; being of particular interest in academia, and early stage prototype development. All of the above methods for direct hydrodynamic modelling – semi-analytical, BEM and CFD – require a considerable amount of skill, however, only the latter two are in widespread use throughout industry. Whilst being more limited in terms of general applicability, semi-analytical methods can provide extremely useful validation data, which might otherwise be difficult to obtain.

Aspects of how these types of models are used are also discussed in Section 1.3.2, which forms part of the discussion on the current research objectives.

Section 2.2.1 provides discussions relating to the potential flow methods. In Section 2.2.2, applications of BEMs are described in the context of frequency-domain, time-domain and nonlinear models. Finally, CFD is addressed in Section 2.2.3.

2.2.1 Semi-analytical methods

The following provides a summary of semi-analytical methods, developed specifically for the multi-body interactions within an array of structures surrounded by a fluid. These were almost exclusively applied to notional WEC array problems, in order to understand the effect of device interactions. In general, these account for radiation and diffraction, with the aim of determining the interaction factor q (Equation (2.1)). The use of these methods generally implies a process of simplifying the physical problem by applying assumptions regarding, for example, omission of wave scattering for the PA method.

Point absorber method

The Point Absorber (PA) method has seen widespread application since it was introduced by Budal (1977). Some other key developments are given in Table 2.1. The individual body dimensions are assumed to be small compared to the incident wavelength, allowing the scattering effect on the incoming wave to be ignored. The *q-factor* can therefore be taken from the solution of the radiation problem alone, which is determined using the excitation forces and damping coefficients. As with the other semi-analytical methods, linear potential theory is used to formulate expressions to evaluate the velocity potential. It should be noted that the term 'point absorber' is often used to describe floating buoy type WECs in a more general sense, and does not always imply that the PA method is used.

Table 2.1: Point absorber research summary

Author (Reference)	Description
Budal (1977)	First array studies using the 'point-absorber approximation', partial optimisation is demonstrated, *q-factor* is defined and is shown to be capable of values greater than unity.
Evans (1979, 1980)	Amendment for the incorrect assumption of 'uniform amplitude of oscillation' in Budal (1977).
Falnes (1980)	As Evans (1979, 1980), independent derivation.
Thomas and Evans (1981)	Study regarding the applicability of the PA approximation when calculating the device displacements (as opposed to absorbed power which is known to be independent of device geometry).
Mei (1983)	Direct relationship provided for the external forces and damping coefficients.
Mavrakos and McIver (1997)	Comparison of the PA, MS and PW methods.

The PA approximation was used by Thomas and Evans (1981) to assess the power captured from arrays of sphere-shaped bodies, making use of the fact that with the PA approximation no knowledge of the precise device geometry is required in order to compute q. The authors essentially carry out an array optimisation study, considering variations in wavenumber κ, device spacing d and wave heading β. A strong variance of q with device spacing is demonstrated for unconstrained motions, with values in the range $0.6 < q < 2.2$ found over a relatively narrow range of the geometric parameter, κd. Constrained motions were also studied, noting that the large displacements experienced for the unconstrained cases were considerably larger than the incident wave amplitudes, and were therefore in violation of linear wave theory.

A modified excerpt of the results presented in Thomas and Evans (1981) has been regenerated below in Figure 2.3. For simple rectilinear arrays of five and ten bodies (arranged in a single row and double row layouts), the absorption length l_{abs} was evaluated by Thomas and Evans

(1981), and was normalised using the dimensional parameter, a, which represented the wave frontage of each device in the array. Opting instead to normalise using the device diameter and the number of devices ($l_{abs}/2aN$), the results can be presented as shown in Figure 2.3. With respect to the performance parameter $l_{abs}/2aN$, the following is observed:

1. $l_{abs}/2aN = 1.0$ implies the array captures as much energy as it 'sees' from the incident wave (i.e. $l_{abs} = 2aN$). This will however be less than the energy from N isolated devices, i.e. mean *q-factor* is less than 1,
2. $l_{abs}/2aN < 1.25$ gives a mean *q-factor* of less than 1,
3. $l_{abs}/2aN > 1.25$ gives favourable interactions, i.e. a mean *q-factor* of greater than 1.

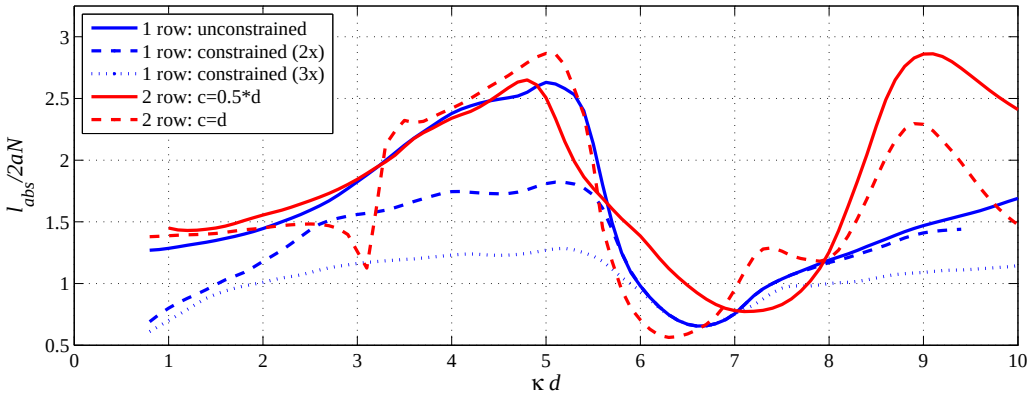

Figure 2.3: WEC array performance results from Thomas and Evans (1981) (regenerated and re-scaled for the present work). κd is a geometric parameter (product of wavelength and device spacing) and the normalised absorption length ($l_{abs}/2aN$) describes the array performance. Arrays with two rows are separated by the distance c.

Mavrakos and McIver (1997) carried out detailed studies on arrays of five equally spaced truncated cylinders using the PA, PW and MS methods (described later in this section). As the 'exact' MS approach is known to represent accurately the total wave field around each body, this was used to benchmark the comparative study. Two values were chosen for the ratio of device spacing over radius $d/a = 5,8$. The authors found that the results for the PA method show reasonable agreement for longer wavelengths, up to around $\kappa a < 1.0$ and $\kappa a < 1.4$ for $d/a = 5,8$ respectively, and beyond this large discrepancies are found. The better performance of the PA method at wider device separations is to be expected, as the no-scattering approximation applies.

Plane wave method

The Plane-Wave (PW) method assumes that the devices are widely spaced, ignores evanescent waves and approximates non-planar outgoing waves as plane waves. This produces a set of simultaneous equations for the plane wave amplitude, allowing straightforward assessment of the hydrodynamic interactions after the scattering and radiation problems are solved for a single device. In this respect it can be regarded as a simplified variant of the direct method described later in this section. A summary of research using the PW method is given in Table 2.2.

Table 2.2: Plane wave research summary

Author (Reference)	Description
Simon (1982)	Adoption of a 'plane-wave approximation' when accounting for scattered waves interacting with neighbouring devices.
McIver (1984)	Extended Simon (1982) with inclusion of a correction term, giving greatly improved results when applied to relatively compact arrays.
McIver and Evans (1984)	Extended McIver (1984) to include evaluation of added mass and added damping.
Mavrakos and McIver (1997)	Comparison of the PA, MS and PW methods.

The PW method is applicable to a wide range of problems and has demonstrated good performance in evaluations of the wave amplitude down to a surprisingly close device spacing. Early application of the PW method emerged from work by Simon (1982), in which simplifications were sought for representations of the scattered component of the wave field. These simplifications assumed that the bodies were axisymmetric, widely spaced and body motions were in heave only, giving a method which sits somewhere between the PA and MS methods, in terms of efficiency and accuracy.

McIver and Evans (1984) modified Simon's solution by including a correction term, consequently making a marked improvement to the accuracy. The authors confirmed good correspondence between body forces obtained using their method and that of the 'exact' method by Spring and Monkmeyer (1974). Linton and Evans (1990) also used Spring & Monkmeyer's exact method to compare the more onerous free-surface elevations, again finding good agreement down to a relatively close device spacing. Unlike the forces, the wave amplitudes are not integrated quantities, making the potential for errors much more significant.

In the previously referenced comparative study by Mavrakos and McIver (1997), the authors show that the hydrodynamic forces can be accurately calculated using the PW method. There may however be errors in the forces measured within the array, with these errors increasing with array size. Erratic behaviour is found for very long wavelengths due to an inversion procedure applied to the damping matrix. The onset of this instability of the PW method

(shown in Figure 7, in Mavrakos and McIver (1997)) occurs at $\kappa a \approx 0.45$ and $\kappa a \approx 0.275$ for $d/a = 5,8$ respectively. By normalising the wavenumber to account for the device spacing d, this instability appears to fall in the range $1.8 < \kappa d < 1.9$. This result is shown in Figure 2.4, using results which have been regenerated from the original study. Pending additional work, this instability may provide a useful working limit for PW studies.

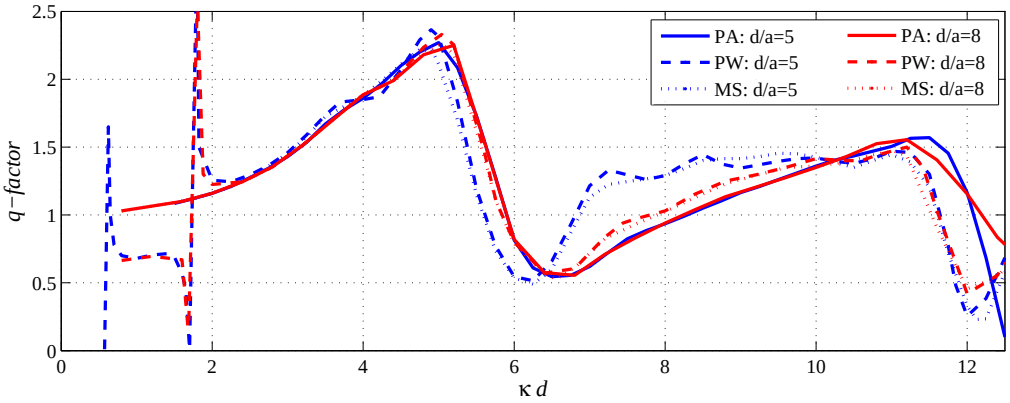

Figure 2.4: Array performance results from Mavrakos and McIver (1997), using the PA, PW and MS analytical methods (the results are regenerated and renormalised for the present work).

Multiple scattering

The Multiple Scattering (MS) technique takes the superposition of the various propagating and evanescent waves scattered and radiated by the array. The computations are simplified due to the fact that there is no need to retain simultaneously the spectra of partial wave amplitudes around all the individual bodies, as the boundary conditions for each are satisfied successively. Twersky (1952) introduced this theory in an acoustic application, Ohkusu (1974) then applied it to floating bodies. Table 2.3 gives a summary of research activity for the MS technique.

Table 2.3: Multiple scattering research summary

Author (Reference)	Description
Twersky (1952)	Twersky studies the effects of scattered waves, scattered again by adjacent objects.
Ohkusu (1974)	Application of Twersky's Twersky (1952) acoustic multiple scattering technique to floating bodies (four legs of an oil platform).
Mavrakos and Koumoutsakos (1987)	Extension of Ohkusu (1974) of to include evanescent waves.
Mavrakos and McIver (1997)	Comparison of the PA, MS and PW methods.

The effect on a wavefield caused by any number of fixed obstructing objects is not just the

sum of the scattered components of this incident wave at each obstruction, but the sum of the scattered incident wave plus the scattering of the scattered waves (first order scattering), and scattering of those waves (second order scattering), and so on. Twersky (1952) asserted that these effects are not necessarily as insignificant as had been previously believed because phase alignments may cause small scattered interference to superpose into much larger spikes, as confirmed by existing experimental anomalies in the field of acoustics and electromagnetics. This lends itself well to the problem of interactions between closely spaced WECs in water waves where multiple scattering interference is generally significant. Ohkusu (1974) adopted this multiple scattering approach, adding radiating components for the case of floating (and hence oscillating) bodies.

This methodology was extended in Mavrakos and Koumoutsakos (1987); Mavrakos (1991) to include evanescent waves with solutions for arbitrary numbers of vertically axisymmetric bodies (in any array configuration with any individual body geometries). Any number of orders of interactions may be obtained to give the total wave field.

Direct matrix

A summary of research using the Direct Matrix (DM) method is given in Table 2.4. The term direct matrix is associated with methods that perform an exact analytical assessment of a problem in which the boundary conditions are applied directly to all bodies simultaneously, allowing all unknowns to be evaluated in a single matrix inversion procedure. The velocity potential for any field point is calculated by taking the superposition of the incident wave and all scattered waves for each of the N bodies in the problem. To evaluate the wave amplitudes at each body, the set of equations that result are split into their real and imaginary parts. The force components on the bodies are finally evaluated after integrating the pressure on the wetted surface of each body.

Spring and Monkmeyer (1974) first carried out this technique for a two cylinder, bottom mounted problem. They found that, when compared to a single cylinder, forces increase by as much as 60% to 65%. The authors also noted that the force ratios obtained from their studies were periodic with variation of device spacing, resembling the Bessel functions that are used to translate local coordinate frames. As the application of this particular method is limited to simple bottom mounted geometries, it can only contribute to evaluations of certain types of WECs, such as Oscillating Water Columns (OWCs).

Kagemoto and Yue (1986) carried out an exact method (as far as is possible using linearised theory) to give the wave excitation forces, hydrodynamic coefficients and second-order drift forces in a selection of array problems, including that of floating bodies. This combines the work of Spring and Monkmeyer (1974), Simon (1982) and Ohkusu (1974), becoming applicable to a far wider range of WEC problems due to the inclusion of evanescent waves. It is executed using only the diffraction interactions from a single body and hence removes the need

Table 2.4: Direct matrix research summary

Author (Reference)	Description
Spring and Monkmeyer (1974)	Introduced the direct matrix method and applied this to a pair of bottom mounted cylinders identical and dissimilar.
Kagemoto and Yue (1986)	Combined the direct matrix method of Spring and Monkmeyer (1974) with the MS technique of Ohkusu (1974) and extends applications to floating bodies.
Linton and Evans (1990)	Rework of Spring and Monkmeyer (1974) with inclusion of significant simplifications. Applies to bottom mounted cylinders.
Yilmaz and Incecik (1998)	Use is made of Kagemoto and Yue (1986) along with the solution by Garrett (1971), applied to a group of truncated cylinders.
Chakrabarti (2000)	Extends the direct matrix method with further efficiencies, applied to floating bodies.
Child and Venugopal (2010); Child (2011)	Adaptation of Yilmaz and Incecik (1998) with a direct application in WEC array research. Supplementary optimisation routines (parabolic intersection and genetic algorithms) are also used.

to evaluate all of the *n-order* scattering components for the other bodies interfering with the incident wave. The authors found excellent agreement of their solution with the exact Hybrid Element Method (HEM) of Yue *et al.* (1978), in which an entire array is modelled in one assessment.

Other more recent work on the DM method include Linton and Evans (1990), a rework of the method by Spring and Monkmeyer (1974) in which a major simplification is identified. This again applies only to bottom mounted cylinders and may find more applications in studies of fixed offshore platforms. The authors ultimately find very efficient expressions for the free surface amplitude, for both the near-field and far-field regions.

Child and Venugopal (2010) used the direct method, whilst also arranging the array layout of buoy type WECs using two optimisation techniques: a Genetic Algorithm (GA) and an approach termed Parabolic Intersection (PI). Using a partial wave notation, based on the assumption that the components can be combined linearly, a set of discrete expressions were used to describe the scattered and radiated wave fields.

Because GAs are simply optimisation routines, their application is not limited to the DM method. Child and Venugopal (2010) demonstrated that they are particularly well suited to problems in which an absolute optimum solution is not deemed essential. It would usually be

assumed that this type of problem would take a long time to solve using more conventional methods and in many cases, there would be limited knowledge of the rational optimisation functions. Given the complex nature of interactions within an array of WECs, a GA routine can be used to rapidly generate acceptable solutions.

The PI method employed in Child and Venugopal (2010) involved a more analytical approach, positioning devices on the peaks of waves that were diffracted by neighbouring devices. Each WEC can be positioned in a way that maximises the constructive interference with its neighbours, so that the scattered waves are in phase with incident waves as they reach the neighbouring device. PI identifies very regular shaped array layouts, which tend to be symmetrical and highly sensitive to changes in incident wave direction. The highest *q-factors* obtained by Child and Venugopal come from application of their GA method, rather than PI. In the GA case it has been accepted that an element of randomness exists with the generation of the array shapes.

2.2.2 Boundary element methods

The Boundary Element Method (BEM) is a well-established technique used to study floating bodies using potential flow theory. Wetted surfaces are panelled, either into planar surface elements or curved patches, using splines. Pressure fluctuations at the surfaces result in a normal force, applied at the centre of each element, which can then induce body motions. Other external constraints can be included, allowing representation of the mechanical stiffness and damping characteristics of a power take-off system. BEMs can be simplified by formulating in the frequency-domain, however use of the time-domain enables the inclusion of non-linear external loads and non-linear hydrodynamics.

An outline requirement of BEMs is that there must be an appropriate Green's function solution to translate the volume problem into a surface problem. This allows the evaluation of the velocity potential in the whole fluid domain. Added complexity when dealing with nonlinear codes includes discretisation of the free surface, which changes upon every time step. This allows any floating bodies to reorientate prior to the application of the Green's function.

Frequency-domain BEMs are considered a fairly standard approach in hydrodynamic modelling. More recent efforts to model control problems, nonlinear external loading and time varying responses have resulted in a shift towards time-domain modelling. Even with these added complexities, these methods tend to be highly efficient, without the need for High Performance Computing (HPC). Given their capacity to model many degrees of freedom (e.g. DOF$>$20), these methods are both versatile and powerful, with some examples dynamically linked to secondary models, such as in wave-to-wire codes (Forehand *et al.*, 2015). The existing literature is discussed in the following subsections, along with some more general application of the frequency-domain methods. It is noted here that many of the time-domain codes rely on an initial frequency-domain solution.

Linear BEM (frequency-domain)

Codes such as WAMIT, ANSYS AQWA, Aquaplus and Nemoh operate in the frequency-domain, and are generally used to provide matrices for the added mass $A_{ij}(\omega)$, added damping $B_{ij}(\omega)$ and excitation force X_i caused by mode i. These terms are required in order to evaluate the complex excursion amplitudes $\hat{\xi}_j$ using equation (2.2):

$$\sum_{j=1}^{6MN} [-\omega^2(M_{ij}+M_{ij}^E+A_{ij}(\omega))+\mathrm{i}\omega(B_{ij}(\omega)+B_{ij}^E)+(C_{ij}+C_{ij}^E)]\hat{\xi}_j = X_i, \tag{2.2}$$

where ω is the oscillation frequency, $\mathrm{i}=\sqrt{-1}$, M_{ij} is the mass matrix and C_{ij} is the matrix of hydrostatic and gravitational coefficients. The system will comprise $6MN$ modes, where M is the number of unconstrained body modes associated with each body, and N is the number of bodies (either coupled or independent). The externally applied mass M_{ij}^E, damping B_{ij}^E and stiffness C_{ij}^E matrices in equation (2.2) can be tuned in order to control the motion of the WECs in a desirable way, such that power output is maximised. Applicability of the linear BEM codes requires that the hydrodynamic problem is suitably linear, and that the motion of any floating bodies remains small compared to wave height. Larger excursions that can alter the hydrostatics of a WEC must be captured in the time-domain.

Table 2.5 provides a brief summary of research carried out using frequency-domain BEMs, which includes two examples of hybrid models. Matsui and Tamaki (1981) used a BEM to evaluate hydrodynamic parameters of each device within an array, with the subsequent interactions calculated using an MS approach. Goo & Yoshida carried out a similar process using a BEM for the single devices and then applying the DM method to account for the interactions.

Table 2.5: Boundary element method, frequency-domain research summary

Author (Reference)	Description
Matsui and Tamaki (1981)	BEM used for hydrodynamic properties of each device, with interactions between devices calculated using a multiple scattering approach.
Goo and Yoshida (1990)	BEM used for hydrodynamic properties of each device, with interactions between devices calculated using a direct matrix approach.
Chakrabarti (2000)	As Goo and Yoshida (1990) with simplifications.
Cruz *et al.* (2010)	Resolution of inter-device hydrodynamic interactions for an array in an irregular sea-state.

Cruz *et al.* (2010) presented a linear BEM solution as the basis for a software tool (GH Wavefarmer), designed to evaluate the effects of array geometry and wave farm control. Their study assumed an array of four heaving cylinders set out at the four corners of a square with excitation forces generated by an irregular Bretschneider spectrum. The influence of

the nondimensional wave frequency *ka* on the *q-factor* is investigated. The authors make a comparative assessment between these preliminary results and the semi-analytical methods by Yilmaz and Incecik (1998) and Siddorn and Eatock Taylor (2008), both of which agree well. The array is then studied in irregular waves in two scenarios - tuned (in damping only) to give discrete control terms for each WEC, then tuned by applying the same control term to all four WECs, adopted from a preliminary single WEC analysis. Neither case is optimised for the irregular sea for all time, thus each term can be described as passive for that sea. A more complex active control would ensure that external loading on each WEC would suit each representative wave group frequency within the irregular sea state. Control terms in the external stiffness matrix C_{ij}^{E} can also be introduced to give reactive control. By introducing additional degrees of freedom and multi-body WECs the control philosophy will become more complex still.

Interesting comparisons are also presented for arrays responding to equivalent Bretschneider and JONSWAP spectra, using a range of PTO settings. The results of this study are shown in Figure 2.5.

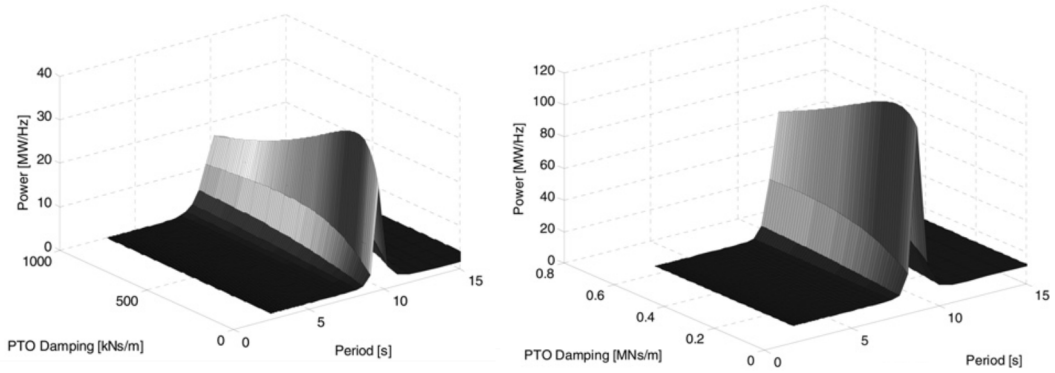

Figure 2.5: Power capture results from equivalent arrays, responding to Bretschneider and JONSWAP wave spectra (from Cruz *et al.* (2010)).

Linear BEM (time-domain)

In order to study transient system responses or consider nonlinear external loading it is necessary to construct models in the time-domain. If a linearised solution is acceptable, it is possible to use a frequency-domain model to determine hydrodynamic coefficients and then convert to the time-domain, or to evaluate directly in the time-domain using an appropriate solver. The convolution terms that arise from the time-domain formulation are problematic however, irrespective of the approach. Table 2.6 provides a summary of developments in time-domain modelling of wave energy systems.

Taghipour *et al.* (2008) presented an excellent summary on system identification for time-domain formulation. The various methods for convolution term replacement are described

Table 2.6: Boundary element method, time-domain research summary

Author (Reference)	Description
Cummins (1962)	Considered the boundary value problem in which the potential was separated into two parts — one valid during the impulse and the other valid afterwards — to give the Cummins equation.
Ogilvie (1964)	Developed relationships between the time-domain and frequency-domain responses, i.e. relating equations (17) and (19).
Taghipour *et al.* (2008)	Considered a system identification procedure for a hybrid frequency/time-domain model.
Westphalen *et al.* (2011)	A study of two different array control strategies, one tuning to the incident wave only and the other to incident wave and scattered and radiated waves from neighbours.
Babarit *et al.* (2012) &	"Wave-to-wire" modelling, in which the time-domain response provides a time history of power output to the grid.
Forehand *et al.* (2015)	A "Wire-to-wave" model, which imposes dynamic grid constraints through the power take-off system, onto the moving components of a small WEC array.

in detail, with an example provided. The authors describe three possibilities that exist when transforming to a state-space representation of the frequency-domain results, and a fourth that allows direct computations in the time-domain. The hydrodynamic coefficients $\mathbf{A}(\omega)$ and $\mathbf{B}(\omega)$ are computed in the frequency-domain in the first three procedures to provide Rational Transfer Functions (RTFs) that can be fitted to state-space models. The fourth solution is evaluated in the time-domain only and hence no RTF is required. An estimate for the state space model is generated using the retardation functions $\mathbf{K}(t)$ only. Commercial software packages such as Achil3D are capable of carrying out these types of assessments.

As summarised by Taghipour *et al.* (2008), either $\mathbf{A}(\omega)$ or $\mathbf{B}(\omega)$ can in fact be used in the first procedure to provide a Frequency Response Function (FRF). This can be used to generate an RTF, which is then converted into an ordinary differential equation, and then a state space model. The second approach requires the coefficients $\mathbf{M}$ and $\mathbf{C}$ as well as $\mathbf{A}(\omega)$ and $\mathbf{B}(\omega)$ to evaluate either force-to-motion or force-to-velocity FRFs. The RFT is then evaluated and fitted to a state-space model using regression techniques. The third procedure uses $\mathbf{A}(\omega)$ and $\mathbf{B}(\omega)$ to find the frequency response $\mathbf{K}(j\omega)$ before the RFT is fitted to the state-space model.

Time-domain studies on a simple two body array have been carried out by Westphalen *et al.* (2011), adopting two different control strategies. The first establishes externally applied control terms by tuning the WECs independently, considering only the incident wave forces when

optimising the PTO characteristics. The second control method considers the incident wave force, plus the force from the additional effects of diffraction and radiation caused by the other WEC. It transpired that the two methods give similar results except when the devices were closely spaced and sea states were small, i.e. when the relative effects of radiation are prevalent. This suggested that an independent device controller was adequate and hence preferable to a more complex global array controller.

Babarit *et al.* (2012) present work using a Wave-to-Wire (W2W) model, in which the performance of eight different WEC devices are compared at five different sites along the European coastline. Hydrodynamic parameters are initially obtained using a frequency-domain BEM code, with subsequent inclusion of nonlinearities in the derived time-domain models to account for viscous losses and the effects of end stops (a result of real device constraints). The authors make their final comparisons using three parameters that relate the device's effectiveness to its construction and control characteristics, in order to make some outline economic observations. These parameters are the absorbed energy per characteristic mass $[kWh/kg]$, the absorbed energy per surface area $[kWh/m^2]$, and the absorbed energy per root mean square of the PTO force $[kWh/N]$. From this evaluation, the authors find that the performances of the different device types are comparable with the exception of the bottom-fixed oscillating flap, which scores less favourably in characteristic surface area calculations.

Fully nonlinear BEM (time-domain)

The linear solutions presented thus far give relatively rapid evaluations of a floating body problem. The nonlinear time-domain models naturally require more computational effort. Examples of nonlinearities include effects resulting from increased wave steepness and nonlinear hydrostatics. The latter of these can be significant for a number of device classes, including attenuators. Treatment of these nonlinear hydrodynamic effects involves meshing of the free surface, and reorientation of the floating bodies upon every time-step.

A summary of work using nonlinear BEM techniques is given in Table 2.7. A series of developments in nonlinear potential flow hydrodynamics followed from the work of Longuet-Higgins and Cokelet (1976), through to the application of a nonlinear method by Kashiwagi (2000) to two wedge profiles, representative of the mid-section and bow of a ship's hull. The mixed Eulerian-Lagrangian method introduced by Longuet-Higgins & Cokelet was adapted in various publications, each seeking simplifications to the nested problem. The major complication appears when attempting to address the temporal derivative of the velocity potential $\dot{\phi}(= \partial\phi/\partial t)$ that appears within Bernoulli's pressure equation. The motion of any floating body under study is obtained using the solution of $\dot{\phi}$; however, to evaluate $\dot{\phi}$ the motion of all floating bodies must be known.

The problem is generally approached as a boundary value problem, where use is made of Laplace's equation to describe the fluid motion in the interior of the domain, and Bernoulli's

Table 2.7: Boundary element method, nonlinear time-domain research summary

Author (Reference)	Description
Longuet-Higgins and Cokelet (1976)	Introduced the mixed Eulerian-Lagrangian method.
Wu and Eatock Taylor (1996)	Application of an artificial function to replace the time derivative of the velocity potential. This simplification is carried out to decouple the dependency on the body acceleration due to the waves.
Kashiwagi (2000)	Application of the method used by Wu and Eatock Taylor (1996) to a sections of a ship's hull, supported by scale testing.
Field (2013)	Presents results from a number of linear, nonlinear and blended BEMs, to provide validation of a CFD model of a ship's hull.

equation to define a zero pressure condition at the free surface. Bernoulli's equation is used again to evaluate pressures and resulting force and moment integrals over the body surfaces, giving rise to changes in the motion of the floating body at each time step. The fluid domain boundary condition on the body itself is a function of the body motion. As the body velocity can be obtained using information from the preceding iterations, the problematic terms within the body surface boundary condition are those describing the body's acceleration. Wu and Eatock Taylor (1996) (adopting an approach previously used by Lighthill (1979) and Molin (1979) to study second-order diffraction force problems) proposed decoupling this dependency by solving for an artificial function ψ_i instead of $\dot{\phi}$, allowing a simultaneous solution of the acceleration and velocity potential in what was previously two separate boundary value problems.

It is widely known that second-order wave loadings are the main source of slow drift forces in slack moored floating bodies. Second-order drift forces can be obtained from the linear BEM results using the Haskind relations, which give a convenient solution to the problem without explicit evaluation of the second-order potential.

A number of nonlinear BEM codes are summarised by Telste and Belknap (2008) and Field (2013). These include LAMP-4 (SIAC-Annapolis), NFA (SAIC-La Jolla) and NSHIPMO (Univ. of Michigan), and also a range of blended linear/nonlinear codes, including LAMP-1 and LAMP-2, AEGIR-2 (Applied Physical Sciences and Flight Safety Technology) and FREDYN (Marin). The blended codes have been developed in order to achieve a degree of nonlinearity where possible, typically treating Froude-Krylov force component* and hydrostatics as nonlinear, and addressing the more difficult radiation and diffraction using a linear approximation

*The Froude-Krylov force component considers the underlying effects from the ambient wave conditions, excluding any secondary diffraction or radiation effects.

Field (2013). There is currently no evidence that these codes have been applied to wave energy conversion.

2.2.3 Computational fluid dynamics method

The application of Computational Fluid Dynamics (CFD) to the study of wave energy conversion is becoming increasingly common. In general, research into wave energy applications of CFD is at a less mature stage than with other forms of hydrodynamics solvers, especially with regard to WEC arrays. A key obstacle to the wider application of CFD is the processing requirements for relatively basic studies, usually restricted to a single WEC. CFD solvers do however provide solutions that account for highly nonlinear processes, giving an approximate solution to the full Navier-Stokes equations, accounting for viscosity and turbulence. Studies involving arrays must be simplified due to the prohibitive computational requirements, and at present there are very few studies that demonstrate this. It is noted here that accurate representation of the free-surface is notoriously difficult using CFD codes, often making Validation and Verification (V&V) an arduous process.

Given the capacity of CFD to model complex nonlinear problems, it is possible to model floating or partially constrained structures in extreme wave conditions, evaluating slamming forces, overtopping/green water and wave breaking, as well as important phase information for all dynamic load considerations. This has proved to be a particularly useful application for CFD, which cannot be demonstrated using other methods. There are also examples of studies involving WECs operating under normal conditions; however, evidence of validated cases are uncommon. The latter subject is tackled using less computationally intensive methods, and indeed further evidence is required on the treatment of the wave radiation problem using the relatively recent free surface resolving CFD codes. A summary of research into the use of CFD for wave energy is provided in Table 2.8.

Fluid-structure interaction

In terms of free surface flow around a structure, the existing literature fits broadly into two categories: studies involving structures that move in a known and prescribed manner (including static/fixed structures), and studies involving a free or partially constrained moving body, which responds dynamically to pressure and velocity variations in the flowfield. The latter is termed Fluid-Structure Interaction (FSI), which requires an additional motion solver component within the CFD application in use[†]. This type of study allows an explicit two-way calculation that accounts for the time-varying forces on the body caused by the fluid, and the force and boundary constraint changes reciprocated by the body.

[†]A commercial example of an FSI solver is the 'Dynamic Floating Body Interaction' (DFBI) component within Star-CCM+. The open source CFD application OpenFOAM provides this functionality via 'interDymFOAM'.

Table 2.8: Computational fluid dynamics (CFD) research summary

Author (Reference)	Description
Yang *et al.* (2005)	Dam break is used as an example of extreme wave loading, on 1, 2 and 4 fixed cylinders (not directly applied to WECs).
Agamloh *et al.* (2008)	Application of CFD to two buoy WEC array (cylinders) resolving body motions directly using CFD.
Westphalen *et al.* (2009)	Detailed comparison of four different CFD codes applied to WECs.
Hu *et al.* (2011)	Application of AMAZON-SC to a cylinder with hemispherical base, floating and validated.
Bonfiglio *et al.* (2011, 2013)	Application of OpenFOAM and 'interDyMFOAM' motion solver, various geometries, validated.
Yu and Li (2013)	Development of a two-body floating WEC model using STAR-CCM+, validated against experimental data.
Ransley *et al.* (2013)	Investigation of wave impact loading on a fixed cylinder using OpenFOAM, validated against experimental data.
Palm *et al.* (2013)	Direct coupling of a finite element mooring solver with OpenFOAM and 'interDyMFOAM' motion solver.

An example of extreme event modelling can be found in Hu *et al.* (2011) who used an in-house package AMAZON-SC 3D to model a Manchester Bobber type device. This code employed a Godunov-type free surface capturing scheme and a Cartesian cut cell method for solid body motions. The diffraction problem was validated against experimental data from tests on a fixed cylinder, showing good correlation. The numerical model was then modified to predict the response of a floating Bobber type device in extreme waves, without further validation. The solvers used in that study accounted for FSI, where the motion of the body was derived from the dynamic forces in the fluid, and vice-versa. Ransley *et al.* (2013) provided another example of a validated fixed cylinder study. Extreme wave conditions were replicated in a wave tank at 1:30 scale to validate a CFD model built using the open source library, OpenFOAM. Encouraging results were provided along with interpretation of the discrepancies.

The radiation problem has been investigated by Bonfiglio *et al.* (2011), who took a particular interest in data from earlier physical tests (Vugts, 1968) and examined the viscous effects experienced by circular and square sections to sway, roll and yaw motions. Both this and an extended study (Bonfiglio *et al.*, 2013) used OpenFOAM, where the air-water interface was treated using the Volume Of Fluid (VOF) method, and again FSI was addressed. Results were presented in terms of the added mass and damping coefficients and were generally in good

agreement with the experiments and theoretical results.

Field (2013) used the commercial package STAR-CCM+ by CD-Adapco to model the same experiments by Vugts (1968), before going on to produce a numerical model to predict the solutions to the diffraction and radiation problems for a ship hullform. The CFD model was accompanied by results from potential flow based codes. The VOF method was used within the STAR-CCM+ model with a segregated flow solver; however, FSI was not accounted for, as the body's motion was prescribed. Both the k-ε and Shear-Stress Transport (SST) k-ω RANS turbulence models were used. Again, the hydrodynamic coefficients derived from both the CFD and potential flow codes generally compared well with the experiments.

STAR-CCM+ was also used by Yu and Li (2013), who considered a two body floating point absorber. That particular system harvests power via the relative motion between the two bodies, the float on the water surface, and a submerged heave plate. The study incorporated FSI and differs from Field (2013) by employing a Lagrangian-Eulerian method for cell movement and deformation. Validation cases are provided for the WEC constrained as a single rigid body, and as two independent moving bodies, making this one of the most advanced published CFD studies involving a WEC.

An example of a dynamically coupled CFD simulation can be found in Palm *et al.* (2013), where OpenFOAM has been linked to a secondary moorings solver through an Application Program Interface (API). FSI was modelled for a floating vertical cylinder, constrained by four mooring cables. The results provided by Palm et al. were not validated at that stage; however, application of the API was demonstrated effectively.

Finally, a series of interesting studies have been presented by Bhinder *et al.* (2011, 2012, 2015) in which CFD has been employed to predict viscous drag on a generic heaving device and surging flap. The authors draw from a long history of work (Stokes, 1851; Morison *et al.*, 1950; Sarpkaya, 1976, 1981; Bearman *et al.*, 1984, 1985; Zheng and Dalton, 1999) on oscillatory flow, and along with other more modern work (Yuan and Huang, 2010) advocate the continued use of the Morison equation for implementation of a viscous drag term. A time-domain code was used along with CFD to evaluate radiation, diffraction and wave-structure interaction cases. Extending the results to annual power production estimations, the inclusion of the viscous drag term was attributed to a significant reduction in power for a surging flap, at 64% of the inviscid case. While the heaving WEC saw far more modest viscous effects (4% reduction), the WECs considered were full scale (10-15m characteristic length) and so the relative drag due to viscosity is far smaller than it would be in a reduced scale tank test, as is considered in the present work. No physical data were presented in those studies, although the detailed methodology for the incorporation of drag forces into potential flow code was demonstrated effectively.

2.3 Geographical scale studies

Global and regional scale numerical wave modelling is an active area of research, undertaken at various research and commercial institutions for wave climate forecasting and hindcasting, using models like WAM 4.5, WAVEWATCH III, SWAN, TOMAWAC, MIKE 21 and Delft 3D. In terms of the more recent application to wave energy, existing literature include examples of modelling wave energy extraction processes to evaluate the resulting impact on the wave climate. The scarcity of field data for this specific purpose means that validation is problematic. Even so, the literature indicates that this methodology might serve as an important preliminary assessment tool for energy extraction at real sites, and also as a key technique for Environmental Impact Assessments (EIAs).

In general wave models can be classified as 'phase resolving' or 'phase averaged'. This section gives an explanation of the various methods and applications with this distinction in mind.

2.3.1 Phase-resolving methods

Mild-slope and Boussinesq methods are phase resolving methods that consider the conservation of mass and momentum to evaluate the free surface elevations with respect to time. The mild-slope and Boussinesq equations themselves represent equivalent linear and weakly nonlinear descriptions respectively. A summary of research work using each of these methods is provided here. The spectral wave (phase averaging) method, which considers an energy balance to investigate how the spectrum evolves, is covered in Section 2.3.2.

Mild-slope method

The mild-slope method treats wave diffraction and refraction over a mildly varying water depth, where it is known that wavelengths and amplitudes will also vary. The dependence of wavenumber κ on water depth can be inferred from the dispersion relation. A new expression is therefore required for the free surface elevation η, on which a number of publications have reported variations of the same result (Mei, 1983), including an early derivation by Berkhoff (1972). The form used in the MILDwave solver for example[‡], which emerged from the work of Troch (1998), takes the depth integrated form of the mild-slope equations (originally provided by Radder and Dingemans (1985)):

$$\frac{\partial \eta}{\partial t} = \left(\frac{\omega^2 - \kappa^2 \bar{C}\bar{C}_g}{g}\right)\varphi - \nabla \cdot \left(\frac{\bar{C}\bar{C}_g}{g}\nabla\varphi\right) \quad , \qquad \frac{\partial \varphi}{\partial t} = -g\eta \tag{2.3}$$

Equation 2.3 describe the evolution of the free surface elevation with time, where either the velocity potential φ or free surface elevation η can be eliminated to give a single time-dependent

[‡]http://www.ugent.be/ea/civil-engineering/en/research/coastal-bridges-roads/coastal-engineering/infrastructure-services/mildwave

mild-slope expression. Here, t is time, g is acceleration due to gravity, ω is wave frequency, $\bar{C}$ is the phase velocity and $\bar{C}_g$ is group velocity.

Table 2.9: Mild-slope method research summary

Author (Reference)	Description
Berkhoff (1972)	Introduces free surface elevation calculations over a mildly varying water depth. (Other authors are credited with similar work shortly after.)
Radder and Dingemans (1985)	Provide depth integrated forms of the mild-slope equations.
Troch (1998)	Makes use of the method provided by Radder and Dingemans (1985), to develop the MILDwave software code.
Mendes *et al.* (2008)	Carried out an assessment of a floating (Pelamis) WEC using REF/DIF software. Wave radiation was not included.
Beels (2009)	Includes wave radiation from a motion based WEC (FO3) in a hybrid solution involving WAMIT (BEM).

A summary of research using the mild-slope equations is provided in Table 2.9. The provision for spatial dependency of water depth and wavenumber makes the mild-slope equations well suited to near coast problems with traditional application to coastal defence, breakwaters, harbour design and environment impact assessments. This has been readily extended to applications in wave energy conversion processes, particularly for fixed WECs, e.g. overtopping devices and OWCs. Power extraction is not implicitly solved, however sponge layers have been shown to give effective representations of WEC absorption characteristics.

A number of studies have also applied the mild-slope method to problems with floating bodies. Mendes *et al.* (2008) carried out an assessment of the Pelamis device installed at the offshore pilot zone in Portugal using REF/DIF mild-slope software with some auxiliary modifications. Beels (2009) went a step further and carried out an evaluation of a motion based device (FO3) in MILDwave and included radiated wave inputs from an independent WAMIT solution. This approach took the radiation outputs from WAMIT and reproduces a corresponding and similar wave response in the MILDwave model from a circular generation line that surrounds the WEC. Those results were compared to the full WAMIT diffraction and radiation results for a single FO3 device and showed reasonable agreement. Application of the mild-slope solver in this way avoided the unmanageable burden on computational resources that would otherwise be necessary to model a large scale array of multiple-float devices.

A common problem with phase-resolving models is suitable treatment of the domain boundaries. Specific boundary conditions must be specified in order to avoid waves being reflected

back towards the area of interest. This includes the boundaries that lie behind any wave generation lines (absorption boundaries and generation lines are discrete). For irregular and omni-directional long crested waves, Beels (2009) gave a good comparative study of generation line configurations, finding a U-shape to be the most effective at generating wave components in the range $0^\circ < \beta < 90^\circ$. Short crested waves were also considered, with the directionality of the separate components accounted for via a spreading factor s.

Beels (2009) introduced a single obstruction to represent an array of devices. This simplified arrangement gave results that were $\pm 40\%$ that of a complete BEM evaluation of the array. On the basis of that result, the author suggested that any economic evaluations of proposed schemes should take a more onerous route, modelling discrete WECs in a solver that can account for interactions. Ultimately, these types of mild-slope studies remove the difficult coupling of the reflection and transmission which is present in Boussinesq methods, but also allows detailed modelling of geometric configurations within the array, something which is not possible with the spectral wave models.

Babarit *et al.* (2013) also presented interesting results from a combined BEM and mild-slope procedure. A similar approach to that of Beels (2009) was used, where interaction effects local to the device were addressed using a BEM (Aquaplus). The resulting solutions were used to calibrate wave properties at a circumscribing generation line in a mild-slope solver (ARTEMIS, a module of Telemac-Mascaret), in order to propagate wave characteristics to the wider domain. The novel approach allowed direct application of boundary conditions through use of far-field coefficients generated by the BEM, known as the Kochin function. This efficient approach yields encouraging results for the simple WEC geometry considered, with accuracy depending on the size of the cylindrical boundary that separates the BEM and mild-slope domains.

Boussinesq models

The linear theory discussed above requires the ratio of wave amplitude and water depth to be small, i.e. the nonlinearity $A/H << 1$. When studying a wave as it approaches a coastal area, the combined effects of reduced water depth and shoaling mean the hydrodynamics can become highly nonlinear. The Boussinesq equations are well suited to this type of problem as they omit the vertical components of the wave equations. This happens to be a reasonable assumption that addresses the fact that the circular particle motions associated with deep water waves become distorted in shallow water. Another important parameter in the derivation of the Boussinesq equations is the dispersion μ^2 ($\equiv (\kappa H)^2$), where in the limiting cases $(A/H) \to 0$ and $\mu^2 \to 0$, the solution becomes linear. Numerical codes that implement variations of the classical Boussinesq equations include the MIKE21 Boussinesq Wave software, first developed by Madsen and Sørensen (1992).

Boussinesq models have been used in the context of wave energy conversion to model interactions around fixed structures such as OWCs or overtopping devices, as summarised in

Table 2.10: Boussinesq method research summary

Author (Reference)	Description
Madsen and Sørensen (1992)	Enhancement of the classical Boussinesq equations in the time-domain, for implementation into the MIKE21 BW software.
Venugopal and Smith (2007)	Investigation of the wave disturbance coefficients in front of and in the lee of an array of 5 large terminator type devices (e.g. Wavedragon) at EMEC site.
Venugopal *et al.* (2010)	Investigation of the wave disturbance coefficients in front of and in the lee of an array of 5 OWC type devices at various spacings and wave frequencies (EMEC site.)

Table 2.10. Venugopal and Smith (2007) used a Boussinesq model (MIKE21) to investigate changes to the wavefield around an array of five hypothetical overtopping devices. Sponge layers were configured around the boundary of a domain (measuring 5×4.5km) representing a coastal region to the west of the Orkney Isles, UK. Waves were generated along lines within the domain, with input conditions provided by a much larger spectral wave model (130×110km, also validated against buoy data). The authors evaluate wave disturbance coefficients h_{wdc} (local significant wave height, normalised by the input significant wave height) in the direction of wave propagation at each WEC location. Venugopal and Smith (2007) found that the wave amplitude is between 13% and 69% lower in the lee of the WECs depending on porosity. The wave amplitudes exhibit partial recovery at a distance of around 500-600m in lee of the array regardless of porosity, which might suggest a suitable location for a second row of OWCs.

A specific challenge when modelling OWCs is the quantification of radiation characteristics. The mechanisms by which power is captured from the waves is very different from that of a moving structure, i.e. via the control of air pressures within the chamber. Implicit modelling of this second fluid phase is not possible by any means other than CFD. These system characteristics can however be given semi-empirical representation as an explicit modelling condition. Venugopal *et al.* (2010) used experimental reflection results independently reported by Thiruvenkatasamy and Neelamani (1997), Tseng *et al.* (2000) and Goda (1985) to determine their solutions for the wave radiation condition. Sponge layers were introduced to represent wave absorbing surfaces within the model, including PTO, enabling control of radiation at each surface. An iterative investigation was carried out at each wave period in order to resolve sponge layer properties. The authors concluded that the array spacing and peak wave periods were both factors that affect wave disturbance coefficients. The maximum disturbances experienced under the incident JONSWAP wave condition peaked at +39% upstream and -41% downstream of the array.

The benefit of using Boussinesq codes in the above applications is that they are capable of resolving a comprehensive set of hydrodynamic mechanisms. These include the combined effects of diffraction, refraction, shoaling, wave breaking, nonlinear wave-wave interactions, bottom dissipation, partial wave reflection and transmission from structures, directional wave spreading and internal wave generation. Solid and permeable structures can be modelled; however, objects in the flow domain must be fixed to the ocean floor (e.g. OWCs), as there are no means to account for the dynamics of a moving object.

2.3.2 Phase averaged spectral wave model

Spectral wave models are based on the principle of wave action conservation, where wave action is a ratio of spectral density to intrinsic frequency. In contrast to other methods that focus on predictions of the surface elevation, the spectral wave methods are phase-averaging, predicting how the characteristics of a wave evolve with time. This method originated from the idea that the ocean waves could be decomposed into components of various frequency, amplitude and direction. The JONSWAP project (Hasselmann *et al.*, 1973) was an important step in the development, with 1st, and then 2nd–generation models emerging from such work, with the latter including parametrised representations of nonlinear waves generated by the wind (Komen, 2004).

A later collaboration titled WAM provided the first of the 3rd–generation models that explicitly included these nonlinear waves. WAM is commonly used, along with other global wave prediction models such as WAVEWATCH III, to provide input boundary conditions to other solvers intended for local or coastal interaction studies, such as SWAN (Delft University of Technology) and TOMAWAC (Electricité de France). The inherent difficulty in validating such large scale models has been overcome through use of data from satellite programmes including SEASAT, GEOSAT and ERS-1 (Komen, 2004). Other notable developments in the spectral wave methods are provided in Table 2.11.

Global wave models (WAM, WAVEWATCH III, etc.) and local models (SWAN, TOMAWAC, MIKE21 SW, etc.) work on similar principles, with the latter including additional descriptions for shallow water behaviour. Local models can theoretically execute oceanic scale problems; however, this inevitably proves unnecessary and inefficient.

It is common for both model scales to use a spherical coordinate system; however, it can be more convenient to work with a Cartesian system at the smaller scale. Discretisation of the local domain can be achieved using structured or unstructured grids. Structured grids can feature more refined nested grid(s) in regions of greater interest, whereas with an unstructured grid it is possible to have a continuously variable cell density. Care must be taken to ensure that the grid captures all relevant seabed features and avoids oversimplified step changes, as model bathymetry is interpolated between grid points (Delft University of Technology, 2011; Millar *et al.*, 2007). These methods have been applied to real sites, including Wave Hub (Millar *et al.*,

Table 2.11: Spectral wave method research summary

Author (Reference)	Description
Pierson (1953)	Application of the concept of ocean wave spectra.
Gelci *et al.* (1957)	Introduced concept of an empirical spectral transport equation.
Phillips / Miles (1957)	New theories of wave generation published.
Hasselmann (1960, 1962, 1963)	Source function for nonlinear transfer derived.
The SWAMP Group (1985)	Distinction made between first and second generation spectral wave models with an assessment of nine existing techniques.
The WAMDI Group (1988)	Introduction of improved physics and a two way wave-wind coupling (WAM).
Holthuijsen *et al.* (1993)	Introduction of the SWAN (Simulating Waves Nearshore) model.
Millar *et al.* (2007)	Application of SWAN to studies affecting the coastal wave climate with a proposed WEC test site (Cornwall, UK).
Le Crom *et al.* (2008)	Application of SWAN to studies affecting the coastal wave climate with a proposed WEC test site (Portugal).
Folley and Whittaker (2009)	*Investigations relating to* control parameter effects in arrays and responses to an irregular wave climate (sub-optimal control).

2007; Smith *et al.*, 2012) and the Portuguese Pilot Zone (Le Crom *et al.*, 2008) to establish the impact on the wave climate following the theoretical installation of a wave farm at each site.

At Wave Hub, Millar *et al.* (2007) and Smith *et al.* (2012) used SWAN to examine the impact on the surrounding wave climate following a reduction in spectral energy density at the array location. Various configurations of barrier and transmission coefficients were used. Millar *et al.* (2007) imposed this reduction in energy equally across all wave frequencies, whilst Smith *et al.* (2012) used a frequency dependent power transfer function. The latter study is understood to be a significant improvement in terms of accuracy, as this accounts for the varying efficiency with which the notional array extracts energy across the frequency spectrum.

Folley and Whittaker (2009) used a linear spectral wave model to investigate the effects of device control within an array in order to find an alternative benchmarking basis from the theoretical maximum power capture of an optimally controlled array. In particular, the authors highlight that the relative performance differences between optimally and sub-optimally controlled arrays may not be that large and that theoretical energy outputs of actively controlled arrays are likely to be overestimated by idealised models. As the geometry of an array is

strongly affected by mooring considerations, access, power smoothing and site utilisation, it may be these factors that have a greater impact on the final design of installed arrays rather than the hydrodynamic interactions.

Some limitations of spectral wave models are discussed by Beels (2009). In applications associated with wave energy conversion, spectral wave assessments tend to have too coarse a grid to model individual WECs, relying instead on modelling an array as a single object, omitting the redistribution of energy within the array. The author also notes concern over methods used which extract energy evenly across all frequencies, although this has since been addressed by Smith *et al.* (2012). Beels also notes that the diffraction feature in SWAN is less accurate when swell waves are dominating, a condition in which the impact on the coastal wave climate is most severe.

2.4 Recent activities

The Seventh Framework Programme (FP7) was an EU initiative which ran from 2007 to 2013, with a key objective being to align research activities with the social and economic needs of the present day. Over 18,000 projects were recorded on FP7, with these spread across a diverse range of themes. A number of projects dealt directly with the development of WECs or combined marine energy systems involving wave energy, with this list including HYDRALAB IV [22], MARINA PLATFORM [23], PolyWEC [24], WAVEPORT, CORES and H2OCEAN. A group of other projects have investigated research coordination and technology enabling (MARINET, EquiMar, WAVETRAIN2 and ORECCA,) with other related work including GeoWAVE, and NUMERIWAVES.

In the UK, the SuperGen UK Centre for Marine Energy Research [§] has been responsible for a vast and broad range of research output for a number of years. This and a number of other research initiatives are supported by the Engineering and Physical Sciences Research Council (EPSRC). UKCMER has recently completed its third phase (October 2011 to September 2016) with its focus on Accelerated Deployment of Marine Energy (coupled 3D modelling, monitoring technology and extreme loading events) and a series of grand challenges: work on novel and future generation concepts; very deep water systems; new materials; very large array systems; instrumentation for extreme environments; very short timescale resource prediction; marine energy platforms and civil integration of large systems.

[§] http://www.supergen-marine.org.uk

2.5 Concluding remarks

2.5.1 Literature summary

The preceding review gives an account of numerical methods available for quantifying hydrodynamic interactions between WECs and the impact of a wave farm on the surrounding wave climate. By considering these two matters, this leads to a distinction between modelling methods, the first of which concerns the hydrodynamic effects due to the presence of a WEC, both on the device itself, and on the other devices in the vicinity. The second relates to wave energy transport to the wider domain. The first of these concerns is the primary focus of this thesis, and as such this literature review has examined the near-field models in greater detail.

Near-field hydrodynamic models

For evaluations of the immediate hydrodynamic effects around a WEC and the resulting interactions with other WECs, traditional analytical methods give approximations that are very much dependent on the underlying assumptions. Given the right range of conditions the methods can be quite useful. Furthermore, the multiple scattering and direct matrix techniques have proven to be fairly accurate for a range of applications. It is worth noting that the required level of skill for these methods can be high, and that processing time can increase rapidly with the number of WECs. The review by Folley *et al.* (2012) provides a very useful summary of these considerations, tabulated against the other methods discussed here.

Linear potential flow theory can also be applied using a BEM. This can provide solutions for devices of any shape, and is a well-established tool in marine engineering disciplines. The nature of interactions between devices can be extracted in the frequency-domain, and reasonably accurate estimations of power production can be obtained. When translated to the time-domain, time dependent processes can be incorporated into models to account for non-linear external loading, dynamic control strategies, transient system behaviour and nonlinear hydrostatic loading. Fully nonlinear BEMs can also be studied in the time-domain. This allows the investigation of more extreme conditions, capturing free surface dynamics, but also entails the increased computational effort of having to continually discretise the free surface.

A further option for device interaction modelling involves application of the Navier-Stokes equations in a CFD solver. This type of investigation will capture viscous effects and turbulence and can give an extremely detailed picture of the hydrodynamics close to the device of interest, providing the model is configured correctly. Generation of realistic waves can prove difficult, but the overbearing consideration when using a CFD code is the time taken to execute analyses. Very few studies have demonstrated application to problems with more than one WEC. Evidence from literature suggests that Reynolds-Averaged Navier-Stokes (RANS) and spectral wave explicit Navier-Stokes Equation (SWENSE) solvers are receiving attention. Recent topics

include the controlled and coupled dynamics of a single floating WEC, and advanced models for extreme wave loading.

Far-field hydrodynamic models

The second category of codes discussed in this review are the geographical scale wave propagation models. Methods that resolve phase descriptions of the wave components include the mild-slope and Boussinesq codes, which solve for conservation of mass and momentum. In contrast, the phase-averaged spectral wave methods model the evolution of wave components by solving the relevant energy balance equations. Generally speaking, spectral wave models are less accurate than phase-resolving methods; however, their ability to model very large domains, even on a global scale, make them extremely useful for resource assessments and for environmental impact studies.

Chapter 3

Background & Theory

The background and theory is presented in this chapter for the numerical models used in Chapters 5 to 7. As an extension to the discussions provided in Section 1.3.2 on the motivation for this work, the outline classification of the problem is described first in this chapter, by considering nondimensional parameters and their specific application to the current problem. In particular, the motivation for challenging the Reynolds number threshold for considering viscous effects is explained, where for the case of a Wave Energy Converter (WEC) array, viscous effects *may* have significant implications, even when the relative magnitudes appear small.

In Section 3.2, the underlying and fundamental principles of linear wave diffraction and radiation theory are provided. This includes: descriptions of the fluid using linear potential theory and the rigid body motion dynamics that characterise the behaviour of the floating device(s). This is followed, in Section 3.3, by descriptions of the time-domain modelling procedures, which provide time varying, linearised predictions of the device displacement, wave elevations and forces, equivalent to the transient physical processes experienced in the tank tests. These models rely on the derived results from the frequency-domain models described in Section 3.2. Section 3.4 follows this with theory relating to the Finite Volume (FV) Computational Fluid Dynamics (CFD) method, which can capture nonlinear processes, and incorporate the effects of viscosity into the numerical predictions.

Both commercial software and research codes were used to deliver the numerical results in later chapters. The application of the theory in Section 3.2 was carried out using the Boundary Element Method (BEM) code: WAMIT* (WAMIT: Version 7, 2012). The time-domain modelling described in Section 3.3 used MATLAB and SIMULINK based codes, originally by Forehand *et al.* (2015), with some modifications for the specific application here. This was supplemented using MATLAB-based code for impulse response modelling, prepared during the present work. All CFD modelling, as described in Section 3.4, was carried out using the commercial code: STAR-CCM+ v10.04 (CD-Adapco, 2015), with post processing carried out using MATLAB.

*http://www.wamit.com

3.1 Problem classification

3.1.1 Characterisation of viscous effects

In the existing literature, the array interaction factor, or q-factor, is often raised as an important consideration when designing a WEC array. Due to the prevalence of this parameter[†], one of the objectives raised for the present work was to provide a methodology for determining how viscosity can affect array performance. The traditional indicator of viscous effects is the Reynolds Number – the ratio of inertial and viscous effects – which is a convenient way of interpreting the expected behaviour of a flow regime. The question becomes: is the traditional limit for discounting viscosity applicable to wave energy arrays? A possible reason this might not be the case is that compound effects are experienced at both 'source and sink ends' of the wave energy transport process, i.e. the radiated waves. Furthermore, although viscous effects may be negligible between fluid 'particles', this does not guarantee that viscous effects are negligible at the body surfaces.

Reynolds number

The processes that lead to positive array effects ($q > 1$) are reliant on independent fluid-structure interaction systems for each moving body. Non-negligible viscous effects may be present for each of these independent systems. In any normal circumstance where an external flow would be considered susceptible to viscous effects, the Reynolds number would be of the order 1×10^4 or less (Hughes, 1993). In the present work, the Reynolds number is[‡]:

$$Re = \frac{\rho \omega l^2}{\mu_w} \approx 4.9 \times 10^5 \tag{3.1}$$

where ρ is the density of water, μ_w is the dynamic viscosity of water, ω is wave frequency and l is the characteristic length of the body in question. This Reynolds number is representative of oceanic conditions, whilst also being considerably higher than the above threshold for viscous effects. What this states is that the viscous effects within the fluid are several orders of magnitude smaller than the inertial effects. This is not to say, however, that viscosity does not play a role within the boundary layer. It is these very localised effects which are examined in detail in later chapters in order to quantify the effects on array interactions.

It is worth noting that any form of damping, including relatively small viscous effects, can cause a significant change in the motion path of a floating WEC system. The much larger forces – gravitational and inertial – are *reactive*, in that they primarily interchange with one another whilst oscillating. The viscous forces, however, combine with wave radiation and other forms

[†]The q-factor can be linked directly to energy yield calculations, and linked indirectly to financial evaluations.

[‡]This Reynolds number definition is in agreement with oscillating body case described in Newman (1977), where caution was also advised against discounting viscosity near body surfaces without specific cause.

of parasitic damping losses, to interact with the *active* force of the power take-off mechanism. In frequency-domain formulations of these systems (see Section 3.2.2), the active and reactive power components are represented by the real and imaginary parts of the complex power respectively. Energy leaves the system via the real part: through the power take-off system, through outward wave radiation (characterised by added damping) and through dissipative losses. In general for both reduced scale model designs and large-scale open water systems, every effort should be made to minimise the latter, which comprises of mechanical friction and viscous effects.

Nondimensional frequency parameter

The nondimensional frequency parameter, which is equivalent to the Froude number for an oscillating system, is defined as follows (Newman, 1977):

$$\omega\left(l/g\right)^{1/2} \approx 1.0 \tag{3.2}$$

where g is acceleration due to gravity. As should be expected for free decay of a floating body, this ratio of gravitational and inertial forces is close to unity. While the discussions above stated that viscous effects were potentially of interest, the viscous forces *within* the fluid are very small compared to the forces due to gravity and inertia (i.e. the Reynolds number is large). In this respect, it follows that the system should scale with Froude number. Again, however, the concerns examined in this work relate to the effects that viscosity has within the boundary layer, and on the rigid body motion of the devices studied. The above Reynolds numbers and nondimensional frequency parameter (which has replaced the Froude number) do not, for example, account for any descriptions of body shape, surface area, surface roughness etc., which may affect the body forces and motion response[§]. For the simple body configurations and arrays studied in this work, discussions relating to the relevance of viscosity are provided in later chapters.

Froude scaling of parameters

Due to the particular focus on reduced scale testing in the present work, it is of interest to note the relationship between scale and the various system parameters for a WEC system. These are summarised in Table 3.1.

A specific complication when working with small scale wave energy converter models is the scaling of the power take-off measurements. When dealing with power capture magnitudes that would be in the kW range for a full scale device, the factor $s^{3.5}$ reduces this power to mW levels for devices of, say, 1:50 scale. The reduced scale mechanical systems that then transfer

[§]These factors are affected by viscosity where, for example, two different WECs might experience contrasting effects due to viscosity, depending on the complexity of their geometries (Payne, 2008).

Table 3.1: Froude scaling law, from Payne (2008)

Quantity	Scaling	Quantity	Scaling
angular acceleration	s^{-1}	linear stiffness	s^2
wave frequency	$s^{-0.5}$	power density	$s^{2.5}$
angular velocity	$s^{-0.5}$	linear damping	$s^{2.5}$
angular displacement	1	mass	s^3
linear acceleration	1	force	s^3
wave period	$s^{0.5}$	power	$s^{3.5}$
linear velocity	$s^{0.5}$	torque	s^4
wave height and length	s	angular stiffness	s^4
linear displacement	s	angular damping	$s^{4.5}$

this power are commonly overcome by friction, making it difficult to extrapolate the useful output of a full scale equivalent system. Equally, bearing friction and external loads from other sources, such as potentiometers sensors, cause similar issues. These can also be difficult to control and difficult to characterise, especially if they are nonlinear. Furthermore, if they are measurable in magnitude during a small scale test at 1:50, they would be up to six orders of magnitude larger in extrapolated full-scale results, when raised to the power 3.5.

3.1.2 Characterisation of nonlinear effects

Keulegen-Carpenter number

The Keulegan-Carpenter number (KC) for the present case is as follows:

$$KC = \frac{u_{max}T}{D} \approx 3.4 \tag{3.3}$$

where the natural period of oscillation $T_0 = 1.143$s, the maximum fluid velocity $u_{max} = 0.93$m/s and device diameter $D = 0.315$m. Interpretations of the KC number by Falnes (2002); Falnes and Hals (2012) have indicated that the ratio of the body excursions (ξ_j) to body radius is equally important. When these lengths are equal, i.e. $\xi_j/(D/2) = 1$, this results in $KC = \pi$. Furthermore, when $KC < \pi$, the flow around the oscillating system should be laminar, and when $KC \geqslant \pi$, vortex shedding is expected to occur. Based on the result from Equation (3.3), and on $\xi_j/(D/2) > 1$ for the initial stages of decay test, vortex shedding should be expected in the current problem. The results from the experiments and CFD results in Chapters 4, 6 and 7 confirm this behaviour, all of which show evidence of nonlinear wave patterns, associated with the WEC behaviour during early stages of the tests.

Bhinder *et al.* (2015) reported a KC number of 3.4 during studies of a similar system, sized at full-scale and notionally sited at EMEC (Orkney, UK, significant wave height, $h_{s,max} = 11$m). The theoretical device measured 10m in diameter, which corresponds approximately to the equivalent full-scale construction of the models studied in this thesis.

Classification of waves

Further to the discussions above regarding nonlinear processes, such as vortex shedding, the nature of the waves themselves required classification before any involved analyses. Wave gauge data from the experiments were available for specific locations, the nearest to the wave source being positioned at $x = 5D = 0.1575$m, which showed peak wave heights of around $h = 8$mm. Preliminary models using WAMIT also provided wave heights in the immediate vicinity of the WEC, where h peaked at around 15mm. For the waves which were generated during the decay test, the following was identified from the data: $\omega_0 = 5.497$rad/s; $T_0 = 1.143$s; $\lambda_0 = 1.99$m. This fell into the intermediate water depth classification; however, it was close to the deep water case (the water depth H, was 0.7m).

The range of wave conditions which were experienced during the entire duration of the WEC decay tests are shown approximately in Figure 3.1, using an adaptation of the classic depiction by Le Méhauté (1976). This suggests that only a limited proportion of the overall results may have involved weakly nonlinear waves, which, for the conditions experienced, is not surprising. This would only be expected for a brief period at the start of the decay and would only occur

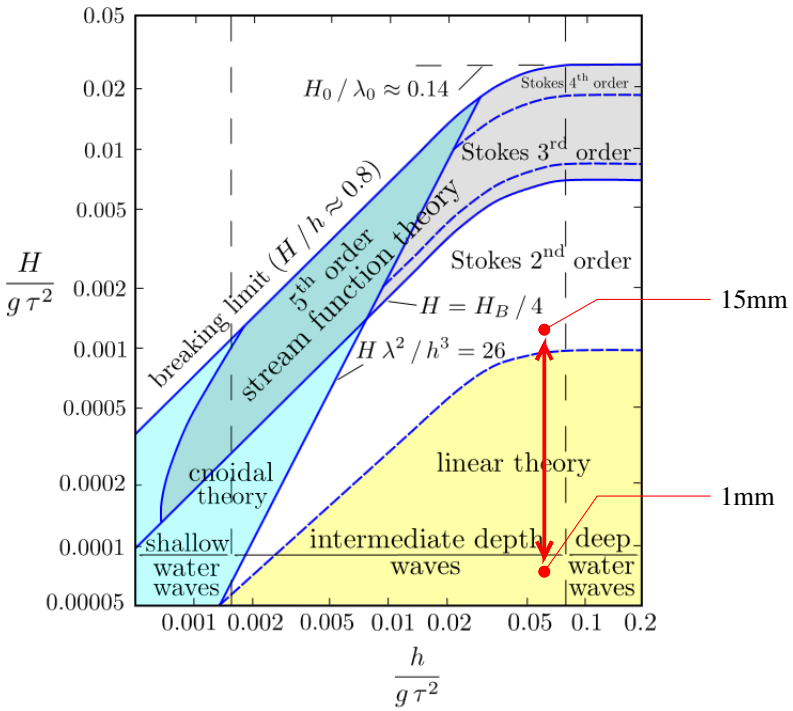

Figure 3.1: Le Méhauté (1976) diagram, depicting wave theory and characterisation (image by Kraaiennest - Own work, CC BY-SA 3.0, https://commons.wikimedia.org/w/index.php?curid=6601051). In the figure, H is wave height, h is water depth, τ is wave period, λ is wavelength and g is acceleration due to gravity.

very close to the WEC. Regarding the nonlinear waves identified in the data and numerical results, it is worth noting that tests carried out for various drop heights lower than $\xi_0 = 0.2$ (see Section 6.6.2) sustained similar nonlinear behaviour, even in cases where all conditions fell within the linear theory range in Figure 3.1.

3.2 Linear diffraction and radiation theory

A large amount of the existing research on WEC hydrodynamics concerns that of linear wave theory. A number of well-established resources exist on this subject, such as Newman (1977), Sarpkaya (1981), Mei (1983), Acheson (1990) and Falnes (2002). The specific application here uses WAMIT, a Boundary Element Method (BEM) code developed at Massachusetts Institute of Technology. The theory relating to this implementation in particular can be found in WAMIT: Version 7 (2012), which is described in this section.

In the WAMIT numerical code, the computations are executed sequentially using two subprograms. To deliver the required set of hydrodynamic descriptions of the fluid domain, the potential solution is evaluated for each relevant incident wave condition (all combinations of frequencies and directions) and each wave radiation condition from the moving bodies (for each degree of freedom in the entire system[¶], at all specified frequencies). This first computational stage is executed by the `POTEN` subprogram. Evaluation of the derived quantities, such as velocities, pressures, forces, free surface elevations and hydrodynamic coefficients, is delivered using the second stage `FORCE` subprogram.

Where solutions for a large numbers of frequencies and wave headings are requested, the `POTEN` subprogram can take a considerable time to run. Likewise, where a large number of panels are used to construct the solid geometries, this will have a direct effect on the number of unknowns required to solve the boundary value problem, which will increase run time. Due to the formulation of the solution in the frequency-domain on the other hand, the computations used to obtain the derived results are relatively rapid, and can therefore be recomputed efficiently. The hydrodynamic coefficients are fundamental to the time-domain evaluations, which are discussed in Section 3.3.

The theory and numerical procedures for the `POTEN` and `FORCE` subprograms are described in Sections 3.2.1 and 3.2.2, respectively.

[¶]The domain may contain multiple moving bodies, each with up to six rigid body modes, with the possibility of generalised modes between coupled structures.

3.2.1 The linearised hydrodynamic model

Basis for the linear model

Application of linear wave theory implies the following assumptions:

- water is incompressible, inviscid and irrotational;
- wave height is small compared to the wavelength and water depth;
- constant water depth;
- turbulence and surface tension effects can be neglected.

This set of assumptions allows substantial simplification of the mathematical descriptions of fluid flow. An irregular, multi-directional sea can be decomposed using the principle of superposition, provided that the wave steepness is sufficiently small. This notion of linearity relies on all of the assumptions listed above, these being discussed in more detail in the following subsections.

When the above assumptions are reasonable, this freedom to apply the superposition principle allows for solutions for single component harmonics to be recombined to form more complex fluid behaviour. This enables modelling of representative 'real sea' wave spectra, such as JONSWAP or Pierson-Moskowitz, and of multi-component scattering of diffracted and radiated waves around fixed or moving bodies.

Potential flow

The dynamics of the linearised floating body model follows from frequency-domain solutions which describe the kinematics of the simplified potential flow. In general, the principal assumptions behind this approach are that the fluid is inviscid, and is irrotational. Removing the effects of viscosity avoids the treatment of any diffusivity which would otherwise be present in the fluid. Fully irrotational flow also implies that the fluid must be inviscid; however, more specifically than this, the nature of the flow must be such that the curl of the velocity $\mathbf{u}$ is zero throughout the entire domain:

$$\nabla \times \mathbf{u} = 0 \tag{3.4}$$

From Helmholtz's theorem, any vector field can be decomposed into two components: a rotational field and an irrotational field. Having assumed that the rotational component of the velocity can be ignored, the velocity is purely irrotational, which implies that the following is true:

$$\mathbf{u} = \nabla\Phi \tag{3.5}$$

where Φ is the scalar velocity potential. As the kinematics may now be described in terms of the scalar field Φ, this condition can be combined with the continuity equation ($\nabla u = 0$) for incompressible flow to give Laplace's equation:

$$\nabla^2\Phi = 0 \tag{3.6}$$

This potential flow therefore has solutions which are harmonic in time. The flow may be described in the frequency-domain in terms of the complex velocity potential φ:

$$\Phi = \mathrm{Re}\{\varphi e^{\mathrm{i}\omega t}\} \tag{3.7}$$

where ω is the frequency of the oscillations in the flow and $\mathrm{i} = \sqrt{-1}$. It follows that all flow properties and physical descriptions of the system may adopt complex notation, characterised by the same frequency ω. Different solutions exist for the three discrete processes[‖] which may feature any number of independent frequency components, that of:

1. background wave conditions, described using φ_0;
2. the scattering of waves around solid bodies, φ_S;
3. wave radiation from moving bodies, φ_R.

The solution may involve a linear combination of multiple incident wave frequencies or wave headings (e.g. for spread, irregular seas), multiple scattering processes and multiple radiation processes. Unlike the highly nonlinear Navier-Stokes equations (see Section 3.4.1) for rotational and viscous flows, fundamental solutions exist for the linear system, for each of the discrete processes described above.

Due to the potential flow satisfying Laplace's equation, the fundamental solutions take the form of a Green's function, that of the *wave source potential* $G(\mathbf{x};\boldsymbol{\xi})$ (Lee and Newman, 2004). For infinite and finite water depths, the wave source potential is given by Equation (3.8), and Equation (3.9), respectively:

$$G(\mathbf{x};\boldsymbol{\xi}) = \frac{1}{r} + \frac{1}{r'} + \frac{2K}{\pi}\int_0^\infty \mathrm{d}\kappa\, \frac{e^{\kappa(z+\xi_z)}}{\kappa - K} J_0(\kappa R) \tag{3.8}$$

$$G(\mathbf{x};\boldsymbol{\xi}) = \frac{1}{r} + \frac{1}{r''} + 2\int_0^\infty \mathrm{d}\kappa\, \frac{(\kappa+K)\cosh\kappa(z+H)\cosh\kappa(\xi_z+H)}{\kappa\sinh\kappa H - K\cosh\kappa H} e^{-\kappa H} J_0(\kappa R) \tag{3.9}$$

where:

$$r = \sqrt{(x-\xi_x)^2 + (y-\xi_y)^2 + (z-\xi_z)^2}$$
$$r' = \sqrt{(x-\xi_x)^2 + (y-\xi_y)^2 + (z+\xi_z)^2}$$
$$r'' = \sqrt{(x-\xi_x)^2 + (y-\xi_y)^2 + (z+\xi_z+2H)^2}$$

In the above, the position vector $\mathbf{x}$ of the point of interest (with components x, y, z, with the datum at the free surface) and position of the point source $\boldsymbol{\xi}$ (with equivalent components ξ_x, ξ_y, ξ_z) are separated by R, with the datum height defined at the free surface. K and κ are the respective wavenumbers in infinite and finite water depth (H) and J_0 is the Bessel function of

[‖] These processes are assumed discrete in linear wave theory, however in reality, the complete system may be highly nonlinear.

order zero.

The resulting velocity potential for the scattered waves is as follows:

$$2\pi\varphi_S(\mathbf{x}) + \iint_{S_b} \varphi_S(\boldsymbol{\xi}) \frac{\partial G(\boldsymbol{\xi};\mathbf{x})}{\partial n_\xi} \, \mathrm{d}\boldsymbol{\xi} = -\iint_{S_b} \frac{\partial \varphi_0(\xi)}{\partial n} G(\boldsymbol{\xi};\mathbf{x}) \, \mathrm{d}\boldsymbol{\xi} \tag{3.10}$$

Wherever an incident wave is present (with amplitude A and heading β), this is defined as:

$$\varphi_0 = \frac{\mathrm{i}gA}{\omega} \frac{\cosh[\kappa(z+H)]}{\cosh \kappa H} e^{-\mathrm{i}\kappa x cos\beta - \mathrm{i}\kappa y sin\beta} \tag{3.11}$$

which may be combined with the wave scattering velocity potential φ_S to give an overall *diffraction velocity potential* ($\varphi_D = \varphi_0 + \varphi_S$), such that:

$$2\pi\varphi_D(\mathbf{x}) + \iint_{S_b} \varphi_D(\boldsymbol{\xi}) \frac{\partial G(\boldsymbol{\xi};\mathbf{x})}{\partial n_\xi} \, \mathrm{d}\boldsymbol{\xi} = 4\pi\varphi_0(\mathbf{x}) \tag{3.12}$$

Here, S_b is the wetted surface of the floating body and n represents unit normals.

The radiation potentials φ_R exist for every rigid body mode which is not fully constrained. The individual radiation potentials φ_j are linearly combined:

$$\varphi_R = \mathrm{i}\omega \sum_{j=1}^{6N} \xi_j \varphi_j \tag{3.13}$$

where ξ_j is the complex excursion of each of the six degrees of freedom (surge, sway, heave, pitch, roll and yaw), for N independent bodies. For all fixed modes, $\xi_j = 0$. In the present work, the radiation velocity potentials φ_j take the special *extended boundary integral equation* form, in order to remove the effects of irregular frequencies. This requires separate integrations over the submerged wetted surface S_b and the interior region** S_{int}, and uses the non-physical velocity potential on the interior surface, φ'_j:

$$\begin{aligned} 2\pi\varphi_j(\mathbf{x}) + \iint_{S_b} \varphi_j(\boldsymbol{\xi}) \frac{\partial G(\boldsymbol{\xi};\mathbf{x})}{\partial n_\xi} \, \mathrm{d}\boldsymbol{\xi} + \iint_{S_{int}} \varphi'_j(\boldsymbol{\xi}) \frac{\partial G(\boldsymbol{\xi};\mathbf{x})}{\partial n_\xi} \, \mathrm{d}\boldsymbol{\xi} \\ = \iint_{S_b} \frac{\partial \varphi_j(\boldsymbol{\xi})}{\partial n_\xi} G(\boldsymbol{\xi};\mathbf{x}) \, \mathrm{d}\boldsymbol{\xi} \qquad \mathbf{x} \in S_b \end{aligned} \tag{3.14}$$

$$\begin{aligned} -4\pi\varphi'_j(\mathbf{x}) + \iint_{S_b} \varphi_j(\boldsymbol{\xi}) \frac{\partial G(\boldsymbol{\xi};\mathbf{x})}{\partial n_\xi} \, \mathrm{d}\boldsymbol{\xi} + \iint_{S_{int}} \varphi'_j(\boldsymbol{\xi}) \frac{\partial G(\boldsymbol{\xi};\mathbf{x})}{\partial n_\xi} \, \mathrm{d}\boldsymbol{\xi} \\ = \iint_{S_b} \frac{\partial \varphi_j(\boldsymbol{\xi})}{\partial n_\xi} G(\boldsymbol{\xi};\mathbf{x}) \, \mathrm{d}\boldsymbol{\xi} \qquad \mathbf{x} \in S_{int} \end{aligned} \tag{3.15}$$

**This is a horizontal surface coplanar with the free surface, which intersects each of the bodies in the domain, and represents the portion of that body which rests above the free surface.

Finally, the velocity potential for the complete diffraction / radiation system is defined as:

$$\varphi = \varphi_R + \varphi_D \tag{3.16}$$

To complete the boundary value problem, the following condition is necessary at the linearised free surface:

$$\varphi_{z=0} - K\varphi = 0 \tag{3.17}$$

on $z = 0$. The surfaces of any solid boundaries in the domain are considered fixed at their hydrostatic resting position, and are characterised by the following conditions for the diffraction and radiation potentials:

$$\varphi_{Dn} = 0 \tag{3.18}$$

$$\varphi_{jn} = n_j \tag{3.19}$$

Discretisation of the integral equations

Frequency-domain solutions from the BEM code WAMIT (WAMIT: Version 7, 2012) are evaluated using the following discrete from of Equations (3.12), (3.14) and (3.15):

$$2\pi\varphi(\mathbf{x}_i) + \sum_{k=1}^{N_b} D_{ik}\varphi_k = 4\pi\varphi_0(\mathbf{x}_i) \tag{3.20}$$

$$2\pi\varphi(\mathbf{x}_i) + \sum_{k=1}^{N_b} D_{ik}\varphi_k + \sum_{k=1}^{N_{int}} D_{ik}\varphi'_k = \sum_{k=1}^{N_b} S_{ik}\left(\frac{\partial\varphi}{\partial n}\right)_k \qquad \mathbf{x} \in S_b \tag{3.21}$$

$$-4\pi\varphi(\mathbf{x}_i) + \sum_{k=1}^{N_b} D_{ik}\varphi_k + \sum_{k=1}^{N_{int}} D_{ik}\varphi'_k = \sum_{k=1}^{N_b} S_{ik}\left(\frac{\partial\varphi}{\partial n}\right)_k \qquad \mathbf{x} \in S_{int} \tag{3.22}$$

where the above includes the matrices:

$$D_{ik} = \iint_{s_k} \frac{\partial G(\boldsymbol{\xi}, \mathbf{x})}{\partial n_\xi}\ \mathrm{d}\boldsymbol{\xi}\,, \qquad S_{ik} = \iint_{s_k} G(\boldsymbol{\xi}, \mathbf{x})\ \mathrm{d}\boldsymbol{\xi} \tag{3.23}$$

Where required, Equations (3.20), (3.21) and (3.22) are evaluated at panel centroids of the discretised wetted surface geometries, of which there are N_b, and the panel centroids of the discretised interior free surface S_{int}, of which there are N_{int}. The final solution is sensitive to the resolution of these panels, due to the assumption that these are planar, and that the derived potentials are constant across each panel.

3.2.2 The oscillating body model

Forces

The model for the floating body system utilises the solutions for the velocity potentials, derived using the potential flow method described in Section 3.2.1 (i.e. the `POTEN` subprogram component of WAMIT). Evaluation of the derived quantities, including pressures and forces, is executed using the `FORCE` subprogram, which relates the potential solution of the fluid, to the rigid body motion of all moving bodies within the domain.

In the frequency-domain, the force balance which is used to determine the motion of the N floating bodies, is as follows:

$$\mathbf{F}^D(\omega) = \mathbf{F}^I(\omega) + \mathbf{F}^R(\omega) - \mathbf{F}^H - \mathbf{F}^E(\omega) \tag{3.24}$$

where $\mathbf{F}^D$, $\mathbf{F}^I$, $\mathbf{F}^R$, $\mathbf{F}^H$ and $\mathbf{F}^E$ represent the force components due to diffraction, inertial effects, radiation, hydrostatic restoring effects and external effects, respectively. The above force matrices (with dimensions $6N \times 6N$) are complex, leading to complex device motion responses $\hat{\xi}_j$. The terms on the right can be described using the complex motion derivatives: $\mathrm{i}\omega\hat{\xi}_j$ and $-\omega^2\hat{\xi}_j$ (where $\mathrm{i} = \sqrt{-1}$ and j is the mode of motion). The force associated with the inertia of a body of mass m_{ij}, for example, is given simply by Newton's second law:

$$\mathbf{F}^I = \sum_{j=1}^{6N} m_{ij}(-\omega^2\hat{\xi}_j) \tag{3.25}$$

The term on the left hand side of (3.24) is the external hydrodynamic force due to the diffracted wave field φ_D. This is caused by the combined effect of incident waves and scattered waves from reflections from all other surfaces in the domain[††]. The force resulting from the integration of the hydrodynamic pressure across the wetted surface of the body S_b, for any mode i, is defined as (WAMIT: Version 7, 2012):

$$F_i^D(\omega) = -\mathrm{i}\omega\rho \iint_{S_b} n_i \varphi_D \, \mathrm{d}S \tag{3.26}$$

The radiation force due to the motion of the body accounts for both the inertia of the fluid and the dissipative transfer of energy from the rigid body motion to the fluid domain. The inertia and damping effects are proportional to $-\omega^2\hat{\xi}_j$ and $\mathrm{i}\omega\hat{\xi}_j$, respectively, with the coefficients being added mass $A_{ij}(\omega)$ and added damping $B_{ij}(\omega)$. In the linear model presented here, the body has been assumed fixed in its hydrostatic resting position. The radiation forces are determined indirectly from the integration of the various radiation potentials φ_j at the fixed body surface,

[††]Wave scattering is accounted for from both moving and stationary bodies. Moving bodies are considered fixed at mean resting positions in the linear model.

via the hydrodynamic coefficients:

$$A_{ij} - \frac{\mathrm{i}}{\omega} B_{ij} = \rho \iint_{S_b} n_i \varphi_j \, \mathrm{d}S \tag{3.27}$$

$$\mathbf{F}^R(\omega) = \sum_{j=1}^{6N} (-\omega^2 A_{ij} + \mathrm{i}\omega B_{ij}) \hat{\xi}_j \tag{3.28}$$

When evaluating the body response in mode j, the linearised hydrostatics ($\mathbf{F}^H = \sum_{j=1}^{6N} C_{ij}\hat{\xi}_j$) and external forces from resistive or spring couplings ($\mathbf{F}^E(\omega) = \sum_{j=1}^{6N} (\mathrm{i}\omega B^E_{ij} + C^E_{ij})\hat{\xi}_j$) can be considered in Equation (3.24), to give:

$$F_i^D(\omega) = \sum_{j=1}^{6N} \Big\{ -\omega^2 \big(m_{ij} + A_{ij}(\omega)\big) + \mathrm{i}\omega \big(B_{ij}(\omega) + B^E_{ij}\big) + \big(C_{ij} + C^E_{ij}\big) \Big\} \hat{\xi}_j \tag{3.29}$$

where C_{ij} is the hydrostatic stiffness coefficient, and B^E_{ij} and C^E_{ij} are the coefficients of the externally imposed forces (damping force and spring stiffness force, respectively). The straightforward treatment of the derivatives by multiplication of $\mathrm{i}\omega$ highlights the ease with which the frequency-domain method addresses the floating body problem.

Power

To obtain power, the product of the forces and velocity is evaluated. It is instructive first to observe the complex relationship between the motion derivatives, and rewrite Equation (3.29) as:

$$F_i^D(\omega) \; = \sum_{j=1}^{6N} \Big\{ \; \mathrm{i}\omega \hat{\xi}_j (B_{ij}(\omega) + B^E_{ij}) \; + \; \Big[-\omega^2 \hat{\xi}_j \big(m_{ij} + A_{ij}(\omega)\big) \; + \; \hat{\xi}_j \big(C_{ij} + C^E_{ij}\big) \Big] \Big\} \tag{3.30}$$

The dissipative coefficients of the velocity, $B_{ij}(\omega)$ and B^E_{ij}, represent the forces which change the kinematics of the system over time. The various terms in the square brackets represent the forces which transfer 'stored' energy between kinetic energy and potential energy, in terms of inertial and spring forces. The net effect of these terms is zero over time, and in the absence of any dissipative terms, the two directly opposing forces would sustain purely harmonic motion. Considering the power associated with each process, Equation (3.31) follows, with the square brackets identifying reactive power driven by energy transfer processes, delivering instantaneous power from kinetic sources, $P_k(\omega)$, and potential sources $P_p(\omega)$:

$$P(\omega) = P_R(\omega) + \big[P_k(\omega) + P_p(\omega)\big] \tag{3.31}$$

where $P(\omega)$ and $P_R(\omega)$ represent the net power and dissipated power, respectively. The com-

plex power can be expressed as in Equation (3.32) (Falnes, 2002):

$$P_j = \frac{1}{2}R_j|\hat{\xi}_j|^2 + \mathrm{i}\frac{1}{2}X_j|\hat{\xi}_j|^2 \tag{3.32}$$

with the reactive power now represented by the imaginary term. Its coefficient X_j is referred to as the reactance, this being the imaginary part of the impedance:

$$Z_j = |Z_j|e^{\mathrm{i}\theta_j} = R_j + \mathrm{i}X_j \tag{3.33}$$

Here, R_j is the resistance in the system, which describes the realised loss in power over time due to dissipative processes.

The reactive power is finely balanced when at resonance, where $\theta_j = 0$. The phase angle θ_j represents a difference in phase between the applied force and the excursion velocity, where the dominance of either stiffness or inertial force is apparent if θ_j is negative (phase advance) or positive (phase lag) respectively. In both cases there is a transfer of energy between the active power $\mathrm{Re}\{P_j\}$ and reactive power $\mathrm{Im}\{P_j\}$ which is undesirable from the perspective of maximising energy extraction.

In general for wave energy conversion, it is desirable to tune external damping and stiffness coefficients B^E_{ij} and C^E_{ij} in order to change the characteristics of the system to match the incident waves conditions, to attempt to sustain resonance. The present work deals with an inherently resonant system, consisting of a small number of identical floats, responding to the free decay of one of the floats. For this situation, the phase angle θ_j is close to zero, and it was possible for energy to remain within the system for a reasonable length of time, due to minimal external external damping effects. This allowed detailed studies of the hydrodynamic processes.

3.3 Time-domain modelling

The formulations introduced in Section 3.2 provide solutions in the frequency-domain, giving complex amplitudes of various quantities which describe the relative magnitudes and phase relationships between the fluid properties, forces and rigid body motions. In general, such evidence, along with derived results for peak and mean power from notional extraction mechanisms, can prove extremely useful when designing systems and for estimating yields, for assessing sites for suitability and environmental impacts. Once results for a particular configuration are assessed, using WAMIT for example, the external constraints (e.g. basic device control) and wave climate can be easily reconfigured to allow straightforward optimisation studies.

Evaluations for more complex aspects of the floating body problem can be delivered using time-domain methods, which utilise the frequency-domain results. These methods are particularly

useful for assessing nonlinear elements within the system (whilst continuing to use linear wave theory), such as nonlinear hydrostatics. The impact on body motion due to dynamic control strategies can be modelled, using external constraints which adapt over time, and can deliver real-time power output estimates using a so-called *wave-to-wire* model. Secondary models can also be configured to interact with the hydrodynamic model through various electrical network scenarios, using a *wire-to-wave* model (Forehand *et al.*, 2015). Similarly, an independent mooring model can also be configured for a two-way model association.

It is also useful in the time-domain to observe the transient behaviour of the system to identify response patterns and to rigorously validate the numerical results against physical data. As part of the work presented in this thesis, the direct comparisons with the CFD models are also a principal concern, which justifies the application of the linear time-domain method discussed in this section.

3.3.1 General methodology

The general approach to delivering time-domain results from numerical models such as WAMIT, is to construct Impulse Response Functions (IRFs) which translate impulses into responses at arbitrary points in the domain, for different quantities of interest. The impulses (i.e. input functions or time series) are the motion paths of the various moving bodies in the systems, and the IRFs are generated using the complex amplitudes of the hydrodynamic coefficients and velocity potentials from the frequency domain solutions. The time-domain responses of these field variables are determined by convolving the motion paths and IRFs.

Interpretation of the necessary time-domain body motions from frequency-domain results requires a separate model based on a state space system. Equivalently, this information can also be derived using other means, such as an analytical model, or can be taken from physical measurements, which would then be used to convolve with the IRFs to give time series of the forces and free surface elevations. In this work, the complete hydrodynamic model is used (state space derived motion paths, this being referred to as the '*time-domain model*'), along with comparative cases using experimental data for the motion path input time series. These two cases are reflected in the Figures 3.2a and 3.2b.

Idealised model

The outline methodology for the time-domain model given in Figure 3.2a indicates the various numerical process stages (white cells), and the system properties which are input or output at each stage (blue cells). The complex amplitudes of the hydrodynamic coefficients and free surface elevations are provided in this work using WAMIT. To evaluate the motion path of the floating body (or bodies), an in-house research code (Forehand *et al.*, 2015) was used, the outline of which is described in the remainder of this subsection. This particular code was used in an unmodified form to deliver the transient results for the floating body motions.

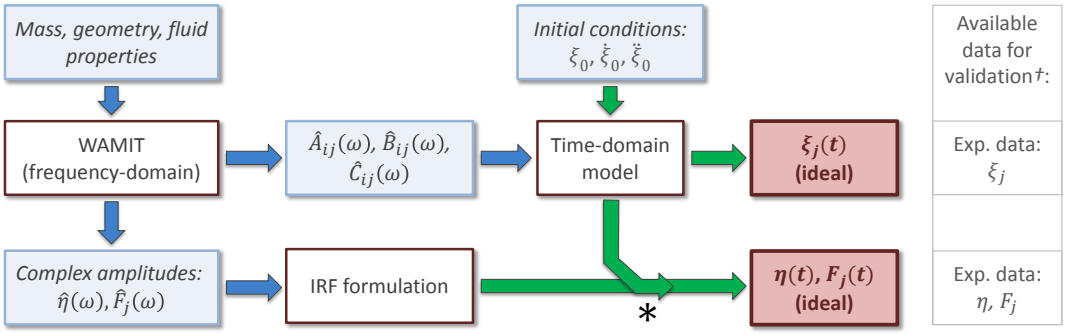

(a) Time-domain response assuming a frictionless mechanical system, in an ideal fluid.

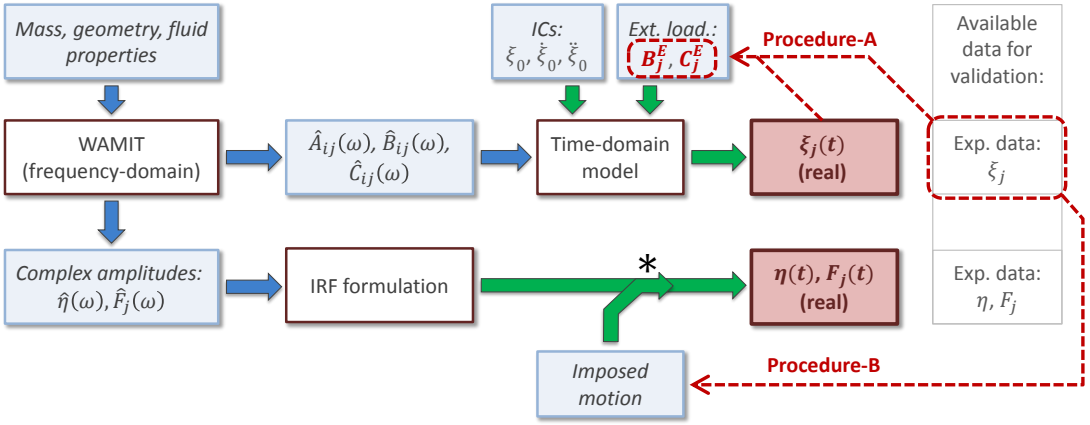

(b) Time-domain response assuming a mechanically damped system, in a real fluid.

Figure 3.2: General methodologies for the application of frequency-domain solutions to obtain time-domain predictions of the WEC excursion, free surface elevation and forces. Notes: blue and green process arrows represent frequency- and time-domain respectively; $*$ indicates convolution operations; † when an idealised systems is modelled, validation is approximate.

Decoupled model for additional dissipative effects

The changes to the methodology shown in Figure 3.2b were considered in order to understand the effects of modelling errors. In the experiments, the system was sensitive to additional factors, including the existence of mechanical damping, viscosity and vorticity. The combined impact of the model assumptions on body excursions may be interpreted through appropriate Verification and Validation (V&V) exercises for the idealised results delivered using the method in Figure 3.2a. This gives no further insight however into the nature of the contributions from the different processes which cause the discrepancy between the numerical and experimental results.

Figure 3.2b indicates two distinct procedures which attempt to characterise the modelling assumptions. The iterative procedure 'A' is a tuning exercise for externally applied damping and spring constraints, relating to the state space computation of the body motions. This estimates the combined effects of mechanical damping, viscosity and vorticity, and while this does not differentiate between these independent processes, some insight may be exposed with regard to the nonlinearity and directionality of the effects.

Procedure 'B' involves decoupling the evaluations of the body motions and the field variables of the hydrodynamic problem, by swapping the input signal to the IRF convolution, from numerically derived data to experimentally derived data. This avoids the compounded effect of modelling uncertainty in the convolution input signal (the body motions) and modelling uncertainty in the field data, derived using IRFs (free surface elevations and forces).

3.3.2 Time-domain floating body model

For the transient response of the system, the time-domain model developed by Forehand *et al.* (2015) was used to evaluate body motions. The referenced model is capable of far more complex multi-body cases[‡‡]; however, the procedure is unchanged as is outlined in this section.

The system of N bodies is described in the time-domain using the Cummins equation (Cummins, 1962):

$$[\mathbf{M}+\mathbf{A}(\infty)]\ddot{\boldsymbol{\xi}}(t)+\int_0^t \mathbf{k}(t-\tau)\dot{\boldsymbol{\xi}}(\tau)\mathrm{d}\tau+\mathbf{C}\boldsymbol{\xi}(t)=\mathbf{f}(t) \tag{3.34}$$

Equation (3.34) is given in matrix form, where the displacement $\boldsymbol{\xi}$ and its derivatives are vectors of length $6N$, and $\mathbf{M}$, $\mathbf{A}(\infty)$, $\mathbf{k}$ and $\mathbf{C}$ are $6N\times 6N$ matrices representing the body mass, added mass at infinite frequency, the radiation impulse response functions and the hydrostatic and gravitational restoring coefficients. Whilst evaluations of the body inertia and hydrostatic spring force are straightforward in the time-domain representation, the effects associated with the dynamics of the fluid are more problematic, this being represented by the convolution of the impulse response functions $\mathbf{k}$, with the velocity. This term accounts for the added mass and added damping, the Fourier transform being the radiation impedance matrix $\mathbf{K}(\omega)$:

$$\mathbf{K}(\omega)=\mathbf{B}(\omega)+\mathrm{i}\omega(\mathbf{A}(\omega)+\mathbf{A}(\infty)) \tag{3.35}$$

To avoid any direct computations on the convolution term in Equation (3.34), using the method adopted in Forehand *et al.* (2015) the response to the hydrodynamics can be determined using a state-space model. This involves establishing rational transfer functions for both added mass and added damping, in order to generate a transfer function in the frequency-domain for $\mathbf{K}(\omega)$.

[‡‡]The method presented in Forehand *et al.* (2015) is specifically designed to deal with cases where, due to extremely high order characteristic equations, the systems become computationally unstable, even if they are mathematically stable.

By arranging Equation (3.34) to solve for the acceleration, the procedure in the block diagram in Figure 3.3 provides the position and its derivatives on successive time steps. In the present work this was configured with the continuous solver `ode15s`, using variable step size.

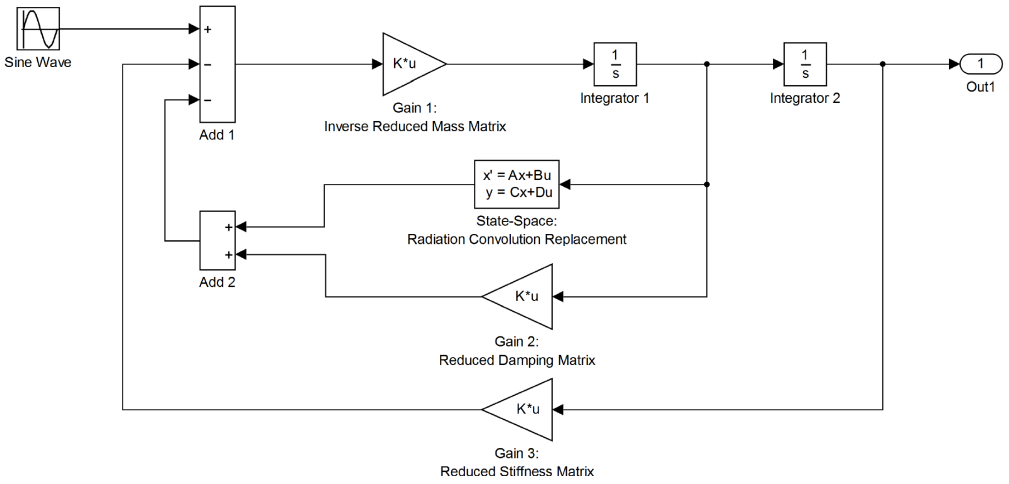

Figure 3.3: Block diagram of time-domain model WEC model.

State-space model

As with the various $6N \times 6N$ matrices in Equation (3.34), the information contained within the matrix $\mathbf{K}$ accounts for cross terms between different modes, i and j, as well as the diagonals $i = j$. For every unconstrained mode within the system, transfer functions are generated for the added mass and added damping, based on comparisons with the WAMIT derived coefficients. A two stage procedure is used, which evaluates an initial approximation using a least-squares method (similar to Levi (1959)) in order to prime the damped Gauss-Newton method for iterative convergence (Dennis and Schnabel, 1983) The polynomial orders of both numerator and denominator are increased sequentially, while the suitability and stability of the transfer function is monitored.

Regarding suitability, when the error fit between the transfer functions and WAMIT derived coefficients is found to fall within $\pm 1\%$, the transfer function is considered appropriate. To demonstrate stability however, it must also be verified that the poles of the transfer function fall within the left hand plane of the pole-zero plot, to ensure that the response is not divergent. For the continuous-time zero/pole/gain model, the order of the numerator is always kept less than that of the denominator.

A state-space model can then be established in the general form:

$$\begin{aligned} \dot{\mathbf{x}}(t) &= \mathcal{A}\mathbf{x}(t) + \mathcal{B}u(t) \\ y(t) &= \mathcal{C}\mathbf{x}(t) + \mathcal{D}u(t) \end{aligned} \tag{3.36}$$

Here, $\mathcal{A}$, $\mathcal{B}$, $\mathcal{C}$ and $\mathcal{D}$ are the coefficient matrices of the state-space system (state, input, output and feedthrough respectively), and $\mathbf{x}(t)$, $u(t)$ and $y(t)$ represent the state variables, the input, and the output. For single-input, single-output cases, the input and output vectors are singular. Due to the nature of the iterative procedure for the generation of transfer functions, an arbitrary number of non-physical states are possible, governed in each case by the order of the denominator for the vetted transfer function. For single mode systems which were studied, the use of 5 or 6 states was necessary.

3.3.3 Time-domain field responses

Using general terminology, frequency-domain evaluations of the various field data output(s) $Y(\omega)$ requires knowledge of the relevant input(s) $U(\omega)$ and *transfer function* $H(\omega)$, giving the simple expression:

$$Y(\omega) = H(\omega)U(\omega) \tag{3.37}$$

For the equivalent time-domain response, the product of the transfer function and input(s) is replaced by a convolution between the respective Fourier transforms:

$$y(t) = h(t) * u(t) \equiv \int_{-\infty}^{\infty} h(t-\tau)u(\tau)\,\mathrm{d}\tau \tag{3.38}$$

where $y(t)$ and $u(t)$ are the time-domain output and input signals, and $h(t)$ is the Impulse Response Function (IRF). The time-domain evaluation of field variables therefore requires two steps:

1. Generate IRFs for the variable of interest, at a set of particular field points;
2. Convolve with the relevant input signal – the excursion time series of the moving body (or bodies), to give the time-domain response of the variable of interest.

Impulse responses have been assessed in this work for radiation forces between neighbouring bodies, and for free surface elevations. The above steps are outlined in the following sub-headings.

Force impulse responses function

The IRF $L_{ij}(t)$ for the radiation force between any two modes, i and j, can be evaluated using the equivalent expressions:

$$L_{ij}(t) = \frac{2}{\pi}\int_0^{\infty} [A_{ij}(\omega) - A_{ij}(\infty)]\cos(\omega t)\,\mathrm{d}\omega \tag{3.39}$$

$$L_{ij}(t) = \frac{2}{\pi}\int_0^{\infty} \frac{B_{ij}(\omega)}{\omega}\sin(\omega t)\,\mathrm{d}\omega \tag{3.40}$$

The nondimensionalisation of field parameters assists further in the evaluation of time-domain results, using the following definitions:

$$\bar{A}_{ij}(\omega) = \frac{A_{ij}(\omega)}{\rho L^k} \qquad \bar{B}_{ij}(\omega) = \frac{B_{ij}(\omega)}{\rho L^k \omega} \tag{3.41}$$

where L is the length scale (against which the solution can be rescaled) and $k = 3$ for translational interactions ($i, j \leqslant 3$), $k = 5$ for rotational interactions ($i, j \geqslant 4$), and $k = 4$ for translational/rotational interactions ($i \leqslant 3, j \geqslant 4$ or $i \geqslant 4, j \leqslant 3$). The nondimensional IRF $\bar{L}_{ij}$ is then given (WAMIT: Version 7, 2012) by:

$$\bar{L}_{ij} = \frac{2}{\pi}\int_0^\infty \left[\bar{A}_{ij}(\omega) - \bar{A}_{ij}(\infty)\right]\cos(\omega t)\,\mathrm{d}\omega = \frac{2}{\pi}\int_0^\infty \bar{B}_{ij}(\omega)\sin(\omega t)\,\mathrm{d}\omega \tag{3.42}$$

The numerical procedure used in the present work to evaluate the integral equation (3.42) was based on the Filon method.

Free surface impulse responses function

Following from the dynamic free surface condition (Equation (3.17)):

$$\eta = -\frac{1}{g}\left(\frac{\partial \varphi}{\partial t}\right)_{z=0} \tag{3.43}$$

It is convenient to express the free surface elevation in nondimensional form $\bar{\eta} = \eta/A$ (A being the wave amplitude), which gives coincident results with the nondimensional pressure and velocity potential at the same locations (WAMIT: Version 7, 2012). For the radiation problem which is of particular interest in this work, there were no background wave conditions, $\bar{\eta}$ may be redefined accordingly as:

$$\bar{\eta} = \frac{\eta}{\xi_j L^n} = KL\bar{\varphi}_j \tag{3.44}$$

where for modes $j = 1$ to 6 the nondimensional velocity potential is:

$$\bar{\varphi}_j = \frac{\varphi_j}{L^{\lceil j/3 \rceil}} \tag{3.45}$$

The corresponding IRFs for time-domain free surface elevations are as follows:

$$\bar{K}_j(t) = \frac{2}{\pi}\int_0^\infty \mathrm{Re}\{\bar{\varphi}_j(\omega) - \bar{\varphi}_j(\infty)\}\cos(\omega t)\,\mathrm{d}\omega \tag{3.46}$$

$$\bar{K}_j(t) = \frac{2}{\pi}\int_0^\infty \frac{\mathrm{Im}\{\bar{\varphi}_j(\omega)\}}{\omega}\sin(\omega t)\,\mathrm{d}\omega \tag{3.47}$$

Time-domain convolution

Regarding the output in time provided by Equation (3.38), the integral is evaluated over the time parameter τ, upon which both u and $h(t)$ depend. The output $y(t)$ can be evaluated numerically by computing the integral successively over all discrete values of time t. Thus y remains a function of t, defined over the range $t = [0, \mathcal{T}]$, which is also the case for the IRF $h(t)$.

The input function must be defined over the range $t = [-\mathcal{T}, \mathcal{T}]$, which implies that some history of the input signal, the length of which is governed by the duration of the impulse $t = [0, \mathcal{T}]$, must also be known. In practice, the input signal tends to be constant for all negative time. For this work, the integral of the complete transfer functions (tending to $t = \infty$) will be zero, giving zero initial free surface elevation and force output signals at $t = 0$.

The numerical procedure involves first, establishing the time parameter τ to obtain the output $y(t)$ at any instant t. At each time t, the integral is evaluated over τ, with definite limits $\tau = [-\mathcal{T}, \mathcal{T}]$. The IRF is flipped, and 'moved' to the current evaluation point t (hence $h(t-\tau)$), and is zero-padded to extent across the range $\tau = [-\mathcal{T}, \mathcal{T}]$. For the first step, $t = 0$, and all non-zero values of the IRF are found in the negative τ domain. For the successive time steps, the IRF shifts to towards the right, until all non-zero values of $h(t-\tau)$ are in the positive τ domain (i.e. at $t = \mathcal{T}$). In the numerical evaluation, $y(t)$ becomes a vector of output results, covering the time-scale $t = [0, \mathcal{T}]$.

3.4 Finite volume method

3.4.1 Navier-Stokes equations

The first observation regarding the mathematical model for fluid flow is that continuum is subject to the principles of conservation: of mass, momentum and energy. In terms of mass, the continuity equation describes the balance between the mass contained within a differential volume and the divergence, resulting from surface fluxes:

$$\frac{\partial \rho}{\partial t} + \nabla \cdot \rho \mathbf{u} = 0 \tag{3.48}$$

Regarding momentum, Newton's Second Law provides the starting point for investigating the dynamics associated with the fluid system:

$$\frac{D(\rho \mathbf{u})}{Dt} \delta V = F \tag{3.49}$$

In Equation (3.49), the kinematics are captured on the left hand side for a volume δV. On the right hand side, the dynamics which result in accelerations of δV, should consider all relevant pressure effects, source effects and viscous effects.

With respect to the conservation of energy within the system, the lack of any relevant temperature effects removes any need to include the energy equation in the present simplified Navier-Stokes equations. Given that for the present work, the following assumptions also apply:

- the flow is incompressible;
- the viscosity is constant;
- viscosity may significantly effect the behaviour of the system;
- all fluid phases behave as Newtonian fluids;
- the only relevant external body force is gravity,

the flow can be described using the continuity equation (Equation (3.50)) and the simplified form of the Navier-Stokes equations, given by Equation (3.51):

$$\nabla \cdot \mathbf{u} = 0 \tag{3.50}$$

$$\rho \frac{D\mathbf{u}}{Dt} = -\nabla p + \rho g + \mu_w \nabla^2 \mathbf{u} \tag{3.51}$$

where p is fluid pressure. In the context of an Eulerian field, the material derivative on the left hand side of the momentum Equation (3.51) includes the partial time derivative, plus the convective term, thus:

$$\rho \frac{\partial \mathbf{u}}{\partial t} + \mathbf{u} \cdot (\nabla \rho \mathbf{u}) = -\nabla p + \rho g + \mu_w \nabla^2 \mathbf{u} \tag{3.52}$$

Whilst it was stated above that viscosity may have an impact on the resulting fluid behaviour, this assumption is one of the main subjects of this thesis. To examine the comparative importance of these effects, the inviscid form of Equation (3.52) is also used in the following work:

$$\rho \frac{\partial \mathbf{u}}{\partial t} + \mathbf{u} \cdot (\nabla \rho \mathbf{u}) = -\nabla p + \rho g \tag{3.53}$$

which, when combined with Equation (3.50), gives the Euler equations for incompressible flow.

3.4.2 The transport equation

In general, the inclusion of source terms within the Navier-Stokes equations implies that influencing factors exist within the system which provide the fluid with some potential to move, due to the transport of momentum. This is true for gravity in the simplified momentum Equation (3.52); however, pressure also behaves in the same manner. By combining the source terms in Equation (3.52), what remains of the convective-diffusive equation may be used generically to consider the transport of other flow properties, represented by the general variable ϕ:

$$\frac{\partial \rho \phi}{\partial t} + \mathbf{u} \cdot (\nabla \rho \phi) = \Gamma \nabla^2 \phi + S_\phi \tag{3.54}$$

where Γ is the general diffusion coefficient, and S_ϕ is the source term for the property ϕ. The above general transport equation forms the basis for mathematical descriptions of the transport of various flow properties applied in the present work. These properties notably include the fluid phase volume fraction and turbulent flow properties, which were considered within the models used to prepare this thesis.

The Finite Volume (FV) CFD method is based on the Eulerian form of the Navier-Stokes equations. To describe a particular region of interest, the Navier-Stokes equations would in theory require integration over that field in order to return all relevant flow properties that describe the behaviour of the fluid(s). However there are no known general solutions to the Navier-Stokes equations. For the transient fluid processes, such as the wave conditions considered here, the equations must also be integrated over time.

The transport equation, integrated over space and time, comprises both volume processes (concerning V, the first term on the left hand side – the transient term, and the second term on the right – the source term) and surface processes (concerning S, the second term on the left – the convective, and the first term on the right – the diffusion term). Following Gauss' Divergence Theorem to convert the latter to surface integrals yields:

$$\begin{aligned} \int_{\Delta t} \frac{\partial}{\partial t} \left(\int_{CV} \rho\phi \, \mathrm{d}V \right) \mathrm{d}t \;\; + \;\; \int_{\Delta t} \int_{S} \mathbf{n} \cdot (\rho\phi\mathbf{u}) \, \mathrm{d}S \, \mathrm{d}t \\ = \;\; \int_{\Delta t} \int_{S} \mathbf{n} \cdot (\Gamma \nabla\phi) \, \mathrm{d}S \, \mathrm{d}t \;\; + \;\; \int_{\Delta t} \int_{CV} S_\phi \, \mathrm{d}V \, \mathrm{d}t \end{aligned} \tag{3.55}$$

3.4.3 Finite volume implementation

The following describes the specific approach taken in this thesis, which has utilised the segregated flow solver component of the commercial CFD code, STAR-CCM+ v10.02. The numerical solution takes the discrete form of Equation (3.55):

$$\frac{\partial}{\partial t}(\rho\phi V)_0 + \sum_f [\rho\phi(\mathbf{u}\cdot\mathbf{a} - G)]_f = \sum_f (\Gamma\nabla\phi\cdot\mathbf{a})_f + (S_\phi V)_0 \tag{3.56}$$

In the above, $\mathbf{a}_f$ is the face area vector and G_f is the grid flux due to the motion of the grid (applicable in this case to the overset mesh only). Equation (3.56) is evaluated as a system of linear equations, for each relevant property, at each grid point, within the discretised and finite domain. Approximate iterative procedures are necessary in order to address nonlinearities introduced by the momentum convection terms. Once these have been appropriately linearised, the closed system of equations can be solved using the algebraic multigrid method.

Various methods are available for the numerical treatment of each term in Equation (3.56); however, the use of first order accurate methods however are generally not advised, due to

lower accuracy and excessive diffusion. For the work presented in this thesis, second-order accurate numerical schemes were used throughout.

Transient term

Temporal discretisation is achieved using a second-order accurate method for the transient term. This uses solutions from three points in time – the current time step, plus the previous two time steps.

Convective term

An upwind second order scheme is used for the convection terms. The face value between node 0 and node 1 is linearly interpolated using a flow direction dependent reconstruction gradient. Having this intermediate value allows the upwind scheme to behave as a central difference, making it nominally second order accurate. STAR-CCM+ provides first order, second order and blended 3rd order MUSCL (Monotonic Upstream-Centered Scheme for Conservation Laws) / CD (Central Difference) schemes for the segregated flow solver. The latter of these is recommended for high-fidelity turbulence simulations (using for example Large Eddie Simulation (LES) or Detached Eddie Simulation (DES)), for acoustics and for aerodynamics (CD-Adapco, 2015); however, it was not deemed necessary for the low flow velocities, and relatively weak turbulent behaviour considered here.

The inclusion of grid flux term G_f in Equation (3.56) allows for movement of the mesh (or parts of the mesh), as is required for the overset method. A corresponding second order grid flux is used for both the rigid body motion / FSI case, and user-defined vertex imposed motion case.

Diffusion term

The diffusion term in Equation (3.56), which concerns the second derivative in space (see also Equation 3.52), is second-order accurate. Due to the use of the *'trimmed cell'* Cartesian mesh, there is no concern regarding the effects of high skewness angles on the computation of gradients for the diffusion term, where throughout most of the domain, the face area vector and adjacent cell centre vector are co-linear. Secondary gradients are used however for all CFD runs in this work, to ensure that the diffusion term is calculated accurately across the entire domain.

Source term

The source term S_ϕ, for the general transport equation is approximated as the average within each cell. For the transport of momentum, $S_{(\rho \mathbf{u})} = (\rho g + \nabla p)$. In terms of gravity, particularly for the incompressible case where ρ is constant, this is an accurate assumption. For general application, approximated value is consistent with the second-order schemes utilised for the other terms (CD-Adapco, 2015).

3.4.4 Turbulence

The presence of turbulence in any flow results in additional momentum transfer, making it necessary to account for these effects wherever turbulent flow is expected. The processes behave as supplementary effects on the bulk flow, the nature of which can be awkward to characterise due to the wide spectrum of length and time-scales involved. The seminal work by Kolmogorov (1941) demonstrated that the spectral distribution may be approximated by the '5/3 law' for a significant intermediate range of frequencies. At the largest length scales, turbulence interacts directly with the mean flow and lies outside the Kolmogorov range. As the spectral energy $E(\kappa)$ decreases with frequency according to $E(\kappa) = \alpha \varepsilon^{2/3} \kappa^{-5/3}$, it eventually cascades down to a dissipative, high frequency, low energy range, in which the viscous and inertial effects are comparable. In the above, ε is the turbulent energy rate, κ is the wavelength of the turbulent fluctuations, α is a constant, approximately equal to 1.5.

Due to the geometries and time scales involved with marine CFD simulations, attempting to directly evaluate the entire range of turbulent length scales (i.e. using DNS – Direct Numerical Simulation) is not practicable. Turbulence modelling has proved acceptable for marine applications, via for example the widely used Reynolds-Averaged Navier-Stokes (RANS) method, as is used here. Where appropriate, greater accuracy can be achieved using the Large Eddie Simulation (LES) method, which evaluates large scale eddies, and models turbulence below a specified scale. LES requires a considerable increase in computational resources, whilst the hybrid Detached Eddie Simulation (DES) approach offers a compromise between the efficiency and accuracy of the RANS and LES approaches.

Reynolds Averaged Navier-Stokes

In the Reynolds-Averaged Navier-Stokes (RANS) approach, numerical closure schemes are necessary in order to address the additional aspects of flow behaviour in a turbulent fluid. The Reynolds decomposition for a transient analysis introduces ensemble averages of flow properties (Φ) which represent the background flow, and fluctuating components (ϕ'), which result from turbulent fluid behaviour. In terms of the velocity, the three components in x, y and z are represented as follows:

$$u = U + u' \qquad v = V + v' \qquad w = W + w' \tag{3.57}$$

where U, V and W are the mean velocity components in x, y and z, respectively, expressed vectorially as $\mathbf{U}$. When the decomposed velocities are applied to the Navier-Stokes equations, terms involving averages of the fluctuations are diminished. However, due to the behaviour of vortices in the turbulent flow, the second moments of the fluctuating velocities (u'^2, v'^2, w'^2, $u'v'$, $u'w'$, $v'w'$), which originate from the nonlinear convection term, are found to be non-zero. This leaves the so-called Reynolds stresses as non-zero contributions within the momentum equations.

Closure schemes involve new transport equations to model additional turbulent properties. Fully anisotropic evaluations may be carried out using a Reynolds Stress Model (RSM), which includes seven further equations[§§]. The widely used isotropic k-ε and k-ω methods require just two additional equations. Furthermore, the single equation Spalart-Allmaras method has been reported for use in marine applications (MARINET, 2002; VIRTUE (The Virtual Tank Utility in Europe), 2009). Cautionary use, however, of one (and zero) equation methods for free surface modelling has also been highlighted within the CFD community.

The Menter Shear-Stress Transport (SST) k-ω model (1994) has been applied in the present work. Two additional transport equations are used to model the turbulence kinetic energy k ($= 1/2[u'^2 + v'^2 + w'^2]$) and the turbulence frequency ω ($= \varepsilon/k$). It is straightforward within the framework of the SST model to control the behaviour of k and ω at near-wall nodes (Wilcox, 1988), as k tends to zero, and ω may be evaluated hyperbolically as:

$$\omega = 6\nu/(\beta_1 y_p^2) \tag{3.58}$$

where ν is the kinematic viscosity and the distance y_p is measured to the nearest wall. This has the benefit over the standard k-ε model of removing any need for wall damping. In the free-stream, however, as the eddy viscosity $\mu_t = \rho k/\omega$ becomes indeterminate ($\omega \to 0$), the k-ε form is reinstated (Versteeg and Malalasekera, 2007). Equation (3.59) is used to evaluate the transport of k. Equation (3.60) or (3.61) is used to evaluate the transport of ε or ω, depending on wall proximity.

$$\frac{\partial(\rho k)}{\partial t} + \nabla\cdot(\rho k\mathbf{U}) = \nabla\cdot\left[\left(\mu_w + \frac{\mu_t}{\sigma_k}\right)\nabla k\right] + \left[2\mu_t S_{ij}\cdot S_{ij} - \frac{2}{3}\rho k\frac{\partial U_i}{\partial x_j}\delta_{ij}\right] - \beta^*\rho k\omega \tag{3.59}$$

$$\frac{\partial(\rho\varepsilon)}{\partial t} + \nabla\cdot(\rho\varepsilon\mathbf{U}) = \nabla\cdot\left[\left(\frac{\mu_t}{\sigma_\varepsilon}\right)\nabla\varepsilon\right] + \left[C_{1\varepsilon}\frac{\varepsilon}{k}2\mu_t S_{ij}\cdot S_{ij}\right] - C_{2\varepsilon}\rho\frac{\varepsilon^2}{k} \tag{3.60}$$

[§§]One equation is required for each Reynolds stress term, along with the transport of the turbulent energy dissipation rate ε.

$$\frac{\partial(\rho\omega)}{\partial t}+\nabla\cdot(\rho\omega\mathbf{U})=\nabla\cdot\left[\left(\mu_w+\frac{\mu_t}{\sigma_{\omega,1}}\right)\nabla\omega\right]+\gamma_2\left[2\rho S_{ij}\cdot S_{ij}-\frac{2}{3}\rho\omega\frac{\partial U_i}{\partial x_j}\delta_{ij}\right]$$
$$-\beta_2\rho\omega^2+2\frac{\rho}{\sigma_{\omega,2}}\frac{1}{\omega}\frac{\partial k}{\partial x_j}\frac{\partial\omega}{\partial x_j} \qquad (3.61)$$

where i, j are indices $1-3$ representing the x, y and z directions, and in particular, x_j replaces x, y and z, and U_j replaces the components of $\mathbf{U}$). SST is a linear eddy viscosity model, in which the Reynolds stresses are assumed proportional to the rate of strain S_{ij} ($=\partial U_i/\partial x_j+\partial U_j/\partial x_i$). The eddy viscosity μ_t in particular is the constant of proportionality for shear stresses, between velocity fluctuations in different orientations (Versteeg and Malalasekera, 2007):

$$\tau_{ij}=-\rho\overline{u_i'u_j'}=\mu_t\left(\frac{\partial U_i}{\partial x_j}+\frac{\partial U_j}{\partial x_i}\right)-\frac{2}{3}\rho k\delta_{ij} \qquad (3.62)$$

The second term on the right hand side, which includes the Kronecker delta function δ_{ij}, corrects for the otherwise diminished normal stresses ($i=j$)[¶¶]. μ_t appears on the right hand side of Equations (3.59) to (3.61) within the diffusion term, where it is used to augment μ_w using the empirically derived constants σ_k,σ_ε,$\sigma_{\omega,1}$ to provide a combined diffusion effect. In addition, the source terms on the right hand side of Equations (3.59) and (3.60) (second sets of square brackets, the rate of production of k and ε, respectively), depend also on μ_t.

Comparing Equations (3.59) to (3.61), the ω equation has an extra cross-diffusion term on the right hand side, which originates from the particular method adopted in Menter's SST formulation for transforming the viscous dissipation ε (Versteeg and Malalasekera, 2007).

A summary of the empirical constants used in Equations (3.58) to (3.61) is as follows: $\beta_1=0.0708$; $\beta_2=0.083$; $\beta^*=0.09$; $\gamma_2=0.44$; $\sigma_\varepsilon=1.30$; $\sigma_k=1.0$; $\sigma_{\omega,1}=2.0$; $\sigma_{\omega,2}=1.17$; $C_{1\varepsilon}=1.44$; $C_{2\varepsilon}=1.92$.

[¶¶]The first term on the right of Equation (3.62), when expanded for all normal stresses, gives $2\mu_t\nabla\cdot\mathbf{U}=0$, for incompressible flow.

Chapter 4

Tank Testing

It was necessary to obtain high quality validation data in order to examine the various complex processes addressed using the Computational Fluid Dynamics (CFD) models. The design and construction of small-scale experimental tests, however, was not undertaken as part of this PhD research. Access to a large dataset was instead granted at an early stage, with this agreement including an active participative role.

Within this chapter, a brief extension to the methodology presented in Chapter 1 is given, followed by descriptions of the experiments used to validate this work. Relevant data from the *'WECwakes'* project (Stratigaki *et al.*, 2014)* is then provided, along with results from spectral analyses and descriptions of synthesised motion functions. These functions have been fitted to the experimental data in order extend the validation measures taken in the Chapters 4 to 7.

4.1 General tank testing methodology

As discussed in Section 1.2, the role that experimental modelling plays in the development of a WEC is closely interlinked to that of the numerical models. However the proof of concept cannot be delivered without undertaking both modelling activities. Furthermore, the objectives of a small scale tank test should be carefully outlined to focus attention on the delivery of validation data for the numerical models, rather than attempting to demonstrate the precise behaviour of a theoretical full scale working system.

The development sequence for the two modelling programmes will most likely begin with preliminary numerical models, which will consider the outline concepts, and begin to define the body geometries, mass distributions and some principal force components. These numerical models will be instrumental in the design of the small-scale physical test systems, which should give due consideration to the limitations of the available facility. Figure 4.1 describes the relationship between the early numerical models and small scale tank tests. This may require a number of iterations in order to develop an accurate and effective test model (steps 1 and 2), and should ultimately deliver indicative results for full scale device performance (step 3).

*The WECwakes project was conducted as part of EU FP7 HYDRALAB IV.

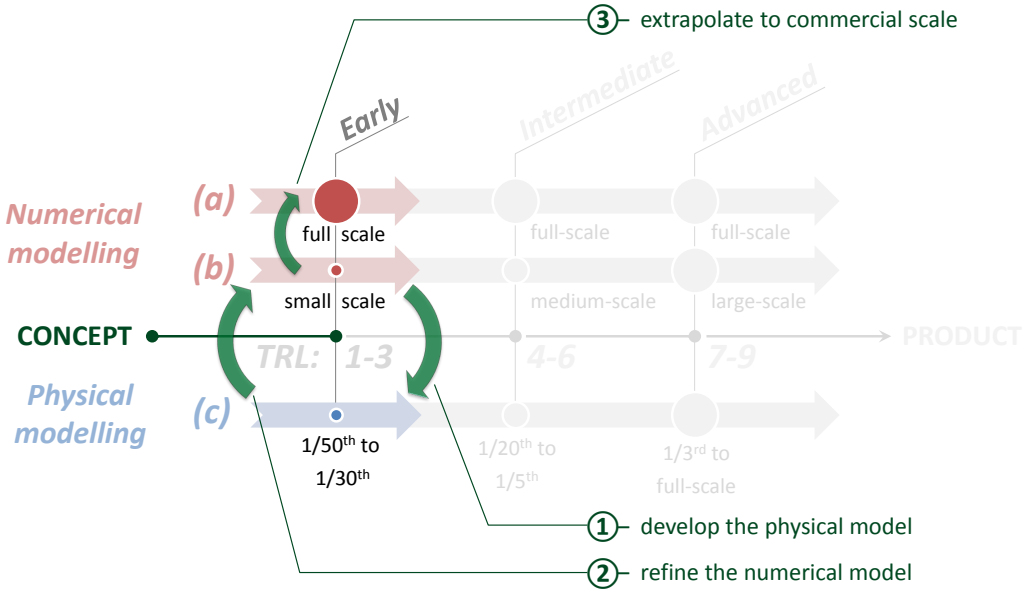

Figure 4.1: An interpretation of the design process shown in Figure 1.6, taken at an early stage of WEC development.

The following summarises the types of experiment which can be carried out as part of a Wave Energy Converter (WEC) tank testing programme:

1. Calibration tests;
2. Sea state tests;
3. Motion response to incident waves†
   (a) Free motion;
   (b) Constrained motion (Power Take-off (PTO) damped);
   (c) Fixed constraint (diffraction tests);
4. Radiation only tests (no incident waves):
   (a) Free decay motion;
   (b) Constrained decay motion (PTO damped);
   (c) Forced (imposed) motion;

When the WEC motion response is tested under incident wave conditions (as denoted †), sea states can take several forms, including: regular beam seas; regular seas with oblique wave headings; irregular long crested waves; irregular waves with spreading (short crested); poly-chromatic wave profiles. These listed wave conditions were all used as part of the WECwakes experiments, described in Section 4.2. In addition, all of the tests summarised in items 1 to 4 above were also carried out, with the exception of item 4c. The only tests used in this work however were the decay tests, in particular those assuming free decay motion (item 4a).

In addition to the wet experiments indicated above, it can also be important to consider a range

of other tests, in which components of the main assemblies are tested in dry conditions. This can include resistive testing of bearings, PTO response testing and sensor calibration. These, again, were considered in the WECwakes project.

The numerical models described in later chapters were designed to reflect the precise geometry and arrangement of the WECwakes experimental setup. In terms of the procedure described in Figure 4.1, the work in this thesis forms step 2 of the early stage development, taking particular care to ensure that the numerical models account for all relevant physical processes in the tests. In the context of the wider process depicted in Figure 4.1, step 1 was carried out in advance of this work, as part of the larger WECwakes project. Step 3 has not been considered here due to the nature of the test assembly, which was designed to provide large quantities of test data for a *generic* shape, rather than be representative of an early stage commercial WEC design.

4.2 The WECwakes project

A period of six days were spent during this PhD project taking part in tank tests at the Danish Hydraulic Institute (DHI) at the beginning of 2013, where assistance was provided for the execution of the WECwakes experiment. The main period of testing for the overall WECwakes project extended across a total of twenty two days of continuous tank operation, undertaken by a team of academic staff and PhD students. The period of involvement for the present work included cases from all test scenarios (items 1-4, except 4c, in Section 4.1) for various arrangements of single and multiple WECs. The only tests relevant to the present work were the free decay tests (item 4a), which were all conducted within this six day window, approximately half way through the main testing programme.

4.2.1 Background of the project

The WECwakes project (Stratigaki *et al.*, 2014) was delivered by a consortium of institutions from across Europe, coordinated by Ghent University, Belgium. The experiment was designed to study the wave field modifications caused by the presence of an array of WECs, with its principal goal to generate large quantities of validation data, for application with a variety of numerical model types.

A total of twenty five small scale WEC models were constructed and tested as part of the project, which can be seen in Figure 4.2. At the time of writing, this remains the largest such example of a small scale WEC array experiment, in terms of number of independent devices. The focus on array scale modelling emerged from the understanding that non-negligible interactions from neighbouring devices may, in theory, affect the performance of a WEC array. These effects can be highly sensitive to the precise geometric arrangement of the array, making it necessary to provide highly accurate numerical models which are capable of capturing the

array interaction effects. When the experiment was commissioned, validation data for array scale systems was limited, with the largest arrays including up to five WECs. Shortly before the WECwakes experiment was carried out, arrays of up to twenty four WECs were tested as part of the PerAWaT project (Folley and Whittaker, 2013).

Figure 4.2: Photograph of the empty DHI shallow water basin containing the twenty five WECs and frame that form the experimental rig[†].

A series of preliminary tests were carried out within the WECwakes project, prior to the main experiments at DHI. Two earlier iterations of the WEC design were tested at Ghent University in 2011 and 2012. Single WEC tests also took place at Queen's University Belfast to develop the PTO system, with further tests at Flanders Hydraulics Research, Belgium, using small arrays of up to four WECs. A particular focus of these latter experiments was to establish repeatable test results, and to confirm reproducibility between the different WEC models. It is noted here that this staged development within the WECwakes project can be regarded as the iterative process between steps 1 and 2, depicted in Figure 4.1.

4.2.2 Description of the device

The WEC geometry considered in the WECwakes project has been adopted for all numerical modelling work presented in this thesis. This consisted of a cylinder with a hemispherical base, with both the diameter and draught measuring 315mm, and a total height of 600mm, as shown in Figure 4.3. The generic float shape, which does not represent any particular pre-commercial WEC design, was suitable partly because of its simplicity (due to being axisymmetric), but also because it was designed to respond energetically to the appropriately scaled conditions in the wave tank. The form and mass of the float design were such that the resonance and drag characteristics were representative of a basic heaving type WEC. The overall mass of each freely moving float was 20.545kg, which included the PTO assembly.

The WECs were designed to behave in a manner which would produce highly repeatable measurement data in terms of device motions, free surface elevations and forces. In order

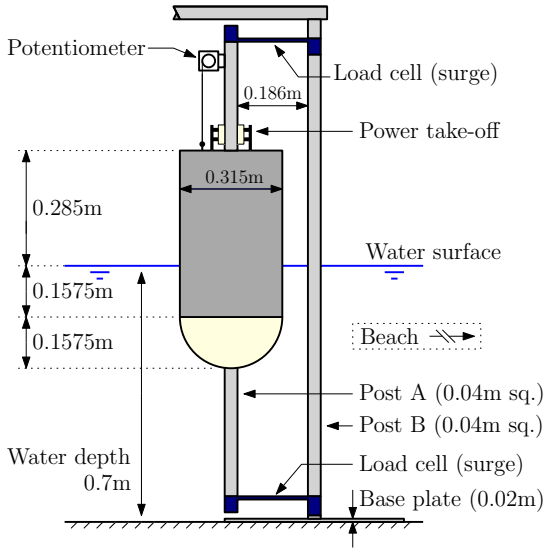

Figure 4.3: Section view of one of the WEC models, including the structural components of the main assembly. Adapted from Stratigaki *et al.* (2014).

to do this, the floats were constrained to move only in the heave degree of freedom. By producing repeatable test results, which could also be measured reliably, the uncertainties in the experiments could be well understood to allow close correlation with the predictive numerical models.

Each float was mounted on a square section vertical post measuring 40mm×40mm, labelled Post A in Figure 4.3. Within the core of each WEC float, a larger square-section extrusion was used to form the axis, sealing the internal volume of the float and providing mounting points for PTFE block-type bearings at the top and bottom of the axis. PTFE blocks were also used to form a PTO system, which pressed against two opposing sides of the square mounting post, forced by springs with adjustable seating positions. The damping that resulted from these friction systems was nonlinear, which can be appropriately modelled using Coulomb damping. The implications of this were explored in detail in Stratigaki *et al.* (2014).

Draw-wire potentiometer sensors (Altheris FD60-500) were used to measure the dynamic device displacement, as shown in Figure 4.3. For all of the WECs concerned with this work[‡], load cells (Tedea-Huntleigh Model 614) were also configured at the top and bottom of Post A. This arrangement required a second post, labelled Post B, which was offset by 226mm in the leeward direction with respect to the wavemaker bank. Where the two Post-Arrangement was used, a small gap existed at the top and bottom of Post A, with the post supported entirely by the two load cells.

Surge forces were measured to correlate nonlinear mechanical damping effects with the instan-

[‡]This work relates only to WECs 1-5, as described in Stratigaki *et al.* (2014). WECs 6-25 were configured without load cells, and featured only a single vertical post (Post A).

taneous lateral loading experienced by each WEC. It was confirmed from earlier tests that these mechanical effects were measurable, therefore to interpret the dynamic behaviour during the tests, a relationship was developed which derived the in-line damping force (in heave), from the surge force. This method of correlating the damping effect and surge force was relevant for test configurations using incident waves, and multiple WEC decay tests (i.e. not for single WEC decay tests, which experience negligible lateral loading). An additional nonlinear mechanical load was also examined by Stratigaki *et al.* (2014), which was caused by the extensions of the potentiometer.

The surge force measurements also provided extremely important validation data. This is particularly useful for the present work, with the interaction forces being of principal interest in the multiple WEC numerical models. These measurements are provided in Section 4.3.2, and are discussed further in the validation results in Chapter 7.

4.2.3 Description of the experiment

The shallow water basin at DHI was used to conduct the main experiments for the WECwakes project, a 0.7m deep rectangular wave tank, shown in plan in Figure 4.4. A single bank of wavemakers ran along a 22m section of one end of the tank. This was faced on the opposing end by a sloping gravel beach, which started at a distance of approximately 20m, rising to above water level at approximately 24m (beach length 5.03m, sloping at 1:5.59). The overall distance between the wavemakers and the opposite tank boundary was 25m. The sides of the test area were formed by rigid guide walls, installed in line with each end of the wavemaker bank. This provided an overall rectangular area of 22m$\times$24m.

The WEC models were set out in a 5×5 array, positioned centrally across the width of the basin, with a distance of 5m between the wavemakers and the front of the array. The frame was configured to allow each of the WEC models to be lifted out of the water completely, to give various array layouts, including rows, columns, square and staggered arrays, as well as single WEC cases.

Figure 4.5 shows the central column of WEC floats, referred to herein as *'WEC-1'* to *'WEC-5'*, which were used for all of the decay tests described in this thesis. In each case, vertical motions were induced by lifting the float upwards to a fixed position, allowing a settling time for any free surface disturbances, and releasing the float from height. During this process, the wavemakers were not used to generate waves, and were configured only to provide active absorption to waves which were generated by the moving floats. Using this method, the following tests were carried out:

- *'OneWEC'*: decay tests of WEC-5;
- *'TwoWEC'*: decay tests of WEC-5, with WEC-4 at rest;
- *'FiveWEC'*: decay test of WEC-3, with WECs-1,2,4,5 at rest.

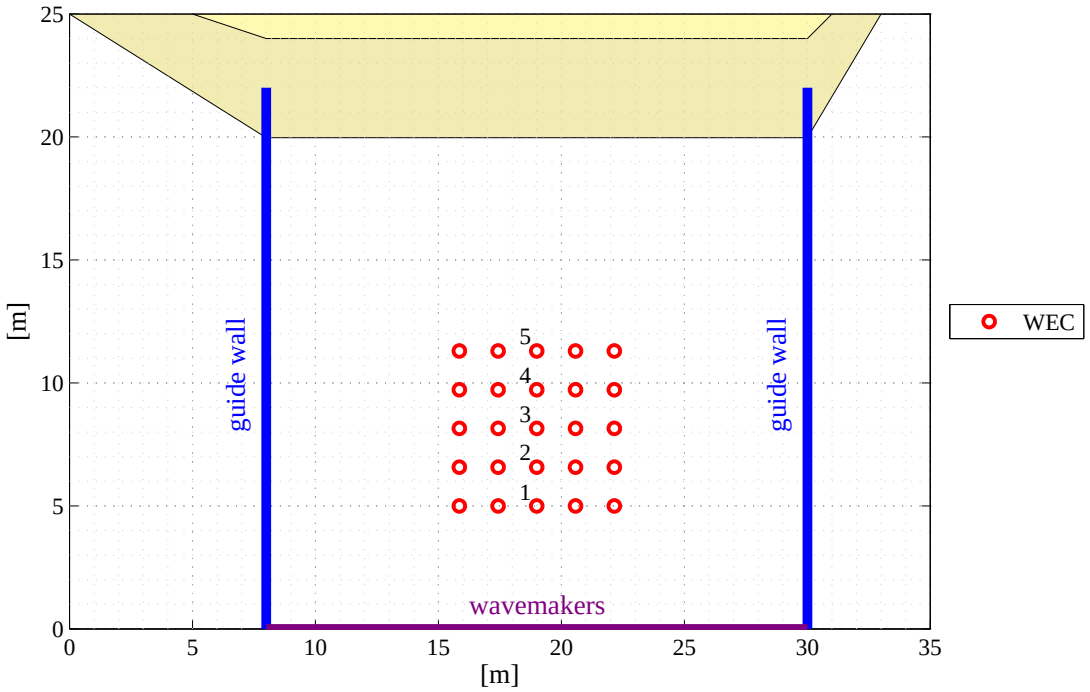

Figure 4.4: Layout of the test basin used during the WECwakes experiments.

Various tests were carried out, with and without the additional damping of the PTO system. Data were captured generally over a 3 minute period, with tests involving at least two repetitions of the decay procedure. Details of the specific tests relevant to the work in this thesis are provided in Table 4.1. The device spacing is expressed in terms of D, the model diameter.

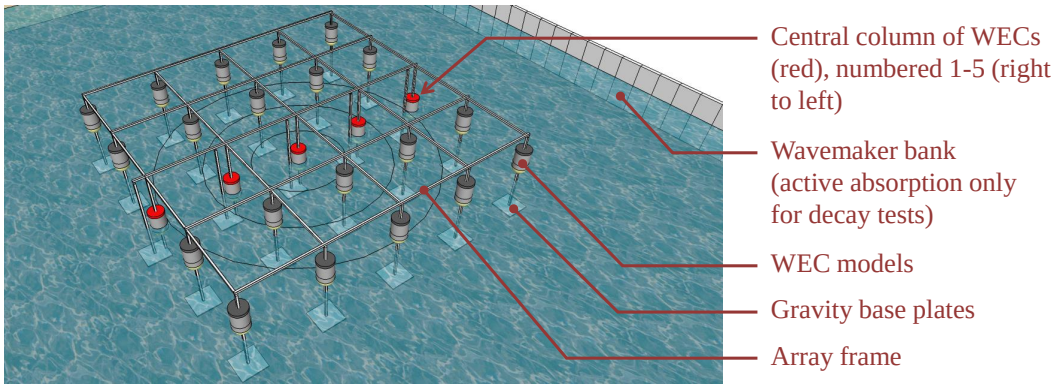

Figure 4.5: Test configuration within the basin, indicating the *FiveWEC* case.

Figure 4.6 gives details of how the experimental rig and instrumentation were configured within the basin. A total of forty one resistive wave gauges were positioned to record a detailed map of the free surface elevation. These were calibrated at the beginning of each test day, with the water temperature monitored thereafter.

Table 4.1: Summary of tests used.

Ref ID	No. of WECs	Spacing	WECs used	No. of sequences	Damping	WECwakes ID
TestID-01	1	–	5	2 [1]	No	T0118
TestID-02	1	–	5	3 [1]	No	T0119
TestID-03	1	–	5	2	No	T0161
TestID-04	1	–	5	2	No	T0162
TestID-05	1	–	5	2	Yes	T0159
TestID-06	1	–	5	2	Yes	T0160
TestID-07	2	5D	5 (4)[2]	2	No	T0171
TestID-08	2	5D	5 (4)[2]	2	No	T0172
TestID-09	2	5D	5 (4)[2]	2	Yes	T0169
TestID-10	2	5D	5 (4)[2]	2	Yes	T0170
TestID-11	2	10D	5 (3)[2]	2	No	T0191
TestID-12	2	10D	5 (3)[2]	2	Yes	T0181
TestID-13	2	15D	5 (2)[2]	2	No	T0195
TestID-14	2	20D	5 (1)[2]	2	No	T0190
TestID-15	5	5D, 10D	3 (1,2,4,5)[2]	2	Yes	T0200
TestID-16	5	5D, 10D	3 (1,2,4,5)[2]	2	No	T0201

[1] Preliminary tests using WEC-5 involved partially submerging the float, and releasing. This different method of initiating the decay test proved more difficult to control consistently. Settling times were also inadequate for these cases.

[2] Neighbouring WECs (in brackets) were at rest at the start of each test.

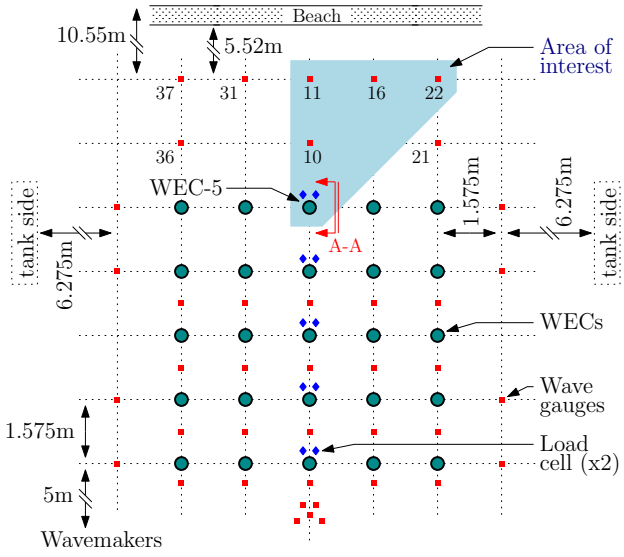

Figure 4.6: Array layout schematic. Adapted from Stratigaki *et al.* (2014).

4.3 Experimental results

For the decay tests, measurements from the relevant potentiometers were of interest, along with readings from the surrounding wave gauges. For scenarios where more than one WEC was in the water, force gauge measurements were also relevant. The sample rate of all recorded data was 40Hz. Details of the sensors used for this work are provided in Table 4.2.

Table 4.2: Summary of sensors used for the decay tests studies (marked ●).

Ref	Description	*OneWEC*	*TwoWEC*	*FiveWEC*
Pot-1	Potentiometer for WEC-1	-	-	●
Pot-2	Potentiometer for WEC-2	-	-	●
Pot-3	Potentiometer for WEC-3	-	-	●
Pot-4	Potentiometer for WEC-4	-	●	●
Pot-5	Potentiometer for WEC-5	●	●	●
WG-5D	Wave gauge (WG-10)	●	-	-
WG-10D	Wave gauge (WG-11)	●	-	-
WG-11D	Wave gauge (WG-16)	●	-	-
WG-14D	Wave gauge (WG-22)	●	-	-
FG-1&2	Load Cells ($\times$2, WEC-1)	-	-	●
FG-3&4	Load Cells ($\times$2, WEC-2)	-	-	●
FG-5&6	Load Cells ($\times$2, WEC-3)	-	-	●
FG-7&8	Load Cells ($\times$2, WEC-4)	-	●	●
FG-9&10	Load Cells ($\times$2, WEC-5)	●	●	●

WEC-5 was chosen as a reference WEC for the decay tests for a number of reasons. As discussed above, this was one of five WECs which were configured with force gauges. The position of WEC-5 at the edge of the array also allowed access via an overhead personnel platform, making it possible to conduct decay tests without causing any other disturbance to the free surface. Preliminary decay tests were also carried out using WEC-1, which met the same requirements; however, more reliable measurements were obtained from WEC-5 during investigative tests. WEC-5 was approximately in the centre of the basin, and being at the back of the array, it was also adjacent to a relatively large area that was free from other obstructions.

A number of wave gauges were included in this region, set out in the same grid pattern as the array (spacing at 5 times the diameter D), four of which have been identified within the blue region Figure 4.6. These gauges, WG-10, WG-11, WG-16 and WG-22, have been used in this work to validate the free surface predictions using the single WEC numerical models. In the proceeding text, all reference to these wave gauges is denoted by their approximate distance to WEC-5, in terms of the diameter $D = 0.315$m. Wave gauges 10, 11, 16 and 22 are thus referred to as *WG-5D*, *WG-10D*, *WG-11D* and *WG-14D*, respectively.

As detailed in Figure 4.3, force gauges were included at the top and bottom of each WEC axis.

For the five WECs concerned here, ten force gauges were used in total, shown in Figure 4.7, and listed in Table 4.2. When used for the validation procedures in Chapter 7, the combined measurements from each force gauge pairing are presented (i.e. total surge force per WEC).

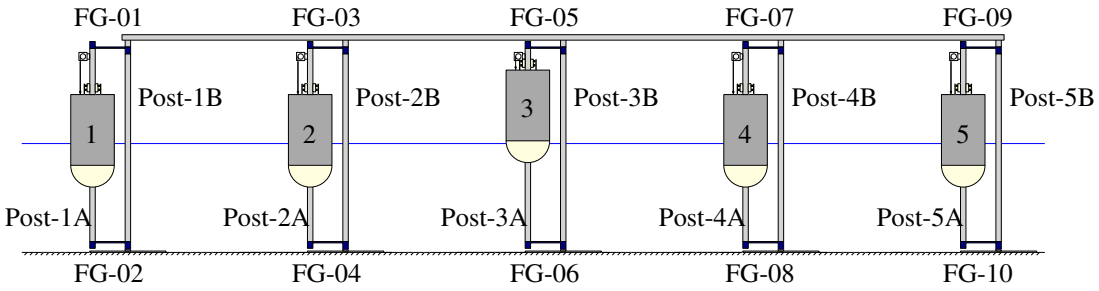

Figure 4.7: Section view of the WEC models and corresponding force gauges from the WECwakes experiment.

4.3.1 Raw data

Excursion

The tests were carried out manually by raising the float out of the water by approximately 0.2m, maintaining the elevated position for a period of 30–40s, and then releasing into the quiescent water. A minimum of 90s was always maintained between any two decay tests. A sample set of unprocessed data is provided in Figure 4.8, which shows the float excursion during two decay test sequences within a period of three minutes. The measurements were characterised by smooth and consistent decay behaviour, with low levels of precision uncertainty relative to the overall measured excursion magnitudes. A small bias of -5.5mm was also experienced, the origins of which are related to the factors discussed below. It is noted that, in contrast to the wave gauges, it was not necessary to recalibrate the potentiometers at daily intervals, and that it was acceptable simply to correct the small bias retrospectively.

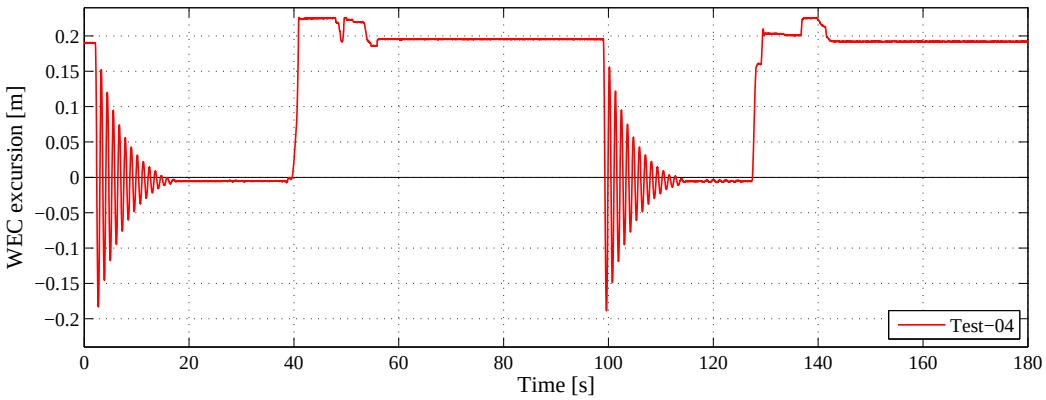

Figure 4.8: Unprocessed potentiometer output for WEC-5, from a sample 3 minute test. Includes two decay sequences (3s and 107s).

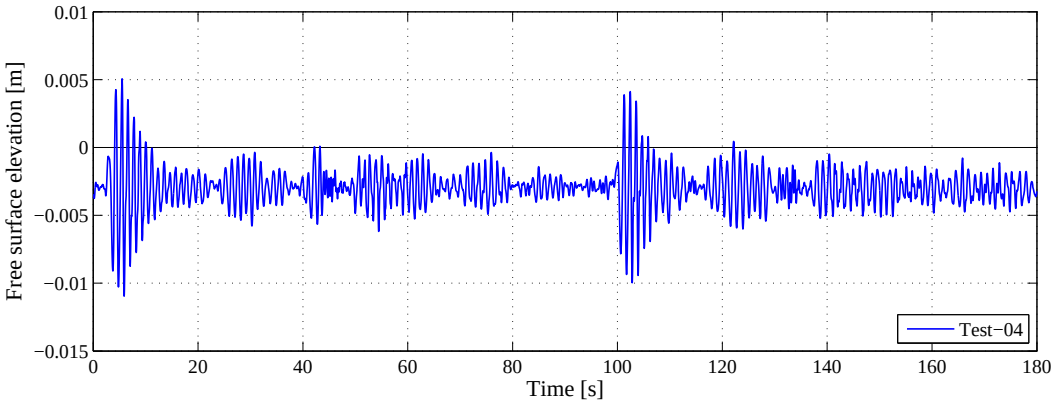

Figure 4.9: Unprocessed wave gauge output for WG-5D, from a sample 3 minute test. Includes two decay sequences (3s and 107s).

Free surface elevations

The corresponding free surface elevation history at WG-5D is provided in Figure 4.9. An observation which is immediately clear is that there is a marked offset from the calibrated zero point. Noting that the test shown was the final test undertaken on that particular day, two factors may explain this behaviour, relative to the calibration setup at the beginning of the day: a real change in water level; and/or a change in water temperature.

Regarding temperature, measurements made from a submerged probe showed that a change in temperature of just 0.025°C was experienced in a period of around 9 to 10 hours, resulting in a negligible change to the resistive characteristics of the water. A known operational factor of the test facility, however, was that the water level in the basin decreased very gradually over the course of a day. The standard procedure taken to address this was to ensure that the basin was topped up to the design water level prior to the wave probe calibration procedures at the start of each test day. From this point onwards, no further water was added to the basin for the remainder of the day, to minimise any uncontrolled changes to the water temperature, or any other fluid properties which could have adversely affected its conductivity. It is assumed here that the measurement bias shown in Figure 4.9 of around -3.1mm was caused by this change in water level. The average bias across all forty one wave gauges also measured -3.1mm.

Reflections are also seen in Figure 4.9. While the amplitudes of these effects measured up to 25–30% of the largest oscillations, the period of interest in these tests was found to be <16s after the WEC was released, beyond which point the WEC was practically at rest. After 16s, straightforward reflection analysis shows that the positions of the external boundaries should cause reflections, which agrees with the patterns shown in Figure 4.9[§]. Very small disturbances to the free surface were also caused by the lifting of the float up to the elevated starting point

[§]This was slightly earlier for the outer wave gauges, which had a shorter line of sight. This is evident in the processed results in Section 4.3.2.

for the proceeding test. However, no decay tests were initiated until the standard deviation of the wave gauge signals were seen to settle below a given threshold, equivalent in physical terms to wave amplitudes of ± 0.1mm. This resulted in a minimum of at least 90s between decay test sequences.

Forces

Figures 4.10a and 4.10b show surge force measurements for WEC-4 during a sample *TwoWEC* test, for the upper and lower force gauges, respectively (FG-07 and FG-08). WEC-4 was hydrostatically at rest, as WEC-5 was released from height over two repeated decay tests, initiated at approximately 5s and 116s. Vibrations though the rig structure can also be seen between 39–56s, when the elevated position of WEC-5 was reset.

While at the elevated position at the start of each test, WEC-5 was supported by the rig. Evidence of non-negligible static loads on the structure can be seen in the sensor measurements, resulting in differing sensor equilibrium positions before and after the decay sequences. This effect is more pronounced for the upper force gauge FG-07, shown in Figure 4.10a, but can also be confirmed from interrogation of the force gauges for WEC-5, as seen in Figure 4.10c (FG-09 and FG-10). In the absence of any static loads, the forces acting on WEC-5 should otherwise be limited to vibration effects directly from the decay tests, and forces caused by wave diffraction and radiation reciprocated by WEC-4. Although this was not the case, and static loads were also registered, these loads did however diminish rapidly following the release of the float. The lasting impact on the relevant results (5–21s and 116–132s for the sample shown in Figures 4.10) was limited to a high frequency vibration within the period 0-1s for each test carried out. These effects are discussed in more detail in Section 4.3.2, where results have been corrected for bias based on the equilibrium resting position *after* the decay tests (both WEC-4 and WEC-5 hydrostatically at rest).

4.3.2 Processed data

The processed results detailed below have been adjusted in accordance with the discussions in Section 4.3.1. With exception of the surge force measurements, these adjustments were limited to corrections to biases, and realignment in time. Vibrations in the force records were also filtered using a Fast Fourier Transform (FFT) procedure. The only additional numerical processing of the data was the provision of an averaged time history for repeated tests. In order to provide accurate averages for the various time series, when realigning with respect to time, it proved necessary in some instances to offset by non-integer numbers of samples. Due to this misalignment of data, it was necessary to use splines to generate an average. This procedure was used only to generate data at the consistent sample points where necessary, and not to perform any other modification to the data.

The mean of the processed and filtered (forces only) results have been used for all remaining work, referred in the various validation Figures in later Chapters as *'WECwakes'*.

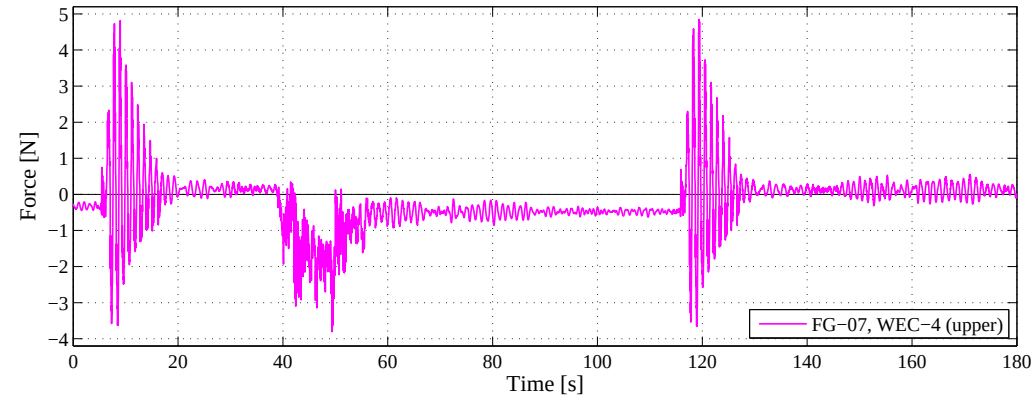

(a) Upper force gauge FG-07 for WEC-4 (initially at rest)

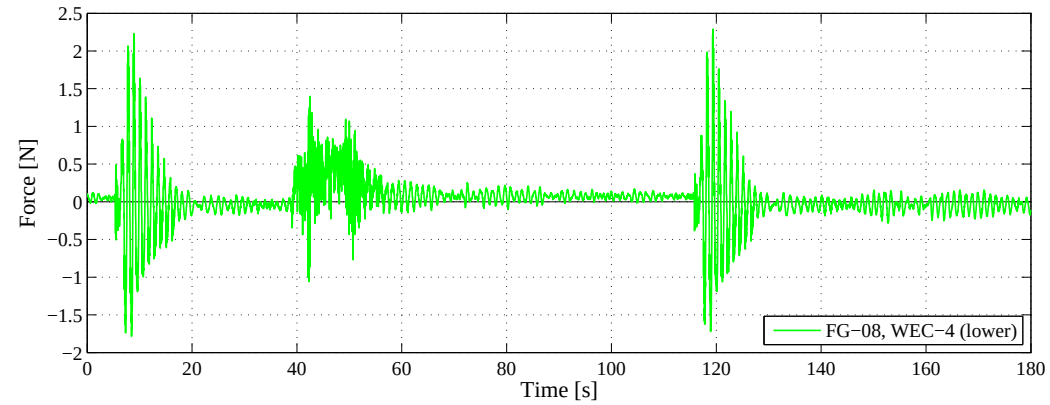

(b) Lower force gauge FG-08 for WEC-4 (initially at rest)

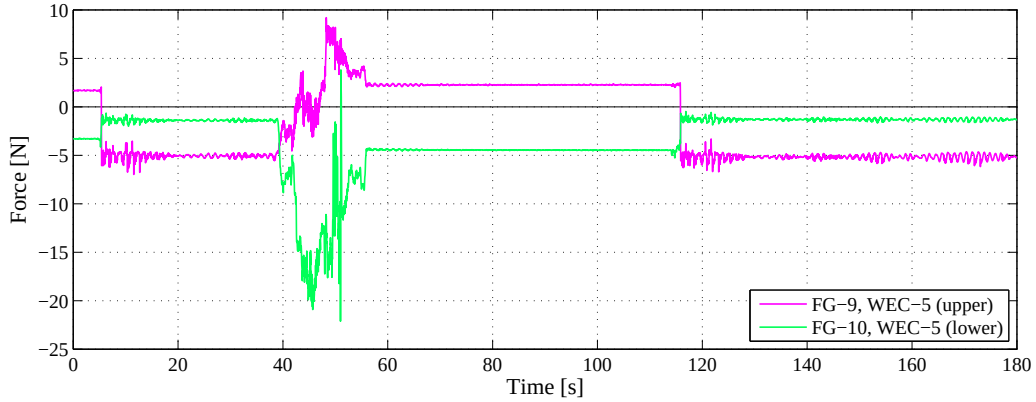

(c) Upper and lower force gauges FG-09 and FG-10, for WEC-5 (raised and dropped)

Figure 4.10: Unprocessed surge force output during a *TwoWEC* test (Test-07). Includes two decay sequences, at 5s and 116s.

Excursion

For the single WEC decay tests, measurements from the potentiometer (ξ) attached to WEC-5 were compared across four repeated tests, shown in Figure 4.11. The responses were normalised to the precise initial displacement for each test (ξ_0), which between the tests measured 0.2m $\pm$ 2.15%. The normalised results show very close agreement, for which the RMS error is <1%. The undamped system oscillated with a natural period of 1.143s, coming to rest in around 16s, or around 13 cycles. Some very small oscillations reappeared at around 20s as a result of reflected waves, which peaked at $\xi/\xi_0 = 0.011$. Nonetheless, the extremely close correlation between repeated tests suggested that the results were very stable.

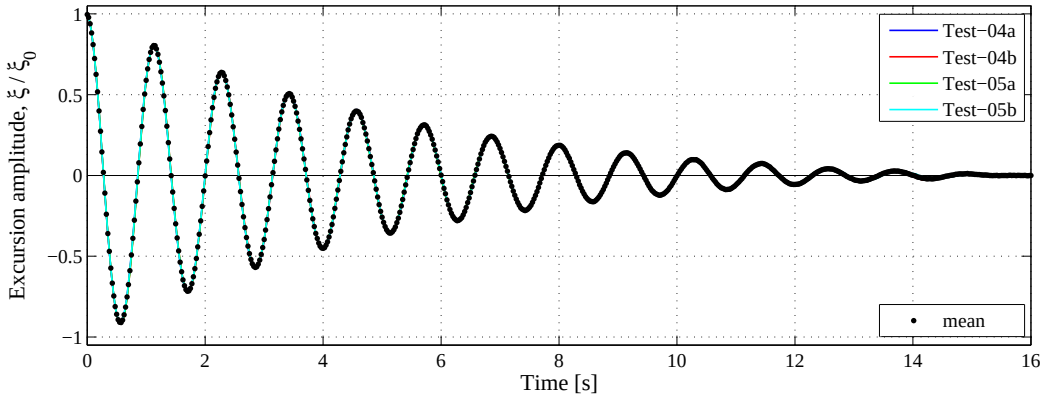

Figure 4.11: Measured WEC responses from four repeated decay tests (including mean).

Free surface elevation

Normalised free surface elevation measurements (η/ξ_0) are presented in Figures 4.12 for wave gauges WG-5D, WG-10D, WG-11D and WG-14D. Correlation between the four repeated tests was acceptable, with RMS errors generally within 12% of the largest mean data measurement ($\eta/\xi_0 = 0.0388$). Significant reflections are clearly visible, however, as was discussed in Section 4.3.1. Although the amplitude of these reflections were significant (at 27%, 43%, 45% and 56% of the primary amplitudes at WGs 5D, 10D, 11D and 14D respectively), in each case there was a clear separation between the primary wavetrain, generated by the oscillatory motion of the WEC, and the secondary wavetrains, which are present due to reflections.

Aside from reflections, a number of other features exist in the wave gauge records that show non-smooth oscillatory behaviour. The reappearance of these features upon repeated tests suggests that they were systematic, and not random. Kinks in the elevation measurements at WG-5D for example can been seen between 4s–7s, recreated faithfully across the four tests. As is demonstrated in Section 4.3.3, these nonlinear effects appear as higher frequency harmonics, which travel to the outer wave gauges with an associated lag, reflecting their lower wave celerity.

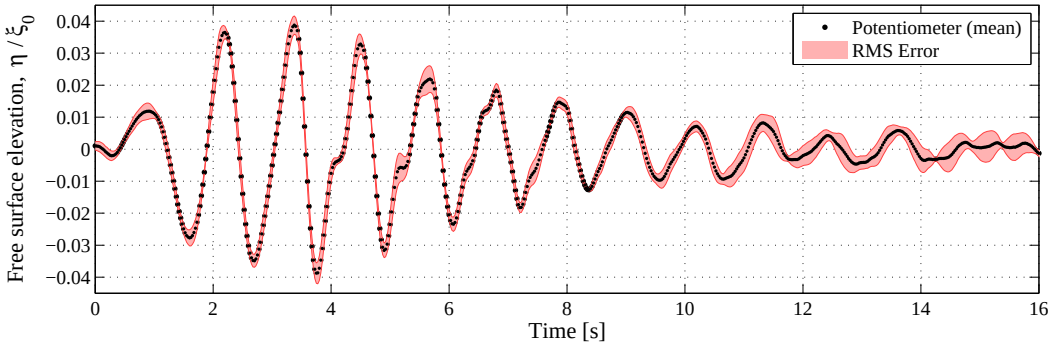

(a) WG-5D

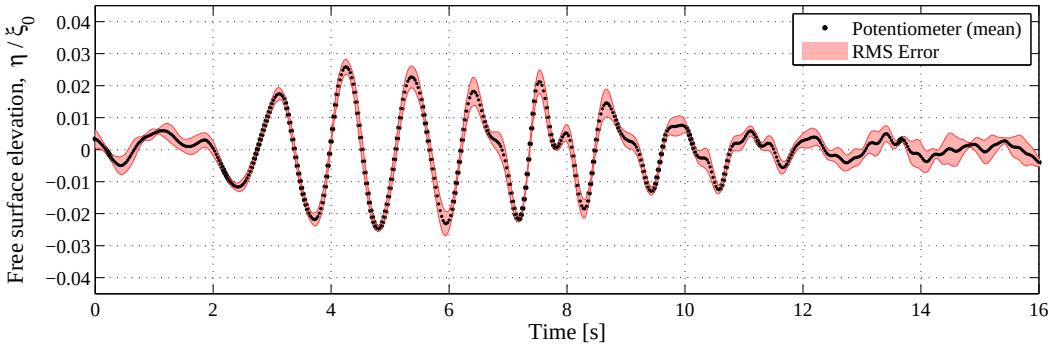

(b) WG-10D

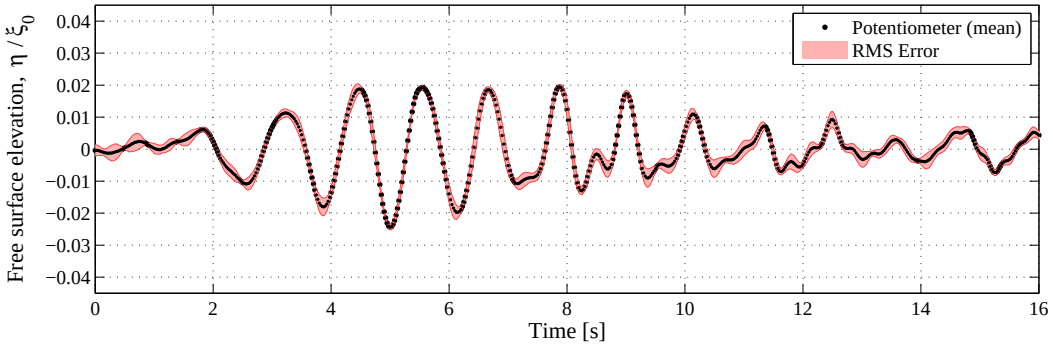

(c) WG-11D

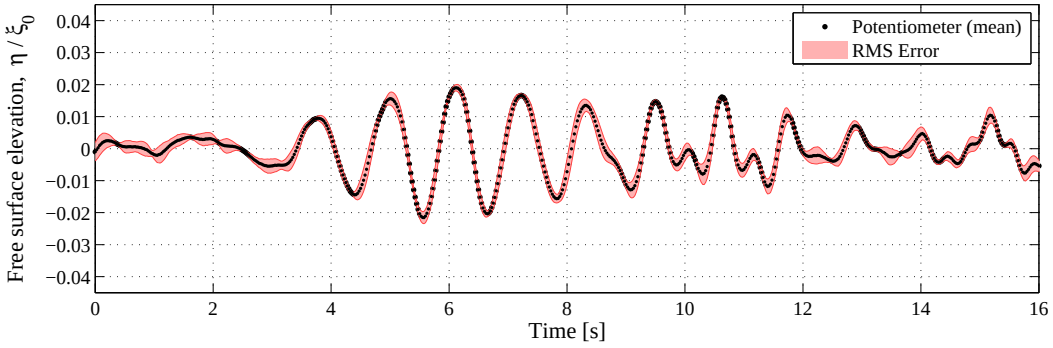

(d) WG-14D

Figure 4.12: Mean wave elevation measurements with RMS error for the *OneWEC* tests.

Forces – TwoWEC tests

Surge forces on the WECs were measured during the experiments to understand the behaviour of friction effects, as discussed in Section 4.2.2. The results described below also provide additional validation data for the WEC interaction problem, modelled numerically in Chapters 4 to 7.

Unlike the wave gauge measurements, which were naturally smooth and oscillatory, the records of forces from the experiments were partially compromised by secondary effects caused by vibrations of the structure. Aspects of pre-test static loading and the associated vibration which followed were discussed in Section 4.3.1, which showed that small effects could be translated between different WEC assemblies attached to the primary frame of the rig. Examination of the force gauges which were not of direct concern in the *TwoWEC* tests, i.e. the force gauges connected to WEC-1 to WEC-3 (which were lifted completely out of the water) showed the same brief vibration between 0-1s, as seen in Figure 4.13. It is noted here that all surge force measurements F_x in the following figures are expressed in nondimensional form, with respect to water density ρ, acceleration due to gravity g, the water plane area of the device S_w and initial device displacement ξ_0.

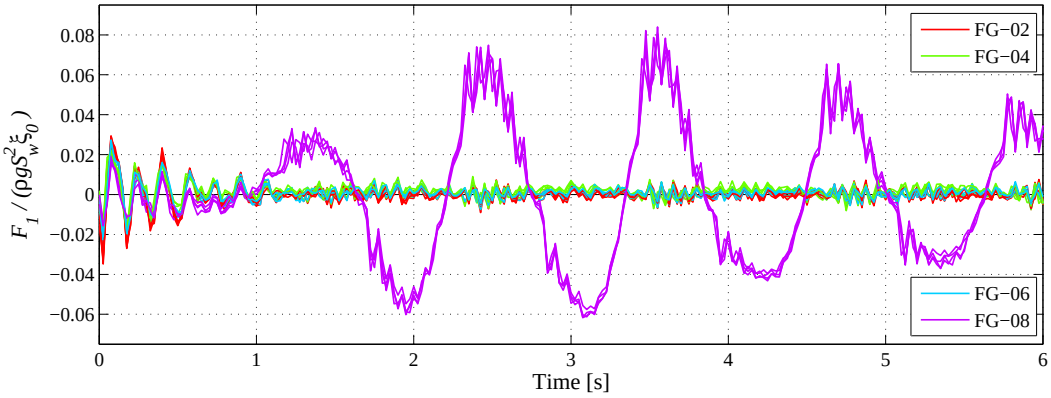

Figure 4.13: Measurements from the lower force gauges for WEC-1 to WEC-4, for four repeated tests. WEC-1 to WEC-3 were omitted from the *TwoWEC* tests.

Processed results for the upper force gauge connected to WEC-4 are provided in Figure 4.14. Additional disturbances, distinct from the initial effects described above, were also sustained throughout the decay process. The consistency of the high frequency oscillations between repeated tests, and the regularity of the patterns seen between the peaks and troughs, suggest that the distortions were caused directly by vibrations from the decay process. The phase of the motion measurements for WEC-4 also coincided approximately with the harmonic force patterns shown in Figures 4.14. This appears to indicate a tendency for the float to experience greater unstable lateral vibrations when it was partially out of the water, and for these vibrations to dampen when the WEC was partially submerged.

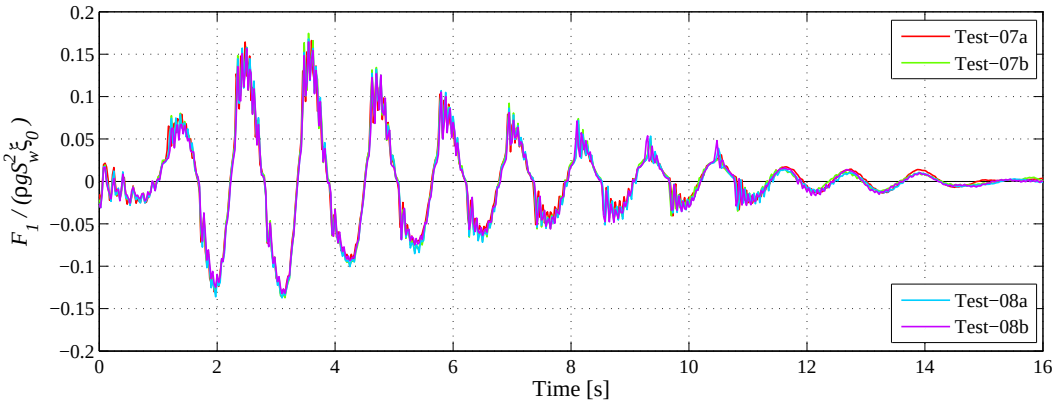

(a) Processed data (0–16s)

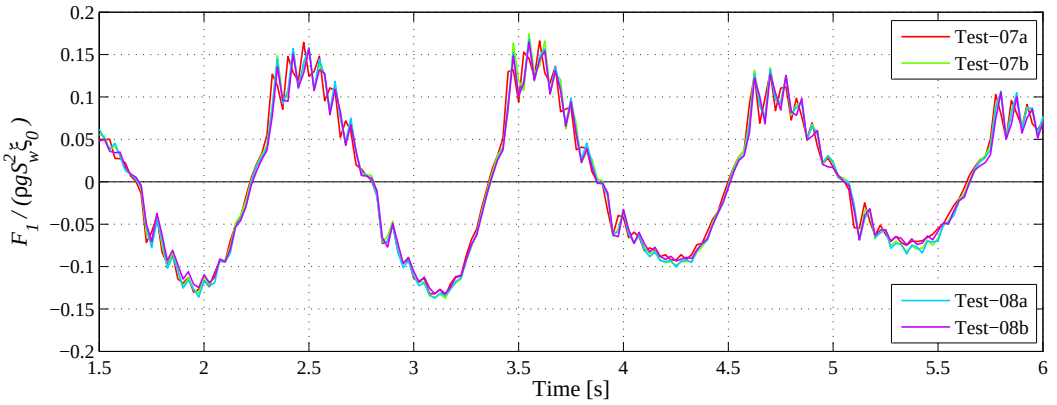

(b) Processed data (1.5–6s)

Figure 4.14: Surge force on WEC-4, due to the free oscillation of WEC-5 (TwoWEC tests).

To validate the numerical models described in later chapters it was useful to remove these unwanted effects, given that they originated from external influences which were unrelated to the physics captured in the computational models. By filtering beyond the fourth harmonic (3.5Hz), the effects of the structural vibrations were removed, demonstrating close correlation between the underlying results. Figures 4.15 shows the filtered results, and the corresponding modifications to the frequency spectrum. Measurements from both upper and lower gauges had nonlinear characteristics, which tended to result in more rapid increases towards peak forces in the outward direction ($F_1 > 0$), and a more gradual change to inward forces ($F_1 < 0$).

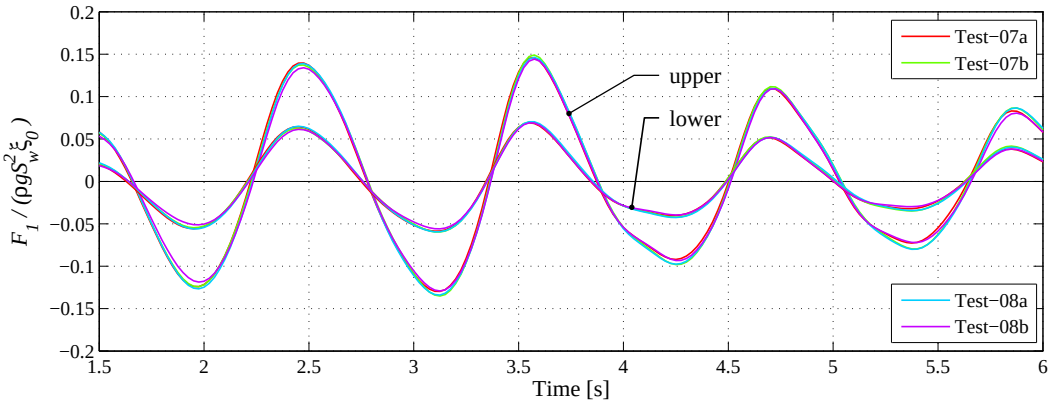

(a) Processed and filtered data (1.5–6s)

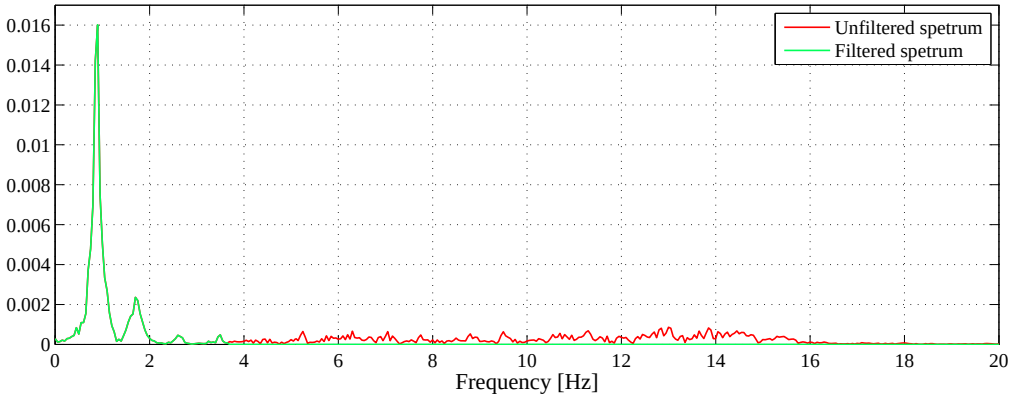

(b) FFT of the signal from FG-08 (lower), during a sample *TwoWEC* test (Test-08b).

Figure 4.15: Filtered surge force on WEC-4, due to the free oscillation of WEC-5 (TwoWEC tests).

Forces – FiveWEC tests

For the *FiveWEC* tests, the central WEC (WEC-3) was released from height, while the neighbouring WECs were hydrostatically at rest, with two positioned at a distance of 5D, and a further two at 10D. Surge force measurements for these tests are provided in Figures 4.16 and 4.17, for WECs positioned at 5D and 10D respectively. Four results were used to provide the mean measurements and RMS error shown in Figures 4.16a, 4.16b, 4.17a and 4.17b. This used two test results (Test-16a and Test-16b), and assumed that the response of both WECs at 5D were equivalent (i.e. both WEC-2 and WEC-4 gave adequately reproducible results), and likewise for the WECs at 10D. This assumption is examined further below.

After filtering the data using the same approach as discussed above, however, a small lag becomes apparent between the peak outward forces for WEC-2 and WEC-4, as seen in Figure 4.16c, which indicates the existence of a systematic event during the experiments. A section of the frame arrangement is provided in Figure 4.7, which shows the positioning of Post-B for

WEC-3, which is thought to cause this particular discrepancy in force measurements. Small errors may also exist due to frame dimension tolerances; however, this is not considered to be the principal cause of this error, as there is no equivalent lag for inward forces ('troughs').

In general, the level of distortion was significantly higher, and more random, in the *FiveWEC* tests. For the inner WECs, however, the force amplitudes between the *TwoWEC* and *FiveWEC* tests compared well. Additional hydrodynamic effects also exist, which are examined numerically in later chapters. For the WECs at 10D spacing, shown in Figure 4.17c, a considerable level of distortion was experienced. The data still provides indicative force amplitudes, which are also used to validate the corresponding numerical models.

4.3.3 Spectral analysis

Aspects of non-smooth oscillatory behaviour were discussed briefly in Section 4.3.2, where it was suggested that systematic effects were responsible for the additional features seen in the wave gauge time histories. Frequency decompositions of the various signals have been generated in order to examine the validity of this statement. By demonstrating that the effects were harmonic, it is possible to identify the origin of the additional effects, and explain their physical presence.

It was necessary to consider the transient behaviour of the signal when analysing the frequency content, due to the relatively rapid damping and natural decay of the system. This required Short-Time Fourier transform (STFT) analysis, using a moving window to generate an array of well defined discrete Fourier series.

Figures 4.18 to 4.21 show spectrograms of the wave gauge measurements for *WG-5D*, *WG-10D*, *WG-11D* and *WG-14D* respectively. An extended length of signal has been shown, in which the reflections can be seen clearly from around 15-18s, at the natural frequency of the decay process f_0 (0.875Hz). With respect to primary physical process of the decay sequence (up to around 15s), the salient features appear at one, two, three and four times the natural period of the system, arriving later at each progressively higher frequency. These spikes, although much reduced in magnitude at the higher frequencies, form a diagonal line in Figure 4.18. Likewise, in Figures 4.19 to 4.21, similar behaviour is observed, with the increased skewness of this line at greater distances from the moving WEC, demonstrating that these features represent wave dispersion. Table 4.3 summarises some observations from the wave gauge measurements.

Table 4.3: Artefacts in the experimental measurements

	WG-5D	WG-10D	WG-11D	WG-14D
Harmonics	2.5s-7s	5s-11s	6s-13s	>9s
Reflections	>17.5s	>16s	>14s	>13.5s

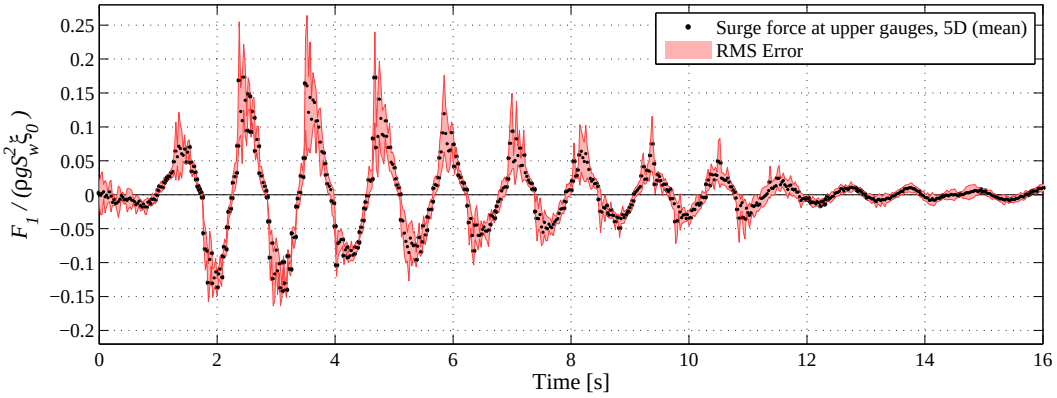

(a) Processed data with RMS error, for the upper force gauges (FG-3 and FG-7)

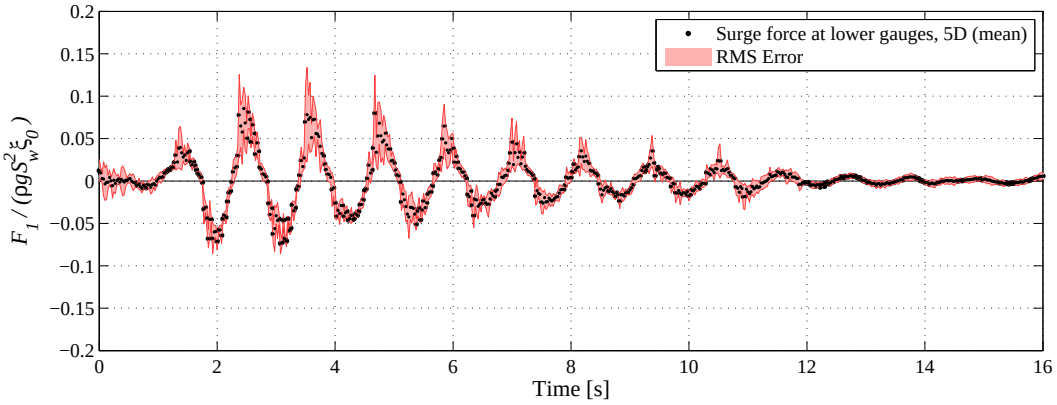

(b) Processed data with RMS error, for the lower force gauges (FG-4 and FG-8)

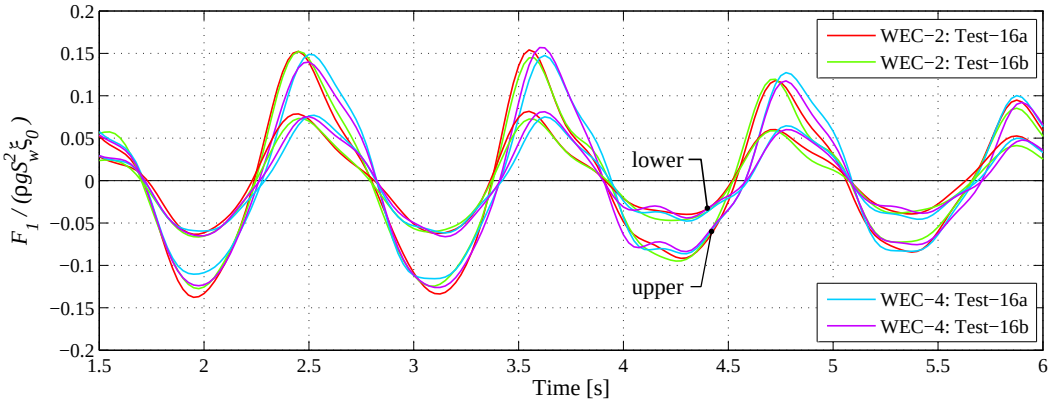

(c) Processed and filtered data

Figure 4.16: Surge force on neighbouring floats positioned at 5D spacing (WEC-2 and WEC-4), due to free oscillation of WEC-3 (FiveWEC test).

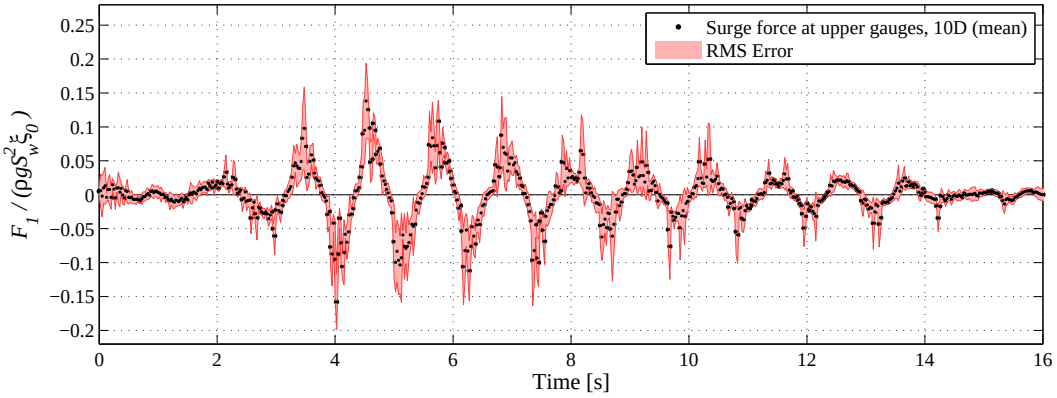

(a) Processed data with RMS error, for the upper force gauges (FG-1 and FG-9)

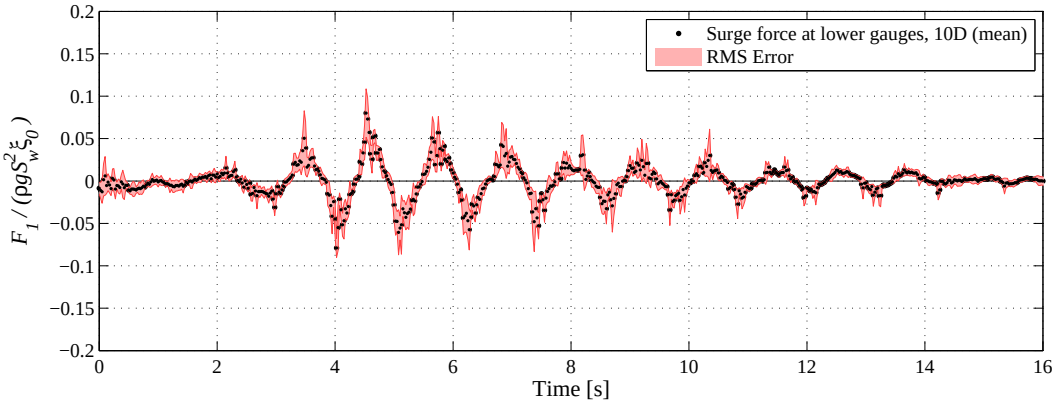

(b) Processed data with RMS error, for the lower force gauges (FG-2 and FG-10)

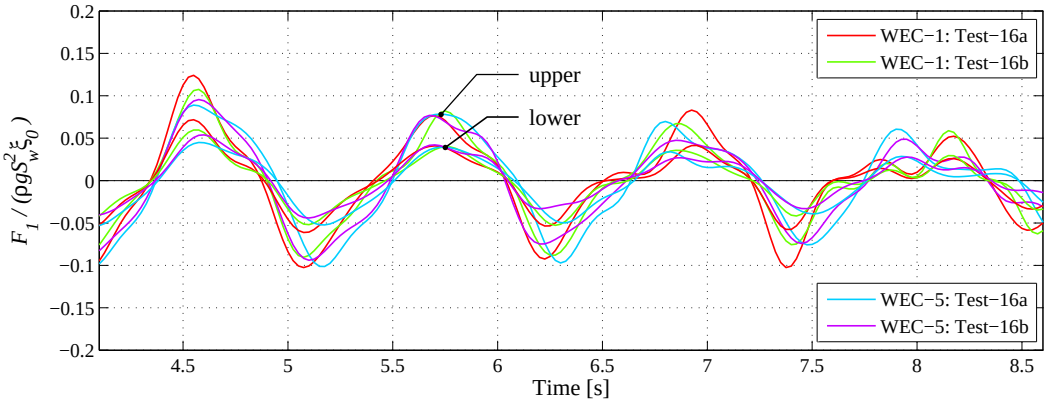

(c) Processed and filtered data

Figure 4.17: Surge force on neighbouring floats positioned at 10D spacing (WEC-1 and WEC-5), due to free oscillation of WEC-3 (FiveWEC test).

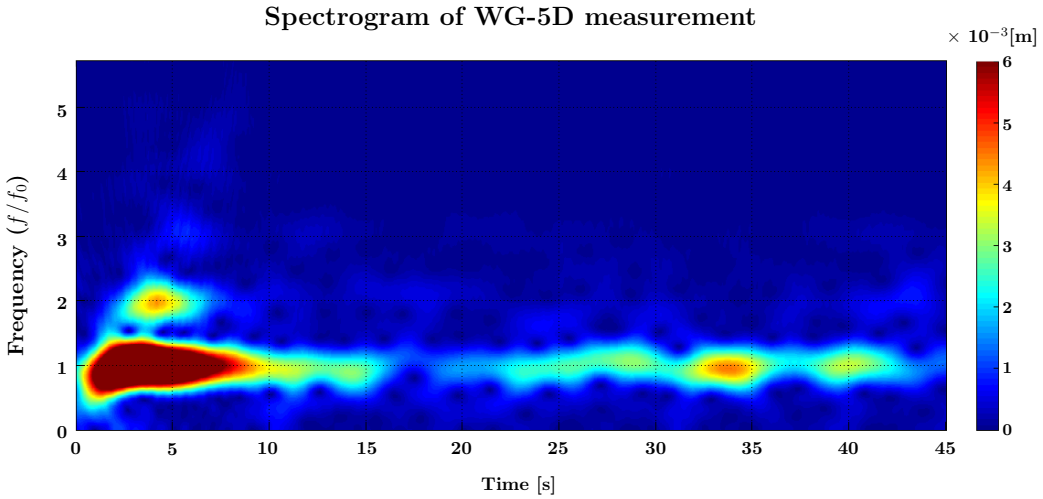

Figure 4.18: Spectrogram of wave gauge measurement from WG-5D during test Test-04b. The colour scale is truncated to 6mm to emphasise disturbances away from the main peak. The frequency (f, Hz) is normalised using the natural frequency, f_0.

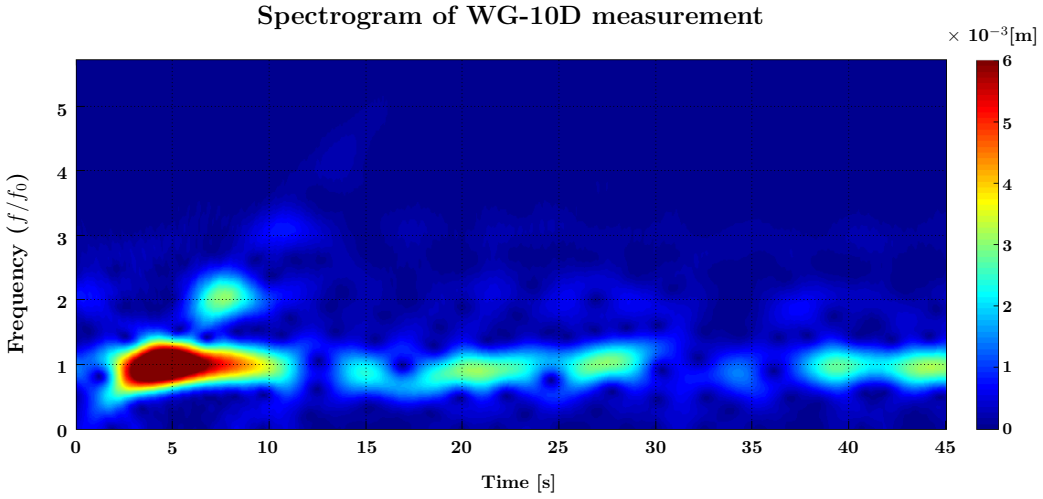

Figure 4.19: Spectrogram of wave gauge measurement from WG-10D during test Test-04b. The colour scale is truncated to 6mm to emphasise disturbances away from the main peak. The frequency (f, Hz) is normalised using the natural frequency, f_0.

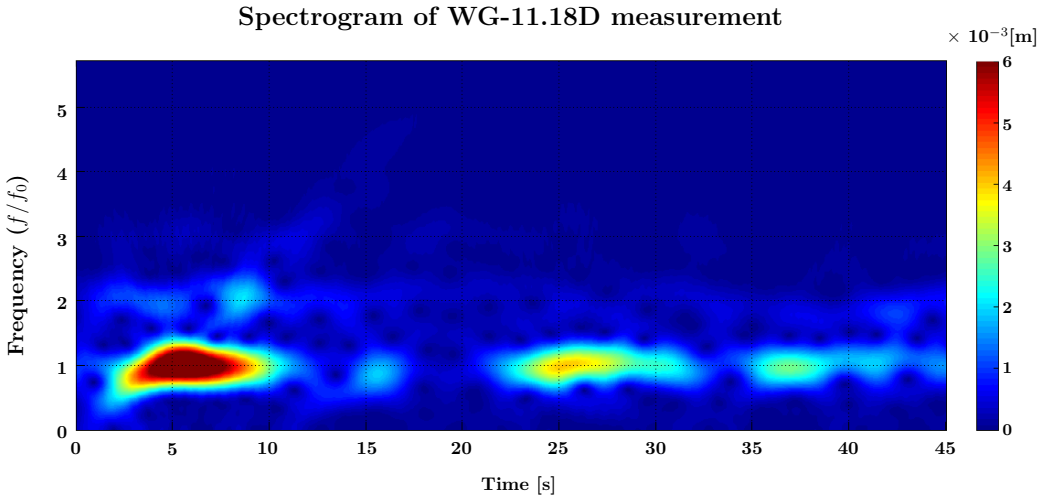

Figure 4.20: Spectrogram of wave gauge measurement from WG-11D during test Test-04b. The colour scale is truncated to 6mm to emphasise disturbances away from the main peak. The frequency (f, Hz) is normalised using the natural frequency, f_0.

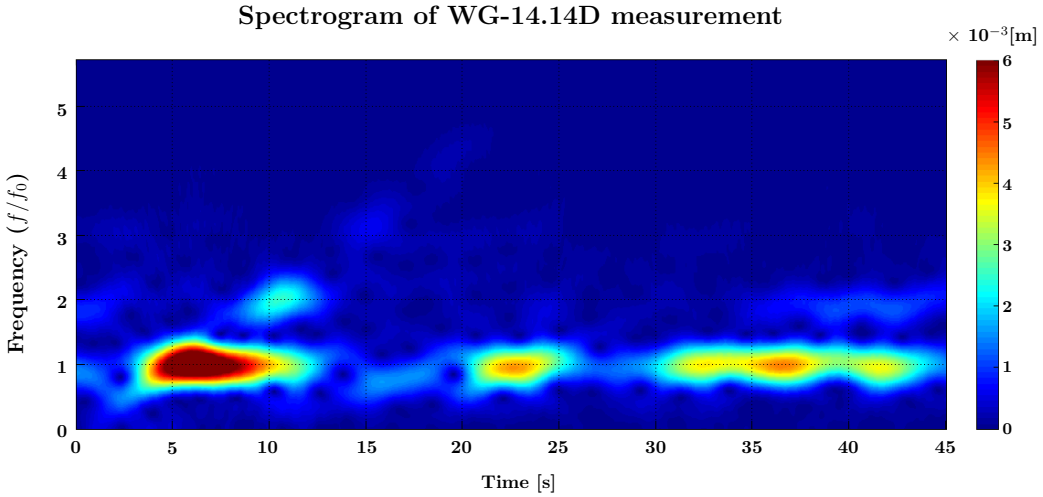

Figure 4.21: Spectrogram of wave gauge measurement from WG-14D during test Test-04b. The colour scale is truncated to 6mm to emphasise disturbances away from the main peak. The frequency (f, Hz) is normalised using the natural frequency, f_0.

4.4 Representative motion functions

It was useful to obtain a numerical expression which described the motion of the decaying device during the various tests. The main purpose of this was to develop an input function to use in conjunction with the numerical models, which allowed decoupling of the hydrodynamic and free body motion problems. Verification and validation of the free surface elevation predictions, for example, required the WEC to move in precisely the same way as in the experiments. Details of general problems associated with imposed body motions are described in Appendix C.1, which highlights the susceptibility of CFD type simulations to severe distortions, even when noise or vibration effects are very small. In a similar way to the extended analyses of the free surface and force measurement using frequency-domain methods described above, this decomposition also provides an enhanced interpretation of the signal in terms of hydrodynamic nonlinearities, and experimental uncertainties.

The numerical expression used to describe the WEC motion is principally an exponentially damped function in time, t, with frequency equal to the resonant harmonic ω_0. The time function of the decay is raised to the power ζ=1.06, which was obtained by identifying the global minima of the L2-norm of the residual, i.e. the difference between the experimental data and basic function. It was evident, as seen in Figure 4.22a, that the residual of the basic function retained various other features and required further treatment. A sequence of additional L2-optimisation steps were executed for appropriate functions that would address these features, each taking the form of a Gaussian profile harmonic signal, giving the expression:

$$\xi/\xi_0 = e^{-(t^{\zeta})/\omega_0} cos(\omega_0 t) - \sum_{i=1}^{N_{cor}} \alpha_i e^{-((t-\beta_i)/\gamma_i)^2} cos(\theta_i t - \vartheta_i) \; . \tag{4.1}$$

N_{cor} defines the number of correction steps, where $N_{cor} = 0$ returns the basic damped function. For the *OneWEC*, *TwoWEC* and *FiveWEC* decay tests, the value of N_{cor} was 6, 12 and 15, respectively, with the various coefficients provided in Appendix B (Table B.1). The harmonic behaviour of each correction component is defined by the frequency θ_i and phase ϑ_i. Where $\theta_i = 0$, the correction is a basic Gaussian curve. The amplitude, position and width of the function shape are defined here by α_i, β_i and γ_i respectively.

As shown in Figure 4.22a, the most prevalent feature of the residual for the *OneWEC* test was a long natural harmonic starting at around 8s, which is thought to stem from the complex behaviour (Coulomb damping) of the PTFE bearings. The initial descent of the WEC was also nonlinear, with a more abrupt downward acceleration in the experiments compared to that of the basic damped function ($N_{cor} = 0$). Again, this is thought to relate to complex dissipation processes during the experiment, possibly relating to water entrainment between the Post-A and the inner shaft within the WEC (i.e. beyond the submerged bearing). This dynamic damping

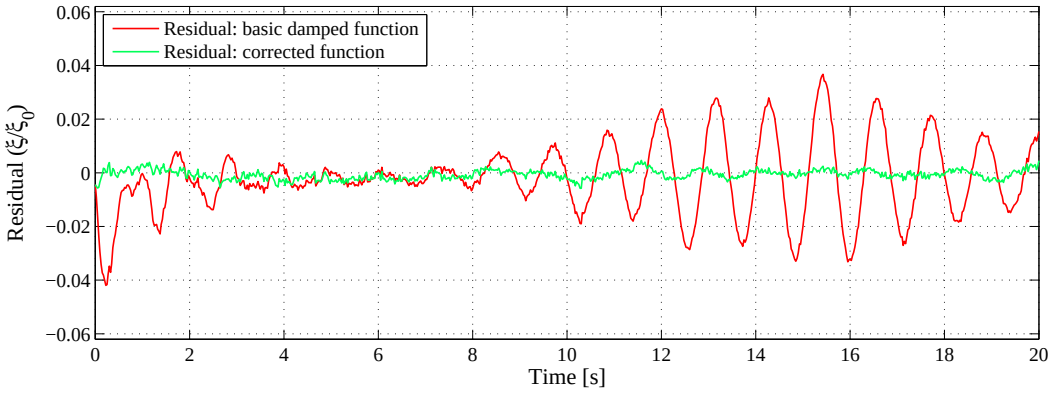

(a) Residual for the *OneWEC* test (WEC-5)

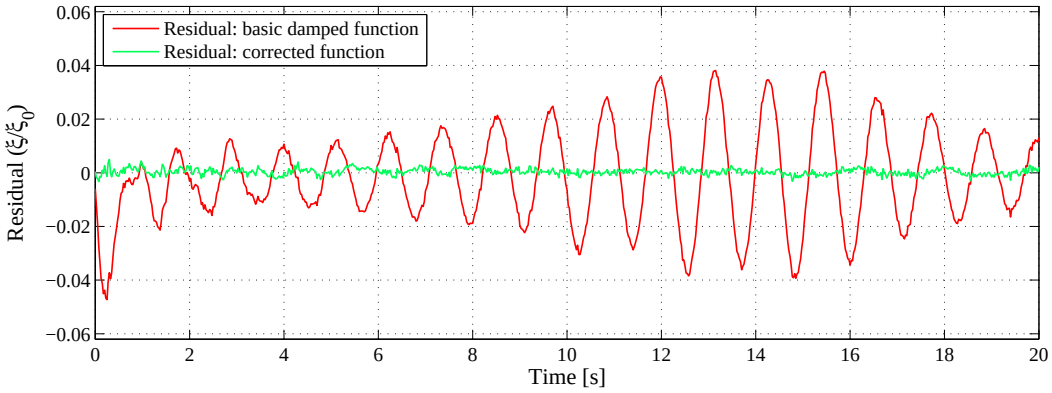

(b) Residual for the *TwoWEC* test (WEC-5)

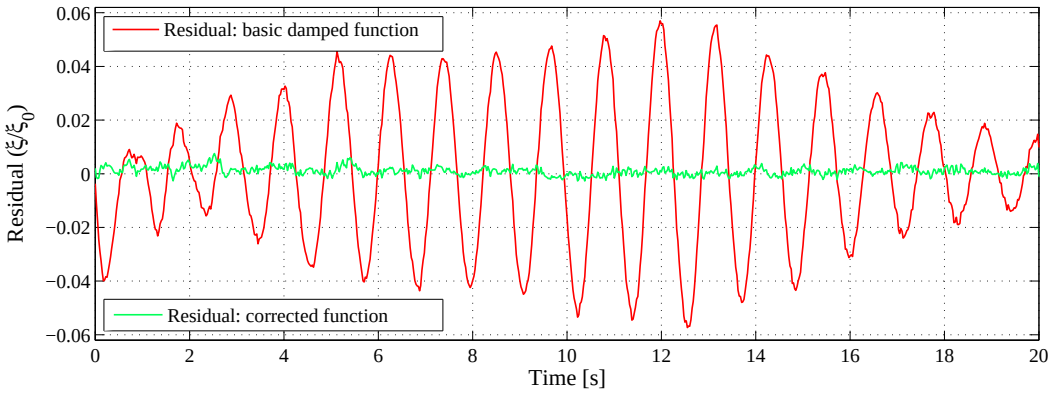

(c) Residual for the *FiveWEC* test (WEC-3)

Figure 4.22: The discrepancy between the measured response and the proposed numerical function for the motion of the decaying WEC, before and after the use of a corrective terms.

condition diminished after 3-4s. In Figure 4.22a, the excursion amplitudes are normalised to a unit drop height, with a peak error for the *corrected function* (shown in green) of 0.6%.

Figures 4.22b and 4.22c provide equivalent results for the *TwoWEC* and *FiveWEC* tests. Additional corrections[¶] were carried out to capture the greater complexity of the multi-body interaction systems. The peak errors for the corrected functions were 0.5% and 0.75% respectively. Appendix A (Figure A.1) provides the individual components used for these functions. As these components were not derived analytically, it is not certain that each individual correction represents a discrete physical processes. The patterns seen in Figures A.1b and A.1c do indicate, however, that measurable interaction effects are experienced, due to the presence of the additional WECs.

[¶]Corrections to the *TwoWEC* and *FiveWEC* motion functions included the original corrections to the *OneWEC* case ($i = \{1-6\}$).

Chapter 5

Linear Potential Flow Model

Following from the theory presented in Chapter 3, the specific application of the linear Boundary Element Method (BEM) is detailed in this chapter. The configurations of the frequency-domain and time-domain models are described, followed by results, presented for one, two and five Wave Energy Converter (WEC) scenarios. These particular WEC arrangements reflect the series of decay tests which were carried out as part of the WECwakes experiments (Stratigaki *et al.*, 2014). The device geometries and physical results from these experiments were described in detail in Chapter 4.

5.1 Frequency-domain model configuration

5.1.1 Model geometries

The WAMIT software takes geometric descriptions of the wetted surfaces of solid bodies in one of two ways – using simple planar panels (`ILOWHI=0`), or using patches defined by bi-cubic splines (`ILOWHI=1`). The first of these two methods was used throughout this work, with the necessary input files generated using MATLAB. Tests were carried out for different configurations of the WEC and posts, as detailed in Table 5.1. The angular separation of symmetry planes used for each model is indicated. Where one plane of symmetry was used, this is described as '180° separation'.

The panel arrangements for the various models are provided in Figure 5.1. Application of the symmetry property in WAMIT allowed corresponding reductions to the system of equations, where the number of unknowns `NEQN` reduced by either half or a quarter, depending on whether one or two planes were used. Figures 5.1a and 5.1b show the *OneWEC* and *OneWEC-a* cases (the latter including 'Post-A'), both of which could be configured with two planes of symmetry (`ISX=1,ISY=1`). Figures 5.1c and 5.1d indicate that only one plane of symmetry was possible (`ISX=1,ISY=0`) when there were additional bodies present, such as the secondary post (case *OneWEC-ab* – including 'Post-B'), or other WECs (*TwoWEC*, *FiveWEC*, etc.). It is noted that the bodies were constructed using the same physical dimensions as the experiments, thus the separation between the WEC centres for the multi-body cases was 1.575m, or 5*D*.

Table 5.1: Inclusion of posts for the time-domain models (marked ●). See Figure 4.7 for post references.

		Symmetry plane separation	Post 1a	Post 1b	Post 2a	Post 2b	Post 3a	Post 3b	Post 4a	Post 4b	Post 5a	Post 5b
T–D	*OneWEC*	90°	-	-	-	-	-	-	-	-	-	-
	OneWEC-a	90°	-	-	-	-	-	-	-	-	●	-
	OneWEC-ab	180°	-	-	-	-	-	-	-	-	●	●
	TwoWEC-a-b	180°	-	-	-	-	-	-	●	●	●	●
	FiveWEC-a-b	180°	●	●	●	●	●	●	●	●	●	●

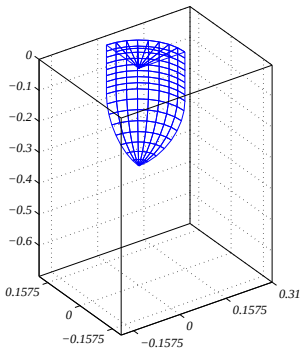

(a) *OneWEC*

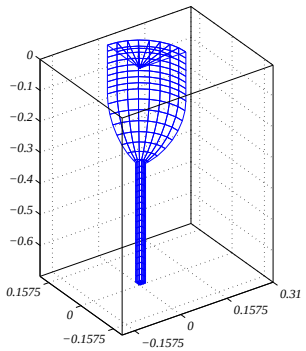

(b) *OneWEC-a*

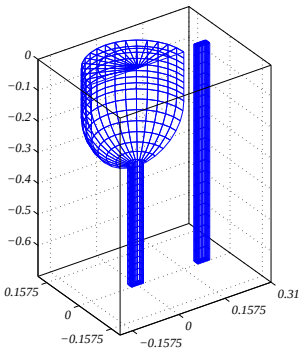

(c) *OneWEC-ab*

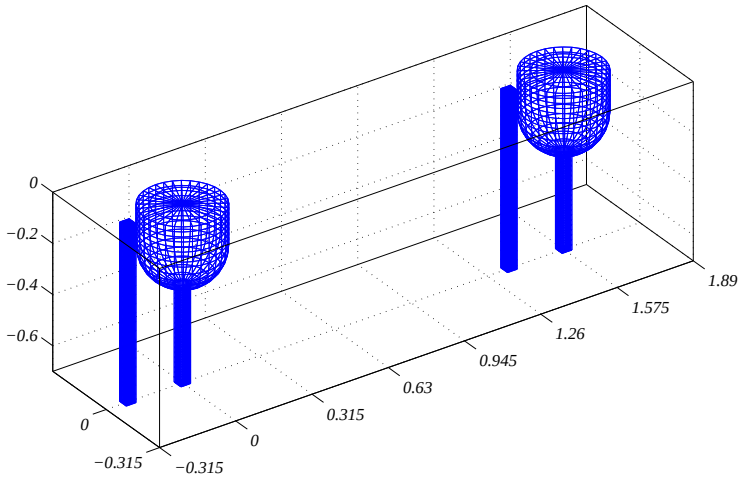

(d) *TwoWEC-ab*

Figure 5.1: Numerical model geometries for the BEM simulations. See Table 5.1 for model references.

Where more than one body was present in the domain, the WEC(s) and the post(s) were configured as independent bodies in the WAMIT simulations. In order to capture the correct flow behaviour and corresponding hydrodynamic coefficients, the base of the WEC had to be adapted at the surface region which intersected with the post. To avoid evaluating any invalid velocity potentials, both WEC and post geometries included an open 'hole' at the intersection between the two bodies, as seen in Figure 5.2. As was described in Chapter 3, the potential solution was evaluated using fixed, mean body positions; as such, the intersecting geometries gave reliable solutions around the region of these additional holes.

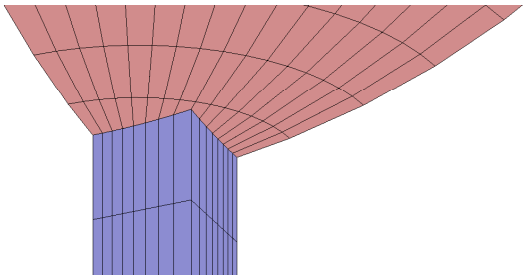

Figure 5.2: Intersection between the WEC geometry and post.

The geometries were also configured to ensure that it was possible to remove the effects of irregular frequencies. This required panels to be defined at the waterline which were outward facing, effectively 'closing' the geometry at the free surface. All panels above the water-plane were omitted, as these should not contribute to the potential solution for the water phase.

5.1.2 Solver configuration

A set of preliminary test cases are summarised in Figure 5.3, which show the complex free surface elevation ($\hat{\eta}$) response at WG-5D for an isolated WEC (corresponding to the model configuration shown in Figure 5.1a). The sensitivity of the solutions to different solver arrangements was examined using these preliminary tests, which showed clear instabilities for some sets of solver parameters and generally resulted in poor agreement at high frequencies. The various numerical model configurations are discussed in more detail under the subheadings below.

Logarithmic singularity treatment

Options in WAMIT (WAMIT: Version 7, 2012) are provided for treatment of the logarithmic singularity in the Green's Function. Two different methods for integrating the singularity may be used; however, it is only permitted to use the more accurate method (where it is separated, and solved analytically across pairs of panels, `ILOG=1`) when the irregular frequency removal option is used (see below). The effect of incorporating the more accurate method is clearly shown in Figure 5.3 for the case of `IRR=0`.

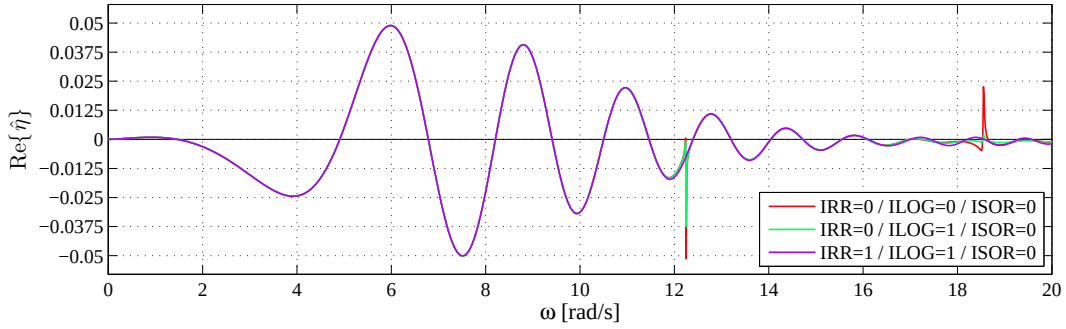

(a)

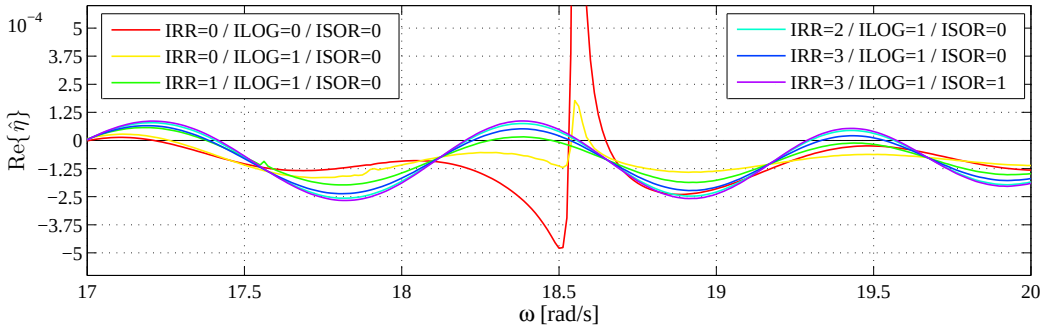

(b)

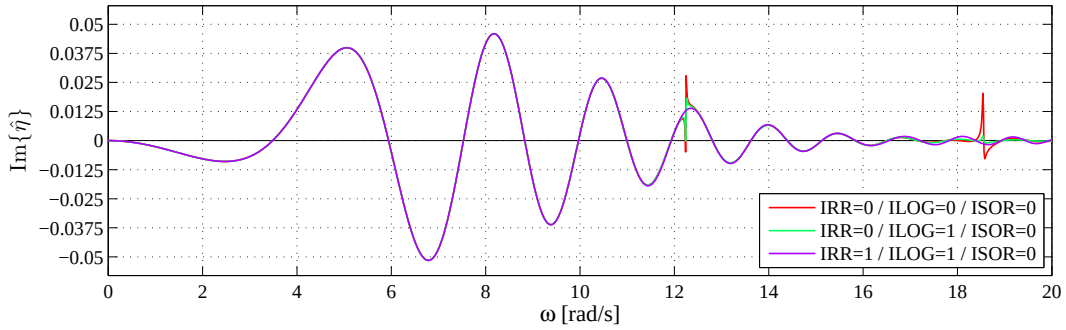

(c)

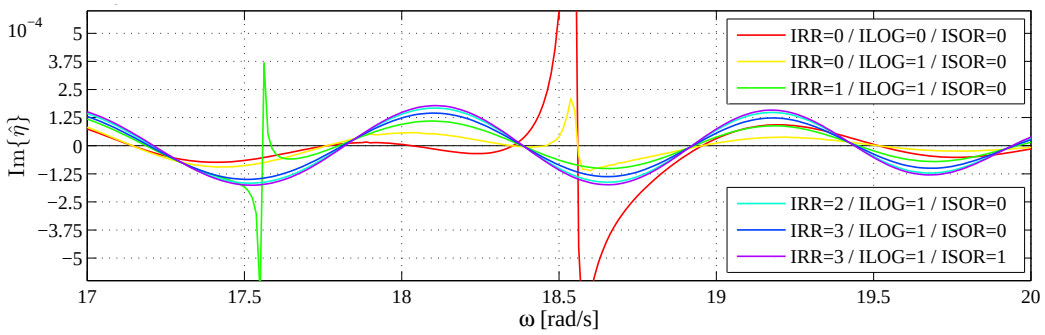

(d)

Figure 5.3: Real and imaginary parts of the complex wave elevation for preliminary studies.

Removal of irregular frequencies

Solutions are required across a wide range of frequencies in order to develop accurate time-domain responses. At higher frequencies, adverse effects associated with irregular frequencies can occur (WAMIT: Version 7, 2012), which may be treated in WAMIT using the *extended boundary condition method* referred to by Zhu and Lee (1994); Zhu (1994) and originally by Kleinman (1982).

The results in Figure 5.3 show clear evidence of irregular frequencies, at around 12rad/s and 18.5rad/s, for both the real and imaginary parts. For one of the configurations that featured the removal of the effects of irregular frequencies (`IRR=1`), an additional frequency was identified around 17.5rad/s. This particular case used a fairly coarse panel configuration on the interior free-surface.

The various options included in WAMIT for the removal of the effects of irregular frequencies (`IRR=1-3`) use different meshing methods for the 'interior surface', i.e. the flat surface which lies on the water plane. This area generally required less strict levels of refinement, compared to the main body surfaces. The most refined panel arrangement (`IRR=2`, which uses the base panel configuration, projected onto the interior surface) gave results which appeared to converge on a consistent frequency response result. Coarser meshes, such as that indicated in Figure 5.1 and the auto generated mesh (`IRR=1` and `IRR=3`, respectively), showed reduced wave elevation amplitudes. For the main results reported in this thesis, the option `IRR=1` was used in a way that enforced the accurate solution obtained using `IRR=2`, whilst also accommodating the hole for Post-A.

Source strength evaluation

An option is available in WAMIT to evaluate the velocity potentials using the source strength formulation. Application of this method is highly recommended when evaluating the fluid velocity near to solid surfaces in the domain, which can be used in particular to improve the accuracy of drift force evaluations. This can add considerable time to execute the necessary computations (around 50% longer for cases considered here), and as evaluation of the fluid velocity in these regions was not a primary concern for this work, the forces were evaluated directly from the velocity potential (`ISOR=0`, default in WAMIT), unless otherwise stated. The effect of this source strength method was examined for selected tests, with limited impact on the results of interest (body motions, forces and free surface elevations).

Solution method

To solve the linear system of equations, WAMIT offers options of direct solution, iterative solution, or block iterative solution (which effectively combines the advantages of both). The iterative method is computationally the most efficient; however, it can also suffer from convergence issues. Given the relatively small system studied here, the direct method (`ISOLVE=1`) was most suitable, as the computations of the solutions were relatively rapid. It is also recommended in the WAMIT: Version 7 (2012) to employ this method when irregular frequencies are removed (`IRR>0`).

5.1.3 Convergence

The numerical solution was verified by demonstrating convergence with respect to panel size, using the *OneWEC* test case (no posts). The configuration of panels used to form the WEC can be seen in Figure 5.4, which shows various levels of mesh refinement. As the simple shape was axisymmetric and was designed to be of roughly equal proportions, in terms of draught and diameter, it was both effective and convenient to treat the main geometric components with the same number of divisions in each direction. For the relatively coarse mesh indicated in Figure 5.4a for example, four divisions were used in the azimuth direction (for the quarter WEC geometry), four divisions for the straight sided draught section, and a further four divisions for the hemispherical base, giving 48 panels (described in WAMIT using the quantity `NEQN` – the number of equations).

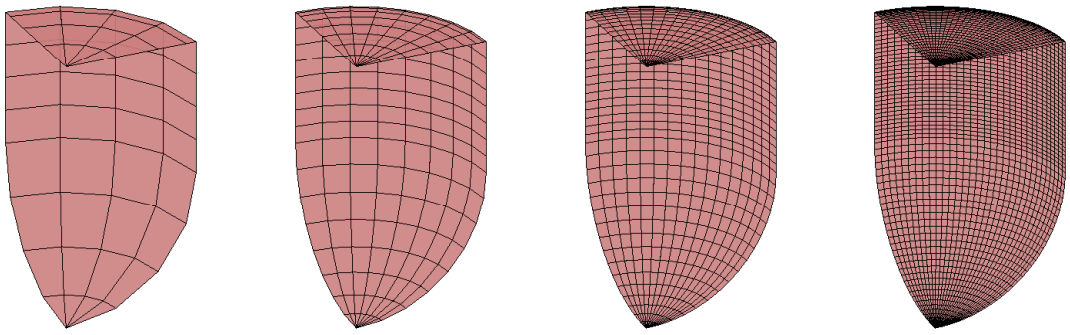

(a) 4 divisions **(b)** 8 divisions **(c)** 16 divisions **(d)** 32 divisions

Figure 5.4: Example WEC geometries (one quarter) for panel convergence studies for using the frequency-domain model.

Geometries were established using the following set of divisions: 3, 4, 6, 8, 9, 12, 16, 18, 27 and 32. These allowed for ratios of refinement of $r = 1.5$ ([4,6,9], [8,12,18], [12,18,27]) and $r = 2$ ([3,6,12], [4,8,16], [8,16,32]).

Solutions obtained using the various meshes differ as a result of numerical errors. This applies to all the evaluated results (including added mass, added damping, forces etc.), however the

effect on the Response Amplitude Operator (RAO) is particularly interesting because this incorporates changes to the natural frequency of the system. For this reason, it was appropriate to examine solution convergence for the panel size using the RAO in a full diffraction–radiation test, responding to incident waves. From the RAO, it was possible to discern both changes to the excursion magnitude (|RAO|) and changes to the natural frequency (ω_0) caused by mesh resolution.

The magnitude of the RAO around the natural frequency is shown in Figure 5.5 for the various meshes. Convergence of the peak RAO magnitude, $|RAO|(\omega_0)$, and ω_0 are clearly visible in the figure. Formally, this was demonstrated using the observed order of accuracy, p_o, which described the rate of change of the solution between the mesh refinements stages. Both $|RAO|(\omega_0)$ and ω_0 were found to agree with the following:

$$p_o = \frac{1}{\ln(r)} \ln\left(\frac{(f_3 - f_2)}{(f_2 - f_1)}\right) \approx 2.0 \tag{5.1}$$

In the above, f generically represents numerical solutions of either $|RAO|(\omega_0)$ or ω_0, and subscripts 1-3 relate to the respective mesh configurations: fine, medium and coarse. The results from Equation (5.1) confirm that the convergence was monotonic, as $p_o > 0$ (i.e. $(f_3 - f_2)/(f_2 - f_1) > 1$).

The numerical error due to the quality of mesh has been examined using the Grid Convergence Index (Roache, 1998; Roy, 2005; ITTC, 2002):

$$GCI = \frac{F_s}{r^{p_o} - 1}\left|\frac{(f_2 - f_1)}{f_1}\right| \tag{5.2}$$

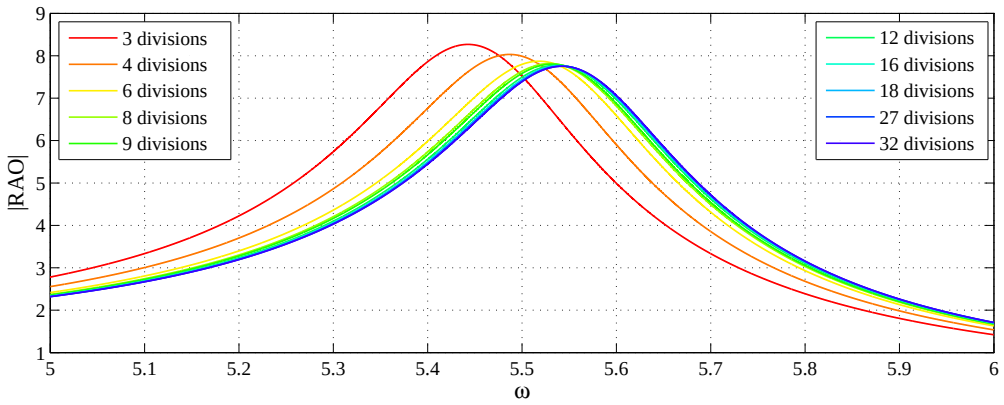

Figure 5.5: The magnitude of the RAO for the various mesh convergence cases, using the frequency-domain model.

This incorporates a factor of safety, $F_s = 1.25$, which is recommended whenever the *GCI* is derived using three mesh cases. The *GCI* is an approximate representation of the percentage difference between the result for the fine mesh (f_1) and an extrapolated result for an infinitely fine mesh. Table 5.2 provides results for the fine mesh case, from the various convergence sets which were summarised at the start of this section (for mesh refinement ratios $r = 1.5, 2$).

Table 5.2: Convergence results, based on RAO (incident wave conditions assumed).

Mesh configuration	NEQN	*GCI* (combined[1])	Estimated processing time for a 10 WEC array[2]
9 divisions in principal directions	243	0.91%	~2 hours
12 divisions in principal directions	432	0.51%	~12 hours
16 divisions in principal directions	768	0.29%	~2 days
18 divisions in principal directions	972	0.23%	~5 days
27 divisions in principal directions	2187	0.10%	~23 days
32 divisions in principal directions	3072	0.07%	~26 days

[1] GCIs were combined according to: $GCI_{combined} = \sqrt{GCI^2_{|RAO|} + GCI^2_{\omega_0}}$.

[2] Global symmetries are ignored. CPU time based on 64-bit, 4 CORE Intel i5-2520M @2.5GHz, RAM: ~4GB.

Based on the above results, 16 divisions were used for all remaining work, for which the numerically evaluated RAO was characterised by a *GCI* of $< 0.3\%$.

5.2 Time-domain model configuration

The time-domain model described in Section 3.3.2 (Forehand *et al.*, 2015) was used to compute the time series responses of the body excursions, forces and free surface elevations. The following outlines the specific details of the model configurations:

- No incident wave conditions were considered (only radiation tests were performed).
- The initial conditions for the free decay problems were as follows:
  - $\xi_0 = 0.2$m
  - $\dot{\xi} = \ddot{\xi} = 0$
- External linear damping was applied via the gain term of the reduced damping matrix, in Figure 3.3.

5.3 Results: OneWEC

5.3.1 Excursions

Effects due to the posts

Figure 5.6a shows the free decay WEC excursion time history from the WECwakes experiments and from the linear time-domain model. The excursions shown in this figure, along all other graphically presented results (also in later chapters), are normalised using the measured damping period T_0, such that one oscillation period of the measurements from the experiment corresponds to $t/T_0 = 1$. This highlights a slight discrepancy in the evaluated results, where $t/T_0 = 0.989$. For this *OneWEC* case, the response was also underdamped. Both of these effects were small over a single period but accumulated to give relatively significant changes over time.

Tests were carried out to examine the influence of hydrostatic considerations due to Post-A on the natural resting position of the WEC. The approximate draught from the experiments was measured as 0.315m (i.e. the straight sided cylindrical portion measured 0.1575m); however, this required corrections in order to reflect the measured mass, and geometries both with and without Post-A. The normal hydrostatic force coefficient $C_{33} = S_w \rho g$ due to the heave motion (where S_w was the cross-sectional water plane area) resulted in resting position corrections of -1.452×10^{-3}m and -8.086×10^{-3}m (draughts of 0.3165m and 0.3231m) for *OneWEC* and *OneWEC-a* respectively. Three results are shown in Figure 5.6b:

1. *OneWEC*: assuming a draught of 0.3165m,
2. *OneWEC**: assuming a draught of 0.3231m,
3. *OneWEC-a*: assuming a draught of 0.3231m.

The *OneWEC** case was non-physical due to the correction which was applied, even though it did not include the post; however, it did illustrate the change to the solution which resulted specifically from the adjusted resting position. *OneWEC**, which sat lower in the water, resulted in reduced damping and slightly larger amplitude oscillations, as should be expected.

As the relative change to added damping due to the presence of Post-A was very small in magnitude, the amplitude of oscillation was almost unchanged between the two numerical tests: *OneWEC** and *OneWEC-a*, as shown in Figure 5.6b. Inclusion of Post-A resulted in a much improved correlation against the measurements with respect to the oscillation frequency. Observations relating to this reduced frequency may be inferred from general arguments for damped systems (Falnes, 2002), applied to the single degree-of-freedom (i.e. concerning modes $i, j = 3$ only):

$$\begin{aligned} \omega_0 &= \sqrt{C^E_{33}/(m + A_{33}(\omega))} \\ \delta &= \big(B_{33}(\omega) + B^E_{33}\big)/2\big(m + A_{33}(\omega)\big) \\ \omega_d &= \sqrt{\omega_0^2 - \delta^2} \end{aligned} \tag{5.3}$$

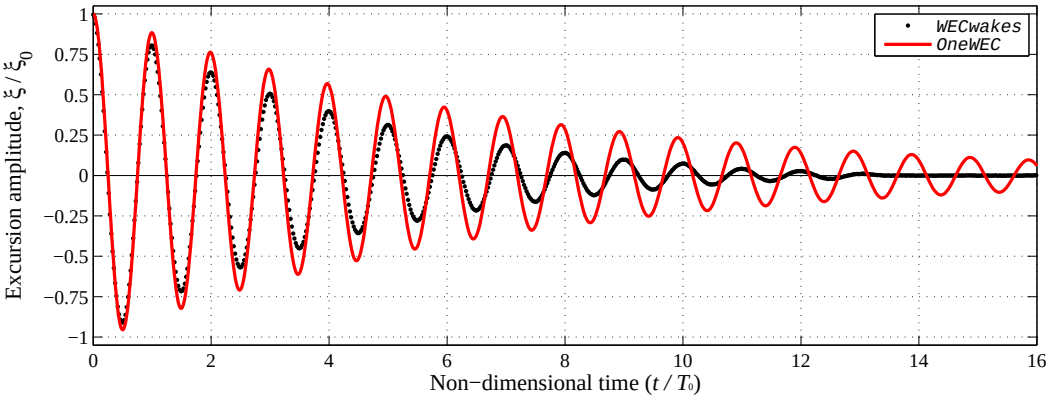

(a) Excursion, without posts (*OneWEC*)

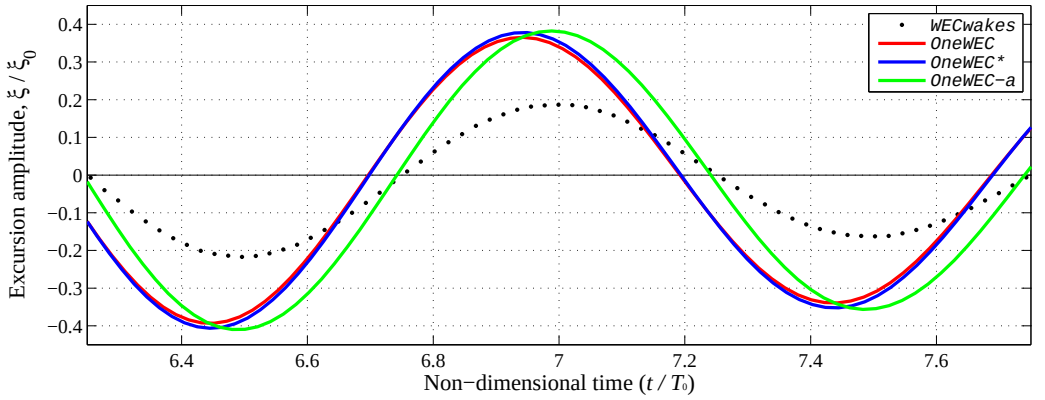

(b) Influence of resting position (*OneWEC* and *OneWEC**), and of Post-A (*OneWEC-a*)

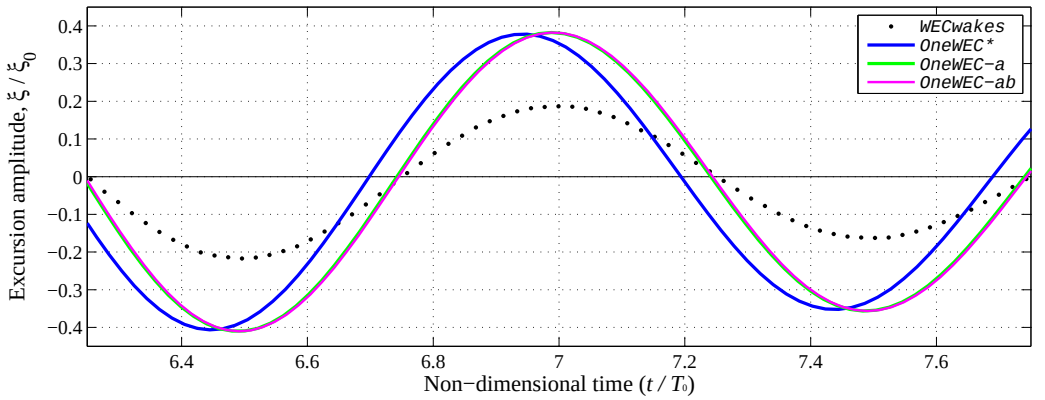

(c) Influence of Post-B (*OneWEC-ab*)

Figure 5.6: Time response of the WEC excursion for the single WEC cases using the time-domain model: *OneWEC*, *OneWEC-a* and *OneWEC-ab*.

In Equation (5.3), $A_{33}(\omega)$ and $B_{33}(\omega)$ represent added mass and added damping, B^E_{33} and C^E_{33} are the externally applied damping and stiffness coefficients, δ is the overall damping coefficient and m is the mass of the body. While the added mass at the damped frequency ω_d showed a decrease for the cases which included Post-A, the hydrostatic stiffness also reduced. The net effect was an increase to the period of the damped oscillation, due to greater influence of the hydrostatics*.

In contrast to Post-A, both added mass and added damping at ω_d increased slightly due to Post-B. This resulted in a further increase in period, although this influence was far smaller than it was for Post-A, as shown in Figure 5.6c. Only added mass and added damping were affected by the presence of Post-B, which clearly had no effect on the hydrostatics.

Effects due to damping: mechanical and viscous

The amplitude discrepancies identified above between *OneWEC-ab* and *WECwakes* were largely due to modelling errors: effects caused by the exclusion of mechanical dissipation, and effects caused by the exclusion of viscosity. In the absence of detailed heave force measurements from the experiments, a useful method to attempt to interpret the relative contributions of friction and viscosity is to model the viscosity, and treat the residual effects as mechanical damping. This viscous model is treated in later chapters (Chapters 6 and 7); however, it is useful here to approximate the combined effects using the linear model.

A series of linear damping cases were examined, with a summary of the results shown in Figures 5.7 and 5.8. A constant $B^E_{33} = 4$Ns/m damping coefficient provided a reasonable linear approximation for the additional damping forces (the various damping coefficients tested have been included in the case descriptions, i.e. 4Ns/m damping was applied for *OneWEC-ab-4*).

At time: $t/T_0 = 7$, which was around the mid-way point in the decay (see Figure 5.7b), the amplitude of the oscillation for the undamped results for *OneWEC-ab-0* was almost twice that of the physical data (197%), whereas for *OneWEC-ab-4* this was just 100.4%. This particular instant, along with other arbitrarily selected peaks and troughs, gives a reasonable way-point for correlating a linear damping term. The linear damping constant, however, will have a limited range of applicability for the entire decay process due to nonlinear behaviour during early stages of the decay (as identified in the experimental data) and significant damping nonlinearities at later stages ($t/T_0 > 8$). For applications involving more general motion patterns, the range of applicability would be more limited still.

---

*A reduction in added damping was also recorded, which should act to increase the damped frequency ω_d. δ was, however, two to three orders of magnitude smaller than ω_0.

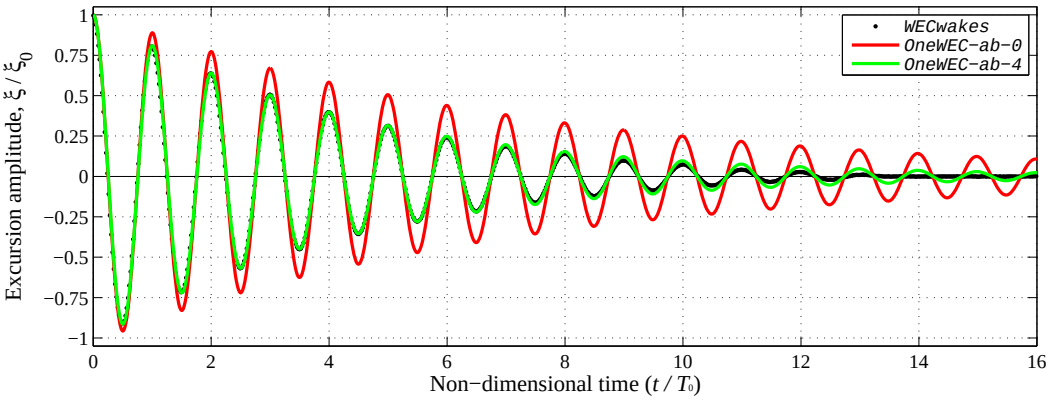

(a)

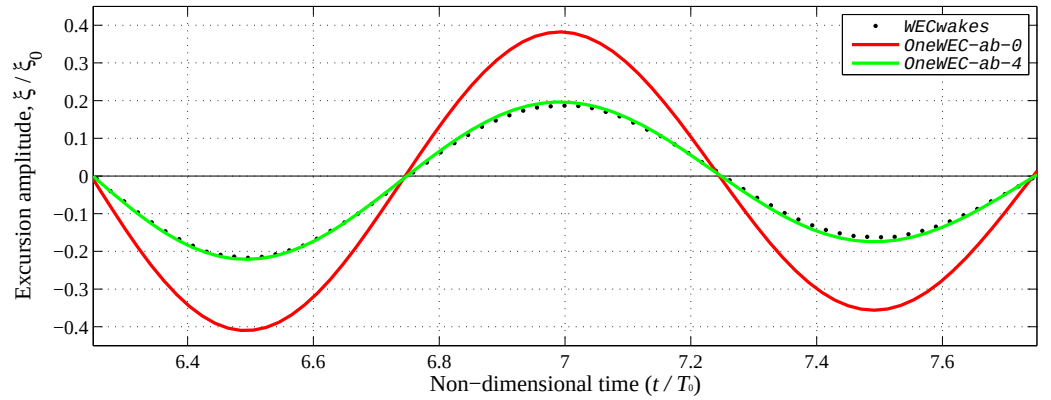

(b)

Figure 5.7: Measured and predicted decay response for *OneWEC-ab* using the time-domain model (with and without linear damping, $B^E_{33} = 4\text{Ns/m}$).

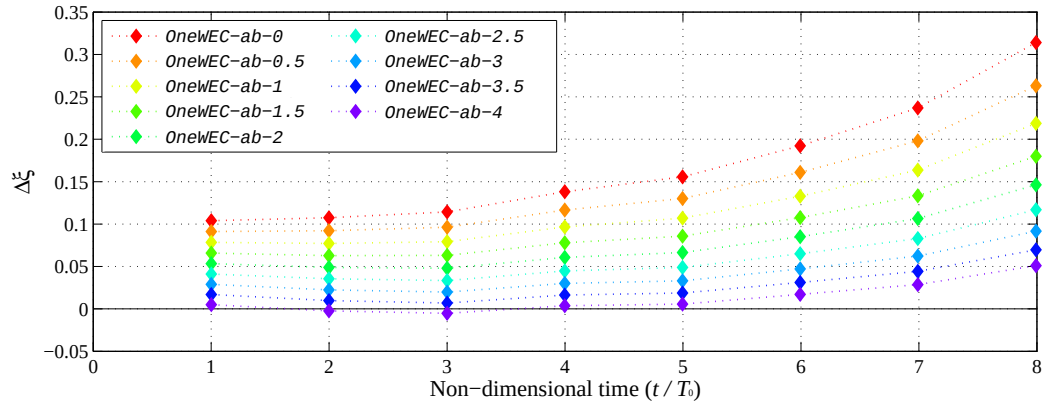

Figure 5.8: Excursion amplitude change $\Delta\xi$ using the time-domain model with various linear damping coefficients ($0 \leqslant B^E_{33} \leqslant 4\text{Ns/m}$).

Figure 5.8 provides a summary of the changes in amplitude between consecutive peaks excursions, for different damping cases in the range 0-4Ns/m:

$$\Delta\xi_n = \frac{(\xi_n^{TD} - \xi_n^{EXP})}{\xi_n^{EXP}} - \frac{(\xi_{n-1}^{TD} - \xi_{n-1}^{EXP})}{\xi_{n-1}^{EXP}} \tag{5.4}$$

where n is an integer representing each peak, and for $n = 0$, $\xi_0^{TD} = \xi_0^{EXP}$. For the range $t/T_0 < 8$ (i.e. in situations where $\xi/\xi_0 > 15\%$), the amplitude changes over time were relatively coherent; however, the relationship was nonlinear. It follows that the overall damping coefficient for the system was nonlinear. In general, however, the approximate linear coefficient $B_{33}^E = 4$Ns/m proved reasonably accurate across a relatively wide range of conditions.

5.3.2 Forces

The various radiation forces F_{ij} in a general six degree-of-freedom system are described using the subscripts i and j to denote the force caused by one mode on another. These forces can be evaluated using Impulse Response Functions (IRFs), derived from the hydrodynamic coefficients (either A_{ij} or B_{ij}). The present application uses the form (WAMIT: Version 7, 2012):

$$L_{ij}(t) = \frac{2}{\pi}\int_{\omega=0}^{\infty} \frac{B_{ij}(\omega)}{\omega} sin(\omega t)\ \mathrm{d}\omega \tag{5.5}$$

The IRF $L_{ij}(t)$ describes the response of the force output, in terms of the body acceleration. The time-domain representation of the radiation force is computed by convolving $L_{ij}(t)$ with the acceleration time history (input), and correcting for the added mass at infinite frequency $A_{ij}(\infty)$ (WAMIT: Version 7, 2012):

$$F_{ij}(t) = A_{ij}(\infty)\ddot{\xi}_j(t) + \int_0^{\infty} L_{ij}(\tau)\ddot{\xi}_j(t-\tau)\ \mathrm{d}\tau \tag{5.6}$$

Here, $\ddot{\xi}_j(t)$ is the acceleration of the body, and τ is the time parameter for the convolution. For the single degree-of-freedom *OneWEC-ab* case, only $F_{33}(t)$ applies. In Equation (5.6), WAMIT provides the necessary coefficients directly for the IRF (Equation (5.5)), and indirectly for the derived motion responses, via the time-domain model.

Time-domain evaluations of the heave force are provided in Figure 5.9, which uses numerically-derived WEC motion input data (*OneWEC-ab-4*, using a linear damping constant $B_{33}^E = 4$Ns/m). The heave force was not measured during the experiments, so it was not possible to validate these results directly.

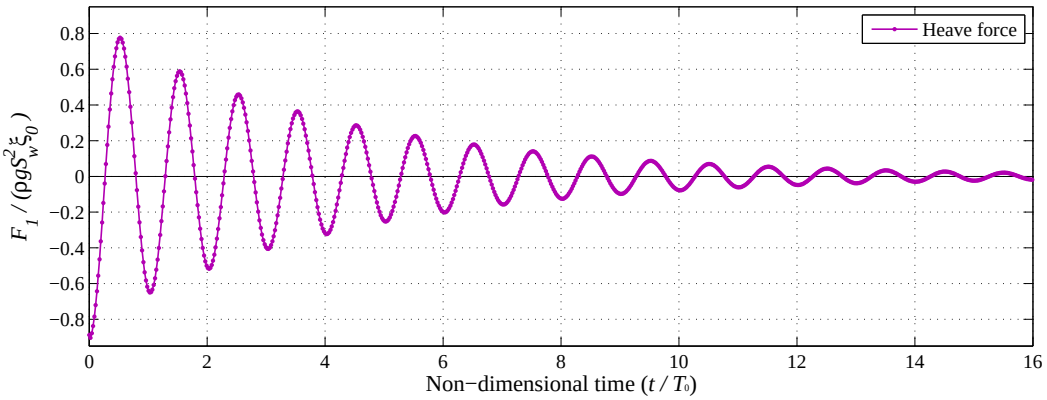

Figure 5.9: In-line heave force, derived from the time-domain model.

5.3.3 Free surface elevations

Validation data were available for free surface elevations, with measurements taken at the locations described in Chapter 4 (Figure 4.6). As it was of interest in the present work to examine numerical evaluations of the transfer of energy between interacting WECs (see array studies in Sections 5.4 and 5.5, and Chapter 7), validation of this process was assessed using the free surface elevation measurements. Using the linear time-domain model, however, the nonlinearities described in Section 4.3.3 could not be captured. Figure 5.10 shows the free surface elevation results from the time-domain model at wave gauge locations: *WG-5D*, *WG-10D*, *WG-11D* and *WG-14D*.

The most notable deviations from the experimental measurements are found over fairly discrete sections of the results. Higher harmonics were shown earlier to exist across the intervals given in Table 4.3, also visible in the spectrogram results provided in Section 4.3.3 (Figures 4.18 to 4.21).

5.4 Results: TwoWEC

5.4.1 Excursions

In the following discussion, as with those in later chapters, the distinction is made here between the test devices used during the experiments:

1. The *'decay WEC'*: the principal model WEC, which was raised and released from a height during the experiments;
2. The *'neighbouring WEC(s)'*: the neighbouring model WEC(s), which responded to the motions of the decay WEC.

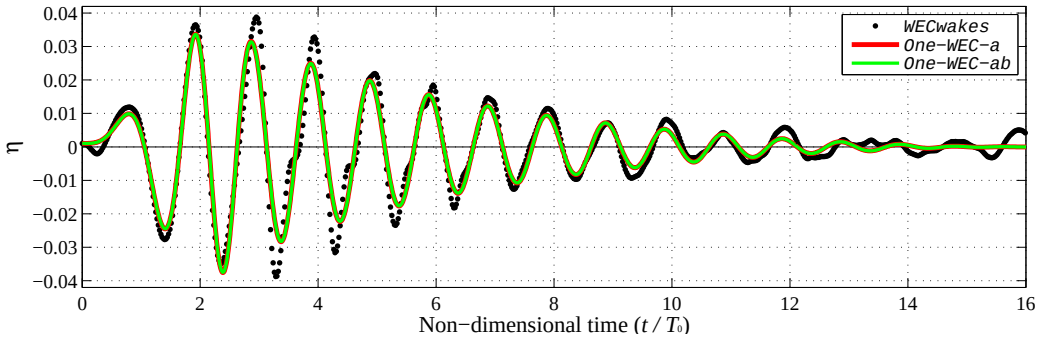

(a) *WG-5D*

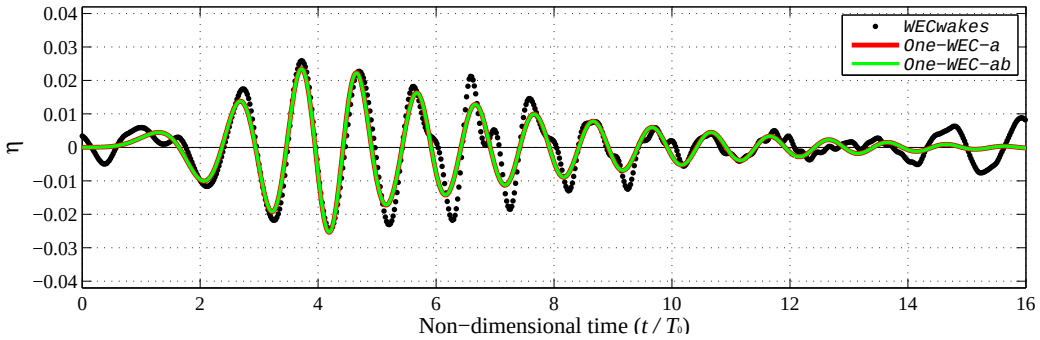

(b) *WG-10D*

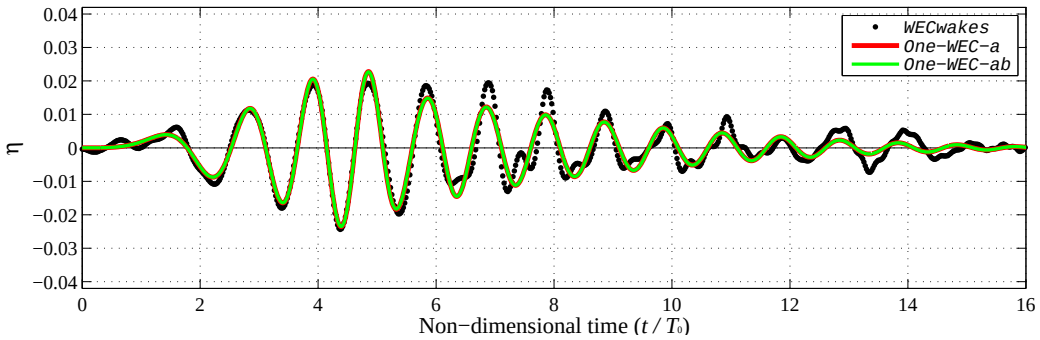

(c) *WG-11D*

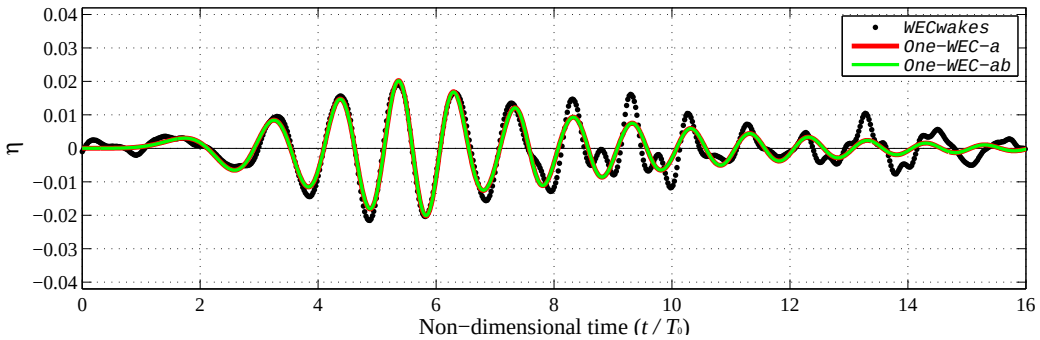

(d) *WG-14D*

Figure 5.10: Time response of the free surface elevations for the single WEC cases using the time-domain model: *OneWEC-a* and *OneWEC-ab*.

Based on the available test data for the *TwoWEC* case, excursion measurements for the decay WEC were used to validate the numerical computations; however, no equivalent excursion data were available for the neighbouring WEC. The decay WEC motions are provided in Figure 5.11a, which again are in close agreement with the experiments. With the linear damping constant $B^E_{33} = 4$Ns/m, the behaviour of the decay WEC was accurately modelled, with only small deviations after around $t/T_0 = 8$.

The change between the excursion history of the decay WEC for the *OneWEC* and *TwoWEC* cases was purely a result of diffraction and radiation due to the presence of the neighbouring WEC. These were secondary wave effects which were very small in magnitude (shown in the later Section 5.5.1). The multiple-WEC decay test experiments were themselves designed to investigate these weak effects, which are replicated numerically within this work.

The stronger primary effects of the diffraction and radiation processes were captured by studying the motion (see Figure 5.11b) and forces associated with the neighbouring WEC, due to the motion of the decay WEC. Peak motion amplitudes of the neighbouring WEC were around 10% of the decay WEC for the undamped motion case, and diminished to around 3% for $B^E_{33} = 40$Ns/m. This latter damping value has been considered during further examinations, carried out using experimental measurements from the *FiveWEC* case, in Section 5.5.1.

5.4.2 Forces

Results from the surge force gauge measurements taken during the experiments were used to validate the surge force predictions from the time-domain model. Figure 5.12 provides results for the surge forces acting on the neighbouring WEC due to the damped ($B^E_{33} = 4$Ns/m) decay motion of the decay WEC (*TwoWEC-ab-4*). These results were derived using the same procedure as described in Section 5.3.2.

The overall agreement between the results and experiments was good, particularly at later stages in the decay after the nonlinear wave behaviour had subsided.

5.5 Results: FiveWEC

5.5.1 Excursions

Figure 5.13 shows the decay WEC excursion for the *FiveWEC* case, where the central WEC in the linear array was released from height, with two WECs on either side at centre to centre distances of 5D and 10D. The agreement was again reasonable, especially earlier in the decay when the larger amplitude motions were sustained, and the effects of Coulomb damping were

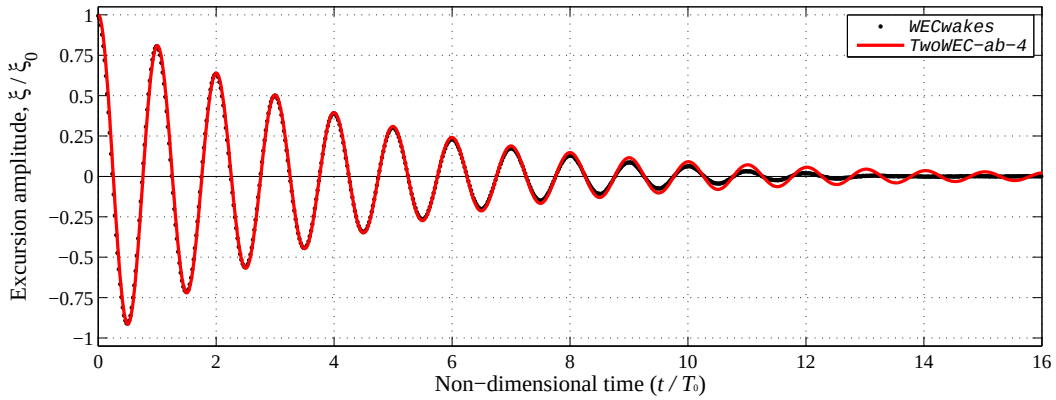

(a) Comparison between experimental measurements and time-domain result with $B^E_{33} = 4$Ns/m for the decay WEC

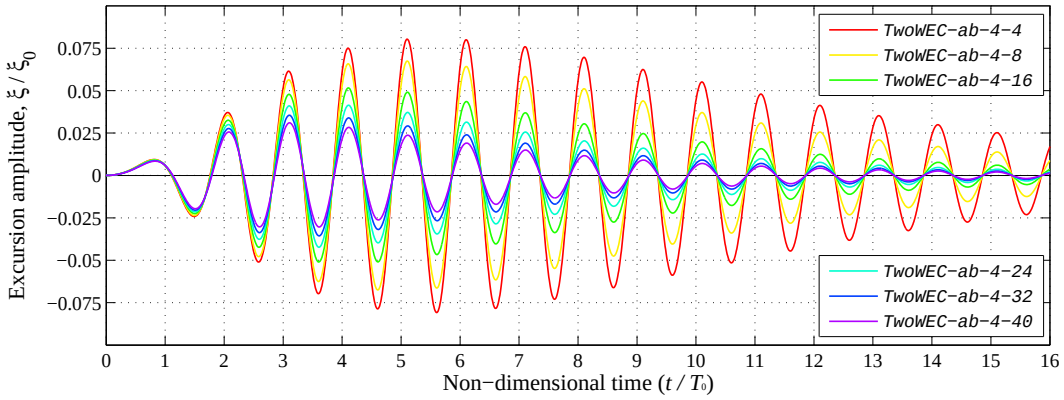

(b) Predicted motion of the neighbouring WEC at 5D spacing, using various external damping levels

Figure 5.11: Excursions of the WECs for the case *TwoWEC-ab*, using the time-domain model.

less evident. It is also of interest to note that the experimental *FiveWEC* tests used a different model WEC as the decay WEC (*WEC-3* instead of *WEC-5*, as used in the earlier tests). The necessary damping constraint within the numerical model was again $B^E_{33} = 4$Ns/m, which demonstrated reproducibility of the physical tests.

The results in Figures 5.13b and 5.13c show the variations in the decay WEC excursions due to the other WECs. This secondary wave diffraction/radiation effect was very small in magnitude for the device spacings considered in this work.

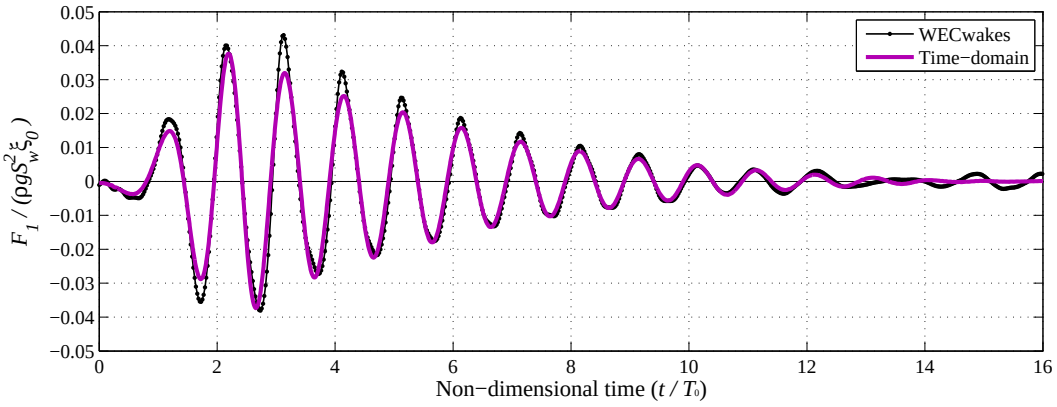

(a) Full time history

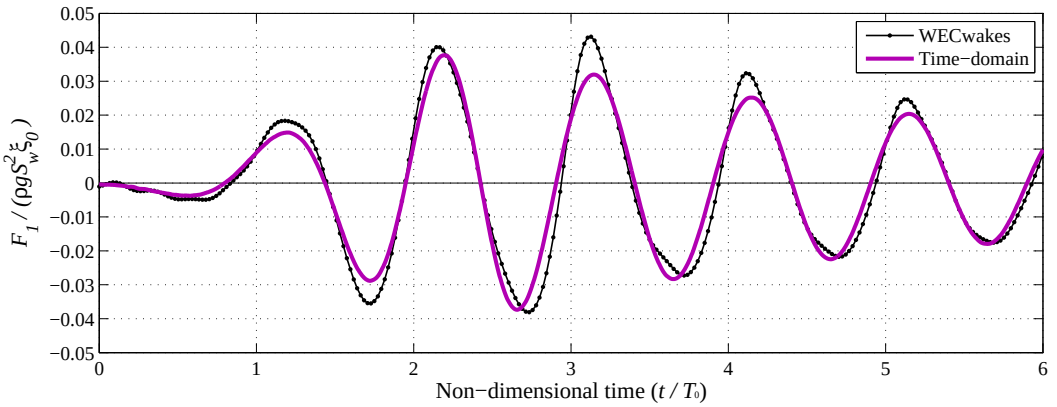

(b) Initial time history between $t/T_0 = 0$ and 6

Figure 5.12: Measured and predicted surge forces acting on the neighbouring WEC for *TwoWEC-ab-4*, using the time-domain model. The computed surge forces are obtained by convolving the IRFs with the measured WEC responses from the experiments. The measured surge forces include the readings from both upper and lower gauges.

The primary wave radiation effects experienced by the adjacent WECs are shown in Figure 5.14, which includes validation data. Aside from the relative significance of the precision errors registered for the measured small amplitude motions, a number of other concerns can be identified for the WECs at 5D and 10D spacings. These include:

1. Significant differences in the measured data were observed between the two WECs positioned at 5D (*WEC-2* and *WEC-4*);
2. Damping coefficient requirements were considerably larger than for the decay WEC, ranging between 10 times and 25 times higher for the neighbouring WECs;
3. The predicted results using the linear time-domain model showed a phase discrepancy, which was more pronounced at earlier stages in the decay.

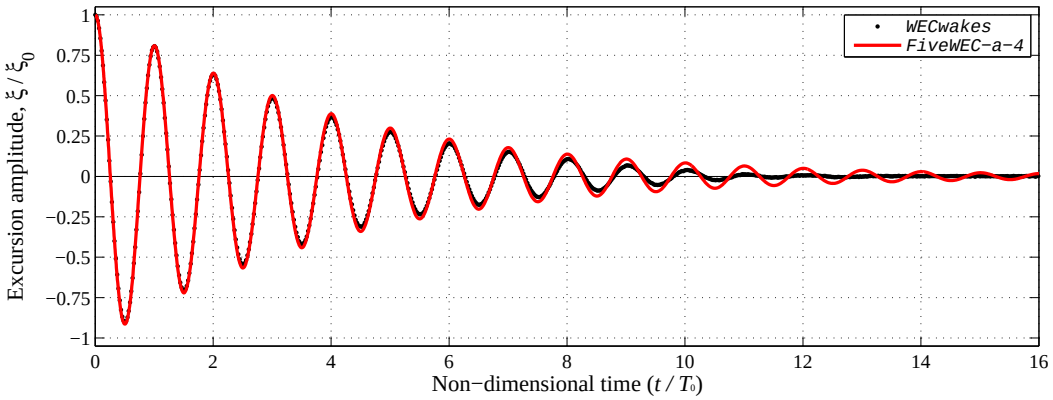

(a) Comparison between experimental measurements and time-domain result

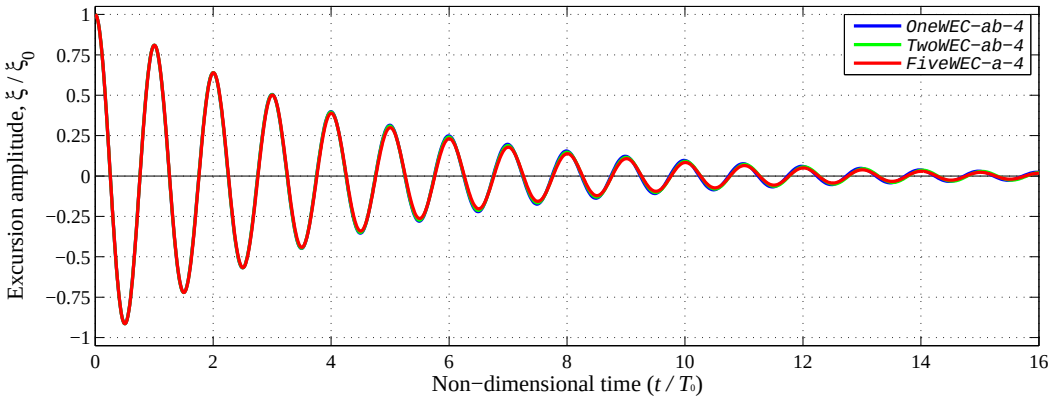

(b) Comparison between one, two and five WEC cases

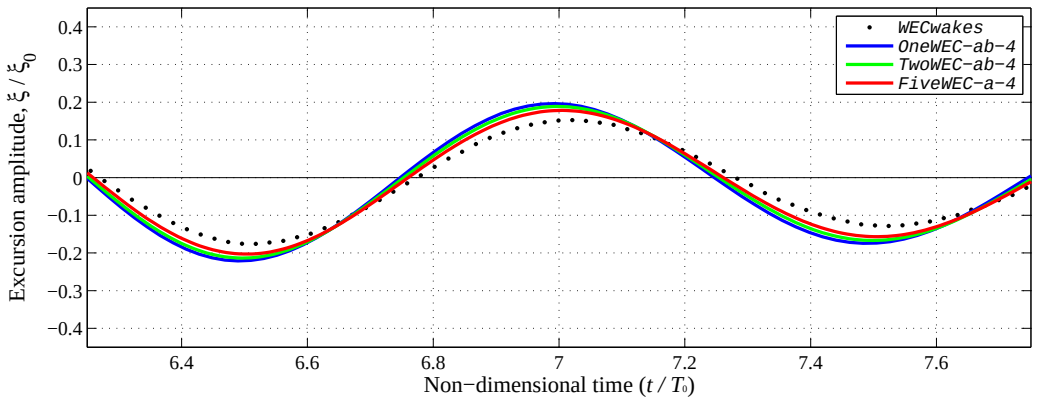

(c) Comparison between experimental measurements (decay WEC from the five WEC case) and one, two and five WEC time-domain cases

Figure 5.13: Excursions of the decay WEC (*WEC-3*) for the case *FiveWEC-a-4*, using the time-domain model.

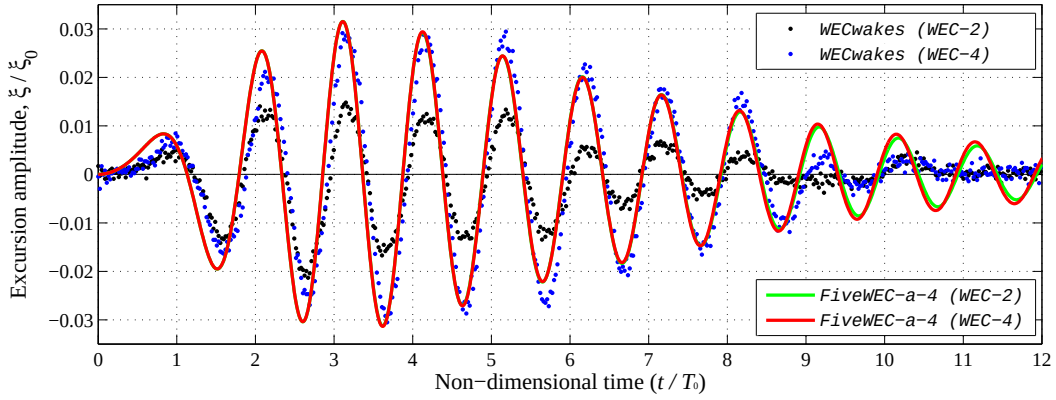

(a) Neighbouring WECs at 5D spacing ($B^E_{33} = 40$Ns/m)

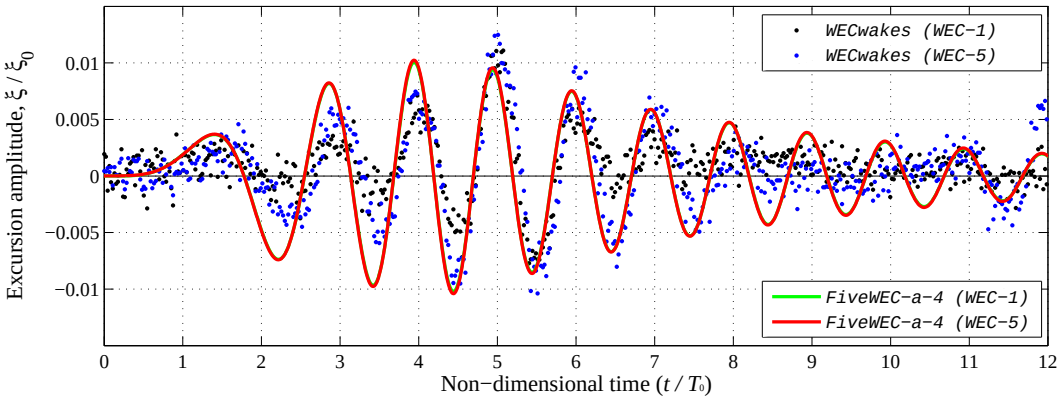

(b) Neighbouring WECs at 10D spacing ($B^E_{33} = 100$Ns/m)

Figure 5.14: Excursions of the neighbouring WECs for the case *FiveWEC-a*, including experimental measurements and time-domain model results.

The first of these concerns presents an issue which may be due to uncontrolled experimental effects. As the two WECs were exposed to similar conditions from the axisymmetric decaying WEC, the discrepancies were attributable to one or more of the following:

1.1 Different mechanical damping conditions may have existed for each of the WECs;

1.2 A ladder was positioned in the vicinity of the decay WEC, in order to carry out the manual operations for the decay tests (this was due to the test WEC being in the centre of the square array, within the footprint of the main experiment rig[†]);

1.3 The positioning of the intermediate posts: Post-2B and Post-3B (as labelled; see Figure 4.7), were different on either side of the decay WEC.

Items 1.1 and 1.2 were uncontrolled experimental effects, whereas 1.3 was systematic and could be captured within the numerical model. The different damping conditions (Item 1.1)

[†]For the *OneWEC* and *TwoWEC* cases, an overhead platform crane was used to conduct manual operations from an elevated position, above the water surface (i.e. no ladder was required).

have been assumed here to be the principal cause, as the WEC models were known to be susceptible to 'stiction'. Due to the magnitude of the discrepancy, Items 1.2 and 1.3 have been discounted here on the basis of the arguments discussed earlier, in relation to Figure 5.6c (negligible effects of Post-B on excursion amplitudes). As the stiction effects were generally addressed during the experiment through application of lubricant at WEC bearings, the diminished measurements for *WEC-2* were considered to be erroneous, and were excluded from the remainder of the results (*WEC-4* provided all validation data for the WEC positioned at 5D).

For the second concern (Item 2 above), the significant increase to damping conditions experienced for the neighbouring WECs ($B^E_{33} \approx 40$Ns/m and $B^E_{33} \approx 100$Ns/m for the WECs at 5D and 10D, respectively) was consistent with the earlier discussions regarding Coulomb damping. At the reduced amplitudes of $\xi/\xi_0 < 0.1$, the neighbouring WECs saw far greater influence of the bearing friction than the decay WEC, although the decay WEC was eventually overcome by the same effects. The damping coefficients used to provide the results in Figure 5.14 gave peak amplitudes of $\xi/\xi_0 = 0.03$ and $\xi/\xi_0 = 0.01$ for 5D and 10D spacings.

The third concern (Item 3) is related to the same mechanisms described for Items 1 and 2 above. The delay in the response of the neighbouring WECs in the measured experimental results indicated that the early stage of the impulse response was affected by inhibited motion, resulting from nonlinear stiction damping effects. This evidence (also Item 2) enforces the need for a fully nonlinear mechanical damping model for the Coulomb characteristics of the damping system.

5.5.2 Forces

Figure 5.15 shows the extended validation results for the time-domain model, using the *FiveWEC* arrangement. The surge force measurements from the experiments were filtered up to the 4th harmonic. These results showed reasonably consistent force response profiles, although the measurements did include fairly prominent nonlinearities.

As the discrepancies in Figure 5.15 were within the known limitations of the linear model, final comparisons between the experimental data and linear potential flow derived surge force predictions were carried out using filtered test data across a narrower band of frequencies, up to the fundamental frequency. These results are provided in Figure 5.16.

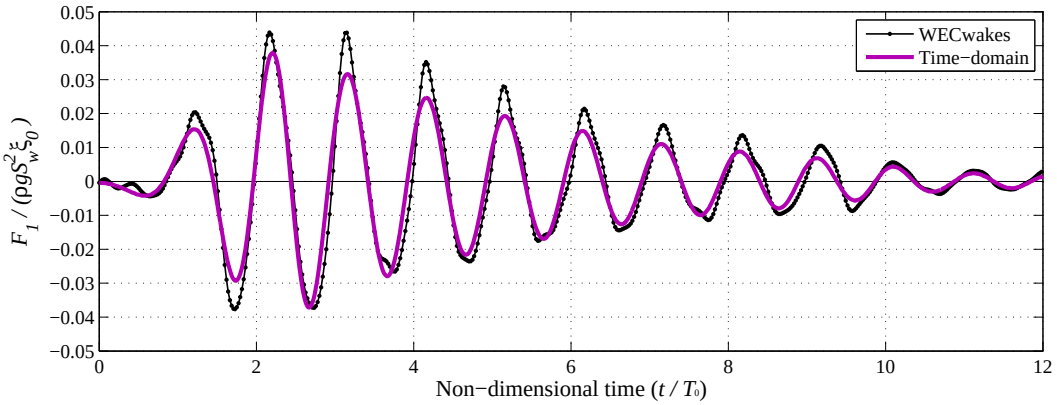

(a) Neighbouring WECs at 5D

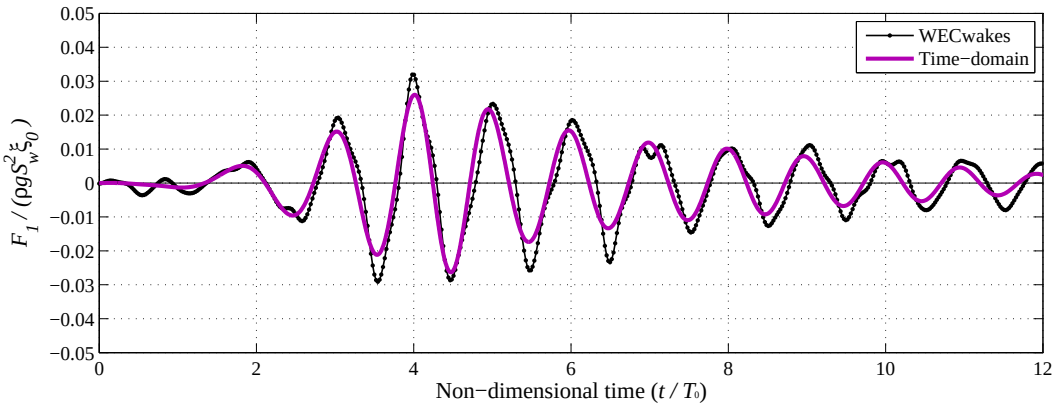

(b) Neighbouring WECs at 10D

Figure 5.15: Measured and predicted surge forces on the neighbouring WECs (to fourth harmonic), using the time-domain model. The measured results are averaged from the two WECs at that distance, and also combined from upper and lower force gauges. The measurements are also passed through a low pass filter up to the 4th harmonic.

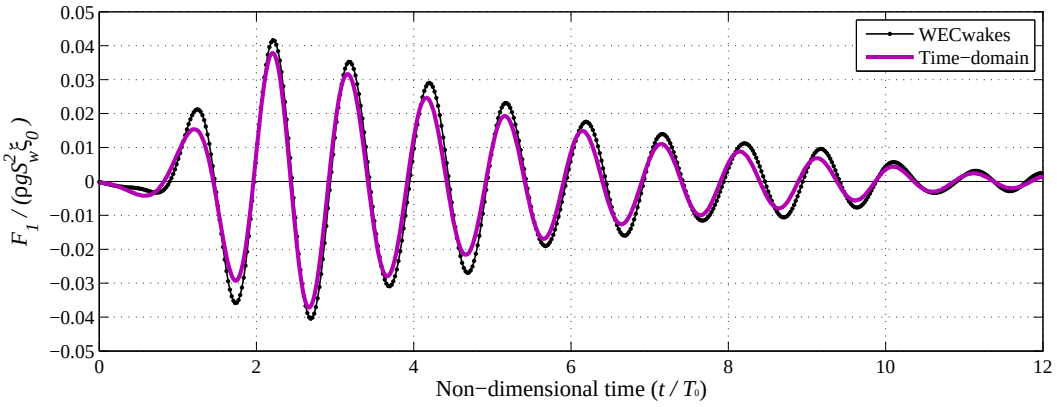

(a) Neighbouring WECs at 5D

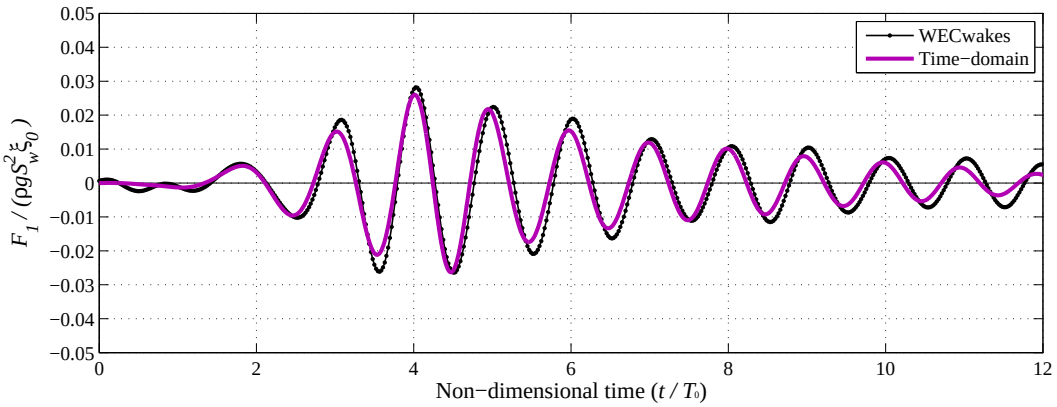

(b) Neighbouring WECs at 10D

Figure 5.16: Measured and predicted surge forces on the neighbouring WECs (to first harmonic), using the time-domain model. The measured results are averaged from the two WECs at that distance, and also combined from upper and lower force gauges. The measurements are also passed through a low pass filter, only including frequencies around the fundamental frequency.

5.6 Summary

In the above discussions, the results obtained using the linear potential flow based time-domain model were examined in detail, with discrepancies highlighted between experimental measurements, where data were available. Demonstration of this process served two purposes, allowing for an enhanced understanding of both the numerical results and the experimental measurements:

1. To interrogate the experimental results beyond the earlier observations made in Chapter 4;

2. To verify and validate the numerical results from the linear model, and to identify modelling parameters and design considerations which form the basis for the extended modelling work using CFD (inclusion/omission of posts, damping etc.)

These purposes are closely related, with both aimed at improving the correlation between the underlying physical data (discounting erroneous or irrelevant data), and the numerical models.

The aim of developing preliminary numerical models of reduced scale tank tests becomes a process of attempting to mimic the experiments as closely as possible, rather than attempting to build a realistic 'full-scale' numerical model at the first attempt. Only once the preliminary numerical models are fully developed, verified and validated should a projected/extrapolated numerical model be considered. This must consider hydrodynamic scale effects (see Chapters 6 and 7) along with scale-related issues for mechanisms within the experiment (specifically damping from bearings and Power Take-off (PTO) systems). This argument is captured in the process diagrams in Chapter 1 – Figures 1.6 and 1.7.

Chapter 6

CFD: Single WEC Model

The justification for using Computational Fluid Dynamics (CFD) was discussed in Section 1.3.2, where the need was identified to model viscous effects and nonlinear behaviour. The commercial finite volume solver STAR-CCM+* was used, which has well developed free surface modelling capabilities. This includes a coupled Fluid-Structure Interaction (FSI) solver, which can dynamically model the effect of a floating body on the fluid, and the reciprocated effect of the fluid on the body. Aspects relating to the theory of the finite volume method are described in Chapter 3.

Results from CFD simulations of the *'OneWEC'* system are presented in this chapter. The configuration and test conditions of this system were the same as in Chapters 4 and 5, which describe the tank tests of the Wave Energy Converter (WEC) models and linear numerical models respectively. The specific objectives of the more complex nonlinear CFD models are discussed first in the following text. A matrix of simulation runs is then provided, which is followed by detailed descriptions of the model configuration, along with aspects of meshing considerations. CFD results for the *OneWEC* system are then presented in the three remaining sections of this chapter, specifically covering the following:

- verification evidence;
- validation evidence;
- extended results from the CFD models.

6.1 Introduction

6.1.1 Modelling objectives

The main objectives discussed in Section 1.3.1 have been extended here in order to outline the detailed requirements of the CFD models. Each of the simulation runs described below in Section 6.1.3 have been selected carefully in order to deliver robust evidence, to support the principal arguments within this thesis.

*STAR-CCM+ v10.02.010, produced by CD-Adapco (http://www.cd-adapco.com/products/star-ccm).

The objectives for the *OneWEC* CFD models are as follows:

1. To deliver verified and validated numerical modelling results;
2. To use the verified and validated results to discern the independent damping processes which occurred during the experiments: from both mechanical effects and viscous effects;
3. To use validated models to examine more detailed physics than possible during the experiments, to study:
   (a) viscous force decompositions (shear and pressure);
   (b) 3D fluid flow descriptions (velocities and pressures);
4. To use validated models for extended application, to simulate events which were *not* carried out during the experiments (testing different initial drop height cases);
5. To identify major difficulties involved with the delivery of a free surface capturing floating WEC CFD model.

Objective 1

As a minimum requirement for any CFD study, Item 1 must provide the level of numerical uncertainty in the results (*verification*), along with the degree of deviation from known physical data, i.e. modelling uncertainty (*validation*). For the work presented in this thesis, these considerations were important when choosing specifically to study a decaying type system, which was characterised by relatively predictable response patterns. Furthermore, experimental uncertainty could also be reduced, due to the repeatability of results from these types of tests.

Objective 2

Arguments for providing a numerical model which captures the complete experiment, including sources of unwanted and uncontrolled dissipation, were given in Chapter 1. Using the BEM model in Chapter 5, it was possible to extract all modelling error, and to crudely treat this as a single combined external effect. The fully nonlinear CFD model used in this chapter allows for significant enhancements to this approach. First and foremost, the modelling error can be reduced, because the solution captures the hydrodynamic behaviour more accurately. The remaining residual will still represent modelling uncertainty, caused by: inaccuracies in hydrodynamic predictions and the uncontrolled 'experimental effects'. By ensuring that the former is minimised using an accurate numerical model, the latter can be studied in more detail, so that it can, in theory, be configured with its own numerical sub-model.

The studying of overall viscous effects is also associated with Objective 2. For numerical models which demonstrate minimal numerical uncertainty, a comparison between Euler and Reynolds-Average Navier-Stokes (RANS) solutions returns the effect due specifically to viscosity. A comparison between Boundary Element Method (BEM) and Euler solutions reveals the theoretical nonlinear hydrodynamic effects which are present in the system[†].

[†]Again, these have been identified in the experiments, and it is demonstrated here that they occur in both Euler

Objective 3

CFD solutions can also be used to interrogate detailed results which cannot be measured practically, including the forces directly associated with fluid shearing at a solid surface. This is raised by Objective 3. The forces resulting from viscous effect, as deduced above, can be interrogated further to allow for more detailed sub-model. Furthermore, flow patterns can be studied in great detail, to study vortex behaviour and pressure effects for example. Many of these interpretations could be either very difficult, or impossible, during a physical experiment.

Objective 4

Objective 4 allows for the application of a model to be used to test new scenarios which were not carried out during the experiments, once an understanding of the numerical system has been fully developed. An example of this is provided in this chapter, where the model WEC was released from various different heights, to investigate the processes which caused the nonlinear wave patterns.

A much more significant extension to the present model is carried out, when the system is modified to accommodate multiple WECs, as discussed in Chapter 7.

Objective 5

The issues surrounding sustained wave propagation across reasonable distances poses one of the most significant challenges in applying CFD to WEC arrays. It is notoriously difficult to construct a model with sufficient refinement, to avoid significant unwanted damping or distortions and reflections. There are a wide range of other challenges which are difficult to anticipate. A number of issues are highlighted, both in the main text and the appendices.

6.1.2 Outline model design and preliminary development

The simulations described in this chapter provide an extension to the results from the numerical models in Chapter 5. In contrast to the linear BEM models, which were scale independent, it was a necessary requirement to use the true physical dimensions of the experimental set up to construct the CFD models, in order to capture the correct balance of inertial, gravitational and viscous forces.

Due to the level of grid refinement in the volume mesh for the free surface capturing CFD method, it was necessary to use symmetry planes to model the axisymmetric body, and by doing so, adopt a wedge-shaped domain. The float was positioned at the inner apex of the wedge, as illustrated in Figure 6.1.

---

and RANS modes.

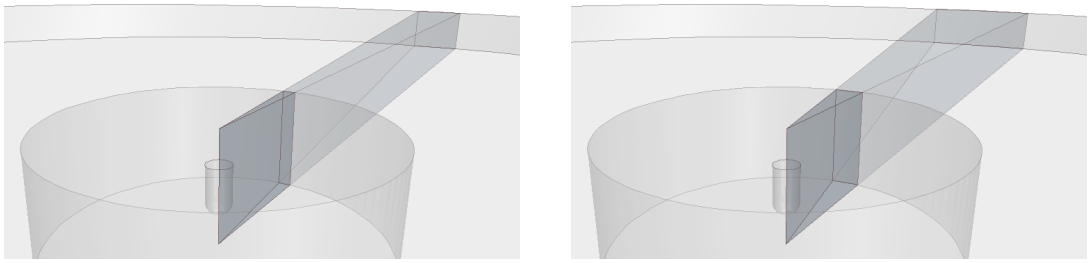

(a) 5° wedge **(b)** 11.25° wedge

Figure 6.1: Preliminary domain geometry test cases for the CFD model.

Preliminary tests were carried out to examine the effect of varying the angle between the two bounding symmetry planes. Wedge angles of 5° (Figure 6.1a), 7.5° and 11.25° (Figure 6.1b) were investigated using consistent mesh designs, which resulted in minimal changes to the simulation outputs. It was sufficient, therefore, to use the 5° domain, noting that angles smaller than this caused mesh design issues. These issues were typically around the central axis, where it was difficult to accommodate the recommended minimum number of four cells across the domain thickness, and in extreme cases, degenerate cells could also form.

Regarding the posts which were present in the experiment (refer to Figure 4.3), it was necessary to omit Post-B in order to suit the axisymmetric domain. The effects of this omission were investigated in Chapter 5, where it was found that associated modelling uncertainty was <0.01%. Inclusion of Post-A was relatively straightforward, where in fact it actually mitigated the meshing issues referred to above for the 5° case, as well as improving the accuracy of the model. It was necessary for the geometry of Post-A to be represented using an approximately circular cylinder profile, as it was not possible to capture the square section profile using the close symmetry planes. In general, for the post and outer surfaces of the wedge region, curved surfaces were avoided in order to mitigate further meshing complications.

The moving surfaces of the WEC were accounted for in the simulations through use of the overset mesh solver within STAR-CCM+. The necessary changes to the mesh as the body moved through the domain were captured by the sliding interface between the two independent fluid regions – the background domain region, and the overset region. Configuration issues were examined over a number of preliminary tests, through which suitable dimensions of the overset region were developed.

Discussions relating to the detailed set up for the fully developed CFD models are provided in Section 6.2. As well as the preliminary considerations above, a number of other issues were also addressed. Detailed description have been provided in the Appendix for the following: numerical ventilation; methods for imposing defined motions on to the WEC; methods for imposing tangential velocities at no-slip walls.

6.1.3 Analysis matrix

The objectives outlined in Section 6.1.1 were addressed by treating specific modelling cases, characterised by the following conditions:

1. Models which excluded dynamic WEC motion evaluations, instead employing the imposed motion functions described in Section 4.4;
2. Models which included dynamic WEC motion evaluations, through Fluid-Structure Interaction modelling (FSI);
3. Models which excluded viscosity (Euler);
4. Models which included viscosity (RANS).

These above conditions were configured to give four principal CFD models, with mixed combinations of motion and viscosity treatment (i.e. combinations of Items 1&2, 1&3, 2&3 and 2&4, in the above). The four simulations are referred to throughout the remaining work in terms of whether imposed motion (*IM*) or Fluid-Structure Interaction (*FSI*) configurations were used, and whether viscosity was neglected (*Euler*) or accounted for (*RANS*) in each case. The four principal model configurations were therefore as follows:

- *IM-Euler*,
- *FSI-Euler*,
- *IM-RANS*,
- *FSI-RANS*.

These simulations correspond to models *CFD-ID-01* to *-04*, shown in Table 6.1. It is worth noting that the particular interest in studying the prescribed motion and FSI cases was to isolate and account for the mechanical dissipation effects in the experiment.

A number of additional simulations were necessary to verify the discretised solutions, i.e. to demonstrate adequate resolution of the mesh and time step. To confirm the degree of convergence in space and time, models were evaluated with three mesh size settings and three time step settings. The various simulations, including *CFD-ID-05* to *-12* in Table 6.1, were used to provide solutions for *coarse*, *medium* and *fine* convergence cases. All of the convergence cases used the RANS solver, in order to demonstrate the degree of uncertainty for the most onerous computations. It was necessary to examine convergence for the body motions results using the fully dynamic FSI solver; however, for all convergence relating to the free surface results, it was prudent to ensure that as the WEC generated the waves, it moved in exactly the same manner during every analysis (i.e. using the *IM* function). This was done to remove any compound numerical error from the two separate results.

It was also necessary to establish the degree of uncertainty in the solution due to the number of inner iterations (N_{it}) performed within each time step. Preliminary verification test cases

Table 6.1: Summary of main *OneWEC* CFD models.

CFD-ID		Solver config.	Convergence[*1] Time, Δt (ms)			Grid, Δz_0 (mm)			Inner iterations[*2]		
			c	*m*	*f*	*c*	*m*	*f*	*c*	*m*	*f*
Main	01	*FSI-Euler*	-	0.3	-	-	-	1.5	10	-	-
	02	*IM-Euler*	-	0.3	-	-	-	1.5	10	-	-
	03	*FSI-RANS*	-	0.3	-	-	-	1.5	10	-	-
	04	*IM-RANS*	-	0.3	-	-	-	1.5	10	-	-
Verif. ξ	05	*FSI-RANS*	0.4	-	-	-	-	1.5	10	-	-
	06	*FSI-RANS*	-	-	0.225	-	-	1.5	10	-	-
	07	*FSI-RANS*	-	0.3	-	2.67	-	-	10	-	-
	08	*FSI-RANS*	-	0.3	-	-	2.0	-	10	-	-
Verif. η	09	*IM-RANS*	0.4	-	-	-	-	1.5	10	-	-
	10	*IM-RANS*	-	-	0.225	-	-	1.5	10	-	-
	11	*IM-RANS*	-	0.3	-	2.67	-	-	10	-	-
	12	*IM-RANS*	-	0.3	-	-	2.0	-	10	-	-
N_{it}	13	*IM-RANS*	-	0.3	-	-	-	1.5	-	15	-
	14	*IM-RANS*	-	0.3	-	-	-	1.5	-	-	20

[*1] For convergence tests, *c*, *m* and *f* refer to coarse, medium and fine resolution.

[*2] The sensitivity of the solution was initially tested for the range $5 \leqslant N_{it} \leqslant 10$, where it was found that the performance of the surface tension solver degraded for $N_{it} \leqslant 9$. Further details are given in Appendix C.2.

for N_{it} were subjected to sensitivity checks for specific numerical issues, described in detail in Appendix C.2. These issues were resolved for the coarse, medium and fine convergence cases (ensuring $N_{it} \geqslant 10$), allowing a coherent verification procedure. Simulations *CFD-ID-04*, *CFD-ID-13* and *CFD-ID-14* in Table 6.1 were used to provide these results. Further details provided in Section 6.4.

6.2 Model configuration

The design of the model was introduced in Section 6.1.2, which described the wedge shaped domain, with the freely floating WEC configured at the inner-most corner. The moving body was treated using the overset mesh methodology, and the resulting motion was either imposed or dynamically evaluated, as described in Section 6.1.3. The configuration of these components are described in this section, along with details of the boundary conditions, initial conditions, and configuration of the turbulence model.

6.2.1 Geometry and boundary conditions

For the WEC geometry considered in this study, the simplified wave radiation from the isolated float was assumed axisymmetric, with circular waves emanating from its vertical axis of symmetry. Two symmetry plane boundary conditions were used to reduce significantly the number of cells required. The resulting geometry adopted for the domain is shown in Figure 6.2, configured as a wedge shape with the symmetry planes separated by 5° in the horizontal orientation.

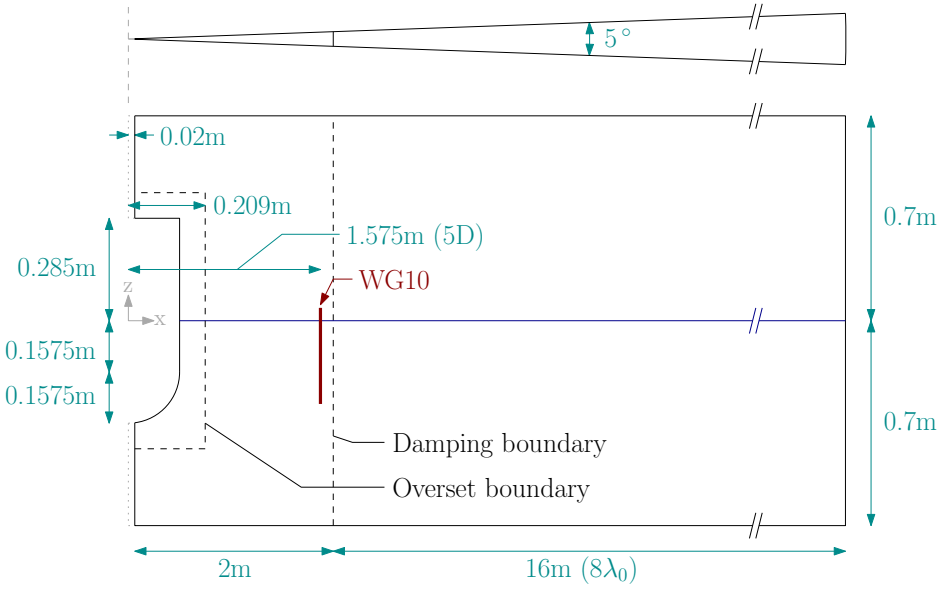

Figure 6.2: Geometry schematic for the CFD model (not to scale).

The wedge shape neglected any other diffracting or reflecting surfaces, such as tank sides, the wavemakers and beach. A number of posts were also present within the basin during the experiments, as described in Chapter 4 (Section 4.2). These were relatively small, measuring 40mm×40mm, and almost all were sufficiently far from the relevant WEC to be neglected. Two exceptions to this were Post A and Post B, as defined in Figure 4.3. These were treated in the following manner:

- **Post A:** This ran directly through the centre of the WEC and was straightforward to incorporate into the domain described above. The profile of the post was approximated as a tessellated circular section, rather than square. The inclusion of this post was in fact beneficial to the domain construction, as it removed the need for excessively skewed cells at the innermost apex.
- **Post B:** It was not possible to incorporate this adjacent post due to the use of symmetry planes. The impact of this omission was examined in Chapter 5 using the linear model, which showed that the effects were of the order 0.01%. This additional post was however modelled in some of the results discussed in Chapter 7.

A second fluid region was constructed in order to represent the moving WEC, as shown in Figure 6.2. This included a limited fluid volume which moved with the float, whilst interacting with the bulk flow across an overset mesh boundary. A linear interpolation method was used to link the two independent fluid volumes.

The outer boundary of the domain was positioned 18m from the symmetry axis, where a non-reflective pressure outlet boundary condition was configured. The air and water volume fractions, α_a and α_w, we controlled using inbuilt field functions: Volume Fraction of Light Fluid and Volume Fraction of Heavy Fluid; to apply dynamic conditioning throughout the simulations. A Volume Of Fluid (VOF) wave damping condition was also prescribed to numerically damp outgoing waves, configured at a distance of 16m from the outlet boundary (retaining a 2m interior region).

A pressure outlet was also used at the upper horizontal boundary, which represented the ceiling of the domain. This was characterised by an air volume fraction $\alpha_a = 1$ throughout the simulation, requiring no special consideration.

The solid surfaces – the WEC boundary, Post-A, and the base of the tank – were configured as no-slip walls. Each had additional specific considerations:

- **WEC boundary:** This was configured to have a fully resolved boundary layer throughout all flow conditions, with the nondimensional wall distance ($y^+ < 1$) as discussed in Section 6.3.3. An implication of this was that numerical ventilation became a significant issue where wall boundaries moved between the air and water phases (see Appendix C.2). This was rectified by employing the surface tension solver, and configuring the local wall conditions accordingly. The Phase Interaction property of the wall surface was set to use a contact angle of 0° (no meniscus).
- **Post A:** The post surface had two independent portions, one static (a domain boundary) and the other moving with the WEC, as part of the overset mesh region. In order to behave in the correct manner, the moving wall boundary of the post was configured to move relative to its parent mesh, with a velocity equal in magnitude and opposite in direction, to the overset mesh. This is discussed in more detail in Appendix C.3.
- **Post A & tank base:** No requirement was recognised to fully resolve the boundary layer for these boundaries. Blended wall functions were used, configured using the default parameters: $E = 9.0$; $\kappa = 0.42$.

With respect to the above solid interfaces, none of these additional considerations applied for Euler type simulations (a slip wall condition applied).

6.2.2 Solver configuration

Segregated flow

The segregated flow solver was used for all simulations, in which the continuity and momentum equations were linked, rather than coupled directly. The pressure and velocity are related using a Rhie-and-Chow type approach combined with a SIMPLE algorithm. The solver was configured using a second order upwind scheme for the convection terms. Secondary gradients for both the interior and boundary surfaces were used and flow boundary diffusion fluxes were enabled.

Implicit unsteady

The implicit unsteady solver was used, with second order temporal discretisation. Three different time step sizes were used to provide the verification cases (discussed in Section 6.4), which varied with the common ratio $r = 4/3$, $\Delta t = 0.4, 0.3, 0.225$ms, also listed in Table 6.1. This small time step was necessary for a number of reasons:

- to suit the implicit unsteady second order temporal discretisation scheme, which requires small time stepping;
- to ensure that the Courant number was appropriate, including at the free surface, to avoid compromising the performance of the High Resolution Interface Capturing (HRIC) scheme;
- to ensure that the interpolation histories between the background and overset continua were maintained.

This final point enforced the overall limiting time step size, as this was the most difficult to achieve. The time step $\Delta t = 0.4$ms ensured that the maximum heave displacement within a single time step $u_{max}\Delta t$, was less than $\Delta z_{min}/2$, where Δz_{min} was the smallest cell height dimension within the overlapping region. By maintaining this association of one cell to its neighbouring counterpart(s) (i.e. the *donor/acceptor* relationship), field data from the previous time step was available for the proceeding step. This is a requirement for the linear interpolation method used by the overset mesh boundary condition.

Eulerian multi-phase with VOF waves

The Eulerian multiphase solver was used, applying volume weighted mixture properties to represent the water and air phases. Constant fluid densities were used: 998.78kg/m^3 for water, 1.18415kg/m^3 for air. Dynamic viscosity was also constant: 0.001108Pa/s and 1.85508Pa/s for water and air respectively.

The VOF principle was applied in all CFD simulations, via the 'VOF Multiphase Model'. This was used to treat the two immiscible fluid phases and allow the formation of a free surface

interface. The common velocity and pressure fields which extended throughout the entire domain were used to describe the behaviour of both fluids, each represented by a unit volume fraction, $0 \leqslant \alpha_w \leqslant 1$, and $\alpha_a = 1 - \alpha_w$. The free surface was defined where $\alpha_w = \alpha_a = 0.5$.

Appropriate behaviour of the free surface was reliant on achieving Courant numbers in the range $0.5 \leqslant Cu \leqslant 1$ at free surface cells. This was a necessary requirement for the HRIC scheme used in the VOF method. The accuracy of the free surface evaluations was also dependent on the use of second order convection terms for volume fraction transport.

The VOF Wave model was used in addition to the above, which provided the field functions for initial conditions and boundary conditions for the *'flat wave'*, or quiescent conditions. This model also provided wave damping functions to avoid reflections from the domain perimeters. For the final runs, this was configured to provide 16m of artificial wave damping, or $8\lambda_0$.

Turbulence

The Menter Shear-Stress Transport (SST) k-ω turbulence model was used to ensure that the near field conditions were captured accurately through the viscous sublayer. Details of this model are provided in Chapter 3. As was the case with the other transport equations, the convection of the turbulence properties was second order, also using secondary gradients. Default coefficients were retained in the turbulence kinetic energy and dissipation equations. Numerical damping of the solution within inner iterations could also be controlled via the 'under relaxation' parameter for the turbulence equations. A small modification was made to remove some non-physical very high frequency free surface disturbances which persisted throughout preliminary verification tests. This was lowered from the default value of 0.8, to 0.7.

Initial conditions

Due to the quiescent fluid state at the beginning of the test, zero fluid velocities and level hydrostatic pressure conditions were assigned for the initial conditions. The free surface interface was defined at $z = 0$ throughout the domain. Where the SST (Menter) k-ω model was used, initial conditions for the turbulence model were at default background levels (turbulence intensity was 0.01).

Fluid structure interaction and imposed motions

For imposed motion cases (*IM*), the WEC motion was predefined using the 'user defined vertex' motion property in STAR-CCM+, which was assigned a field function based on Equation (4.1). Use of this method followed earlier complications using table data for the WEC motion path. Further details are provided in Appendix C.1.

The STAR-CCM+ component solver Dynamic Floating Body Interaction (DFBI) was used to model *FSI* cases. Free motion was permitted in heave, and the body was assigned a mass to suit the ratio $1/72$, which reflected the angular proportion of the geometry represented by the numerical domain (5°). Up to ten iterations were permitted for the evaluations of the DFBI solver.

6.3 Mesh

A set of geometrically similar meshes were required in order to provide the necessary results for the grid convergence studies. This was achieved by using a non-conformal[‡], unstructured hexahedral mesh, based on a Cartesian grid. Figure 6.3 shows the layout of the meshes used, with the index i indicating each refinement stage. Due to the nature of the free surface problem, the characteristic dimension of each mesh was considered to be the height of the cells at the free surface, Δz_0 (i.e. in the region characterised by $i = 0$). The physical dimensions were governed by: $\Delta z_i = \Delta z_0 \times 2^i$, where base sizes of $\Delta z_0 = 2.67\text{mm}, 2.00\text{mm}, 1.50\text{mm}$ were used for three convergence cases, using a common ratio $r = 4/3$. Exceptions to this were:

(a) at the WEC surface, which was assigned a specific prism layer configuration to suit $y^+ < 1$;

(b) near the free surface up to a distance of 1.65m from the WEC, where the cell height was fixed to Δz_0 and permitted to expand in the x and y-directions, giving anisotropic cells with maximum aspect ratio of 4;

(c) beyond 1.65m, where a directed mesh was used to allow the radial cell dimension x to expand gradually from $6 \times \Delta z_0$ to $\lambda/2$, the outermost cells being designed to dampen out all outgoing waves.

[‡]Although this mesh included hanging nodes at cell size transitions, the mesh was designed to ensured that the entire free surface was always within a highly refined conformal region.

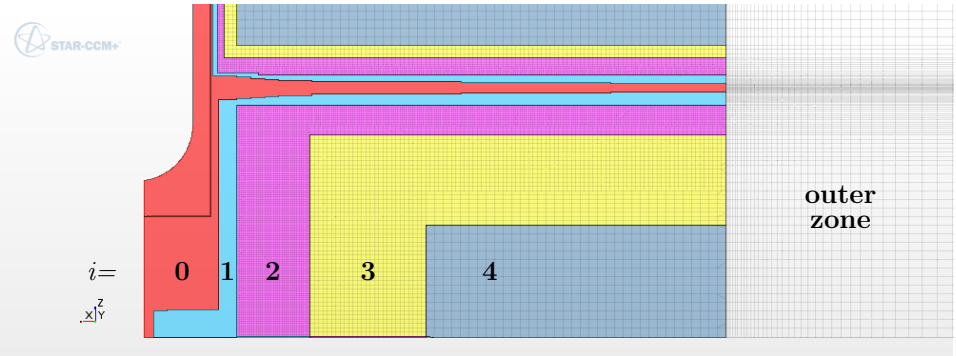

Figure 6.3: Mesh configuration, giving cell size stages based on the index i.

6.3.1 Free surface

A thin strip region was defined in the vicinity of the free surface, characterised by the index $i = 0$ in Figure 6.3. This was configured to capture the entire range of free surface elevations expected throughout the simulations. This free surface region was symmetrical in the $z = 0$ plane, with the region shape and thickness developed initially using outline analytical and potential flow results, and was developed further on an iterative basis throughout the CFD work. In general, the free surface elevation CFD results were very sensitive to the level of refinement in this region, and due to the mesh sensitivity of the interface between the background and overset meshes the highly refined $i = 0$ region also had to extend throughout the large swept volume of the WEC. Refinement to the free surface therefore resulted in significant increases to the computational requirements for simulation processing.

The following requirements were addressed with respect to the well documented issues regarding free surface capturing finite volume methods:

1. The mesh was conformal throughout the swept volume of the free surface. In general the meshing method which was used (trimmer) is characteristically non-conformal; however, hanging nodes are only encountered at mesh refinement transitions. The only mesh transformation used within the free surface region was anisotropic stretching (horizontally), which was performed using a directed mesh, starting at a distance of 1.649m from the WEC. This grid requirement is outlined in ITTC (2011a).
2. The mesh was Cartesian within both the trimmer and directed portions of the mesh. The orientation of the mesh was aligned with the horizontal plane.
3. With respect to the wave height, the recommended minimum number of cells in the vertical direction should be around 20 (ITTC, 2011a), i.e. 10 cells per wave amplitude. There were a number of reasons this was impractical for the present case:
   (a) As the wave radiation pattern was circular, the amplitudes diminished with distance from the WEC and were generally very small throughout most of the domain. At the reference wave gauge WG-5D (1.575m), peak free surface elevations measured around $\eta/\xi_0 = 0.04$ (8mm) in the experiment (see Figure 4.12), therefore cells of

just 0.8mm would be necessary to meet the above criterion.

(b) The transient behaviour of the system resulted in a relatively rapid decay of wave amplitudes, therefore as the wave height diminished as time progressed in the simulations, achieving the 'cell per wave height' criterion became a challenge.

(c) The maximum stroke of the WEC at the beginning of the decay dictated the amount of additional mesh refinement around the overset mesh, both above and below the free surface. As these cells had the same z dimension as the free surface, this had a considerable impact on cell count. The specific reasoning for this requirement is explained in Section 6.3.2.

(d) Due to the grid size being closely related to the time step through the requirements for the HRIC scheme (the limiting free surface Courant number) and the overset mesh interface histories, additional refinement of the grid had associated implications for the size of the times step. In the proposed scheme, the time step was in the range $\Delta t = 2.25 \times 10^{-4}$ and $\Delta t = 4.0 \times 10^{-4}$, as described in Section 6.2.2.

On the basis of the above reasoning, between 8 and 14 cells were used per wave height at the reference wave gauge (WG-5D), depending on the three base grid sizes. The free surface region in the immediate vicinity of the WEC was configured with 32, 44 and 56 cells for the various base sizes, spanning over a 63-66mm thick horizontal band. The mid grid size example can be seen in Figure 6.4.

4. In general, the choice of horizontal dimension Δx for free surface cells should account for the wavelength of any surface waves, whilst also maintaining appropriate aspect ratios. The recommended criteria for the minimum number of cells per wavelength for a second order accurate scheme lies between $\lambda/\Delta x = 80 - 100$ based on the existing literature (ITTC, 2011a; CD-Adapco, 2015; Havn, 2011). Within the inner mesh zone, aspect ratios of 2:1 were used, giving $\Delta x = 5.\dot{3}\text{mm}, 4\text{mm}, 3\text{mm}$ for the various grids. These were all well within the lower limit with respect to the principal wavelength, $\lambda_0 = 1.99\text{m}$. The number of cells per wavelength for the four harmonics seen in Figures 4.18 to 4.21 were as follows:

Table 6.2: Cells per wavelength

Harmonic	Cells per wavelength ($\lambda/\Delta x$)
First	373-664
Second	96-170
Third	42-76
Fourth	24-42

The degree of mesh refinement used throughout the free surface region ensured that the transition between $0 < \alpha_w < 1$ was resolved within a single cell depth, as seen in Figure 6.4. Two further mesh features can be identified in the figure, which are discussed in the following two

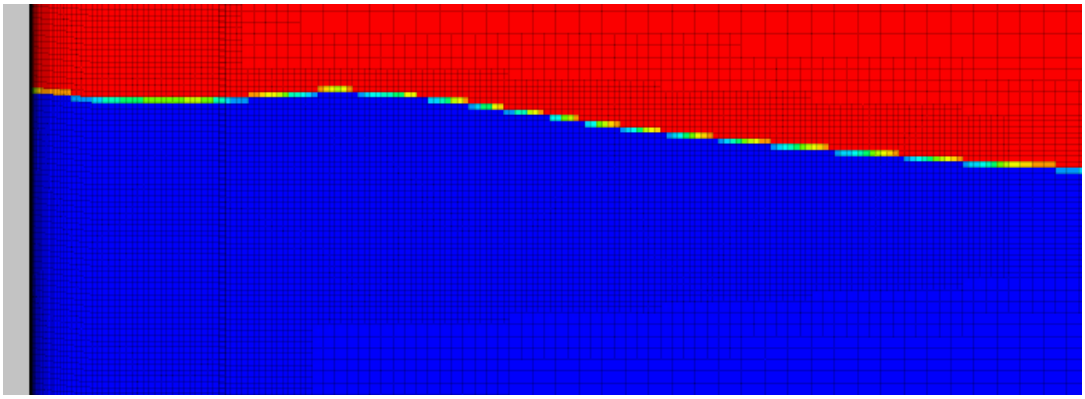

Figure 6.4: Volume fraction around the free surface, close to the WEC (up to around 0.26m) using the CFD model. The wave conditions shown are around the most extreme.

subsections – the highly refined boundary layer region, and the overset mesh interface. It is also noted that, at the instant shown, the WEC is moving downwards ($t/T_0 = 1.20$), where evidence of the additional harmonics can be seen at the left hand side, with a second small crest appearing at the WEC side wall.

6.3.2 Overset mesh interface

To establish flow conditions which can reliably pass between the background and overset regions, it was critical that the interface was treated appropriately. In the overset methodology, field data are not directly linked via any transport equations when flow properties 'pass' between the two discrete fluid continua. Data are instead interpolated between cells which lie in an overlapping region. A requirement of this method is that these cells must be similar in size in both meshes.

The following outlines the mesh design considerations for this work, in relation to the overset mesh interfacing requirements (the donor/acceptor relationship):

- The basic cell dimensions were identical in both meshes, throughout the overlapping region[§].
- The entire vertical edge of the overset mesh was configured to address both the overset mesh interfacing requirements, and the free surface requirements, discussed in Section 6.5.2 ($\Delta z_0 = 1.50 - 2.67$mm).
- The overlapping region also included the swept volume above and below the overset mesh. As the WEC had a maximum vertical displacement of 0.38m, both of these end regions were around 0.4-0.42m in height.

[§]There was generally less control of the size of individual cells which were adjacent to the oblique symmetry planes; however, this was managed by restricting the horizontal dimension of the grid in both overset and background meshes.

- The overlapping region excluded the interior cells of the background mesh which were always 'behind' the overset mesh. As these cells were permanently inactive, their physical size could be increased significantly.

6.3.3 Boundary layer

For the oscillating conditions studied in the decay tests, along the boundary of the moving WEC the flow was expected to reverse on itself at least twice every oscillation cycle, potentially more often if vortices were to come into contact with a boundary. This means, therefore, that the flow *will* have transcended the unacceptable y^+ range, $1 < y^+ < 30$ for significant spells throughout the simulations. Despite the fact that modern CFD codes include *'all-y^+'* blending functions, the switching between wall treatments can add unwanted distortions within the simulation results.

The reasoning above suggests that $y^+ < 1$ should be targeted where possible. Furthermore, aiming to resolve fully the boundary layer should ensure that shear stresses within the fluid will be accurately evaluated, this being a critical result from the present work.

A reasonable estimate was provided for the normal orientated dimension of the innermost cell of the boundary layer, by using the flat plate skin friction coefficient approximation by Schlichting (1979):

$$C_f = [2log_{10}(Re_D) - 0.65]^{2.3} \tag{6.1}$$

where C_f is the skin friction coefficient and Re_D is the Reynolds number. The wall adjacent cell dimension Δy was then found based on the target $y^+ = 1.0$:

$$\tau_w = \frac{C_f \rho u_{\infty,max}^2}{2} \tag{6.2}$$

$$u_\tau = \sqrt{\tau_w/\rho} \tag{6.3}$$

$$\Delta y = \frac{y^+ \mu_w}{\rho u_\tau} \tag{6.4}$$

Here, τ_w is the wall shear stress, u_τ is the shear velocity, μ_w is the dynamic viscosity of the water and ρ is density. The maximum free stream velocity $u_{\infty,max}$, relative to the WEC, was found to be approximately 2m/s from preliminary CFD results. For the fully resolved boundary layer, Δy was estimated to be around 1.2×10^{-5}m.

Various test cases were studied using the full CFD RANS models, to identify the specific conditions to achieve $y^+ \leqslant 1$. Figure 6.5 shows y^+ plotted against the vertical dimension of the WEC, using a reference frame origin $z' = 0$ which coincides with the bottom of the WEC. The maximum measured y^+ was recorded from a series of time samples, taken at $\Delta t = 0.036s$ (in red), with the instantaneous distribution for the peak y^+ case also shown (in green).

From these instantaneous measurements (taken at $t/T_0 = 0.19$), the position of the free surface can been identified in Figure 6.5 at around $z' = 0.26$m. The large spike just below this, at around $z' = 0.225 - 0.235$m, was found to remain highly localised for the other time samples studied. The apparent cause of this effect can been seen in Figure 6.6, where two opposing flows interfere very close to the moving wall. Whilst these peaks are above $y^+ = 1.0$, it is assumed that these effects are isolated.

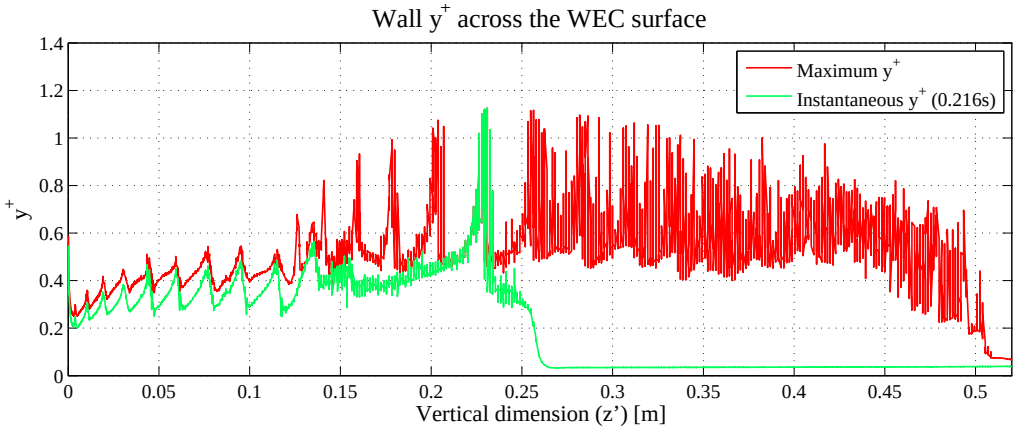

Figure 6.5: Wall y^+ over the surface of the WEC, with reference to the local moving reference frame. Peak values are provided (red), along with an instantaneous condition (green).

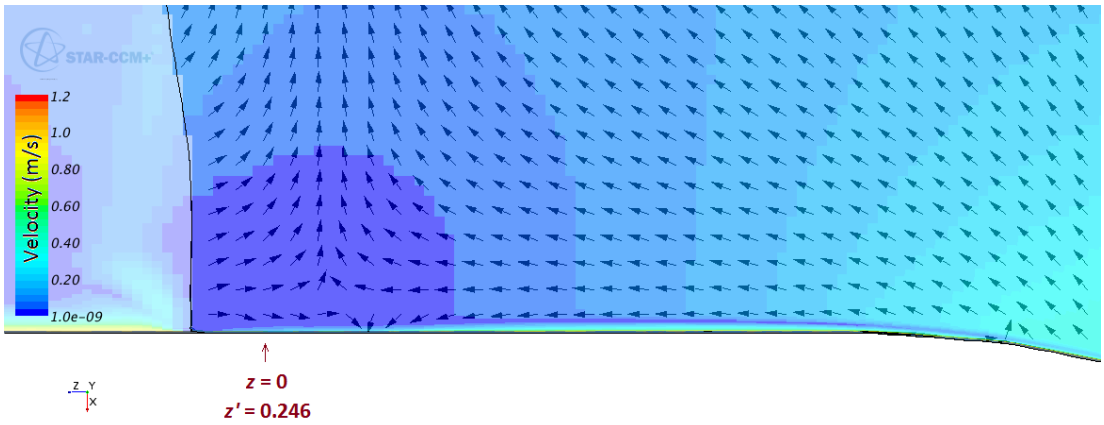

Figure 6.6: Fluid velocities near the WEC surface, evaluated using the CFD model. The plot is orientated at 90°with the WEC moving to the right (downward).

Two additional comments on the y^+ results should be noted. The sawtooth appearance to the profile at $z' < 0.1575$m was caused by the tessellations in the curved geometry of the WEC base, which was hemispherical. This is an undesirable effect which represents a source of modelling uncertainty. In terms of y^+ treatment, however, the results above still demonstrate that effective treatment of the boundary layer has been achieved. The second comment relates to the apparently ongoing sawtooth appearance above $z' > 0.1575$m, for the 'Maximum y^+' result

(in red). This is *not* caused by surface tessellation effects, as this simply shows the localised spike referred to earlier, moving in steps with the data capture rate.

For the three finalised grid convergence cases, the boundary layer was configured with $\Delta y = 1.18 \times 10^{-5}$m. In order to achieve this extremely onerous condition, the prism layer region of the mesh was configured with a very large number of cells, as follows:

1. Number of prism layer cells = 48¶;
2. Prism layer stretching ratio = 1.11;
3. Total prism layer thickness = 16mm.

This relatively deep prism layer also ensured a smooth transition between the curved cell arrangement around the WEC, and the Cartesian trimmer mesh.

6.4 Verification

Formal verification procedures were carried out to examine the level of uncertainty in the evaluated results. Output parameters which were of key interest in the simulations were chosen to test the sensitivity of the results to changes in time step sizes, mesh dimensions and number of inner iterations within each time step, N_{it}. A description of the necessary tests used to perform these checks is provided in Section 6.1.3. In the following sections, a brief description of the verification procedure is given, along with verification evidence for the excursion evaluations of the WEC float, and the free surface elevation in the surrounding fluid.

6.4.1 Method

The sensitivity of CFD to approximations in the underlying numerical schemes will *always* result in numerical uncertainty. This leads to two categories of numerical uncertainty which can be controlled by adapting the configuration of the model – discretisation uncertainty, and iterative uncertainty. Further numerical uncertainty will also be introduced via errors in any data input to the simulation, and due to limitation in machine precision.

The Grid Convergence Index (GCI) (Roache, 1998; Roy, 2005; ITTC, 2002) was used to examine the level of numerical uncertainty associated with discretisation approximations, both in time and in space. A description and definition was provided in Chapter 5, Equation (5.2), which again is used:

$$GCI = \frac{F_s}{(r^p - 1)} \left| \frac{f_1 - f_2}{f_1} \right|$$

Refinement ratios r of $1.3\dot{3}$ for both time step and grid size were configured, as described in Section 6.3. Again, f_1, f_2 and f_3 were the relevant numerical solutions for the three refinement

¶Coarse to fine prism layer cell quantities were described in ITTC (2011a), ranging from less than 10 cells, to over 100 cells, respectively.

cases (f_1 being the finest), and f in this situation represented either the WEC excursion ξ or free surface elevation η. ITTC (2002) recommends a factor of safety $F_s = 1.25$ for cases where monotonic convergence is demonstrated using three grid or time step sizes. Further to this, however, $F_s = 3$ is necessary when two refinement levels are used.

Again, the observed order of accuracy p_o was used wherever possible, defined in Equation (5.1):

$$p_o = \frac{1}{\ln(r)} \ln\left(\frac{(f_3 - f_2)}{(f_2 - f_1)}\right)$$

In contrast to the BEM results in Chapter 5, however, evaluations of the *GCI* for the CFD model were non-routine, due instances of oscillatory convergence / divergence, where observed order of accuracy was found to be $p_o \leqslant 0$. In these situations, the third numerical results f_3 was disregarded and the *GCI* was derived using two solutions, with a factor of safety $F_s = 3$. This does not strictly follow the formal definitions of the verification process, however within the time-scales and resources of this project, there was no practical way to develop the results further.

In situations where the opposite was the case, and the solution converged too aggressively (where the observed order of accuracy p_o was greater than the formal order of accuracy of the underlying numerical schemes, where in all CFD simulations considered in the present work: $p_f = 2$), it was appropriate to derive a *GCI* based on the formal order of accuracy p_f, as this gave a more conservative indication of the uncertainty. In the following results, these are both provided in the result summaries, and are distinguished using the subscripts o and f. Similarly, two different extrapolated results f_o^{extr} and f_f^{extr} are provided. These describe either ξ or η theoretically, at infinitely fine mesh and time resolution.

6.4.2 Excursion

Temporal verification evidence is provided in Figure 6.7, with a summary of results at peak amplitudes provided in Table 6.3. Monotonic convergence was confirmed for variations in the time step Δt, p_o was fairly consistent, however, as $p_o > p_f$, GCI_f should be viewed as the representative numerical error. This gradually increased over the period studied, however the results were very accurate, verified to within 0.32% over the first three oscillation periods.

In terms of spatial convergence, Figure 6.8 and Table 6.4 show mildly divergent solutions (these could equally be oscillatory), however the results appear consistent. Most of the amplitude peaks exhibited these conditions ($p_o < 0$), as such, all results were defined using the two finest mesh sizes Δz_1 and Δz_2, applying $F_s = 3$ to the *GCI*. This indicated uncertainty of up to 1.03%.

6.4.3 Free surface elevation

Verification of the free surface elevations (Figures 6.9 and 6.10, and Tables 6.5 and 6.6) presented a further challenge, in particular for mesh size convergence. The level of uncertainty in the free surface elevations was reasonable for temporal convergence ($< 1.75\%$), where monotonic behaviour was seen throughout. The severity of the divergence with respect to grid size was concerning, however, as the finest mesh was around the limit for what could practically be computed (3.7M cells). Nonetheless, the overall bounds of the results were consistent enough to provide some confidence in the behaviour, which returned a peak GCI_f of around 7.5% for the period studied, based on two grids, and $F_s = 3$.

In general, the free surface elevation results were much more sensitive to numerical uncertainty. Exhaustive testing of detailed areas of the mesh, and of solver parameters were examined, to attempt to address this lack of convergence. These additional measures included fine adjustments to the numerical damping configuration in the solver.

6.4.4 Iterative convergence (N_{it})

Solutions were obtained for various levels of inner iterations N_{it}, to clarify the level of numerical uncertainty associated with solution iterations within each time step. This cannot be formally associated with any refinement ratio (the limiting parameter N_{it} tends to ∞ rather than 0, as had been the case for Δt and Δz_i) therefore p_o cannot be derived and there is no equivalent GCI. Based on solution variation between N_{it} =10, 15 and 20, the residual in the free surface elevation results (see Figure 6.11) varied, 0.3% between fine and medium cases ($N_{it} = 20, 15$) and 0.6% between fine and coarse ($N_{it} = 20, 10$). This was an order of magnitude smaller than the associated solution variation due to mesh and time step sizes, as such it was considered appropriate to use $N_{it} = 10$ for all remaining work.

It is worth noting that $N_{it} = 10$ was also identified as a lower limit, due to the numerical ventilation issues discussed in Appendix C.2.

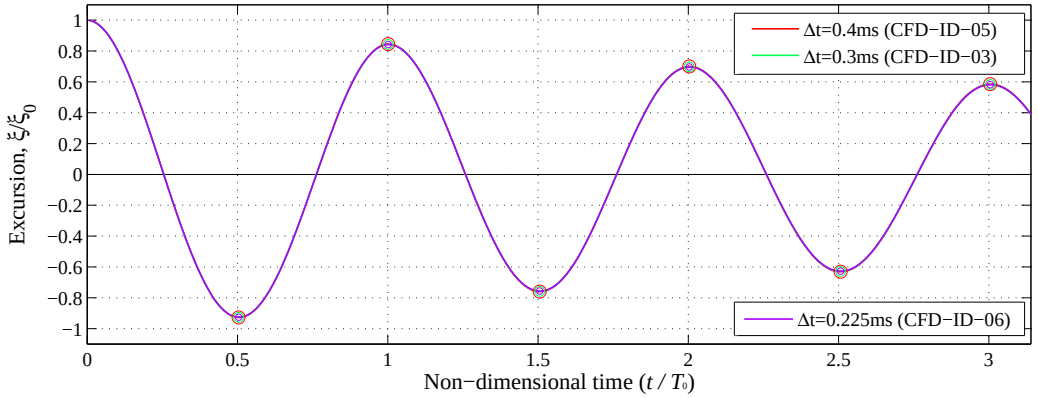

(a) Simulation results, over the period $t/T_0 < 3.1$.

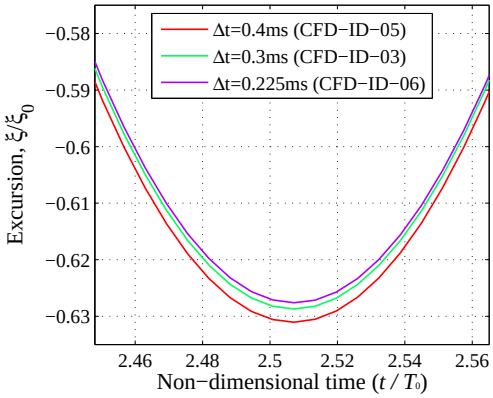

(b) Trough, at $t/T_0 = 2.5$.

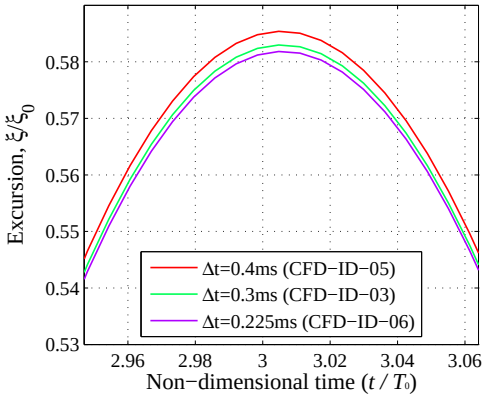

(c) Peak, at $t/T_0 = 3$.

Figure 6.7: WEC excursion results from the CFD model, for the temporal convergence cases: $\Delta t = 0.4, 0.3, 0.25$ms.

Table 6.3: Temporal convergence results for WEC excursion

Peak [#]:	1	2	3	4	5	6
Time (t/T_0):	0.5	1.0	1.5	2.0	2.5	3.0
$f_1 \times 10^2$	-92.60	84.25	-75.68	69.66	-62.76	58.18
$f_2 \times 10^2$	-92.64	84.31	-75.76	69.77	-62.87	58.30
$f_3 \times 10^2$	-92.73	84.48	-75.96	69.97	-63.11	58.54
F_s	1.25	1.25	1.25	1.25	1.25	1.25
p_o	3.12	3.56	2.67	2.29	2.60	2.55
$f_o^{extr} \times 10^2$	-92.57	84.22	-75.60	69.55	-62.66	58.08
GCI_o	0.03%	0.05%	0.13%	0.20%	0.20%	0.23%
p_f	2.00	2.00	2.00	2.00	2.00	2.00
$f_f^{extr} \times 10^2$	-92.55	84.17	-75.56	69.52	-62.62	58.04
GCI_f	0.06%	0.11%	0.19%	0.25%	0.28%	0.32%

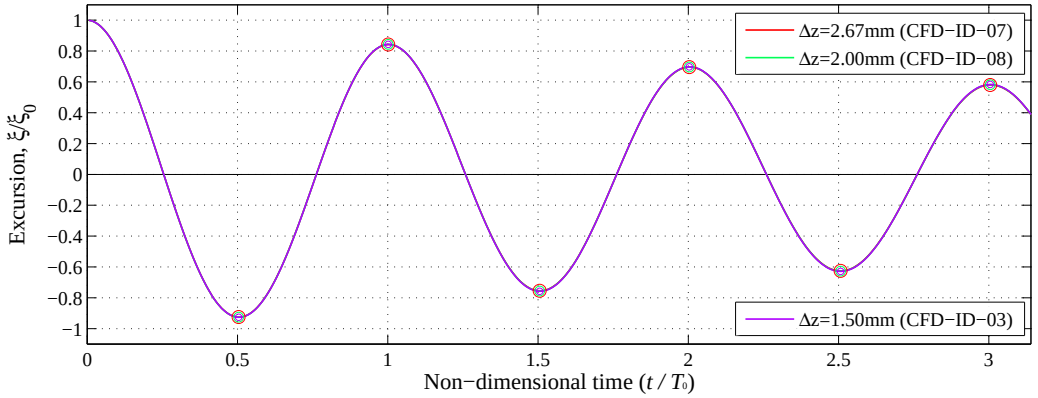

(a) Simulation results, over the period $t/T_0 < 3.1$.

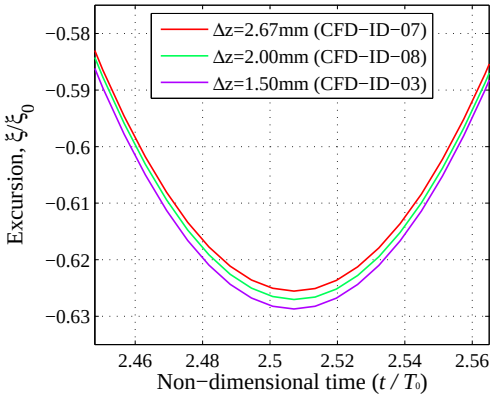

(b) Trough, at $t/T_0 = 2.5$.

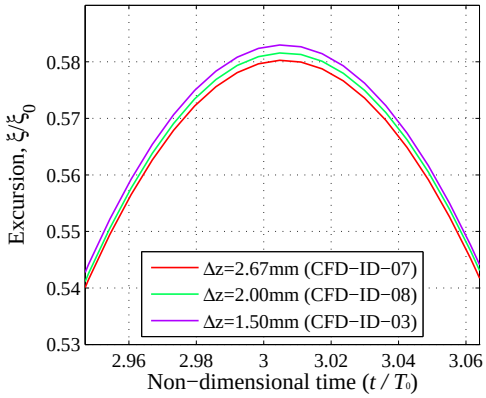

(c) Peak, at $t/T_0 = 3$.

Figure 6.8: WEC excursion results from the CFD model, for the spatial convergence cases: $\Delta z_0 = 2.67, 2.00, 1.50$mm.

Table 6.4: Spatial convergence results for WEC excursion

Peak [#]:	1	2	3	4	5	6
Time (t/T_0):	0.5	1.0	1.5	2.0	2.5	3.0
$f_1 \times 10^2$	-92.64	84.31	-75.76	69.77	-62.87	58.30
$f_2 \times 10^2$	-92.61	84.30	-75.61	69.65	-62.70	58.16
$f_3 \times 10^2$	-92.52	84.20	-75.49	69.54	-62.56	58.03
F_s	3.00	3.00	3.00	3.00	3.00	3.00
p_o	-	-	-	-	-	-
$f_o^{extr} \times 10^2$	-	-	-	-	-	-
GCI_o	-	-	-	-	-	-
p_f	2.00	2.00	2.00	2.00	2.00	2.00
$f_f^{extr} \times 10^2$	-	-	-	-	-	-
GCI_f	0.10%	0.04%	0.77%	0.66%	1.03%	0.93%

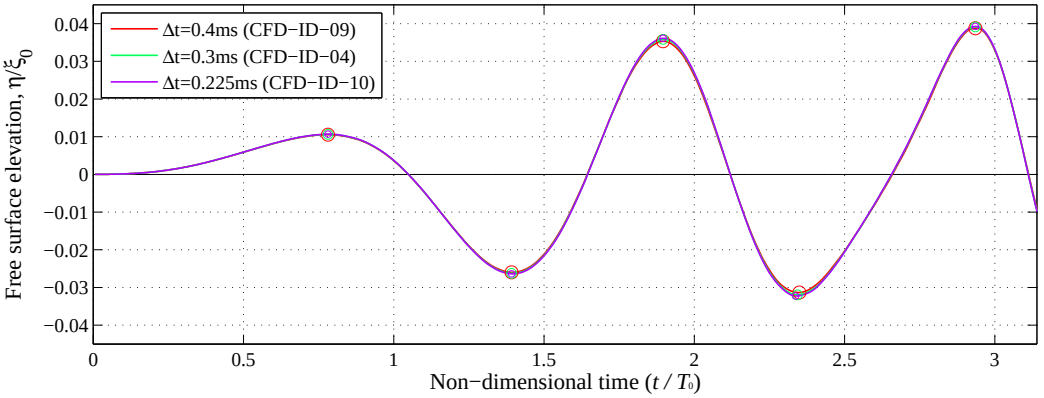

(a) Simulation results, over the period $t/T_0 < 3.1$.

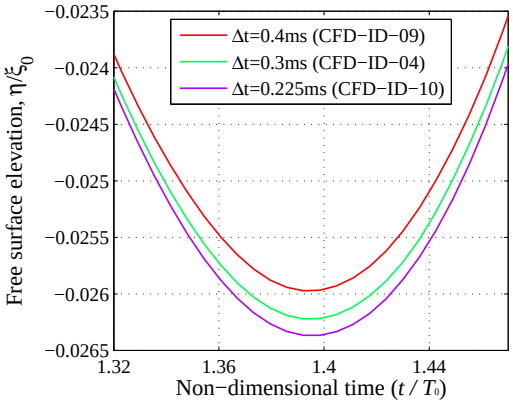

(b) Trough, at $t/T_0 = 1.4$.

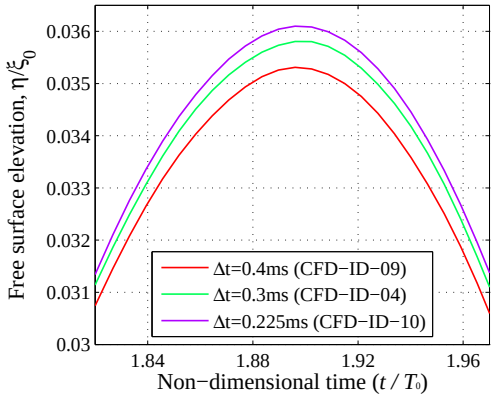

(c) Peak, at $t/T_0 = 1.9$.

Figure 6.9: Free surface elevation results from the CFD model, for the temporal convergence cases: $\Delta t = 0.4, 0.3, 0.25$ms.

Table 6.5: Temporal convergence for free surface elevation

Peak [#]:	1	2	3	4	5
Time (t/T_0):	0.781	1.392	1.896	2.343	2.935
$f_1 \times 10^2$	1.07	-2.64	3.61	-3.22	3.93
$f_2 \times 10^2$	1.06	-2.62	3.58	-3.19	3.91
$f_3 \times 10^2$	1.05	-2.60	3.53	-3.13	3.88
F_s	1.25	1.25	1.25	1.25	1.25
p_o	1.07	1.87	1.89	2.45	3.35
$f_o^{extr} \times 10^2$	1.08	-2.66	3.65	-3.25	3.94
GCI_o	1.75%	0.97%	1.39%	1.12%	0.27%
p_f	2.00	2.00	2.00	2.00	2.00
$f_f^{extr} \times 10^2$	1.07	-2.66	3.65	-3.26	3.94
GCI_f	0.81%	0.89%	1.29%	1.48%	0.57%

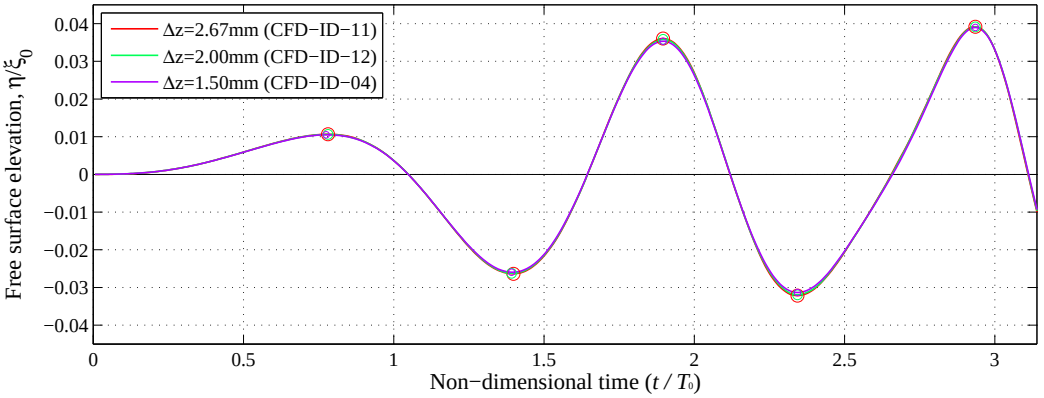

(a) Simulation results, over the period $t/T_0 < 3.1$.

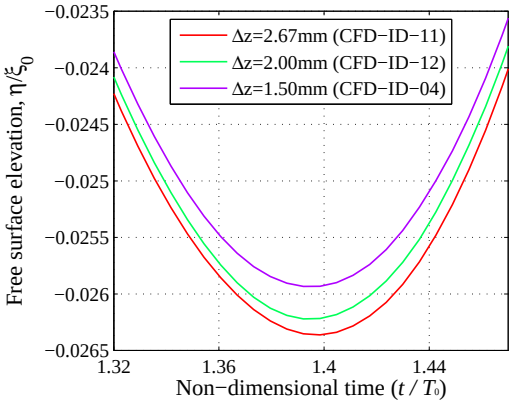

(b) Trough, at $t/T_0 = 1.4$.

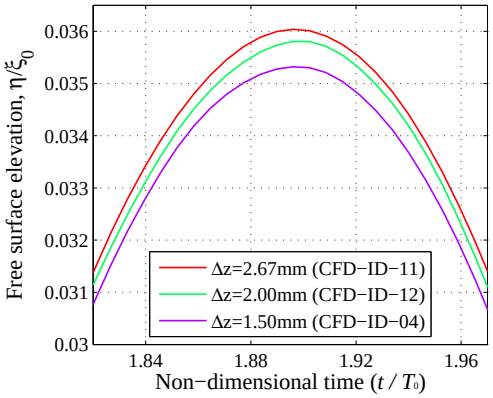

(c) Peak, at $t/T_0 = 1.9$.

Figure 6.10: Free surface elevation results from the CFD model, for the spatial convergence cases: $\Delta z_0 = 2.67, 2.0, 1.5$mm.

Table 6.6: Spatial convergence for free surface elevation

Peak [#]:	1	2	3	4	5
Time (t/T_0):	0.781	1.392	1.896	2.343	2.935
$f_1 \times 10^2$	1.05	-2.59	3.53	-3.13	3.90
$f_2 \times 10^2$	1.06	-2.62	3.58	-3.19	3.91
$f_3 \times 10^2$	1.06	-2.64	3.60	-3.22	3.92
F_s	3.00	3.00	3.00	3.00	3.00
p_o	-	-	-	-	-
$f_o^{extr} \times 10^2$	-	-	-	-	-
GCI_o	-	-	-	-	-
p_f	2.00	2.00	2.00	2.00	2.00
$f_f^{extr} \times 10^2$	-	-	-	-	-
GCI_f	4.52%	4.26%	5.32%	7.52%	1.56%

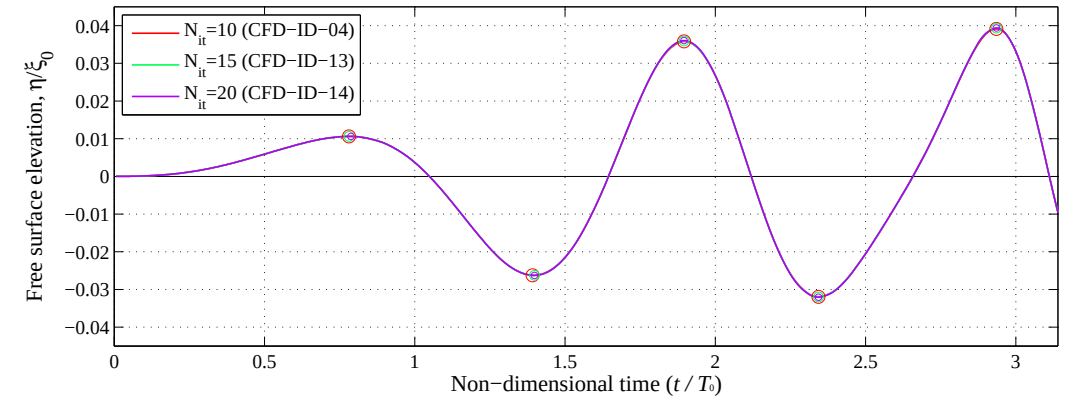

(a) Simulation results, over the period $t/T_0 < 3.1$.

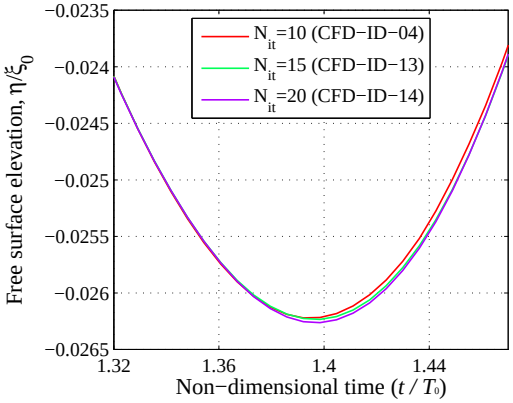

(b) Trough, at $t/T_0 = 1.4$.

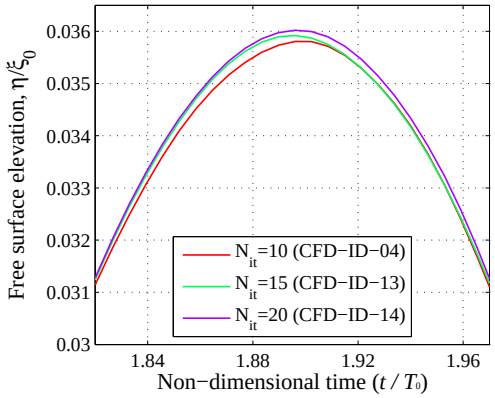

(c) Peak, at $t/T_0 = 1.9$.

Figure 6.11: Iterative solver convergence behaviour for the CFD model, using $10 \leqslant N_{it} \leqslant 20$.

6.5 Results & validation

This section describes results from carefully configured CFD models (the main *OneWEC* CFD runs: *CFD-ID-01* to *-04* in Table 6.1), which were designed to replicate the system responses measured during the experiments. The experiments themselves were selected to give high quality repeatable results, and in particular focused on decay tests in which there were no background wave conditions (i.e. the wavemakers were configured to provide active absorption only, and not to generate waves). Validation of the *OneWEC* model was demonstrated using two test sets from the WECwakes experiments, which were described in detail in Section 4.2, in particular, *TestID-03* and *TestID-04* from Table 4.1. Both tests contained two decay test sequences, giving four repeated results. The experimental uncertainties were discussed in Section 4.3, along with details of how the data were post-processed.

6.5.1 WEC excursion

WEC excursions were only evaluated in *FSI* type CFD simulations, i.e. two of the main *OneWEC* CFD runs: CFD-ID-01 (*FSI-Euler*) and CFD-ID-03 (*FSI-RANS*). The purpose of these particular simulations was:

1. to demonstrate verified and validated results for the WEC motions, and
2. to identify the differences between the results when viscosity was ignored (*FSI-Euler*), and when it was included in the numerical model (*FSI-RANS*).

This residual between *FSI-Euler* and *FSI-RANS* was used here to interpret the relative impact of viscous effects on the device motion. A more detailed examination of viscous effects is provided in Section 6.6.1, where heave forces have been decomposed into the pressure and shear components.

Figure 6.12a shows excursion evaluations from the two *FSI* cases, along with the *WECwakes* results. Table 6.7 provides details of excursion magnitude at around half way through the overall decay sequence ($t/T_0 = 7$), including the result – '*BEM*' – the linear solution discussed in Chapter 5. Both *BEM* and the two CFD results were clearly underdamped in comparison to *WECwakes*, which suggested that other external forces were non-negligible. Comparison between the *FSI-Euler* solution and *BEM*[‖], as in Figure 6.12b, showed very close agreement. Some modelling uncertainties were common between both the CFD and linear methods, most notably the uncertainty due to the omission of mechanical damping effects.

Table 6.7: Peak excursion amplitude, after 7 cycles

	ξ [m]	ξ/ξ^{EXP}
BEM	0.3666	197%
FSI-Euler	0.3598	193%
FSI-RANS	0.2997	161%
WECwakes	0.1865	*n/a*

The following observations have been interpreted from the results shown in Figure 6.12. The residual between *FSI-Euler* and *FSI-RANS* represented (exclusively):

1. the modelling uncertainty due to the omission of viscosity – i.e. the *'viscous effect'*.

The residual between *FSI-RANS* and *WECwakes* represented the following:

2. the modelling uncertainty due to the omission of mechanical damping effects;
3. all other modelling uncertainties (other than Items 1 and 2);
4. all numerical uncertainty (detailed in Section 6.4).

The largest contributing factors to the overall uncertainty are Items 1 and 2, i.e. the cause of the underdamped response is due to viscosity and mechanical dissipation. The relative magnitude

[‖] The Euler CFD solution is a nonlinear, volume discretised form of the BEM method in Chapter 5.

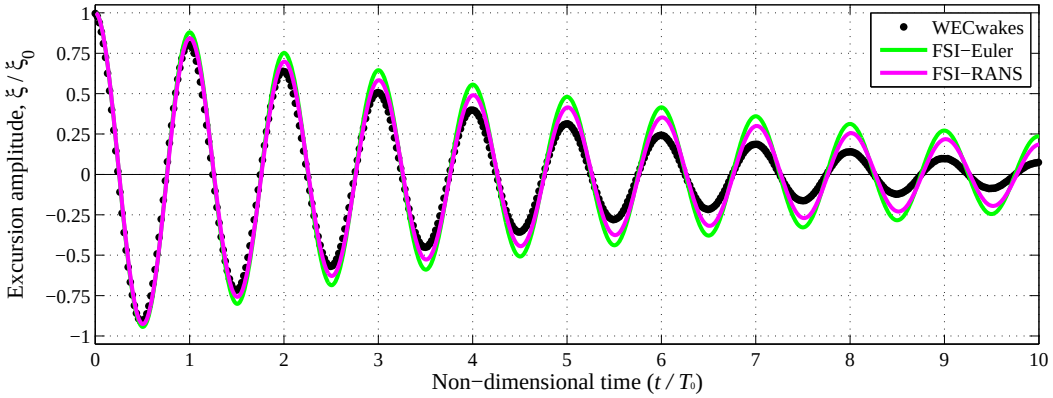

(a) CFD results, including reference results (*WECwakes*).

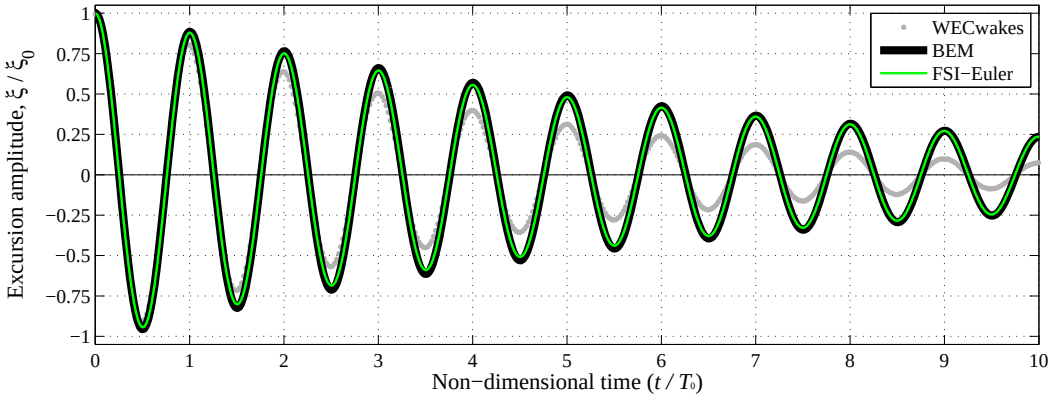

(b) Inviscid results (CFD and BEM), including reference results (*WECwakes*).

Figure 6.12: WEC excursion amplitude evaluations, using CFD, with comparison to the experimental measurements and BEM results.

of the viscous damping effects varied from around 50% to 35% of the total damping effect, across the range $0 < (t/T_0) < 7$.

6.5.2 Free surface elevation

The free surface elevations were evaluated for all of the main CFD runs: CFD-ID-01 to CFD-ID-04. Validation checks were carried out for the free surface evaluations specifically using runs CFD-ID-02 (*IM-Euler*) and CFD-ID-04 (*IM-RANS*). Imposed motion cases were used in order to avoid compounded effects of changes to both the WEC motion and to the free surface evaluations, as would have otherwise been the case for *FSI* simulations. The motion paths in both *IM* cases were identical.

Figure 6.13a provides free surface elevation results at WG-5D, which capture both the general time history and nonlinear effects which were evident in the experimental results. The inflections in the free surface profile were recreated well, and visible gradient differences can be

seen between the ascending and descending free surface, for example around $2.4 < t/T_0 < 3.2$. Given the close agreement between the CFD results and experiments, especially up to around $t/T_0 = 8$, further evidence has been demonstrated that the nonlinear effects examined in Chapter 4 are systematic features of the physical problem. Clearly, it had not been possible to identify these effects using the linear model.

The cause of these features requires further explanation; however, it is clear that they were formed as the transient process initiated, and that they propagated within discrete wave packets (also given the spectral evidence in Figures 4.18 to 4.21). It has been confirmed that these were not due to the presence of Post B in the experiments, as this was omitted from the CFD models. Furthermore, due to the direction of travel of the higher order components, these were not caused by reflections from outer surfaces. An expanded study of the free surface response to various float release heights is provided in Section 6.6.2, which also examines the causes of these nonlinear effects.

Validation of the free surface elevation CFD results can be described in terms of three reasonably discrete phases of the decay response. Over the period $0 < (t/T_0) < 4.75$, the largest differences between the numerical and experimental results were around peak and trough values, as seen in Figure 6.13a. In other respects, the free surface was captured closely in the numerical model, remaining smooth and stable throughout the nonlinear response. These effects appeared to be most severe when the wave amplitudes were largest, which may suggest a slight deficiency in the ability of the employed mesh to capture these slightly steeper waves.

During the period $4.75 < (t/T_0) < 9$ shown in Figure 6.13b, the numerical evaluations were reasonably consistent, including only small amplitude irregularities. Beyond $t/T_0 > 9$, however, the predictions became very much dominated by instabilities, as seen in Figure 6.13c. During this period, in physical terms the wave amplitudes were very small, at around < 0.2mm.

In contrast to the earlier validation of WEC excursions in Section 6.5.1, there was limited interest in examining the effects of viscosity, which should not in theory have any impact on wave propagation. Differences were observed between the *(*Euler) and *RANS* results, however, due to small changes to the free surface in the vicinity of the WEC, and to differences in the numerical behaviour of each model.

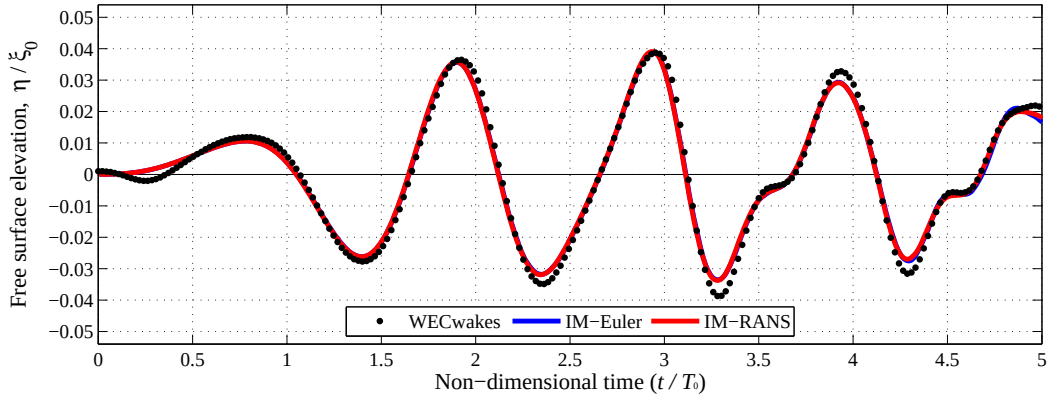

(a)

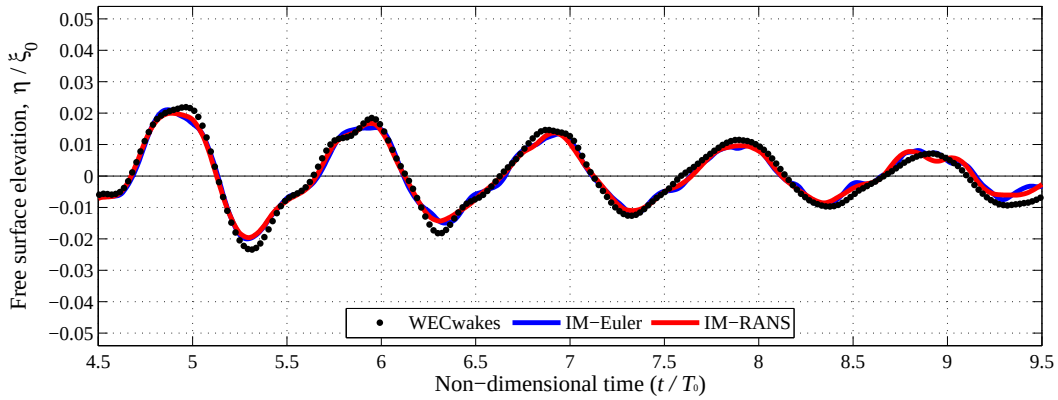

(b)

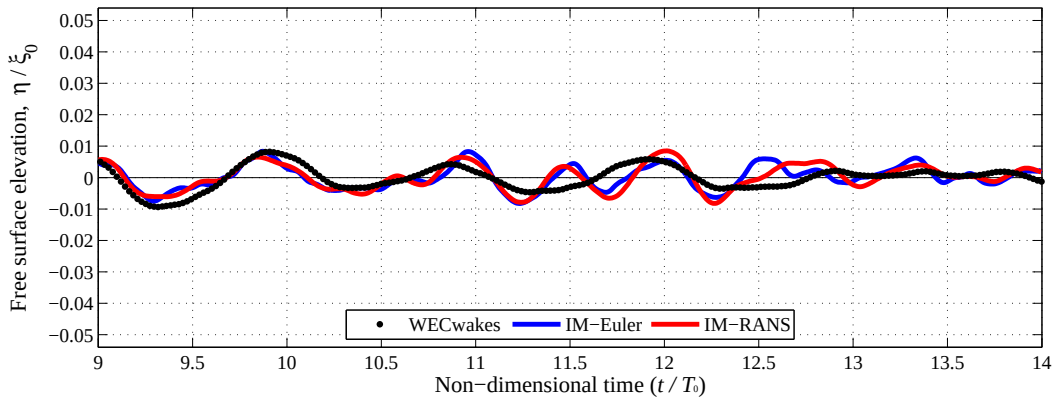

(c)

Figure 6.13: Free surface elevation evaluations at WG-5D, using CFD, with comparison to the experimental measurements.

6.6 Extended results

6.6.1 Viscous effects

Heave forces

A detailed examination of the discrete viscous and rotational effects of the fluid was achieved by monitoring the two components of the fluid forces acting on the WEC – the pressure force, $F_{3,P}$, and shear force, $F_{3,\tau}$.

$$F_3 = F_{3,P} + F_{3,\tau} \tag{6.5}$$

Furthermore, $F_{3,P}$ can be split into two further subcomponents, which describe:

1. the pressure force due to inviscid effects, $F_{3,p(Euler)}$, (i.e. from bulk fluid movement);
2. the pressure force due to viscous effects, $F_{3,p(visc)}$.

Equation 6.5 becomes:

$$F_3 = F_{3,p(Euler)} + F_{3,p(visc)} + F_{3,\tau} \tag{6.6}$$

and it is clear that for Euler simulations, $F_{3,p(visc)} = F_{3,\tau} = 0$ and $F_3 = F_{3,P} = F_{3,p(Euler)}$. For describing the viscous effects on the other hand, the viscous pressure force has been defined as:

$$F_{3,p(visc)} = F_{3,p(RANS)} - F_{3,p(Euler)} \tag{6.7}$$

where $F_{3,p(RANS)}$ was the total pressure force evaluated during the relevant RANS simulations. The description in Item 1 above also emphasises the fact that $F_{3,p(Euler)}$ is closely related to the potential solution, which can be described in terms of the added mass and added damping. The potential solution will of course neglect the rotational effects which gave rise to the nonlinear behaviour of the Euler solutions, shown for example in Figure 6.13.

Before examining the results from this decomposition of F_3, it was useful first to compare the linear (BEM) and nonlinear (CFD) results to assess qualitatively the validity of the solutions. Figure 6.14 shows evaluations of F_3 from the *BEM*, *FSI-Euler* and *FSI-RANS* numerical models. The force response for the *BEM* solution was derived by convolving the CFD WEC excursions from *FSI-Euler* (i.e. the solution shown in Figure 6.12a), with the impulse response function (IRF) for the heave force. This was done to provide a linear result which was equivalent to the inviscid CFD run. The results generally agree very well, especially in terms of amplitude; however, a small phase lag was apparent for the *BEM* results, measuring around $t/T_0 = 0.05$.

Figure 6.14a also highlights comparative differences in in-line force F_3 for the *FSI-Euler* and *FSI-RANS* simulations. The total force in Figure 6.14 shows an apparent effect of viscosity over time, which measures approximately 15% at the trough at $t/T_0 = 7$, around halfway through

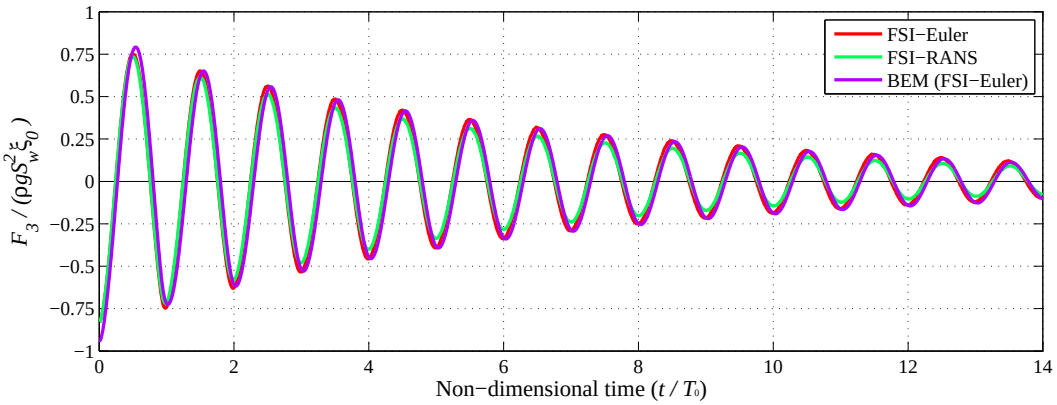

(a) Results for the *FSI* cases.

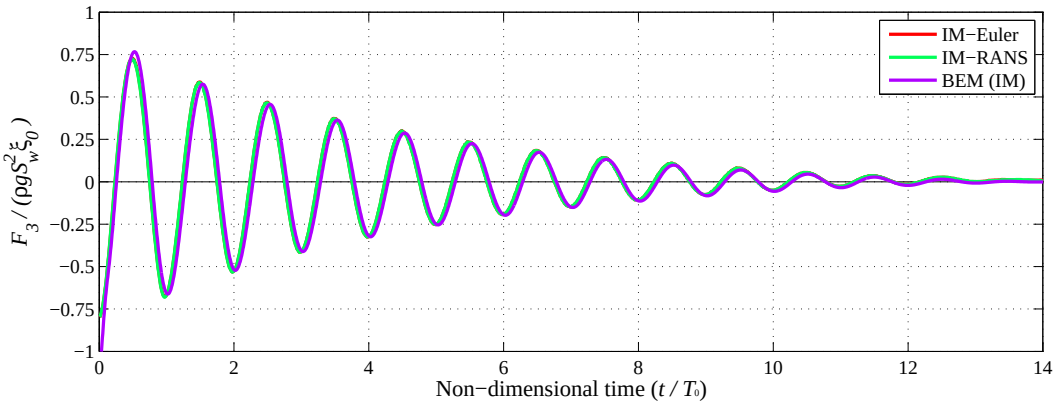

(b) Results for the *IM* cases.

Figure 6.14: In-line (heave) force F_3, acting on the WEC surface. Comparison between the *BEM*, *(*Euler) and *RANS* numerical models.

the complete decay sequence. This must however be recognised as a compound effect, which includes both of the following:

1. changes to the forces acting on the WEC, directly due to viscosity, and
2. changes to the forces due to the new motion path of the WEC, indirectly due to viscosity.

To develop this argument further it was necessary to avoid this complication and to decouple these effects – i.e. examine the forces using the *IM* cases shown in Figure 6.14b, to focus on Item 1 above. The two force response curves $F_{3,p(Euler)}$ and $F_{3,p(RANS)}$ appear almost identical in Figure 6.14b; however, the residual ($F_{3,p(visc)}$, as Equation 6.7) shows a coherent trend, as seen in Figure 6.15.

It was possible directly to extract the *shear force* $F_{3,\tau}$ from the RANS solution, also provided in Figure 6.15 for the *IM-RANS* case. The peak pressure and shear viscous forces were around 0.8% and 0.95% of the total force, respectively. While these were two orders of magnitude smaller than the total force, a non-negligible cumulative effect was still experienced over the

course of the decay, detailed in Table 6.7 and Figure 6.12a.

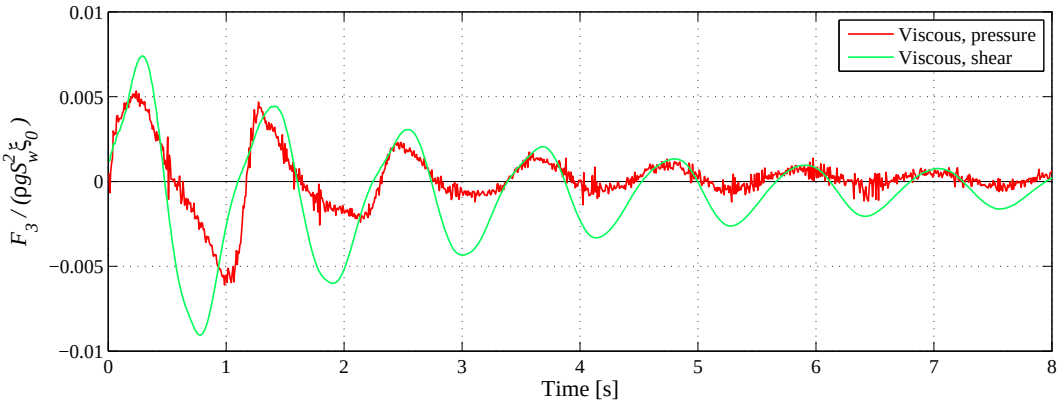

Figure 6.15: Viscous in-line (heave) forces, for the *IM-RANS* numerical model: viscous pressure force $F_{3,p(RANS)}$, and viscous shear force $F_{3,\tau}$.

An expanded discussion relating to the heave force $F_{3,p(visc)}$ and $F_{3,\tau}$ is provided in Appendix C.2, which examines the effects of numerical ventilation.

Flow velocities & pressures

Detailed scalar and vector field results of the flow conditions were extracted to monitor the behaviour of the model, and to provide enhanced interpretations of the flow characteristics. The sections shown in Figures 6.16 and 6.17 give the velocity and pressure profiles from the *FSI-RANS* simulation at $t/T_0 = 1.22$, just after the WEC began its second stroke. The particle motion paths can generally be described as 'orbital' at moderate distances from the WEC, with a downward and outward direction immediately around the WEC. This corresponds to the changes in pressure seen in Figure 6.17, which show the highest pressures around the very bottom of the WEC. The fluid is close to a stagnation condition within this region, with high pressure and low velocity (relative to the WEC surface).

An important region in terms of the differences between the inviscid and viscous flows can be seen around the transition between the hemisphere and cylinder sections of the float. In Figure 6.17 this appears as a region of low pressure; however, this is most clearly seen in Figure 6.18b (at $t/T_0 = 1.09$), where a thin layer of fluid can be seen to accelerate over the final section of curvature of the WEC base. Figure 6.18 shows a marked difference in conditions between inviscid and viscous cases, with the former only capturing a more gradual velocity gradient over a much less defined layer. Figure 6.19 (at $t/T_0 = 1.22$) shows how this faster moving fluid evolves into an elongated vortex, which starts to impact on the free surface elevation.

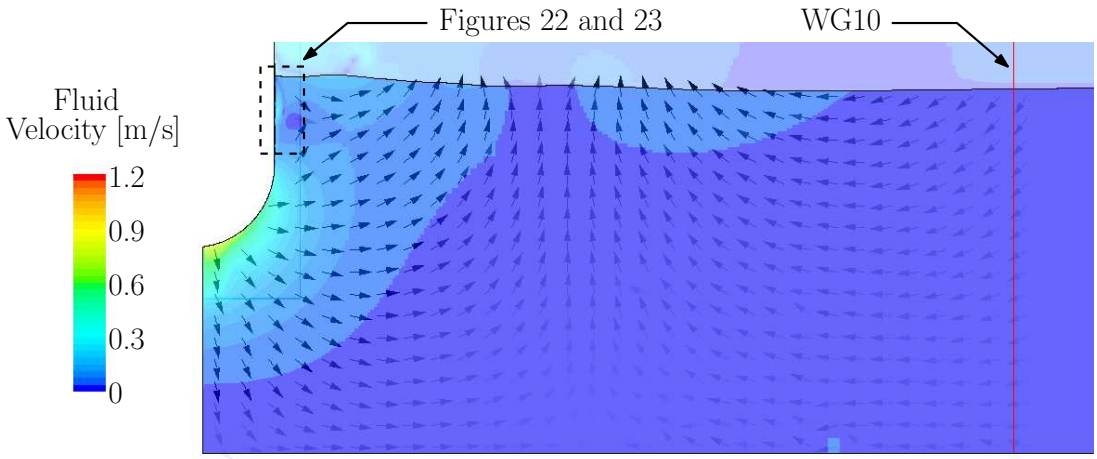

Figure 6.16: Velocity map from *RANS-FSI* results, at $t/T_0 = 1.22$, during the second downward stroke. The velocity vectors are uniform in size, with magnitudes depicted by the scalar contours.

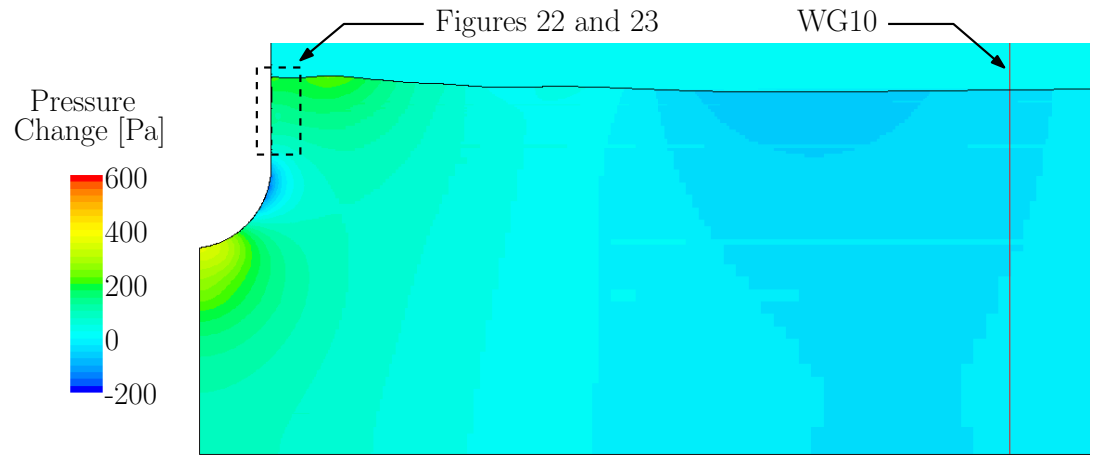

Figure 6.17: Pressure map from *RANS-FSI* results, at $t/T_0 = 1.22$, during the second downward stroke. The pressure shown is the change from hydrostatic conditions, $p - \rho g H$.

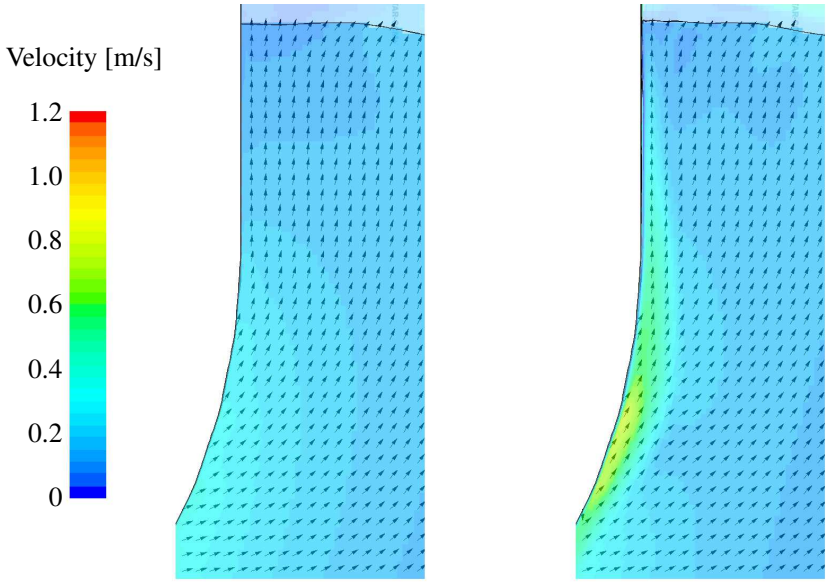

(a) *EULER−IM* (b) *RANS−IM*

Figure 6.18: Velocity map from at $t/T_0 = 1.09$, at the beginning of the second downward stroke, for (a) *EULER-FSI*, and (b) *RANS-FSI*. The velocity vectors are uniform in size, with magnitudes depicted by the scalar contours.

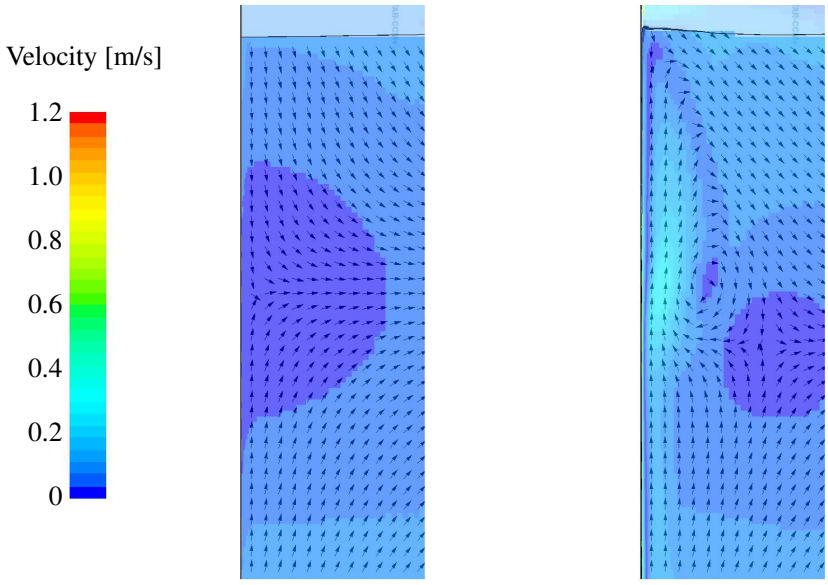

(a) *EULER−IM* (b) *RANS−IM*

Figure 6.19: Velocity map from at $t/T_0 = 1.22$s, during the second downward stroke, for (a) *EULER-FSI*, and (b) *RANS-FSI*. The velocity vectors are uniform in size, with magnitudes depicted by the scalar contours.

6.6.2 Nonlinear effects

Numerical model tests using lower drop heights were carried out following the verification and validation of the original CFD models, discussed in Sections 6.4 and 6.5. As described in Sections 4.3.2 and 6.5.2, the resulting wave radiation patterns included higher harmonics that were observed in a consistent manner across both the processed experimental measurements and the various CFD cases, including the inviscid Euler simulations. It is noteworthy that, when hydrostatically at rest, the straight-sided draught of the float measured 157.5mm, as detailed in Figure 4.3. This resulted in the curved base protruding above the free surface, when elevated to the point of release (200mm). One of the purposes of the numerical models tested in this section was to investigate the relationship, if any, between the initial drop height and the magnitudes of these nonlinear components.

An additional objective of these tests was to improve the correlation between the CFD results and the BEM, discussed in Chapter 5. When attempting to validate results from the linear potential flow models, two observations were made. The first was that when external damping conditions were appropriate, WEC excursion evaluations were in close agreement with the experimental measurements, therefore the numerical results for WEC motion were valid. The second observation was that free surface elevation predictions, derived using Impulse Response Functions (IRFs) from WAMIT, were seen to deviate significantly from the validation data, which was characterised by significantly nonlinearities processes, as stated above. By attempting to weaken this nonlinear behaviour through lowering the initial drop height, the extended run of CFD simulations was used to provide an indirect qualitative validation procedure for the potential flow model.

The initial displacement of the WEC in the experiments was $\xi_0^{EXP} = 200 \pm 4.3$mm, and for the CFD work was $\xi_0^{MOD} = 200$mm. Figure 6.20 shows extended CFD results for $\xi_0^{MOD} = (160, 120, 80\text{mm})$ for the normalised free surface elevation at WG-5D, along with the linear results from the potential flow code. A clear reduction in the magnitude of the higher frequency components can be seen with the peaks and troughs generally drifting towards the linear results, and the inflections becoming increasingly flattened out. However, a reduction in ξ_0 to just 40% of its original value still yields differences between the CFD and potential flow results, which are attributable to nonlinear behaviour.

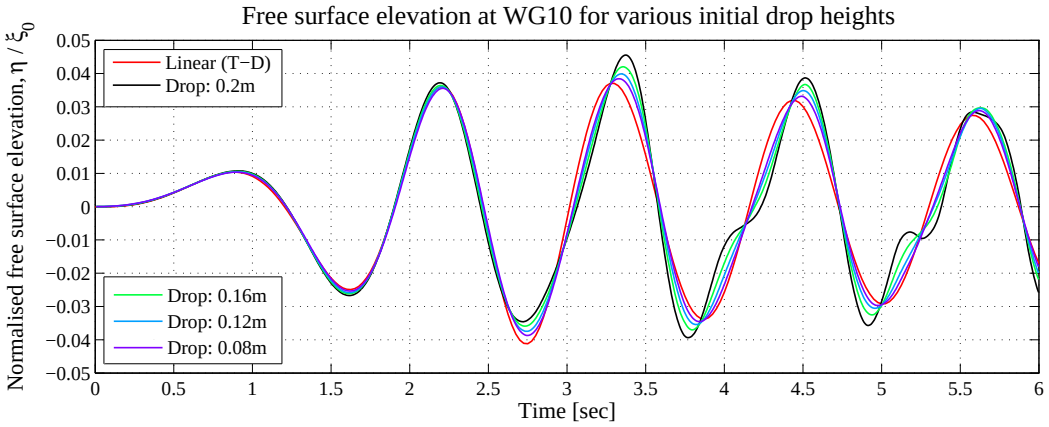

Figure 6.20: Free surface elevation at WG10, comparing CFD results at various drop heights.

6.7 Final comments

The work presented in this chapter focused purely on the numerical evaluations for an isolated WEC case, using the finite volume CFD method. As such, in terms of the primary objectives of this thesis, this represents only a step in the overall process to interpreting nonlinear and viscous effects for a small WEC array. The specific purpose of this chapter, was to outline the rigorous assessment procedure required for developing appropriate CFD solutions to the floating body, free surface problem. This model can then be adapted for application in an array configuration, as discussed in Chapter 7.

The specific objectives stated at the beginning of this chapter have been addressed as follows:

1. Verified and validated numerical modelling results were provided for the sinlge WEC case. For the device motions, the numerical uncertainty was 1.0% and 0.3% due to finite resolution of spatial and temporal discretisations. For the wave elevations these were 7.5% and 1.75% due to space and time resolution.
2. Use was made of RANS, Euler and WECwakes data, to extract the force due directly to viscosity. Mechanical effects were controlled in the numerical model by imposing the measured data upon the moving WEC.
3. Detailed results were interrogated from the CFD model to provide a decomposition of forces which were due to viscous effects: the resulting from shearing of the fluid $F_{3,\tau}$ and from changes in pressure distributions as a result of viscous driven vorticity, $F_{3,p(visc)}$. Both forces were of the same order of magnitude, were nonlinear, and were found not be aligned temporally with respect to one another.
4. An extended model was configured to study variations in drop height, to investigate the nonlinear wave formations identified during the experiments. Although a relationship was identified between the initial height and the strength of the nonlinearities, a fully linear pattern was not obtained from any of the cases studied.

5. A range of difficulties were identified and discussed in order to provide useful guidance where possible. The following issues were successfully resolved: mesh configuration for sustaining waves and removing distortions, numerical ventilation, overset mesh interface distortions due to motion prescription. The following issues were not fully resolved: identification of monotonic convergence for the free surface numerical evaluations.

As the results from this chapter represent an enhancement on the earlier linear BEM results, the following evidence can be provided at this stage:

A The nonlinear wave generation processes around the WEC at the beginning of the decay was replicated successfully using CFD, confirming that the systematic effects are linked to the hydrodynamic problem. It is noteworthy that confirmation was provided that these effects were not caused specifically by viscosity, as both RANS and Euler simulations captured the detail closely. Although the release height of the WEC was linked to the strength of the nonlinear wave components, the additional harmonics were not caused exclusively by the partial exposure of the hemispherical base when it was lifted above the still water level during the experiments.

B The incorporation of viscous effects within the numerical model showed that while force magnitudes were small, the non-negligible effects can be identified over time, particularly in relation to device excursions.

Chapter 7

CFD: Multi-WEC Model

The preceding work described in Chapters 5 and 6 resulted in the development of verified and validated numerical models of the *OneWEC* problem. Progressing from the Boundary Element Method (BEM) to Computational Fluid Dynamics (CFD) allowed the inclusion of nonlinear system behaviour and viscous effects. The final research objective described in Section 1.3 was identified in order to deliver an enhanced approach to Wave Energy Converter (WEC) array modelling, in which nonlinear and viscous effects are accounted for in the array interaction problem. The method for achieving this is to extend the CFD model developed in Chapter 6 to include two, then five WECs. This adopts a well understood approach and accounts for lessons learned from the earlier development of the *OneWEC* system. A number of these issues are described in detail in Appendix C, for the *OneWEC* case.

Results from CFD models of the *TwoWEC* and *FiveWEC* systems are presented in this chapter. Following on from the previous work, the same generic WEC model configuration was adopted for both the decay WEC (primary), and the neighbouring WECs (secondary, initially at resting), as described for the tank tests in Chapter 4. The geometric model constructions for the multi-WEC cases were equivalent to those described for the numerical models in Chapter 6, while meshing and symmetry conditions were specific to each model. The following outlines the discussions provided in this chapter:

- specific multi-WEC objectives,
- analysis matrix for multi-WEC tests,
- model configuration,
- mesh configuration,
- results.

7.1 Introduction

7.1.1 Modelling objectives

The objectives outlined in Section 1.3 have been extended here to set out detailed requirements of the *TwoWEC* and *FiveWEC* CFD models. The specific requirements of the numerical models developed in this chapter have been considered below:

1. To reconfigure previously verified and validated numerical models to include secondary, neighbouring WECs;
2. To deliver validated numerical modelling results for the multi-WEC arrangements, i.e. to accurately capture the interaction effects between neighbouring WECs, and identify the modelling deficiencies in the solution.
3. To relate the nonlinear wave radiation conditions which were identified in Chapter 6 for the *OneWEC* arrangement, to the nonlinear interaction forces extracted from the multi-WEC cases.

7.1.2 Model design & setup

The physical dimensions and geometric configurations of the multi-WEC models were consistent with the equivalent single WEC tests, described in Chapter 6. The following modifications were necessary to accommodate additional WECs.

- The overall domain shape was rectangular, rather than wedge shaped, to allow for the placement of neighbouring WECs along a single common longitudinal axis. With regard to the use of symmetry planes:
  - for the *TwoWEC* model, a single symmetry plane was used, running through the common axis, i.e. through all WECs and posts (50% 180° domain);
  - for the *FiveWEC* model, a second symmetry plane was configured perpendicular to the common axis (25% 90° domain);
- Two independently floating bodies were included in the *TwoWEC* system, governed by the numerical solutions from the Dynamic Floating Body Interaction (DFBI) solver in STAR-CCM+, with both bodies halved through the symmetry plane. For the *FiveWEC* model, three DFBI systems were configured, due to the second symmetry plane. The decay WEC (which was released from height) was represented by one quarter of the original WEC geometry, with the neighbouring WECs represented by halved geometries.
- As configurations of symmetry planes resulted in significantly larger computational domains, the outer boundaries were moved inwards to limit the number of cells. Limited impact on relevant results from the multi-WEC tests were demonstrated when then the domain dimensions were reduced from 18m to 12m, in part due consideration of a shorter test duration.

- Adjacent posts (Post-1B, Post-2B etc.) were included in the domain as wall boundaries in the *TwoWEC* model. This was not possible in other cases where two symmetry planes were used. Table 7.1 provides details of the various post configurations in all tests (including the linear model, for reference).

Table 7.1: Inclusion of posts in the main simulation models (marked ●). See Figure 4.7 for post references.

		Symmetry plane separation	Post 1a	Post 1b	Post 2a	Post 2b	Post 3a	Post 3b	Post 4a	Post 4b	Post 5a	Post 5b
BEM	*OneWEC*	90°	-	-	-	-	-	-	-	-	-	-
	OneWEC-a	90°	-	-	-	-	-	-	-	-	●	-
	OneWEC-ab	90°	-	-	-	-	-	-	-	-	●	●
	TwoWEC-a-b	180°	-	-	-	-	-	-	●	●	●	●
	FiveWEC-a-b	180°	●	●	●	●	●	●	●	●	●	●
CFD	*OneWEC*	5°	-	-	-	-	-	-	-	-	●[1]	-
	OneWEC-a	90°	-	-	-	-	-	-	-	-	●	-
	OneWEC-ab	180°	-	-	-	-	-	-	-	-	●	●
	TwoWEC-a-b	180°	-	-	-	-	-	-	●	●	●	●
	FiveWEC-a	90°	●	-	●	-	●	-	●	-	●	-

[1] Circular approximation of post included.

7.1.3 Analysis matrix

Rather than test the sensitivity of the model behaviour to viscous effects and friction damping, the model configurations for the multi-WEC cases were developed in order to provide validated results for array interaction forces, the simplest case being for just two WECs.

A combination of the two body motion methods described in Section 6.1.3 was used: the Imposed Motion (*IM*) and Fluid Structure Interaction (*FSI*) cases. The decay WEC which was raised and dropped was configured using (*IM*), based on modified functions which suited each particular array layout. Avoiding direct simulation of the decay WEC motions in this way (i.e. avoiding FSI) ensured that the modelling errors studied in Chapter 6 were not carried through to the interaction models. For more general studies where different scenarios may be of interest, however, it would ultimately be greatest interest to model a fully FSI solution.

The neighbouring WECs were modelled using the *FSI* method, in order to investigate the previ-

ously untested situation, where the neighbouring WECs oscillate in response to the radiated/diffracted wave field, albeit through a very limited amplitude range ($\xi/\xi_0 < 0.05$). As in Chapter 6, the motivation for this is to provide an interpretation for mechanical dissipation in the systems, in this case for very small motion amplitudes. An added complexity for this array case, or more specifically the diffraction case (*OneWEC* being radiation only), is that there are now surge forces present. This additional force interacts with the bearing system used in the physical model. Between carrying out single-WEC tests, multi-WEC tests, FSI and IM tests, it was possible to develop an understanding of the nonlinear fiction forces generated specifically by interaction between the devices.

7.2 Solver configuration

The configuration of the various solvers for the multi-WEC models was largely as described in Section 6.2.2, for the *OneWEC* case. The following differences applied to the *TwoWEC* and *FiveWEC* cases.

- The Volume Of Fluid (VOF) wave damping function used at the perimeter of the domain was 5m.
- Where FSI type evaluations were required for either decay WEC or neighbouring WECs, the body mass assigned to each floating body was appropriate for the symmetry conditions used.
- The predefined imposed motion (*IM*) function was based on Equation 4.1 as before; however, additional components were used to recreate the appropriate motion paths for the decaying WEC. Further details relating to the imposed motion functions for the primary decaying WEC are provided in Section 4.4 and Appendix B (Table B.1).
- The secondary neighbouring WECs which were included in these studies were all configured as independent bodies, each governed by their own FSI evaluations.

7.3 Mesh

A completely different approach was taken to the design of the mesh for the multi-WEC array models. In contrast to the pseudo-2-dimensional design of the mesh in Chapter 6, the fully 3-dimensional nature of the array problem required a wide angular separation of the symmetry planes, in order to model omnidirectional wave radiation and diffraction. Due to the significant increase to the volume of the numerical domain, the resolution of the mesh was rationalised considerably, whilst the boundaries of the domain were also reconfigured.

The meshes used for the array models – *TwoWEC-ab* and *FiveWEC-a*, are shown in Figure 7.1. A total of 3.51M cells were used for the *TwoWEC-ab* model, with 3.74M used for the *FiveWEC-a* model.

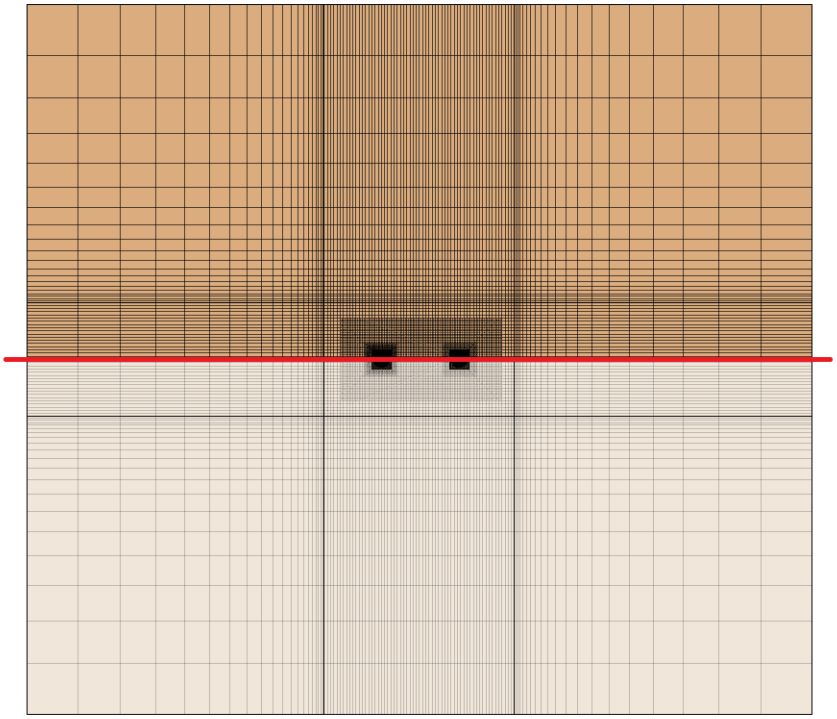

(a) *TwoWEC* case (half domain)

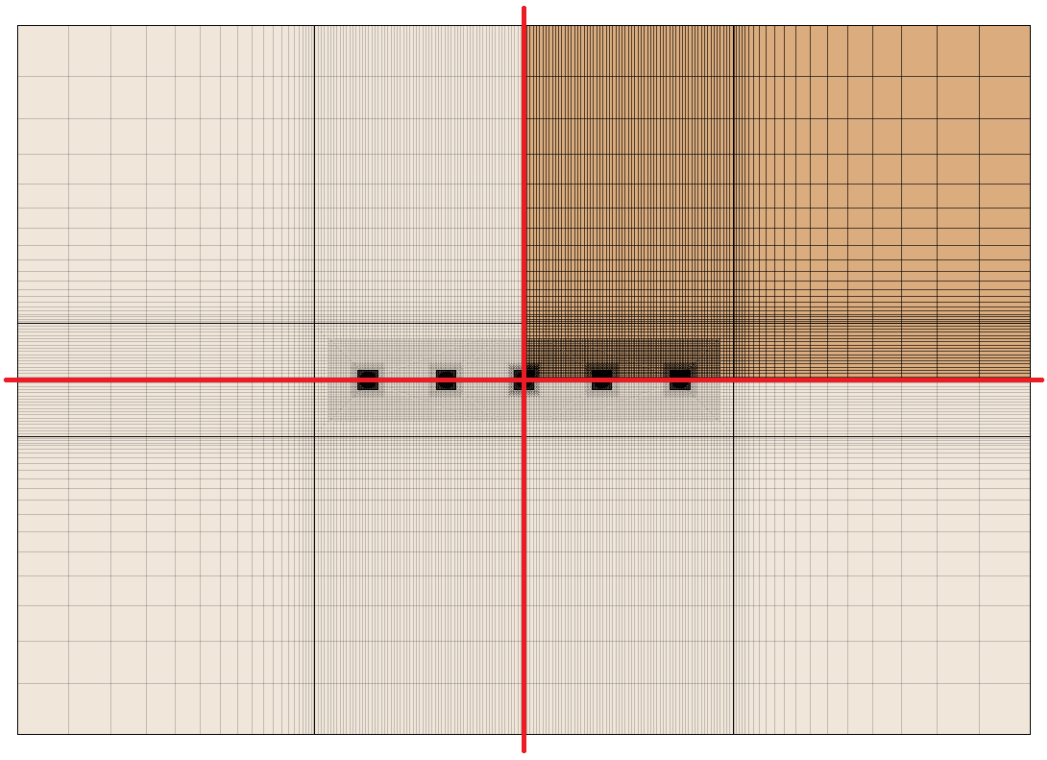

(b) *FiveWEC* case (quarter domain)

Figure 7.1: Sections taken through the free surface, for the *TwoWEC* and *FiveWEC* meshes (CFD model). Symmetry is indicated conceptually, to show the full basin.

The general approach to the mesh design was to retain the Cartesian characteristics of the mesh as far as was practical. This avoided non-trivial complications associated with developing an adequate radial mesh, and allowed from much greater flexibility when establishing adequate levels of refinement. Furthermore, the design of the overset mesh interfaces could be carefully considered, in the manner described in Section 6.3.2. The final meshes used for the array models featured bands of refinement across the entire domain, shown horizontally and vertically across the plan view in Figure 7.1.

The changes described above had relatively significant implications with regard to solution quality, particularly for later spells in the decay test. The lack of mesh refinement and treatment of boundaries caused the most significant issues. This included loss of fluid mass to outside the domain, which is discussed in Section 7.4.

7.3.1 Free surface

The same design principles and challenges discussed in Chapter 6 applied to the design of the multi-WEC cases. The mesh used, however, was coarser than the highly resolved single-WEC cases. This was necessary in order to reduce the number of cells to a manageable quantity for the much larger domain. The refinement subregions used to concentrate the smallest cell sizes were designed to capture accurately the free surface behaviour immediately around the WECs, including the area in between the WECs, as seen in Figure 7.2. The free surface cell sizes were configured to coarsen rapidly, moving outward in the other directions.

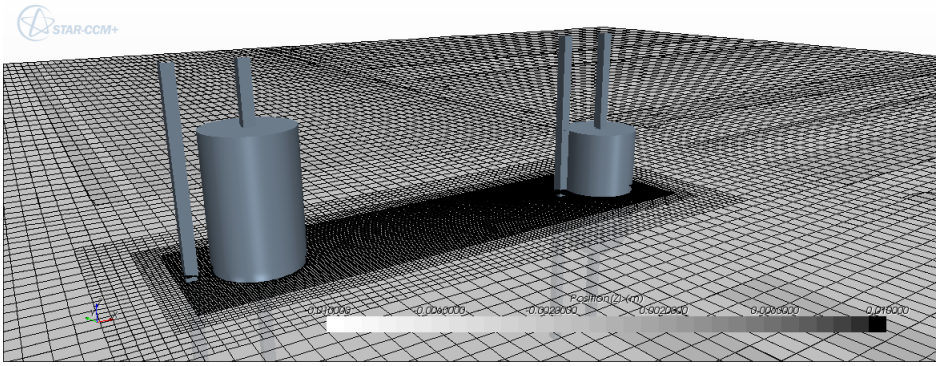

Figure 7.2: Symmetry is indicated conceptually, to show the full basin.

7.3.2 Overset mesh interface

For each of the WECs, an independent overset mesh was necessary, resulting in a total of four computational regions for the simulations involving five WECs, which included the background region and allowed for symmetry. The same principles were adopted from the *OneWEC* cases, to design how the overset mesh regions should interface with the background region, as described in Section 6.3.2. An additional consideration for the models presented in this chapter (specifically the *TwoWEC* cases) was the presence of Post-4B and Post-5B. The overset mesh region was formed using a square section cylinder, and was sized to avoid any interference with the adjacent posts.

The background mesh was configured to suit the swept volume of each specific WEC, in order to avoid unnecessary refinement of the mesh around WECs with small amplitude motions. This is reflected in Figure 7.3 which shows the decay WEC on the left, having a stroke of ~0.38m, and the limited refinement around the neighbouring WEC, which in response had a peak stroke of approximately 0.04m (for undamped numerical case). As was described in Section 6.3.2, all background cells which were 'behind' overset meshes were configured to have relatively coarse refinement.

7.3.3 Boundary layer

The same principles were applied to the design of the boundary layer mesh, as was discussed in Section 6.3.3 for the single WEC cases. The following describes the boundary layer configuration for the multi-WEC cases:

1. Number of prism layer cells = 18;
2. Prism layer stretching ratio = 1.36;
3. Total prism layer thickness = 8mm.

Using this configuration, the innermost cell dimension was $y = 0.0114$mm. This ensured that the boundary layer was fully resolved for all flow conditions, during the transient analysis. The outer cells in the boundary layer prism layer were configured to ensure that an acceptable transition was achieved between the surface wrapped cells and the purely Cartesian bulk region just beyond the prism layer.

7.3.4 Damping boundary

The perimeter cells were configured to ensure that the predominant wavelength was suitably damped ($\lambda_0 \approx 2$m), by spacing computational nodes half a wavelength apart. This method of assisted diffusion was accompanied by the in-built numerical VOF wave damping function within

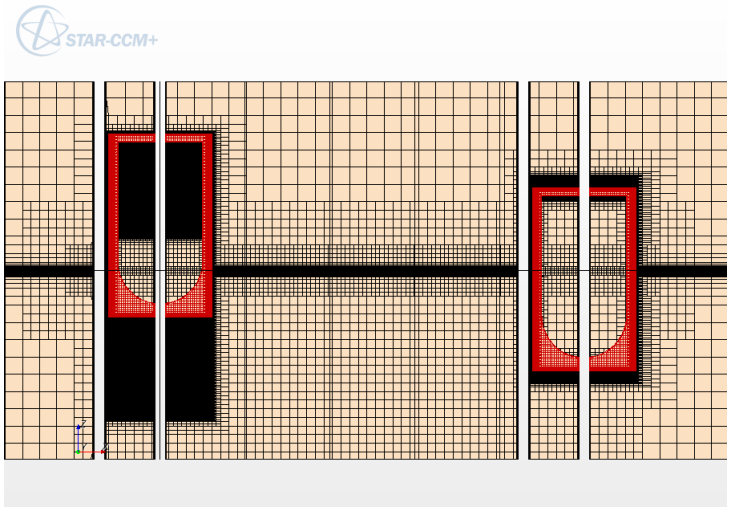

Figure 7.3: Section of mesh used for the *TwoWEC* CFD cases, truncated at either side. Two overset meshes are indicated in red.

STAR-CCM+. Cells were configured to expand gradually from 32mm to 1m in the horizontal orientation, over a distance of 6m. No significant reflections from mesh transitions back to the interior region were observed due to this configuration as stretching of the mesh was sufficiently smooth and gradual.

7.4 Results – OneWEC, 90° domain

Tests for the revised domain for the multi-WEC problems were carried out to identify issues and highlight limitations with the array models. A test using the *OneWEC-a* case was arranged using a 3D domain (shown previously in Figure 7.1b), which was suitable for the *FiveWEC* model. This featured two symmetry planes, separated by 90°, and had a region of higher resolution mesh within the vicinity of the WECs, up to around 4m from the origin (the axis of the decay WEC). The arrangement used for the test case is shown in Figure 7.4, which also identifies wave gauge locations at 5D separation from the origin. Similar details are provided for 10D and 14D separation, in Figure 7.6 and Figure 7.8 respectively.

7.4.1 Free surface elevation

Figure 7.5a shows wave gauge measurements taken at *WG-5D-x* and *WG-5D-y*. Both gauges were 5D away from the WEC, and were positioned along the *x*- and *y-axis* respectively. Despite the coarsening of the mesh in the *y* direction after a relatively short distance, the overall amplitudes were sustained within a range close to that of the results recorded along the *x* direction. The disparity between the results from the two gauges is clear, however, in terms of how well

the higher harmonics were captured. Figure 7.5b shows a degree of consistency between the nonlinear behaviour for the 90° domain case, for the wedge domain case (Chapter 6) and the *WECwakes* results (Chapter 4). Two issues are clear from these results:

1. Numerical damping is present, causing degradation of the wave gauge results over time.
2. There is a net downward movement of the free surface shown with time. This was an undesirable numerical effect of the model arrangement which also affected the remainder of the array studies. This is discussed further in the next sub-section.

Figures 7.7 and 7.9 show results from 10D and 14D positions, which again showed results for the gauges located within the finer mesh region (*WG-10-x* and *WG-10-y*) which were reasonably consistent with the experiments. In the y direction, towards the coarser mesh refinement, the results degraded significantly by 10D, and were severely damped by 14D, as indented in the design of the mesh. Once again, however, the same downward movement of the free surface was observed at 10D and 14D separation distances, which is discussed in more detail below.

Finally, a direct comparison is provided in Figure 7.10 between the wedge-shaped domain used in Chapter 6, and the 90° domain with two symmetry planes, at wave gauges: 1D, 2D, 3D and 4D. Again, both the numerical damping effect and the net downward movement of the free surface are clearly visible. The same nonlinear components are, however, represented in both. These gauge locations are also examined in Section 7.5.1 for effects associated with the addition of a neighbouring WEC.

Mass loss from the numerical domain

Persistent issues surrounding the drop in free surface levels comprised one of the significant shortcomings of the VOF method presented here. This remained unresolved in the present work, due to conflicting requirements to suppress the outgoing waves and conserve mass appropriately to preserve the physical integrity of the model. Mass loss from this type of model tends to be associated with numerical diffusion, and from nonphysical interactions with open outlet boundaries. Both of these mechanisms were employed in order to damp outward moving waves, which was a necessary requirement from the outset. This has been cited as an important area of future work in Chapter 8.

It is worth commenting on the physical magnitude of the effects reported in Figures 7.5, 7.7 and 7.9. Whilst the relative magnitude remains an ongoing concern, one of the main challenges presented by the highly sensitive decay problem was the physical scale of the wave amplitudes and motion responses. The largest residual shown in the above results measured $\eta/\xi_0 = 0.0082$ (at *WG-14D*, $t/T_0 = 8.3$), i.e. 1.6mm, which was less than the thickness of the free surface cells.

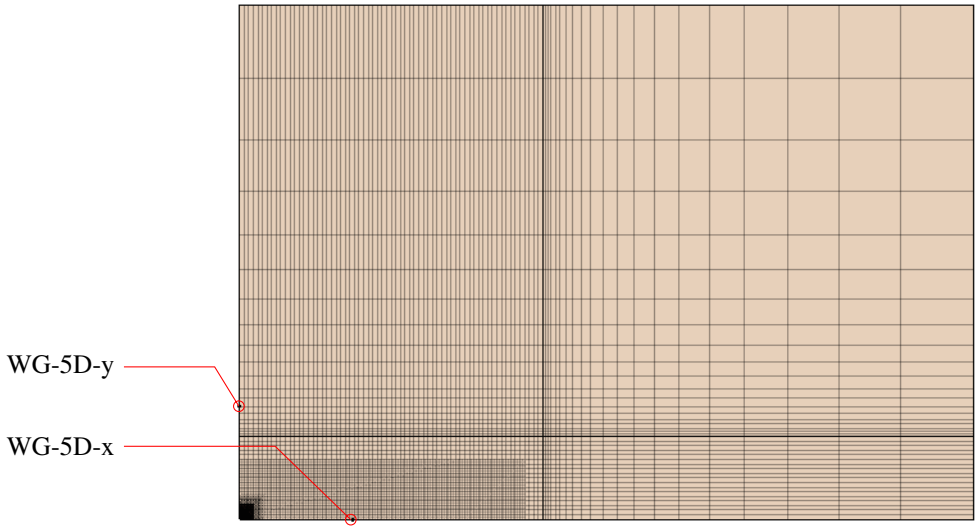

Figure 7.4: Plan view of the free surface mesh for the 90° domain, for the *OneWEC-a* test.

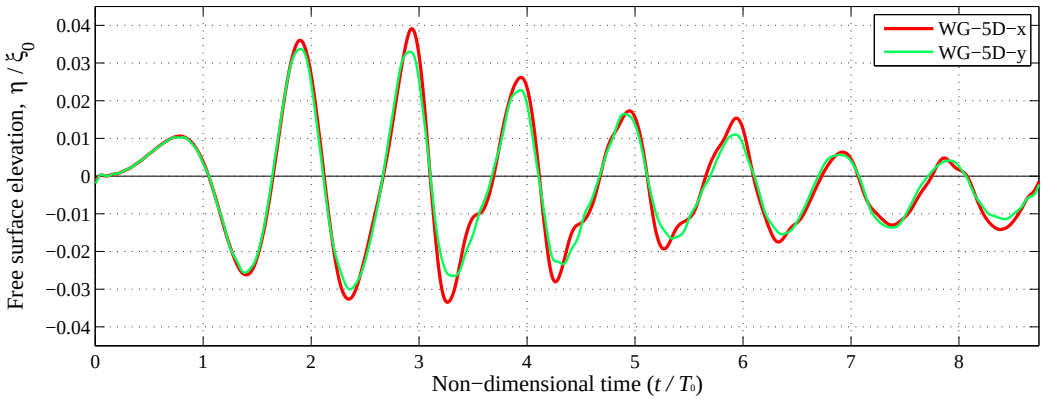

(a) Comparison between *WG-5D-x* and *WG-5D-y*, for the 90° domain

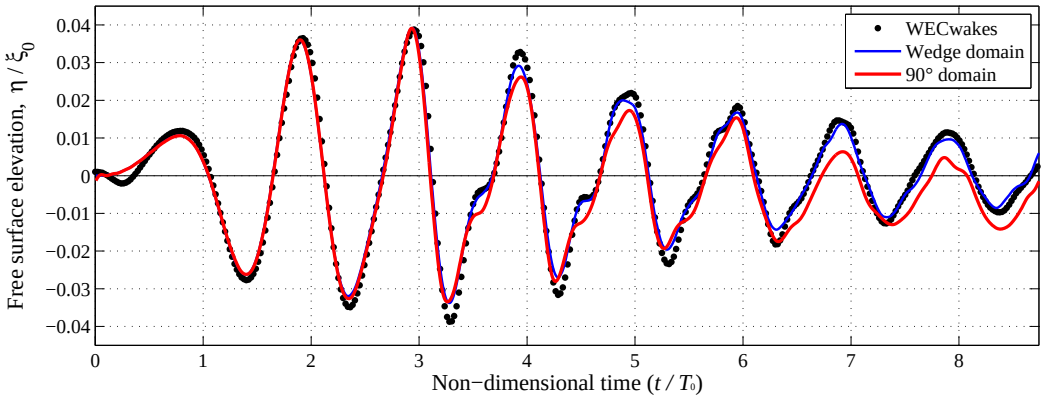

(b) Comparison of the 90° domain, wedge domain (as used in Chapter 6), and WECwakes data, at *WG-5D-x*

Figure 7.5: Free surface elevation time series at 5D, using the 90° domain.

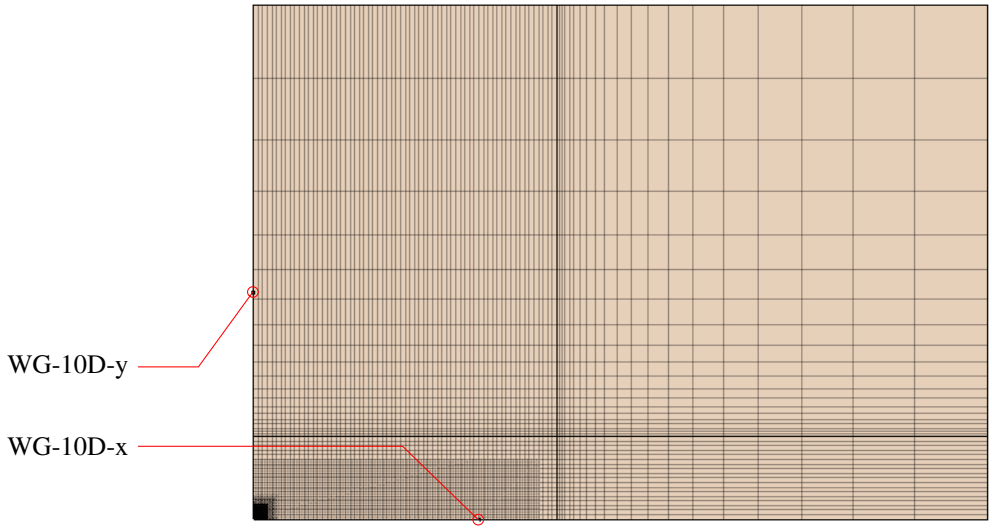

Figure 7.6: Plan view of the free surface mesh for the 90° domain, for the *OneWEC-a* test.

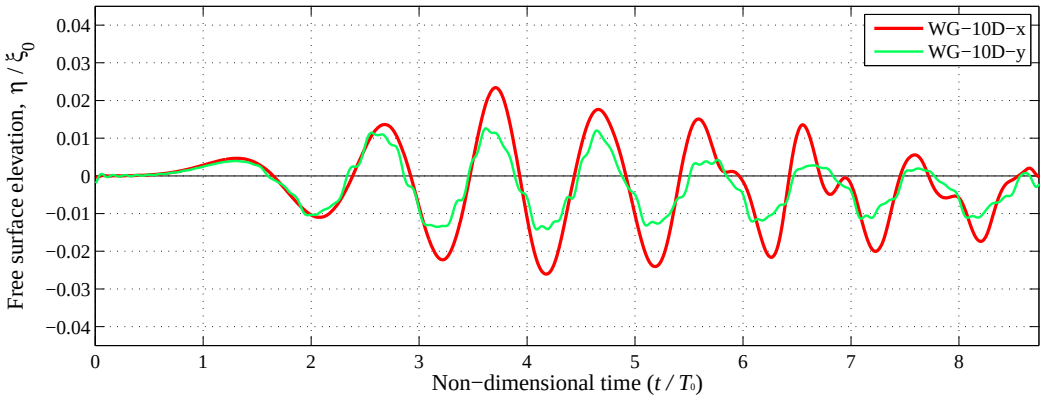

(a) Comparison between *WG-10D-x* and *WG-10D-y*, for the 90° domain

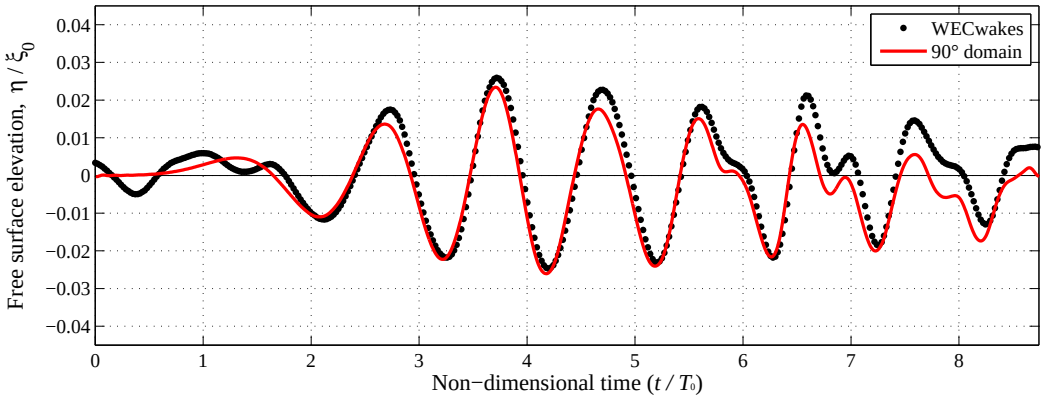

(b) Comparison of results for the 90° domain, and experimental measurements, at *WG-10D-x*

Figure 7.7: Free surface elevation time series at 10D, using the 90° domain.

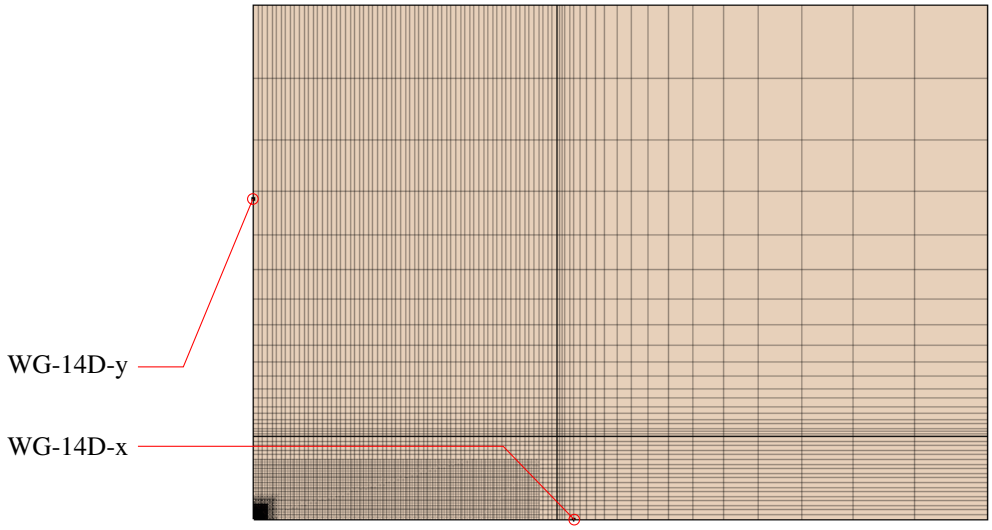

Figure 7.8: Plan view of the free surface mesh for the 90° domain, for the *OneWEC-a* test.

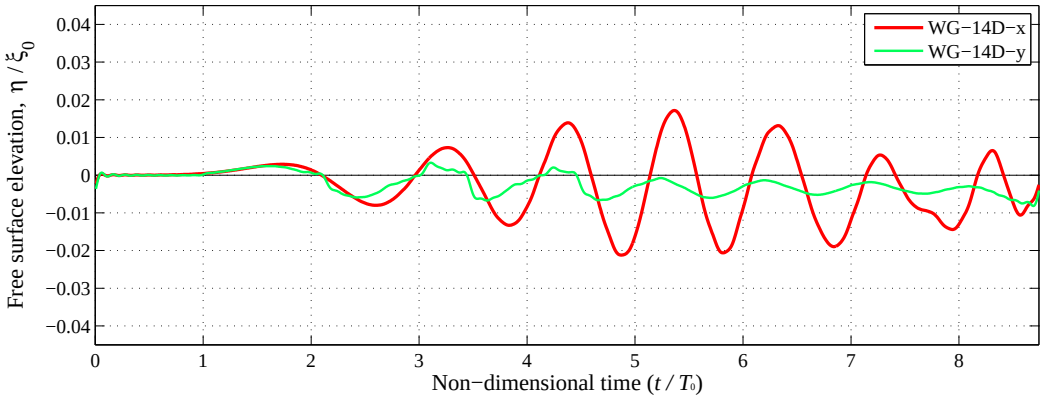

(a) Comparison between *WG-14D-x* and *WG-14D-y*, for the 90° domain

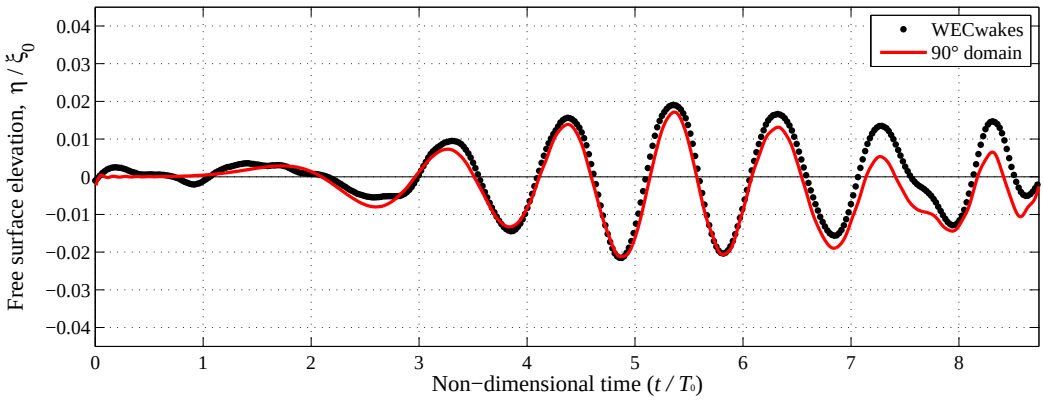

(b) Comparison of results for the 90° domain, and experimental measurements, at *WG-14D-x*

Figure 7.9: Free surface elevation time series at 14D, using the 90° domain.

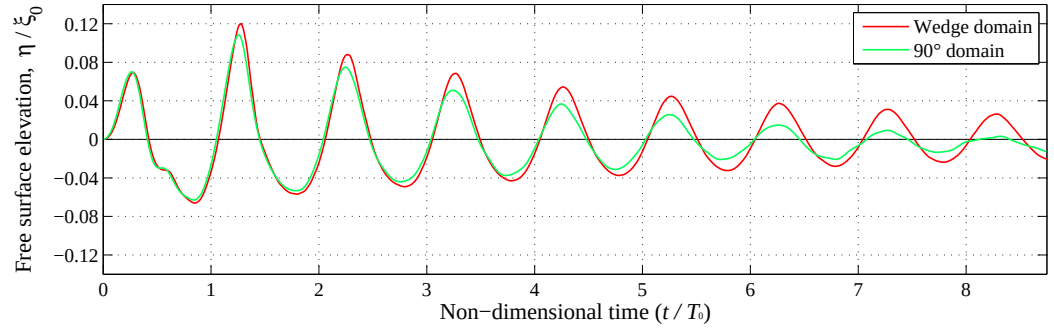

(a) *WG-1D*

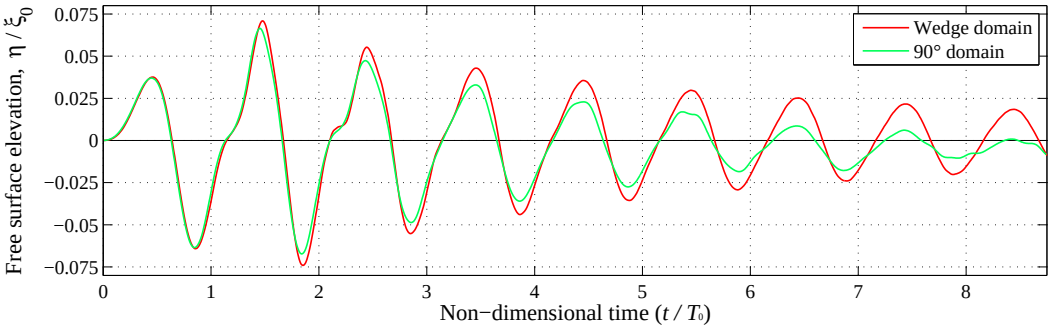

(b) *WG-2D*

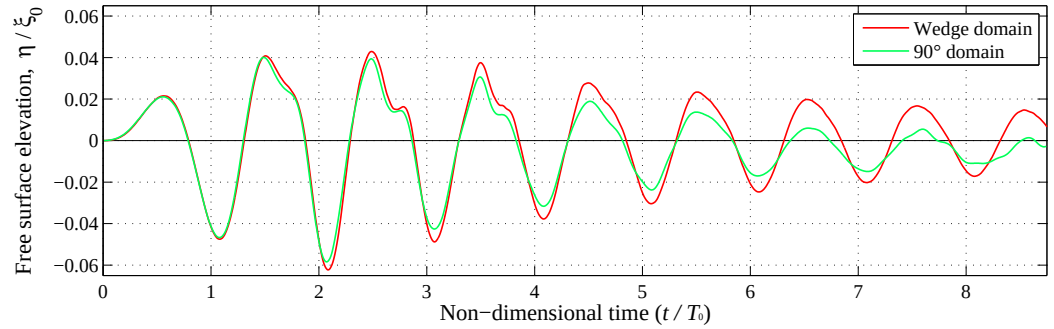

(c) *WG-3D*

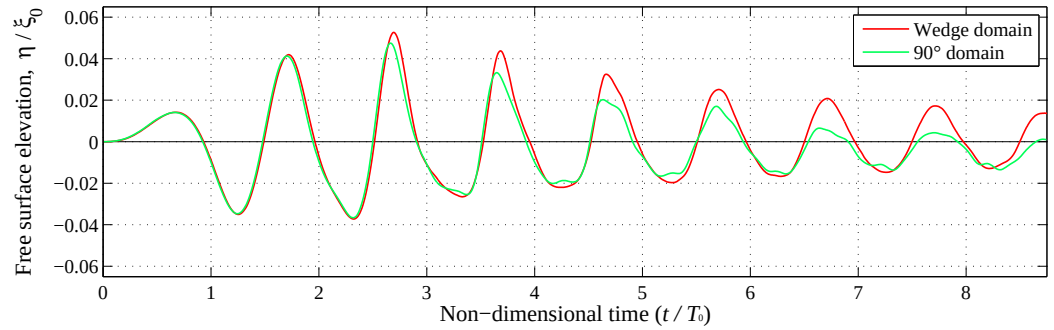

(d) *WG-4D*

Figure 7.10: Free surface elevation time series comparisons between the CFD results for the wedge shaped domain and 90° domain.

7.5 Results – TwoWEC

7.5.1 Excursion

The excursions of the neighbouring WEC are examined here to interrogate primary and secondary wave radiation effects. These effects are defined here as follows:

1. *Primary wave radiation:* waves generated by the decay WEC, which interact with the neighbouring WEC(s);
2. *Secondary wave radiation:* waves generated by the neighbouring WEC(s) as a result of induced motions, re-radiated to neighbouring WECs (including the decay WEC).

As previously for the *TwoWEC* case, primary and secondary wave radiation effects were present, as the neighbouring WEC responded to the decay WEC motions. Using CFD, the model described here was configured as follows:

1. Decay WEC: Imposed Motion (*IM*) was applied, using a function specifically developed for the *TwoWEC* case, allowing for secondary wave radiation effects on the decay WEC;
2. Neighbouring WEC (5D spacing): Fluid-Structure Interaction (*FSI*) was evaluated, to understand 'primary wave radiation' effects.

As the decay WEC motion was based on the controlled function – *IM*, which mimicked the measured motions from the experiments (as described in Section 4.4), the secondary wave radiation effects were not examined here using CFD. These secondary effects were found to be small in magnitude, and were reliably evaluated using the BEM solver and time-domain code (see Section 5.5.1). Although not studied in detail, these effects were inherent in the motion functions which were used to replicate the measure motions of the experimental models.

The neighbouring WEC motions seen in Figure 7.11 demonstrate measurable primary wave radiation effects. For the idealised models (both time-domain and CFD), the neighbouring WEC positioned at 5D experienced peak amplitudes around of $\xi/\xi_0 = 0.1$ due specifically to wave radiation, i.e. 10% of the decay WEC initial position. In the experiments, however, peak amplitudes were of the order $\xi/\xi_0 = 0.03$*, which was attributed to significant damping effects at small excursion amplitudes, considered to be caused by Coulomb damping and stiction.

The undamped CFD and time-domain results generally compared well in Figure 7.11a. Evidence of the effects found in Section 7.4.1 is visible, with a gradual downward trend in WEC position resulting from the drop in wave level over time. In addition to this effect, the Euler result also recorded a larger amplitude of motion. As both are inviscid, the differences are due to the following:

1. Nonlinear modelling discrepancies, other than viscous effects;
2. Numerical discrepancies between the time-domain model and CFD.

---

*These data were not available for the *TwoWEC* case, but can be inferred from the results shown in Figure 5.14a for the *FiveWEC* case.

The effects due to viscosity are shown in Figure 7.11b, which reduced amplitudes by approximately 1% per oscillation.

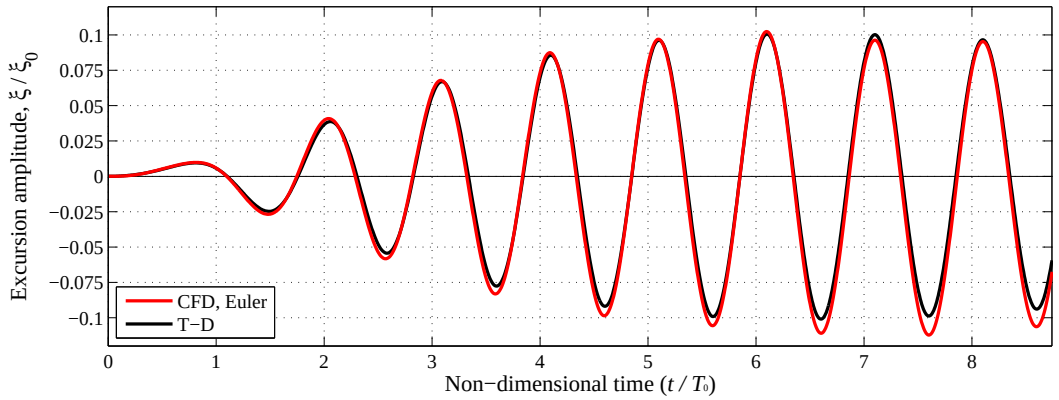

(a) Nonlinear effects on excursion amplitude: Time-domain (potential flow) and Euler CFD results

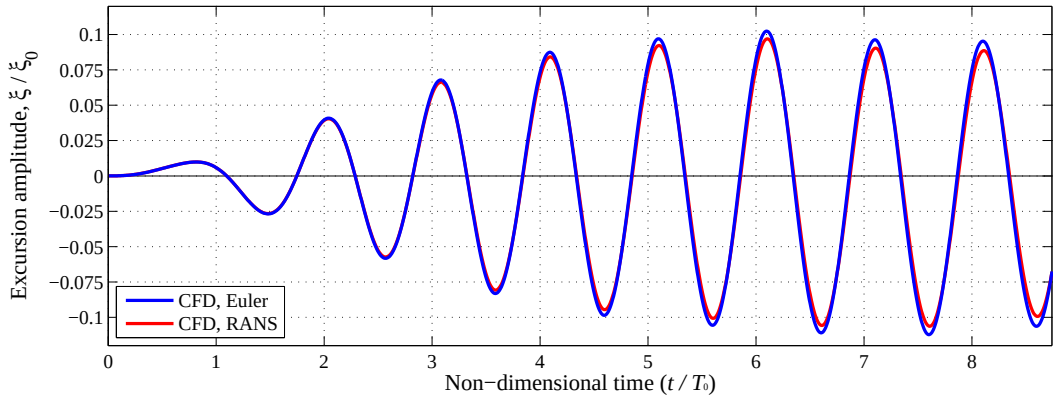

(b) Viscous effects on excursion amplitude: Euler and RANS CFD results

Figure 7.11: Motions of the neighbouring WEC for (*TwoWEC* case, neighbouring WEC undamped), using the same imposed motion for both time-domain model and CFD.

7.5.2 Free surface elevation

Wave gauge evaluations are provided for the region between the two WECs: at 1D, 2D, 3D and 4D in Figure 7.12. The comparison between the *OneWEC-a* and *TwoWEC-ab* cases shows additional wave components due to diffraction and radiation associated with the neighbouring WEC, and additional posts. *WG-3D* and *WG-4D* feature the strongest of these effects, which include increased peakedness and an apparent drift in phase (particularly *WG-4D*). Both of these effects are due to superposition of the different wave components. At *WG-1D* and *WG-2D* these are less prominent, appearing as relatively minor effects at later stages in the decay.

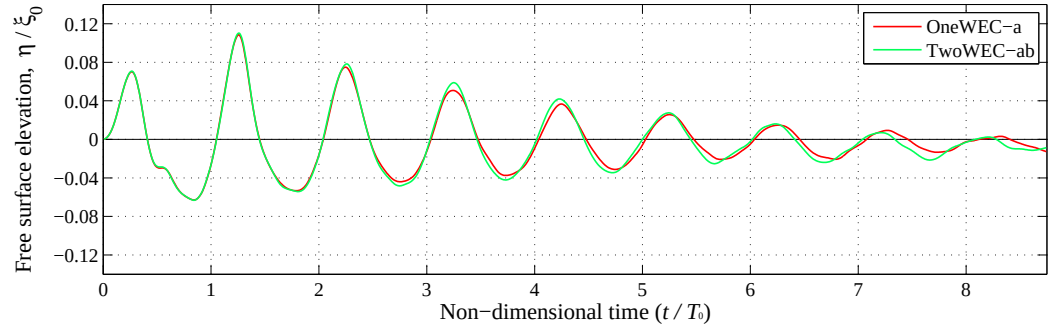

(a) *WG-1D*

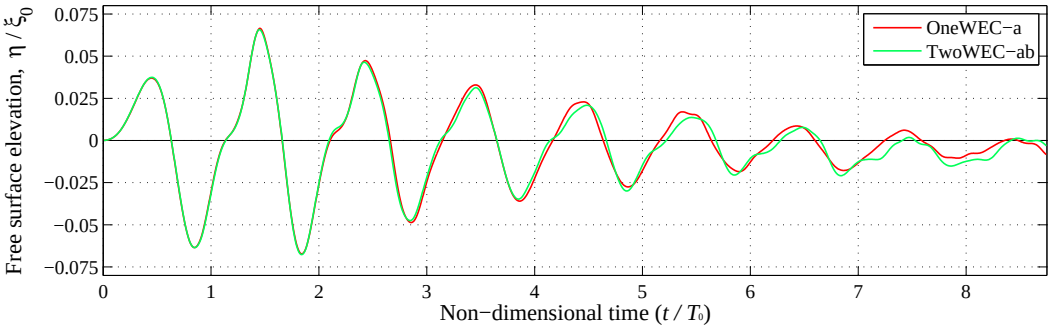

(b) *WG-2D*

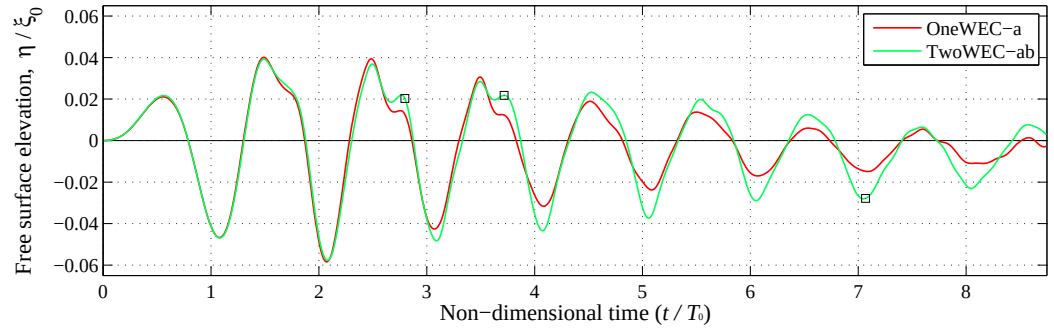

(c) *WG-3D*

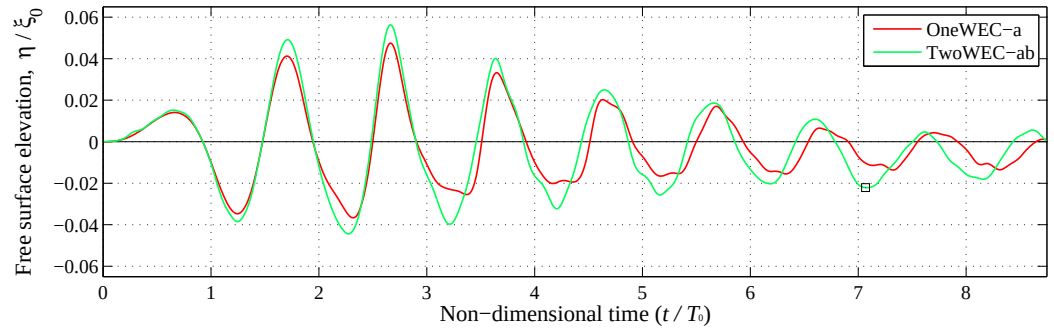

(d) *WG-4D*

Figure 7.12: Free surface elevations comparisons between the CFD cases: *OneWEC-a* and *TwoWEC-ab*. Markers (□) correspond to contour plots: Figures 7.13, 7.14 and 7.15.

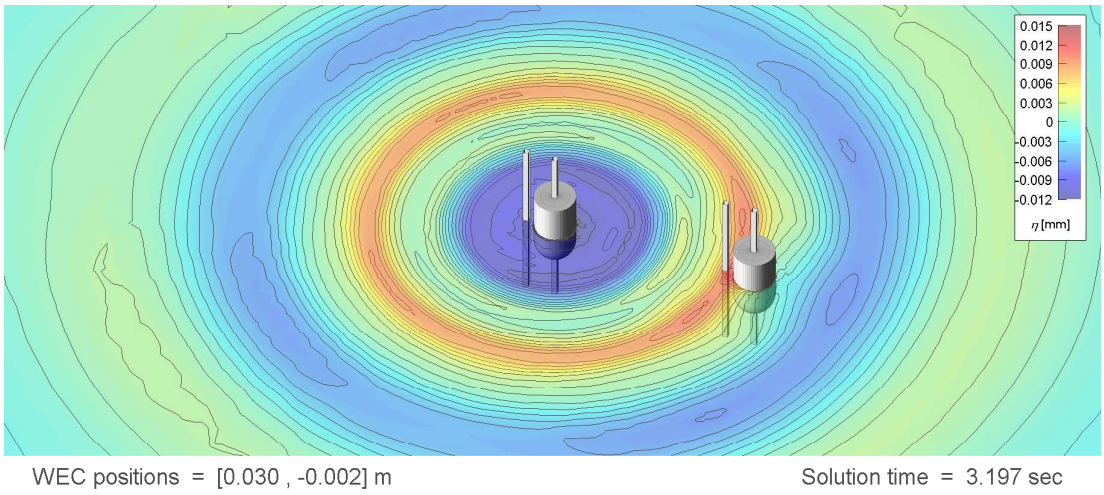

(a) Free surface elevation (contours: 1mm separation)

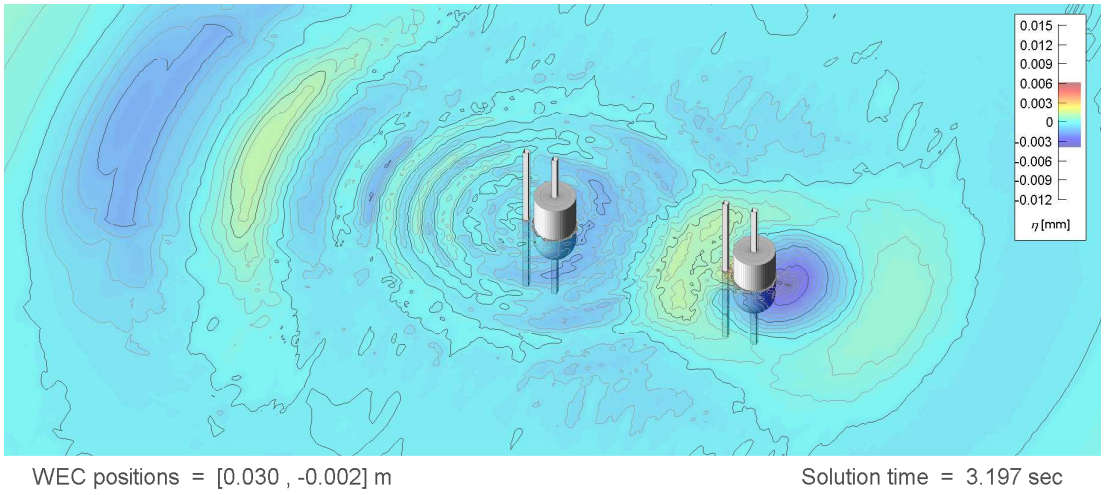

(b) Residual effects due to the neighbouring WEC and the adjacent posts (contours: 0.25mm separation)

Figure 7.13: Free surface elevations due for the *TwoWEC-ab* case, at $t/T_0 = 2.80$. The results have been mirrored at the symmetry planes in order to visualise the entire domain.

Corresponding free surface contour plots are provided in Figures 7.13, 7.14 and 7.15, showing selected instantaneous conditions which correspond to features in Figures 7.12c and 7.12d (marked: □). Subfigures 7.13b, 7.14b and 7.15b show residual effects between the *OneWEC-a* and *TwoWEC-ab* cases. With the cause of these changes being attributed to the additional structures in the basin (the moving neighbouring WEC and the stationary posts: *Post-4A*, *Post-4B* and *Post-5B*), the additional processes are due to wave radiation and diffraction.

The local effects from diffraction around *Post-5B* (farthest to the left) are clearest in Figure 7.13b, which form a radial pattern centred around the post. These waves were measured consistently at 0.2267m wavelength, at a frequency exactly three times the fundamental frequency of the decay. This observation is closely linked to the earlier discussion regarding higher

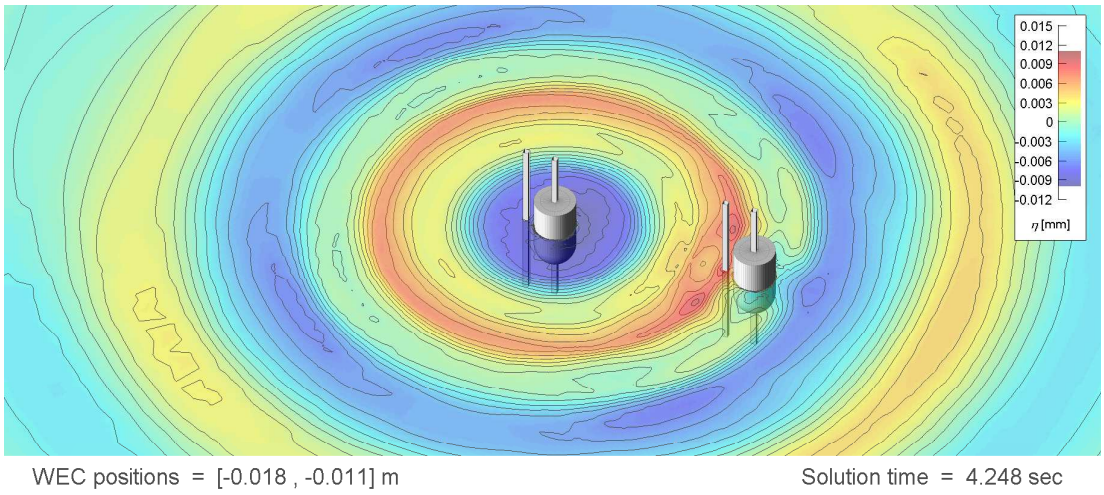

(a) Free surface elevation (contours: 1mm separation)

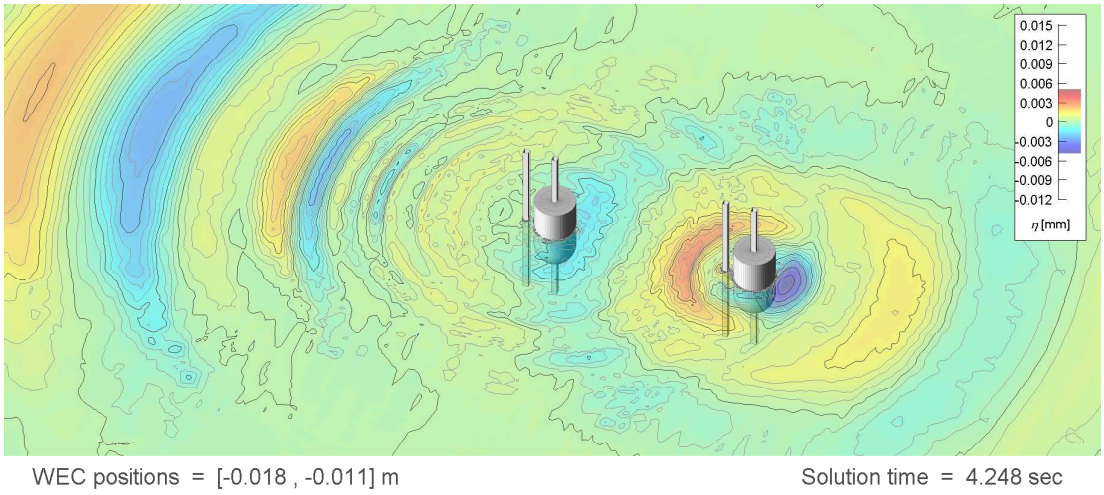

(b) Residual effects due to the neighbouring WEC and the adjacent posts (contours: 0.25mm separation)

Figure 7.14: Free surface elevations due for the *TwoWEC-ab* case, at $t/T_0 = 3.72$. The results have been mirrored at the symmetry planes in order to visualise the entire domain.

frequency components. Within the experiments, *Post-5B* was present in all decay tests. The above results imply that this post contributed to the strength of the third harmonic, recorded at *WG-5D* and beyond, and may have been the principal cause for the occurrence of this frequency. Nonetheless, the stronger second harmonic component was still recreated in the *OneWEC* CFD studies in Chapter 6, which omitted *Post-5B*.

Wave diffraction and radiation around the neighbouring WEC can be seen in Figures 7.14b and Figure 7.15b respectively. Around *WG-3D* and *WG-4D* (also see Figure 7.12), the two time instants show relatively large crests and troughs associated directly with the neighbouring WEC. Whilst these effects are clearly represented, the results still suffer from uneven degradation away from the refined core of the domain.

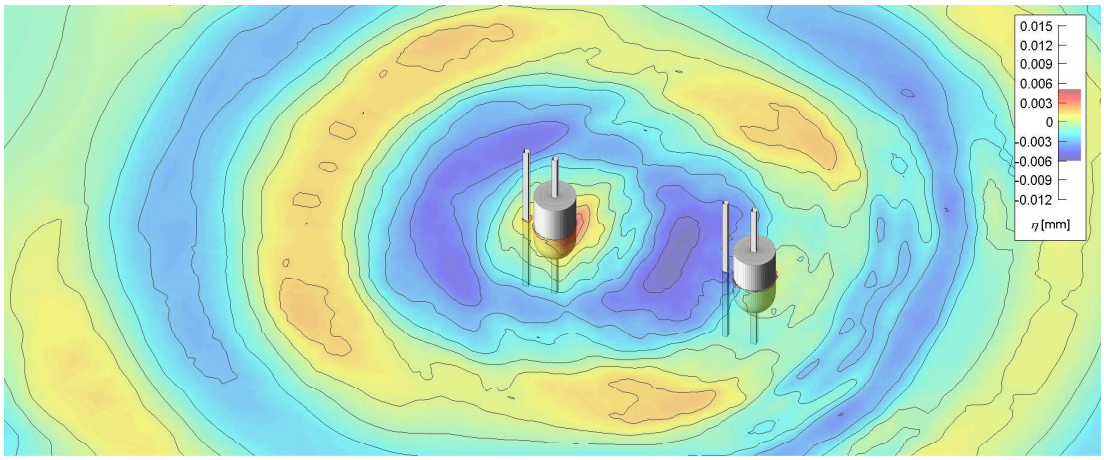

(a) Free surface elevation (contours: 1mm separation)

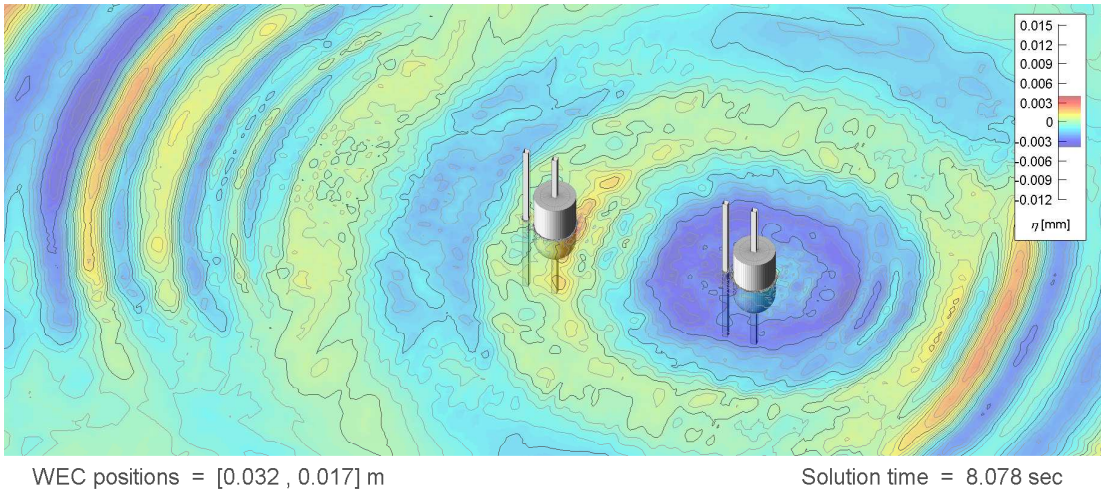

(b) Residual effects due to the neighbouring WEC and the adjacent posts (contours: 0.25mm separation)

Figure 7.15: Free surface elevations due for the *TwoWEC-ab* case, at $t/T_0 = 7.07$. The results have been mirrored at the symmetry planes in order to visualise the entire domain.

7.5.3 Surge forces

Figure 7.16 shows the surge force acting on the neighbouring WEC (WEC-4), due to the motion of the decay WEC (WEC-5). For the filtered and processed WECwakes measurements (see Chapter 5), forces from both upper and lower wave gauges were combined to give a total surge force acting on the WEC. The potential flow derived results from Chapter 5 are provided in Figure 7.16a, followed by the improved non-linear CFD solution in Figure 7.16b. While the linear potential flow results are reasonably well represented in terms of phase, rate of decay and general amplitude trends, the missing non-linear components result in reduced peak forces.

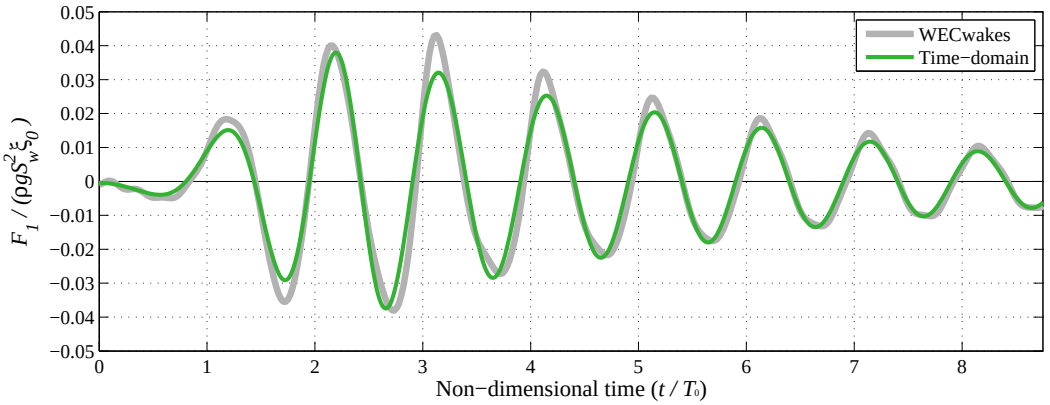

(a) Time-domain (potential flow) result

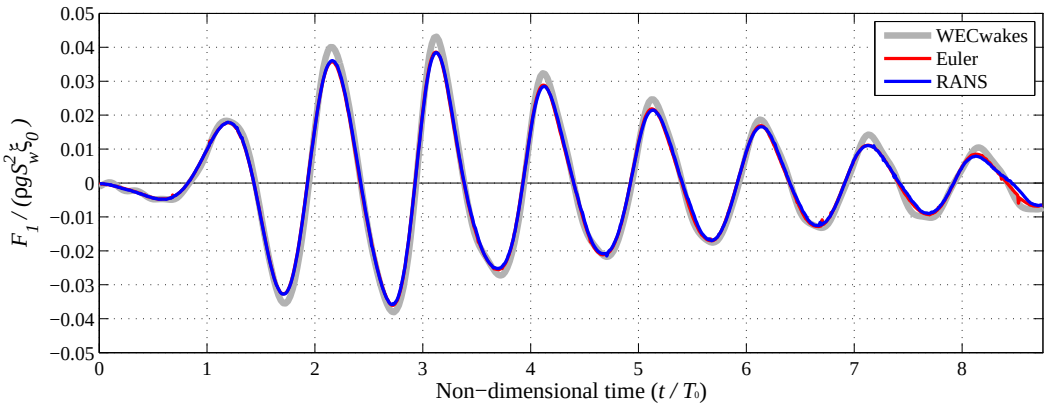

(b) CFD results: Euler and RANS

Figure 7.16: Surge force acting on the neighbouring WEC during the *TwoWEC* CFD analysis.

The Euler and RANS results in Figure 7.16b show very close agreement with the experiments, although peak values were slightly reduced. Discrepancies for all three cases (time-domain, Euler and RANS) are summarised in Figure 7.17. While the force magnitude remained relatively high during the period $2 < t/T_0 < 6.1$, the predicted force using the Euler and RANS solvers were within the range 10-13%. During the same period, the time-domain results were underestimated by as much as 25%, due to the omission of higher frequency effects. With respect to the negative forces (i.e. forces directed towards the decay WEC), the discrepancies were generally smaller for both time-domain and CFD results, and included instances where the computed force from the time-domain model was higher than the measured force.

It was not possible to draw any relevant conclusions from the comparison of surge forces between the Euler and RANS CFD cases, as the effects were too small. Evidence of more distinct behaviour was noted at later stages in the decay ($t/T_0 > 6.1$); however, the solution was known to degrade during these later stages.

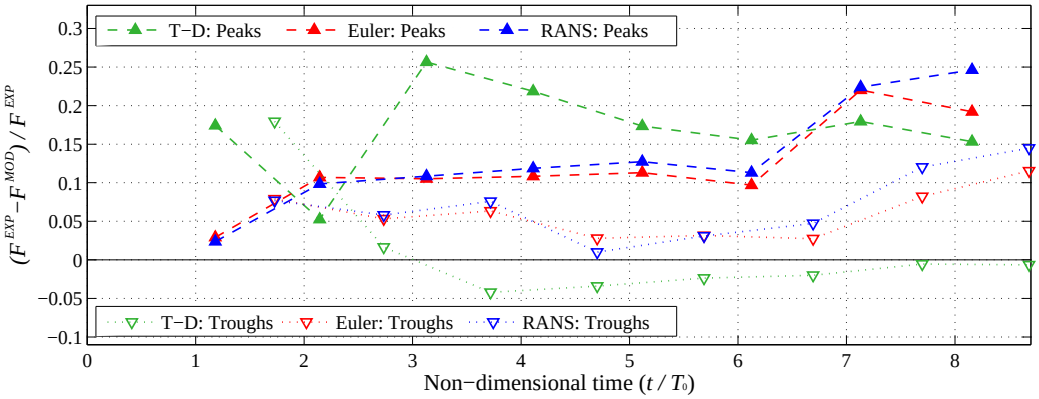

Figure 7.17: Normalised residuals for the surge force between time-domain model and Euler / RANS CFD cases.

7.6 Results – FiveWEC

Body motions for the *FiveWEC* models presented below were configured as follows:

1. The appropriate *IM* function (see Section 4.4) was used for the decay WEC (*WEC-3*);
2. All remaining neighbouring WECs (*WEC-1*, *WEC-2*, *WEC-4* and *WEC-5*) were configured with the FSI solver.

7.6.1 Excursion

It was not of interest to examine the decay WEC here, because the motion was imposed. Euler and RANS CFD solutions are provided for the neighbouring WECs in Figures 7.18 and 7.19. Results are provided for the WECs positioned at 5D and 10D, including corresponding experimental measurements and time-domain results. The large disparities between the undamped numerical results and experimental measurements were discussed in Section 5.5.1. The earlier analysis using the linear potential flow results indicated that constant external damping terms of $B^E_{33} = 40$Ns/m and $B^E_{33} = 100$Ns/m could be applied to the WECs at 5D and 10D respectively, in order to reproduce approximate results.

At the present stage, where no form of external damping has been applied within the CFD model, the time-domain results act as an intermediary system which can be easily tuned to perform validation checks. When both CFD and time-domain models are undamped, the results are generally in agreement with the earlier observations from Section 7.5.1:

1. A net downward movement of the free surface (and WECs) occurs, due to loss of mass of the water VOF phase.
2. The amplitudes are within 15% throughout when compared against the time-domain results (the normalised residual is shown in Figure 7.18c);
3. Comparison between the Euler and RANS solutions is as expected, with a steady and moderate damping effect due to viscous flow (this was ~1% per oscillation for the WEC at 5D, ~1.25% per oscillation for the WEC at 10D, as seen in Figure 7.19c);

Regarding points 1 and 2 above, the residual seen in Figure 7.18c highlights nonlinearities in the Euler CFD results. Where negative values are shown, the amplitude of the CFD result was larger than for the time-domain solution. Where the peaks crossed from negative to positive, the evidence of the downward drift of the WEC position is also clear in the Figures 7.18b and 7.19b. Relatively large changes to the residuals were recorded between oscillations, and no systematic behaviour could be identified.

A relatively clear trend was observed following the addition of viscous effects, between Euler and RANS CFD models. The residual takes an approximately linear path, exhibiting steady cumulative damping effects. The gradient of these effects is consistent between both WEC positions; however, at 10D, where the WEC excursions are smaller in magnitude, the damping becomes increasingly dominant at later stages in the decay.

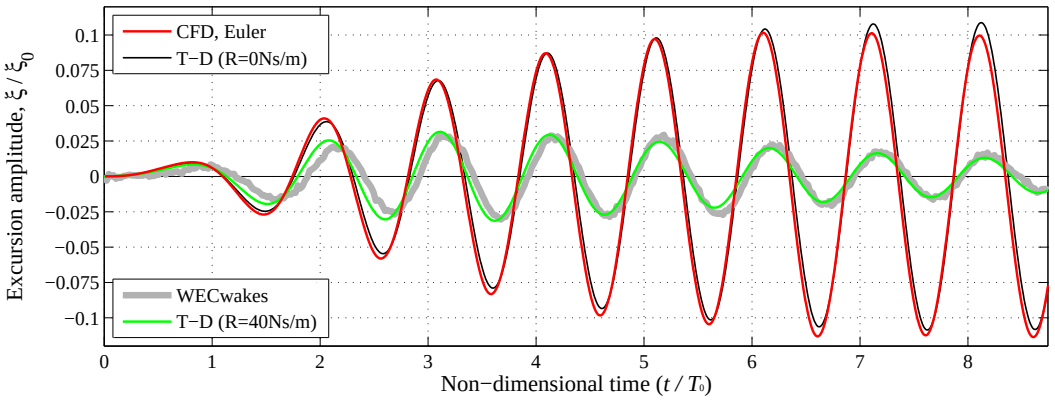

(a) 5D

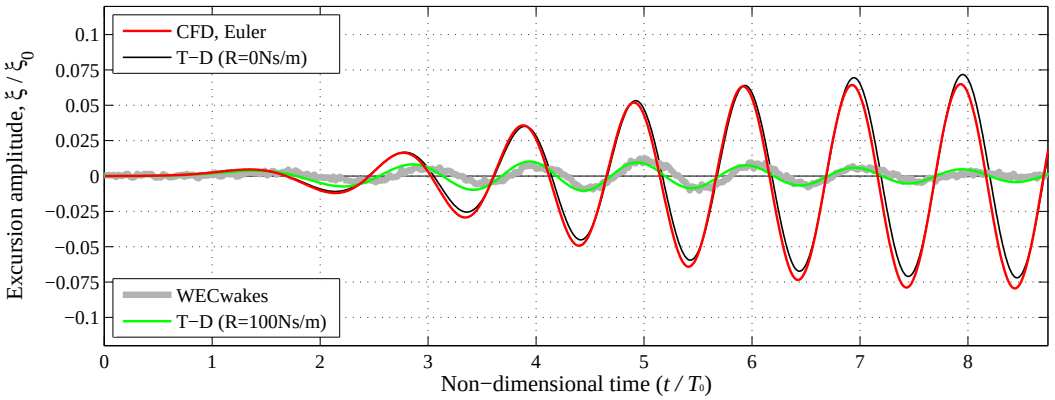

(b) 10D

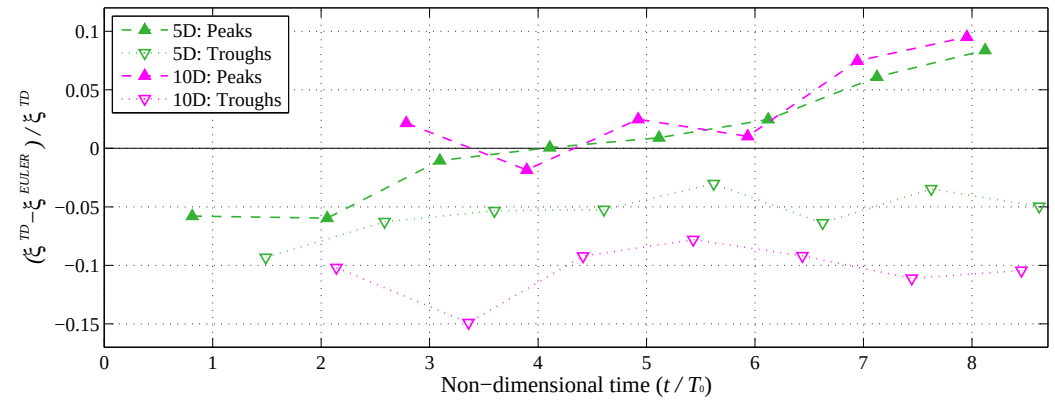

(c) Residual between time-domain and Euler results

Figure 7.18: WEC excursion results for the Euler CFD model, compared against time-domain results.

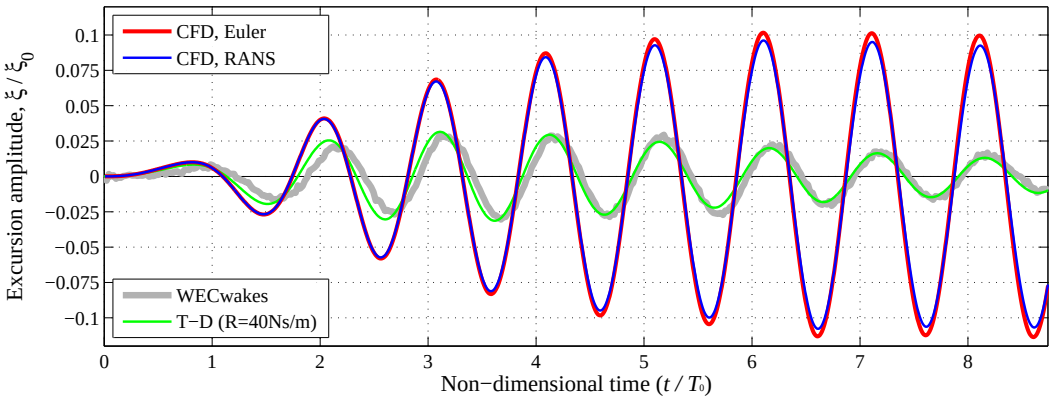

(a) 5D

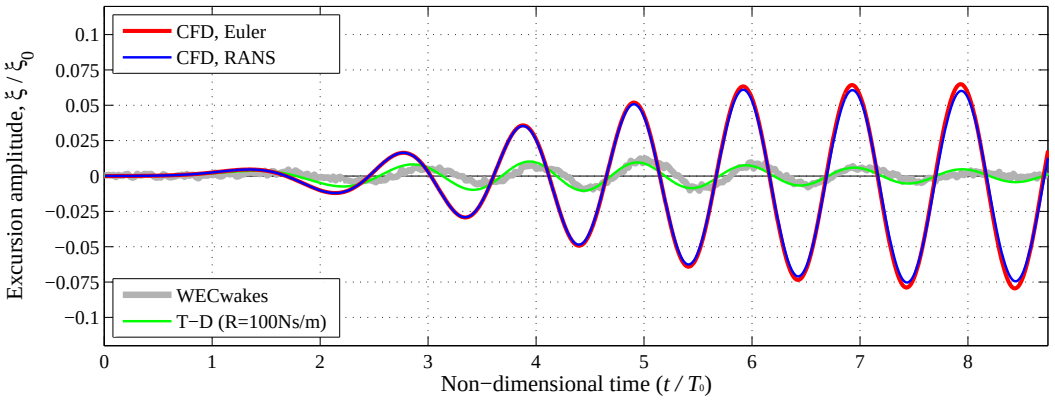

(b) 10D

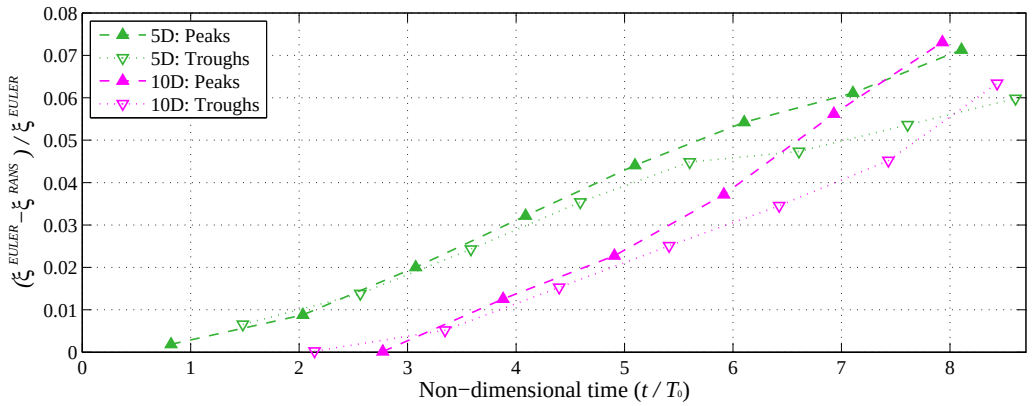

(c) Residual between Euler and RANS results

Figure 7.19: WEC excursion results for the RANS CFD model, compared against the Euler model (showing viscous effects).

7.6.2 Free surface elevation

The predicted free surface from the *FiveWEC-a* model is provided in Figure 7.20a, with the residual effects between *OneWEC-a* and *FiveWEC-a* cases shown in Figure 7.20b. Similar observations can be made to those highlighted for Figure 7.14, where wave diffraction and radiation is apparent in the vicinity of the neighbouring WECs at 5D, and weaker effects are emerging from the outer WECs at 10D. Another visible feature in the residual effects is the radial wave pattern associated with the main decay WEC, which has occurred due to the secondary interaction effects with the other bodies within the numerical domain.

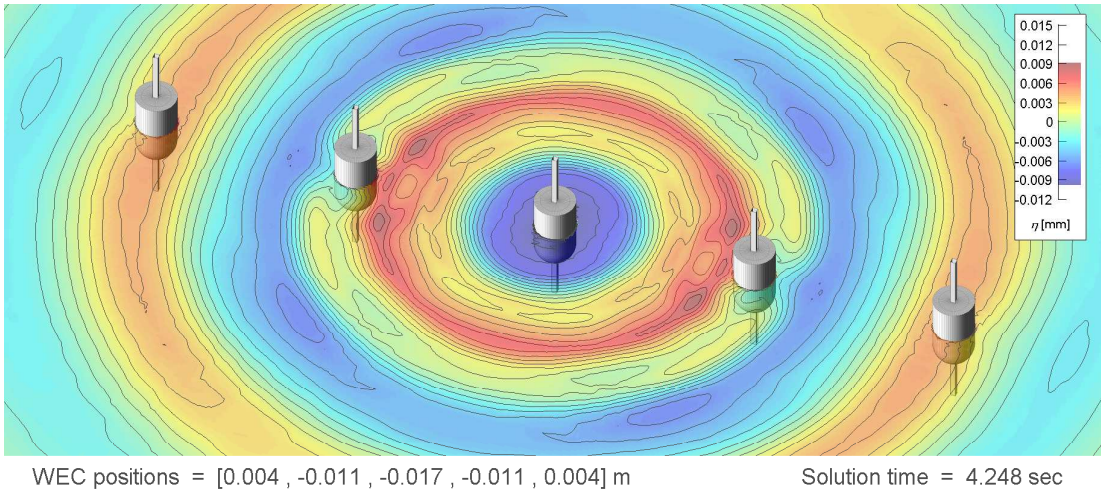

(a) Free surface elevation (contours: 1mm separation)

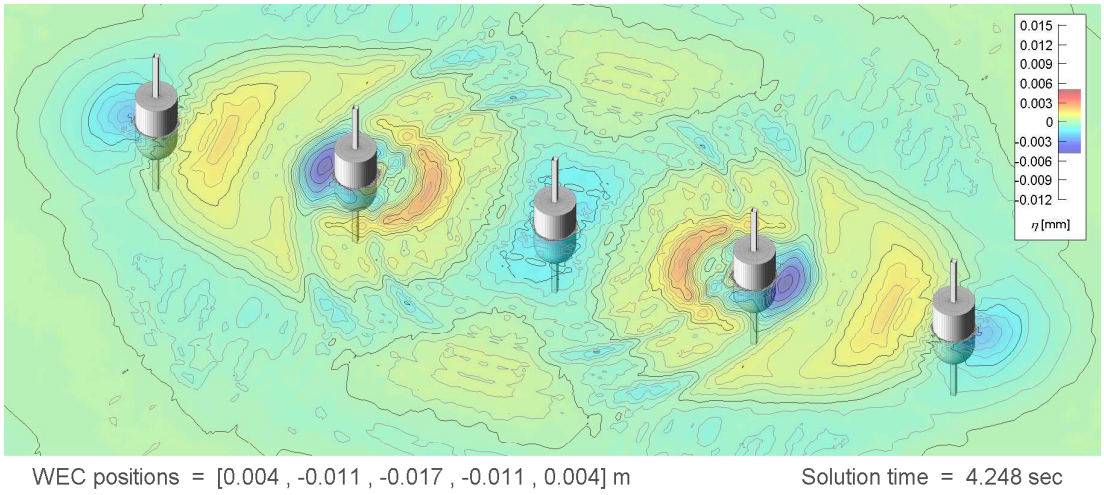

(b) Residual effects due to the neighbouring WECs and the adjacent posts (contours: 0.25mm separation)

Figure 7.20: Free surface elevations due for the *FiveWEC-a* case, at $t/T_0 = 3.72$. The results have been mirrored at the symmetry planes in order to visualise the entire domain.

7.6.3 Surge forces

Surge force evaluations from the *FiveWEC-a* CFD models are provided in Figure 7.21, for the neighbouring WECs at 5D and 10D, resulting from the decay of *WEC-3*. For both 5D and 10D, the surge forces are captured reasonably accurately using the CFD models, with discrepancies generally confined to peak amplitudes.

The normalised modelling error at peak values is provided in Figure 7.22a, which did not appear to be characterised by any coherent tend, although they generally increased with time. Errors fell in the range <20% for earlier periods of the decay, before increasing up to around 40% by $t/T_0 = 8$. Instances were also recorded where the numerical results exceeded the physical measurements, shown as 'negative' in the error plot. Whilst these modelling errors are relatively large, relevant disparities were generally limited to peak forces, with the amplitudes captured reasonably accurately elsewhere, including around nonlinearities in the force profiles.

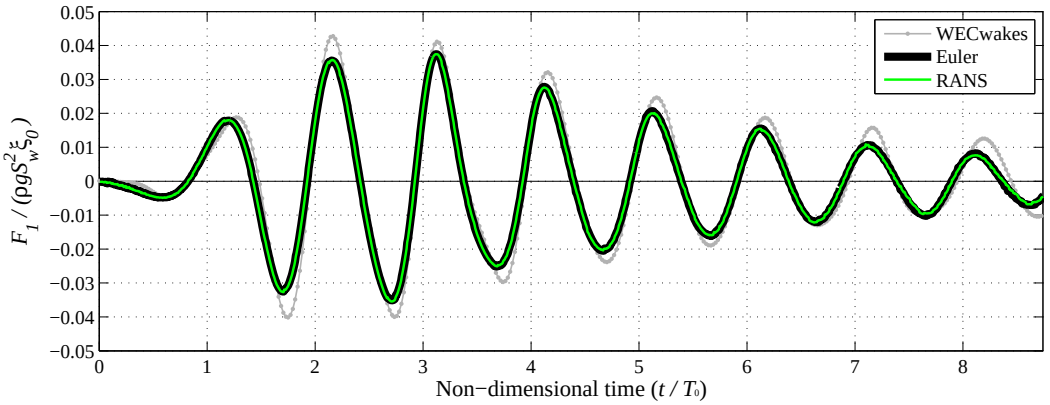

(a) WECs positioned at 5D

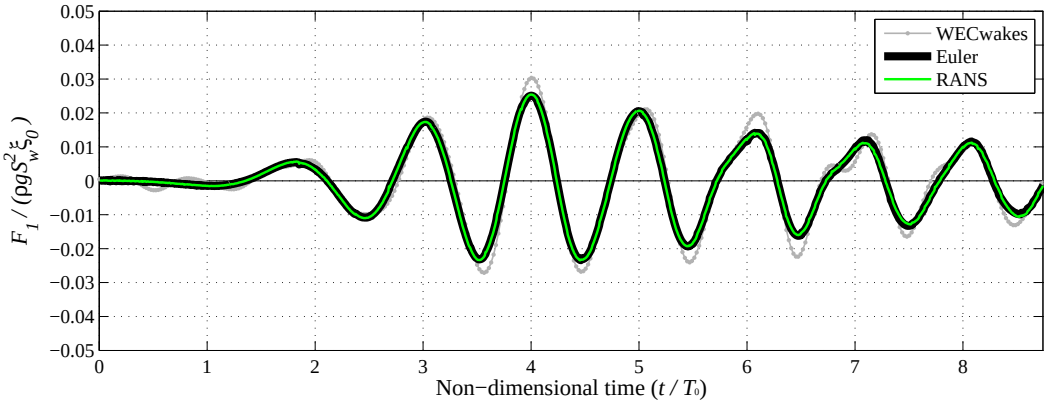

(b) WECs positioned at 10D

Figure 7.21: Surge force acting on the neighbouring WECs during the *FiveWEC* CFD analysis.

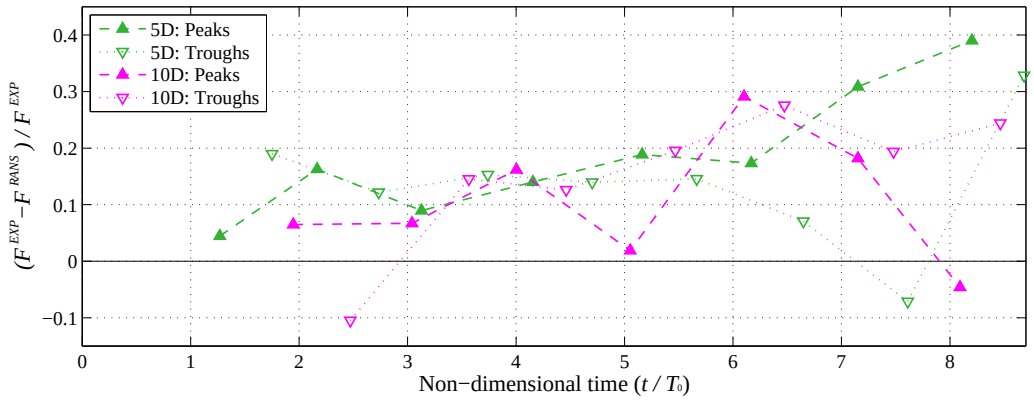

(a) Modelling error for RANS results

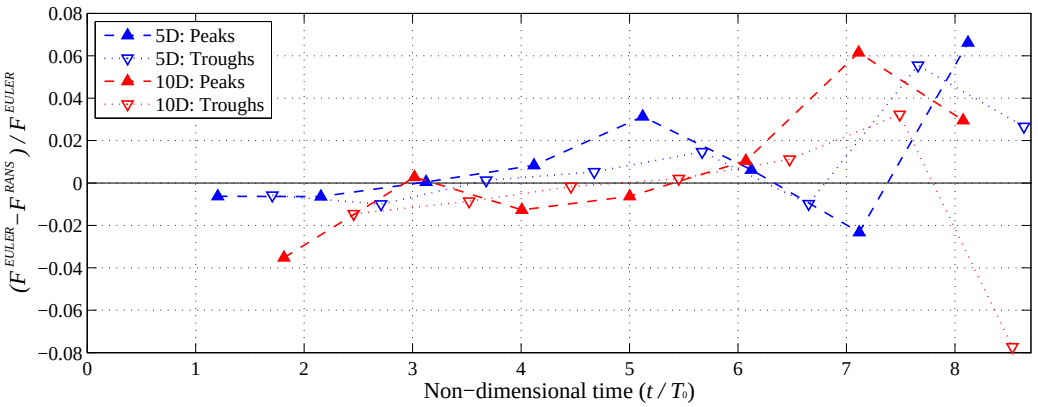

(b) Residual between Euler and RANS models

Figure 7.22: Normalised error/residual for the various surge force results from the CFD models.

With respect to power delivery and energy capture over a sustained period, the modelling error is likely to be considerably less for systems which include power take-off mechanisms.

From comparisons between the Euler and RANS surge force results in Figure 7.22, it was unclear whether any physical explanation could be linked to the effects of including viscosity in the model. Although the Euler and RANS models generally diverged with time, there were many instances where this trend reversed. Differences between the results peaked at 8% for the period considered.

7.6.4 Heave forces

For the system configuration considered the heave forces were of primary concern, as these had a direct effect on the motion of the single degree-of-freedom system. Heave force results from the *FiveWEC-a* CFD models are shown in Figure 7.23a for the decay WEC and neighbouring WECs.

No corresponding measurements from the experiments were available to validate heave forces. Correlated time-domain results, convolved with motion responses from the present results, are also shown in Figure 7.23 with the residual between time-domain and Euler cases provided in Figure 7.23b. The models provide comparable results for the heave force, with peaks within 12% for significant force magnitudes, and troughs within 2.5% throughout the period studied. A localised discrepancy is also present at the start of the decay, as well as a slight phase shift for the entire sequence.

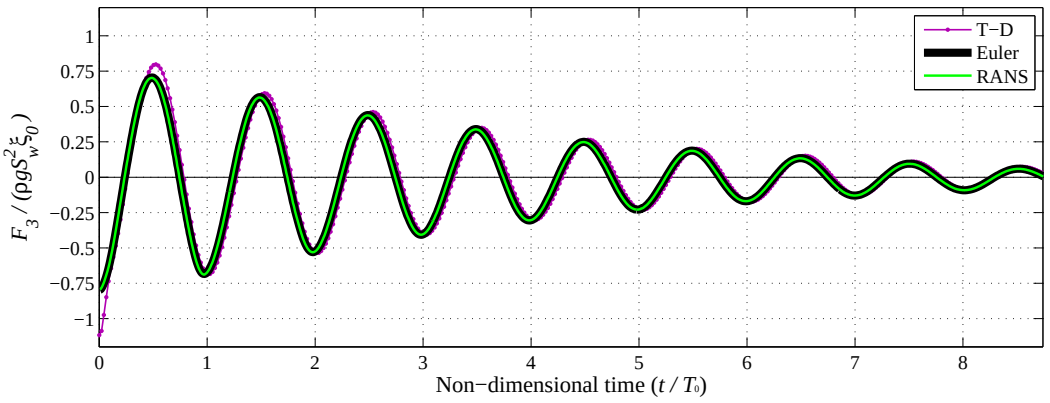

(a) Heave force

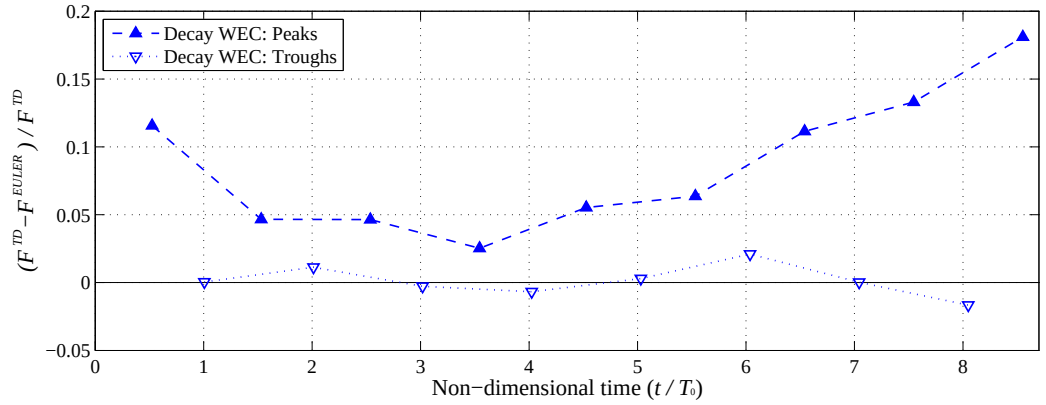

(b) Residual between time-domain and Euler models

Figure 7.23: Time history of heave force acting on the decay WEC, using the time-domain and CFD models.

Heave forces have been summarised in Figure 7.24 for the neighbouring WECs, showing Euler and RANS solutions. Comparative results for these WECs at 5D and 10D, as well as the main decay WEC, are also provided in Figure 7.25, in order to identify changes specifically due to viscosity. Viscous effects were again found to be of the order ~1% per oscillation. Coherent trends were identified between the two numerical models, for all three WEC positions. Two outlying values were found for troughs at 10D (▽) which resulted from minor, highly localised irregularities.

Shear forces extracted directly from the CFD model are also provided in Figure 7.26. As was described in Section 6.6.1, the direct shearing process only constitutes part of the overall viscous effect, with the apparent viscous pressure forces measuring comparable peak values in the earlier studies. The forces involved are several orders of magnitude smaller than the total dynamic loads, so it is therefore likely that Figure 7.25 offers greater practical benefit in establishing an empirically derived viscous damping curve for input to a time-domain based model.

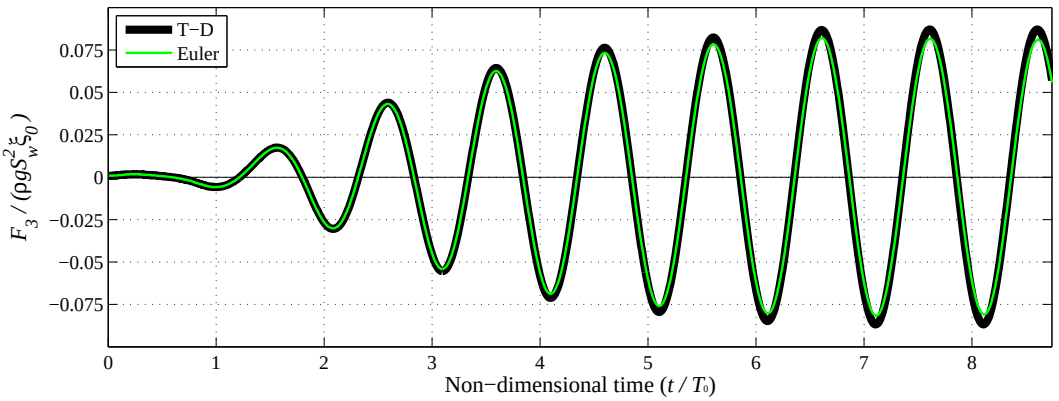

(a) Neighbouring WECs at 5D

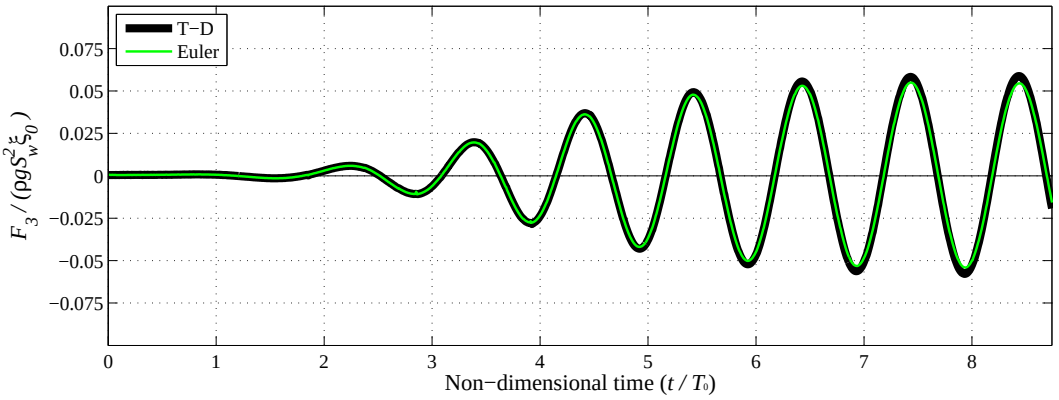

(b) Neighbouring WECs at 10D

Figure 7.24: Time history of heave force acting on the neighbouring WECs, using the CFD models.

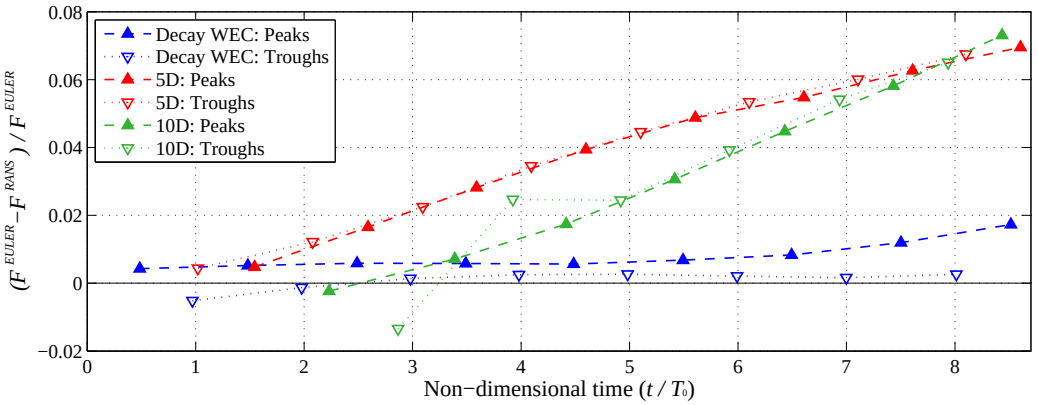

Figure 7.25: Normalised residuals between Euler and RANS CFD models, for heave forces.

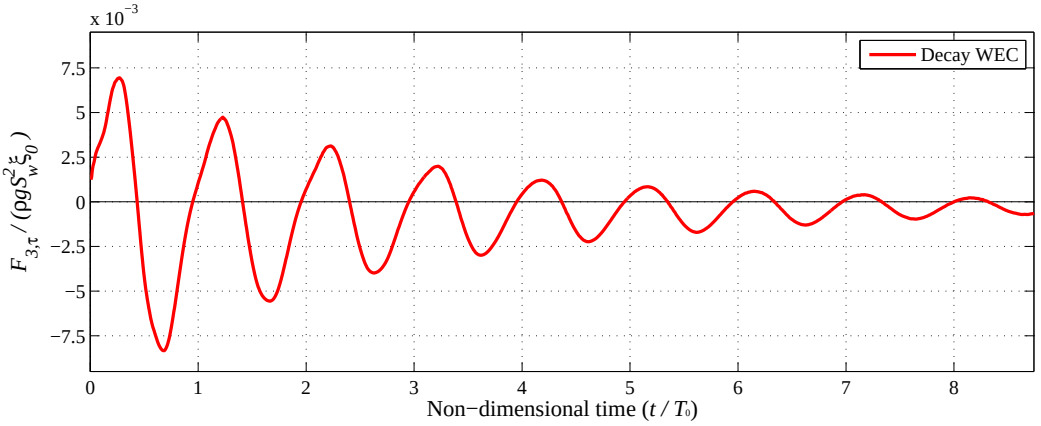

(a) Decay WEC

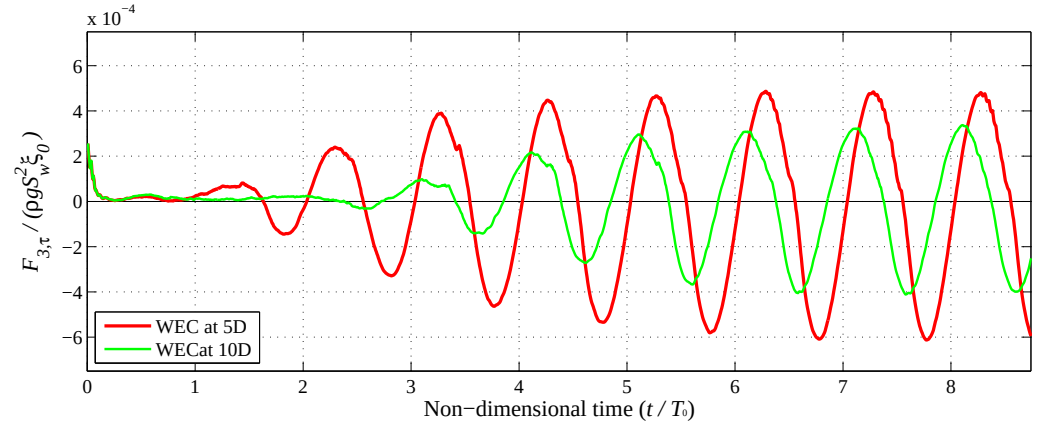

(b) Neighbouring WECs

Figure 7.26: Time history of shear force in heave, acting on the decay WEC and neighbouring WECs, using the CFD models.

7.7 Final comments

CFD results were provided for the multi-WEC models, and were examined in terms of device excursions, free surface elevations and forces, using both inviscid and viscous forms of the CFD model. Due to the specific nature of delivering CFD solutions for free surface capturing system with multiple fluid-structure interactions, the detailed model descriptions provided in Chapter 6 were extended, highlighting changes to the model designs. Only a limited number of runs were possible using the revised arrangement, due to the computational requirements. These runs included:

1. *OneWEC-a* RANS;
2. *TwoWEC-ab* Euler;
3. *TwoWEC-ab* RANS;
4. *FiveWEC-a* Euler;
5. *FiveWEC-a* RANS.

The results generally gave close reproductions of the experimental measurements and previous numerical results, where data were available. Additional characteristics of the system were exposed using the CFD models, such as idealised viscous damping behaviour, and processes which were linked to aspects of nonlinear wave generation. Numerical issues existed for the present models, in particular the loss of mass of the water VOF phase, which caused a gradual lowering of the free surface with time.

As with earlier chapters, the results were aimed specifically at correlating the numerical and experimental results, including effects which resulted from the arrangement of the experimental setup. The motivation for the application of CFD is to demonstrate a methodology for exposing nonlinear processes, such as hydrodynamic effects which generate higher order wave components, viscous effects and mechanical dissipative effects. Ultimately, bespoke numerical sub-models are necessary for the discrete systems that control hydrodynamic dissipation and mechanical dissipation, due to the fact that they will scale differently between tank test and ocean-scale prototype.

Chapter 8

Conclusions

Background

Wave energy offers great promise as one of the significant contributors to sustainable energy models of the future. In the right locations, the vast amounts of power being continually transferred across the oceans can, in theory, be tapped into on an industrial scale, allowing coastal countries to de-carbonise their energy networks.

The technical and economic obstacles however are proving extremely challenging at present. The immature wave energy industry has suffered setbacks in recent years, with the survivability, reliability and operability of devices often coming into question. Problems can also in part be traced back to the uncertainty of real behaviour of devices at sea, which brings uncertainty into energy yield calculations, as well as financial calculations. Taking lessons from the oil and gas industry where truly unbelievable feats of engineering have been achieved at sea, given powerful enough incentives, the rewards from wave energy must be demonstrated reliably on a commercial basis to progress the development of the technology, and establish wave power as an option for large scale energy generation.

One factor which is often excluded from power calculations is the effects of viscosity. Initial checks which can be carried out to assess the relative importance of viscous effects can qualify the appropriate exclusion of viscosity from the numerical models. The highly sensitive interactions between devices, however, will experience compound effects at both source and sink of the transported energy between devices, i.e. via the radiated waves. The widely accepted notion that amplified energy yields are possible from positive array interactions (q-factors greater than unity) is therefore potentially sensitive to viscous effects.

Traditional methods for incorporating the viscous properties of fluids are well established, in the form of the various Computational Fluid Dynamics (CFD) methods. Attempting to design a complete working Wave Energy Converter (WEC) system using only CFD is a highly impractical approach, due to the number of simulations required, and length of time required to carry out each study. To make the most appropriate use of CFD, the method proposed here is to focus on a specific set of highly refined experimental data, such as that from decay tests, to investigate the very sensitive damping effects from mechanical systems (bearings, mechanisms

and sensors), and damping due to viscosity. In the present work, the effects of any power take-off systems were overlooked, in order to avoid suppressing the hydrodynamic effects, and in particular, the effects of viscosity.

Summary of research

From the research questions posed in Chapter 1, the first two questions relate to both the direct interest in quantifying the relative viscous effects, and the approach to developing a framework to model the complete small scale system:

1. How important are viscous effects in relation to the WEC array interaction problem?
2. How should small-scale experimental effects be treated in a numerical model of a WEC array?

To study the viscous effects associated with a small-scale WEC system, it was necessary to obtain high quality tank test data for a model WEC array. A short period was spent at the Danish Hydraulics Institute assisting with a significant project which took place in 2013 (Stratigaki *et al.*, 2014). This featured a square array of twenty five generic heaving WECs, constructed at approximately 1/30th scale. Establishing how the viscosity would affect interactions involved detailed scrutinisation of the data. Due to the specific interest in exposing the viscous effects on the interactions between devices in an array, it was of particular interest to study the decay tests, which were highly repeatable, with the corresponding wavefield characterised by a very clean radiated wave pattern. Preliminary processing of this data, however, highlighted other nonlinear hydrodynamic behaviour which required additional consideration.

Preliminary numerical models were then provided using the Boundary Element Method (BEM) code WAMIT (WAMIT: Version 7, 2012), followed by translations to the time-domain using a research code originally developed by Forehand *et al.* (2015). Comparisons between the physical and numerical results exposed relatively significant damping effects, which occurred due to a combination of viscous and mechanical processes.

Overall, discrepancies between the linear numerical model and the experimental data were associated specifically with the following:

1. Nonlinear hydrodynamic effects, where no known link was identified in the present work to any physical/hydrodynamic processes;
2. Nonlinear mechanical effects, due to bearing friction, sensor resistance (potentiometer);
3. Effects due to viscosity;
4. The numerical uncertainty.

During the numerical analysis, Item 4 was quantified and minimised when reviewing panel convergence for the BEM solution, resulting in a numerical uncertainty of ~0.3%. On the basis that this was both small, and quantifiable, this could effectively be accounted for in the above. The perceived problem which has been challenged in the present work, is that Items 1 to 3 could

have comparable effects, but could scale differently when assessing a larger prototype system. This is an area that can be overlooked when using a simple linear model. The aim therefore was to decompose this combined damping effect using a set of carefully configured models, including CFD. This somewhat complicated arrangement was required, in order to assess the affects of viscosity.

Through use of Euler (inviscid) and Reynolds-Average Navier-Stokes (RANS) (viscous) simulations, a direct comparison was made which separated out Item 3 above. Furthermore, given that both BEM and CFD models were suitably verified (both to within ~0.3% for the excursion measurements), Item 1 above was discernible from the residual between the inviscid CFD case (Euler) and BEM, which differed only according their capacity, or lack thereof, to model the nonlinear hydrodynamic processes. This difference, in terms of body excursions, between the Euler and BEM results for a small 5 WEC array (Figure 7.18) peaked at around 15% over the period studied $1 < t/T_0 < 8$, showing sporadic behaviour. With regard to the viscous effects on WEC excursions, the change due to viscosity was smaller, at around 7% over the period $1 < t/T_0 < 8$ (or, 1% per cycle). A peak viscous effect of around 7% was also found for the surge forces over the same period, for devices which were spaced five diameters apart. This small affect was recorded across the different CFD model configurations, and while this represented a relatively weak interaction effect, over many cycles this could culminate into a measurable affect with regard to power production. This would form a further area of important future work.

This reasonably complex system could, in theory, be decomposed into: a linear potential flow results, followed by the three nonlinear process: Items 1 to 3, above (on the basis that the numerical error was small). This framework, of successive deduction of the viscous effect, nonlinear effects and mechanical effects, has been applied thorough the numerical work, and was considered in response to Question 2 from Section 1.3.1. This complete procedure was not developed further as a dynamic model at this stage, however, this has been reported as a significant area for future work.

The most involved part of the present work, was the construction of suitably verified models, as posed by Question 3:

3 What measures are required to construct a valid finite volume, CFD model of a floating WEC array?

This required a large number of CFD models to establish appropriate designs for the mesh and model configurations. A number of major issues were encountered, which have been referred to in the main text, most notably:

- numerical ventilation;
- oscillatory convergence;
- body motion prescription;
- numerical damping;

- free surface distortion;
- mass loss from the domain;
- computational processing.

This provides some indication of the difficulties involved and time-scales necessary to conduct such work. Much or the final results were very encouraging in terms of accuracy, and ultimately, the present studies would not have been possible without the use of CFD. A particularly important aspect which was delivered by the current work, was the capturing of the nonlinear waves, generated by the WEC.

Future work

The following areas of research have been considered as pertinent extensions to the present work:

1. Characterisation of nonlinear wave formations during the decay;
2. Development of a fully parametric model for the viscous effects, linked directly to the velocity of the model, and the near-wall velocity of the surrounding fluid;
3. Examinations of more general tank conditions, including responses to incident waves and different array configurations, in order to assess power production.

Appendix A

Additional Figures

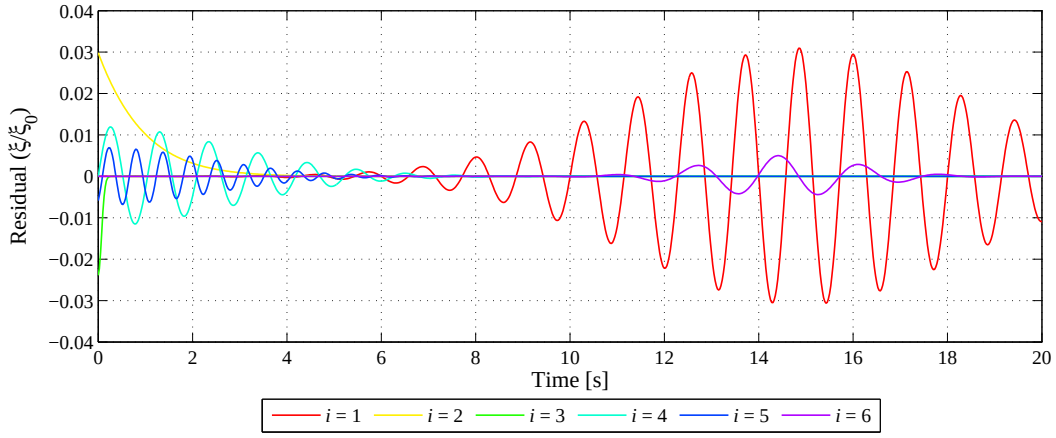

(a) One-WEC test (WEC-5)

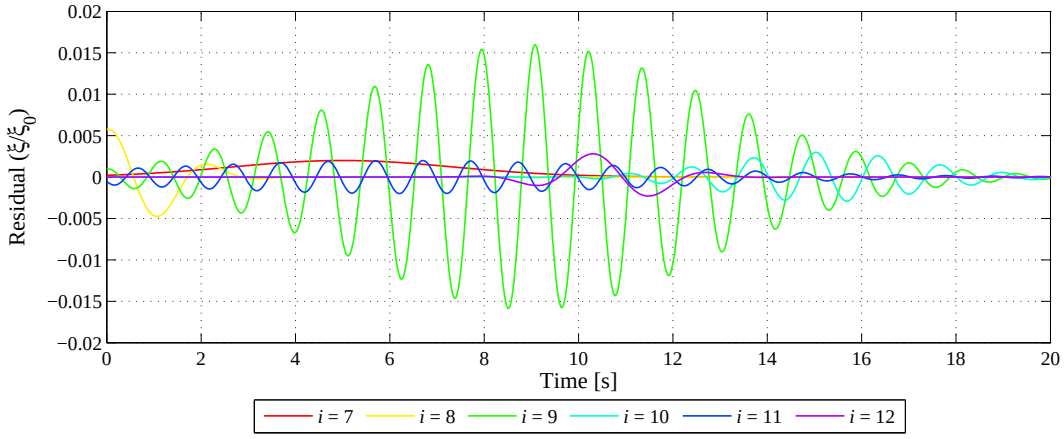

(b) Two-WEC test (WEC-5)

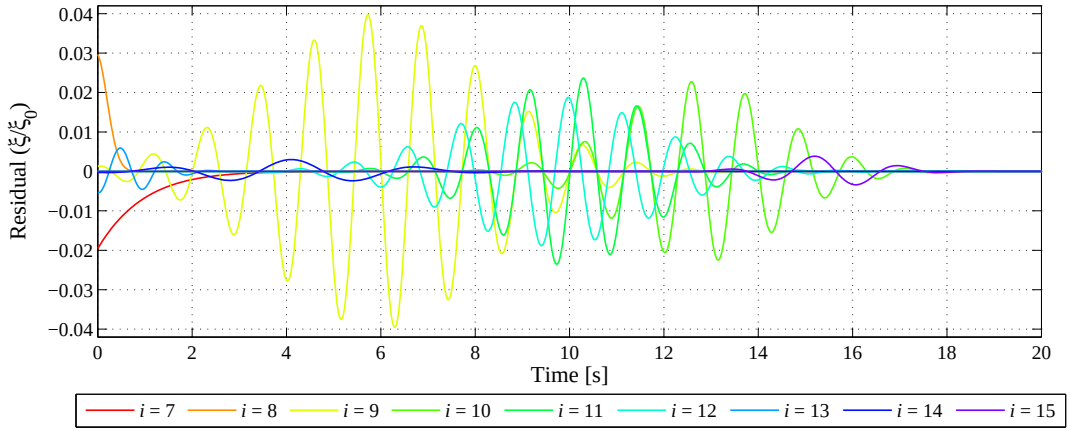

(c) Five-WEC test (WEC-3)

Figure A.1: Correction components for the WEC motion functions, derived from the experimental measurements (Section 4.4).

Appendix B

Additional Tables

Table B.1: Motion function coefficients

	i	α_i	β_i	γ_i	θ_i	ϑ_i
1-WEC, 2-WEC & 5-WEC cases	1	0.031	14.890	5.000	ω_0	0
	2	7.265	-10.703	4.566	0	0
	3	-0.0239*	-0.001	0.100	0	0
	4	0.012	0	3.922	6.016	1.580
	5	0.007	0	3.247	11.010	2.562
	6	0.005	14.477	2.227	3.603	1.655
2-WEC case only	7	0.002	5.000	3.333	0	0
	8	0.006	0.328	1.600	2.755	0
	9	0.016	8.984	5.376	5.537	0.002
	10	0.003	15.186	2.959	4.733	2.010
	11	0.002	6.380	7.299	6.237	4.126
	12	0.003	10.698	1.608	2.355	5.295
5-WEC case only	7	-4.765	-10.703	4.566	0	0
	8	0.030	-0.037	0.333	0	0
	9	0.040	5.964	3.236	ω_0	0.050
	10	0.023	12.801	2.364	ω_0	0.050
	11	0.024	10.037	2.299	ω_0	0.050
	12	-0.019	9.662	2.941	ω_0	1.426
	13	-0.006	0.370	1.115	6.515	0
	14	-0.003	4.154	2.656	2.298	0
	15	0.004	15.469	1.518	3.350	0.566

Table B.1 gives coefficients for the prescribed motion functions described in Section 4.4. Three functions are defined by Equation (4.1):

1. The displacement of WEC#5 in isolation (1-WEC case), using $i = \{1-6\}$.
2. The displacement of WEC#5 for the 2-WEC case, using $i = \{1-12\}$.
3. The displacement of WEC#3 for the 5-WEC case, using $i = \{1-15\}$.

*α_3 used to ensure unity for normalised initial condition.

Appendix C

Additional Modelling Considerations

C.1 Motion prescription

For the evaluations carried out using CFD it was of interest to prescribe the motion of the WEC for certain runs, in order to ascertain how the radiated waves formed and compare against the wave gauge measurements. By making the WEC move in the precise way that it did in the physical tests, the positioning of the solid surface becomes an external condition which is then imposed on the fluid domain, and the resulting free surface elevations represent the closest match to the corresponding wave gauge measurements from the experiments. In contrast to the Dynamic Floating Body Interaction (DFBI) case where the mechanical system was assumed frictionless, imposing the 'floating body' motion in this way results in a more realistic radiated wave condition, which effectively accounted for mechanical friction.

The implementation of this external condition required careful consideration. Whilst overcoming issues with a preliminary application of the experimental data within the CFD code, it was found that recurring incidences of extremely distorted flow conditions at otherwise remote areas could be attributed to *user defined vertex motion* property of the solver, implemented via data tables of time series. These seemingly unrelated regions of considerable distortion were found to be non-physical and highly problematic in terms of solution quality. The model component which experienced the most significant degradation was the overset mesh interface, between the body-attached mesh and the background domain. The corresponding results can be seen in Figures C.1 and C.2.

In general, the overset mesh requires very particular treatment with regard to the local cell size and shape, whilst also being sensitive to the method of interpolation between the two distinct fluid regions. In this situation, it was also apparent that large pressure gradients across the bulk flow, including effects from more remote parts of the domain, caused significant issues at the very sensitive overset mesh interface. Moreover, for the case highlighted here, extremely small steps were discovered in the executed positioning time histories, even though they were not present in the raw data or imported time series lists. This caused huge, very high frequency pressure vibrations throughout the neighbouring regions, effectively causing an impedance to the flow across the overset mesh interface.

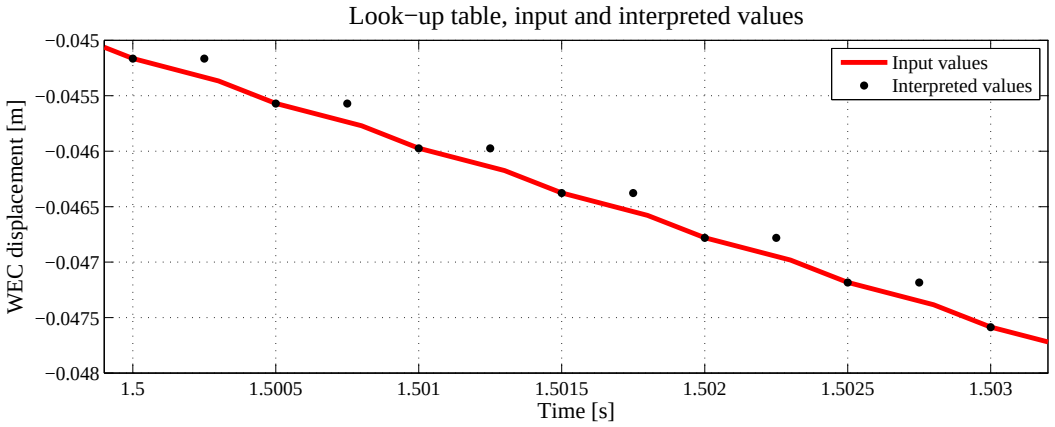

Figure C.1: Comparison between sample input data (table) and actual motion of the WEC in the CFD model. This issue was only present in preliminary simulations using 'Table (iteration)' method of the 'User defined vertex motion' property.

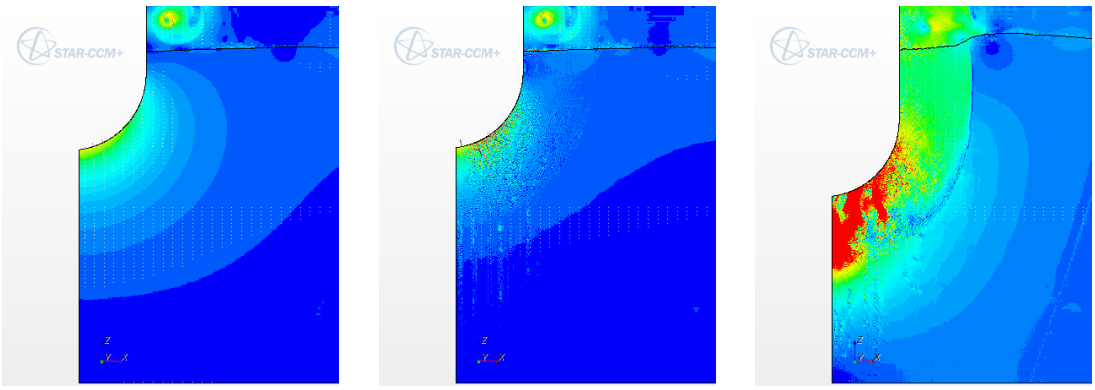

(a) $T = 1.00000$s **(b)** $T = 1.00625$s **(c)** $T = 1.44375$s

Figure C.2: Velocity magnitude around WEC (in section). Results shown are from one of the problematic CFD cases.

Various methods were tested with regard to physical data application within the CFD model, including the use of splines to interpolate to timestep frequency (40Hz to 4000Hz) and filtering/smoothing of the position data and its derivatives. The errors discussed above proved to be systemic in the data table method, requiring the development of an numerical motion function, designed to mimic the actual behaviour of the WEC during the experiments. This was implemented directly as a field function in STAR-CCM+, and was applied specifically to runs described herein as with 'prescribed motion'. All other results involving the WEC(s) employed the DFBI solver.

C.2 Numerical ventilation

The importance of boundary layer treatment on the WEC surface was discussed in Section 6.3.3, where it was acknowledged that the viscous sub-layer should be fully resolved for the oscillating system to allow for all possible fluid velocity scenarios, including zero relative velocity when the flow reverses. By targeting $y^+ < 1$ the unwanted switching between the resolved condition and wall functions could be avoided. This resulted in wall adjacent cell dimensions of 1.2×10^{-5}m.

For the fully resolved boundary layer, the appropriate zero relative fluid velocity condition was enforced at the wall surface for both water and air. Where the surface transcended the two Volume Of Fluid (VOF) phases, however, the recognised *'numerical ventilation'* issue was observed for all preliminary RANS simulations, where convection of phase volume fractions, α_w and α_a, was restricted in a manner which was non-physical. This, in effect, entrained a very thin layer of air across parts of the submerged WEC surface, causing improper development of the boundary layer, and lowering shear resistance at the WEC wall.

Tests were carried out using a number of different configurations, including localised sub-model cases, for boundary layer sensitivity checks. Mesh configurations around both free surface and boundary layer regions were preserved from the main CFD simulations while different modifications were made to the fluid properties. The behaviour of the multi-phase VOF system was carefully monitored at the free surface – solid boundary interface, while the no-slip wall was moved with the same velocity profile as the WEC in the main simulations.

It was not deemed necessary within the present work to treat the interaction between the air phase and moving structure with the same rigour as the fluid-structure interactions from hydrodynamic effects. It followed that it was not necessary to attempt to resolve an aerodynamic boundary layer, and that the properties of this interface could be modified in certain ways to address the issues discussed here. The following two methods were explored:

1. Above the free surface, an initial water volume fraction of 100% ($\alpha_w = 1.0$, $\alpha_a = 0$) was imposed on cells in close proximity to the WEC surface, effectively applying a thin water film to the surface of the WEC:

$$\alpha_w(\Delta y, z) = \begin{cases} 0 & \text{if } \Delta y > 1.0 \times 10^{-5} \text{ and } z > 0 \\ 1 & \text{elsewhere} \end{cases} \tag{C.1}$$

2. At the wall adjacent nodes, the viscosity of both water and air was effectively reduced to zero, permitting localised removal of shear stresses and the permeation of water to the wall boundary. At a position of $z = -0.02$m below the free surface the viscous property of the water was restored, below which the boundary layer could develop. An inviscid

air film was applied to the entire WEC surface, above $z = 0$:

$$\mu_w(\Delta y, z) = \begin{cases} 1 \times 10^{-12} & \text{if } \Delta y < 1.0 \times 10^{-5} \text{ and } z > -0.02 \\ \mu_w & \text{elsewhere} \end{cases} \tag{C.2}$$

$$\mu_a(\Delta y) = \begin{cases} 1 \times 10^{-12} & \text{if } \Delta y < 1.0 \times 10^{-5} \\ \mu_a & \text{elsewhere} \end{cases} \tag{C.3}$$

Both methods established either complete or partial wetting of the solid boundary as it passed below the free surface, however, additional disturbances were introduced within the boundary layer, with neither method providing effective results.

Similar issues were reported by Viola *et al.* (2012) during assessments of racing yacht hulls. A method was demonstrated whereby one or more source/sink terms were applied to the fluid phases (source for the water phase, and sink for the air phase) over a highly localised region. This had the effect of forcing the entrained air out of the affected cells, in a similar way to the methods described above. In the referenced work, however, wall functions were used for the boundary layer, which was configured to meet the criteria $y^+ \approx 30$.

A method proposed by CD-Adapco (provided via direct contact with the producer of the STAR-CCM+ software) involves modelling surface tension, which allows for the formation of a meniscus as part of the evaluations. The effectiveness of this particular method is demonstrated in Figures C.3 to C.8 below.

Figure C.3 shows various conditions experienced around the WEC surface at different times on a macro-scale. Despite the relatively fine detail seen with cells of 1.5mm height clearly visible, the effects of numerical ventilation remain hidden. Studying at micro-scale around $t = 1$, seen in Figure C.4, a VOF mixture exists ($0 < \alpha_w < 1$) within the two cells nearest the wall, each measuring around 0.012mm in depth to suit $y^+ = 1$. This was consistent with the fluid behaviour witnessed across the initially dry portion of the WEC, throughout the entire duration of the preliminary test simulations.

Inclusion of surface tension provides the equivalent results shown in Figure C.5, demonstrating appropriate treatment of numerical ventilation issues for the test case. The solution was sensitive, however, to the number of inner iterations used per timestep, N_{it}. Assessments of further test cases using $5 < N_{it} < 20$ provided the results shown in Figure C.6 for the initial descent, which shows the volume fraction at the WEC wall, stretched horizontally by a ratio of 20:1 to highlight numerical ventilation. $N_{it} = 10$ provided a sufficient level of convergence to ensure that the the issues were resolved.

The resultant effect on body forces due to viscous effects ($F_{3,p(visc)}, F_{3,\tau}$) are provided in Figure C.7. Over the first oscillation, force amplitudes were shown to be around 20% less when surface tension was excluded, and numerical ventilation was evident. Effects from the use of different

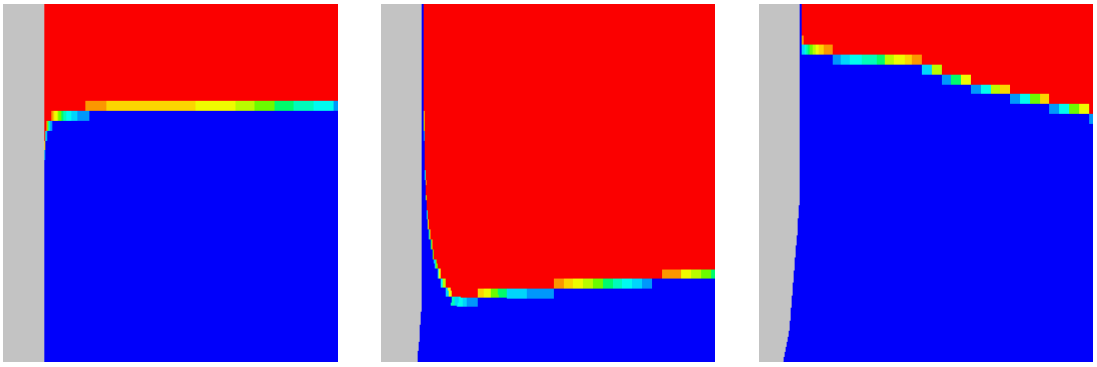

(a) $T = 0.274$s (downward motion during first oscillation)

(b) $T = 1.051$s (upward motion during first oscillation)

(c) $T = 1.202$s (beginning of second descent)

Figure C.3: Free surface interface behaviour in the RANS CFD model, before numerical ventilation treatment.

contact angles of the meniscus were investigated with no associated effects found. A contact angle of $0^{\circ}$was used for all remaining work.

The resultant effects on excursions from numerical ventilation are provided in Figure C.8, which shows a 13% cumulative reduction in viscous effects when surface tension was omitted.

C.3 Wall velocity specification

The wall surface used for the post and WEC wall differ in treatment due to their independent motions. Both are defined as boundaries of the moving overset mesh region, and are fixed to the motion path of the overset mesh*. The wall of the WEC was suitably treated by this condition, where the oscillating flow regime sees the fluid closest to the WEC move with the same velocity as the WEC (the boundary layer develops from the relative motion of the WEC in the surrounding water).

The post wall boundary, however, was configured with a corrective velocity, equal in magnitude and opposite in direction to the WEC velocity, to ensure that this surface has a global velocity of zero. This was implemented in STAR-CCM+ using the Tangential Velocity Specification property. For the various motion cases in this thesis, the appropriate function from Section 4.4 was used, depending on whether the particular study involved one, two or five WECs. To provide a velocity, a central difference scheme was used, based on motion data with a sample rate of 2500Hz. Wherever DFBI was used, the velocity was extracted directly from the DFBI solver.

*The post is actually represented by boundaries which are defined within the overset mesh *and* domain mesh. Provided the tangential velocity of the wall is defined correctly, as explained in this section, the post should be consistently defined along it's entire length, despite being composed of two different numerical constructions.

(a) General view **(b)** View of free surface interface **(c)** Wall cell scale, sub-surface

Figure C.4: Volume fraction at $t = 1.00$s for the *IM-RANS* model, excluding surface tension. The black rectangles in (a) and (b) represent the extent of views (b) and (c), respectively.

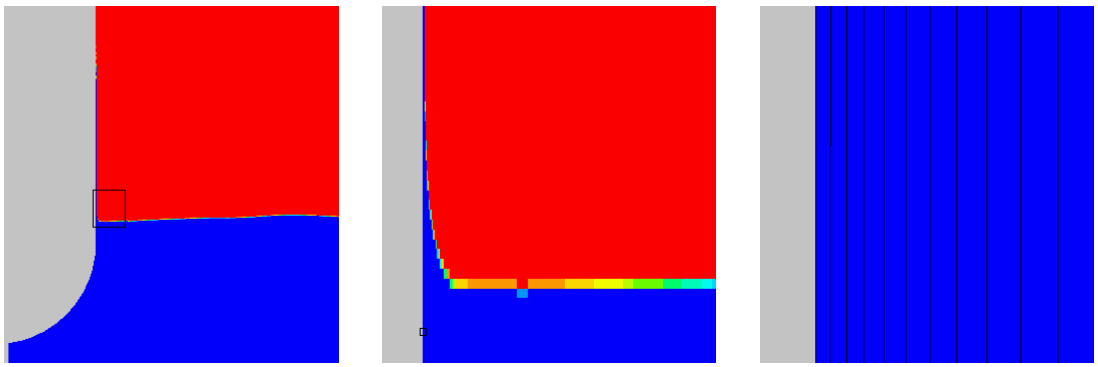

(a) General view **(b)** View of free surface interface **(c)** Wall cell scale, sub-surface

Figure C.5: Volume fraction at $t = 1.00$s for the *IM-RANS* model, including surface tension. The black rectangles in (a) and (b) represent the extent of views (b) and (c), respectively.

(a) 5 inner iterations **(b)** 8 inner iterations **(c)** 10 inner iterations

Figure C.6: Sensitivity of numerical ventilation (air entrainment) at the WEC wall due to the number of inner iterations. The scale in the vertical direction is compressed by a ratio of 20:1, relative to the horizontal scale (*IM-RANS* model, including surface tension).

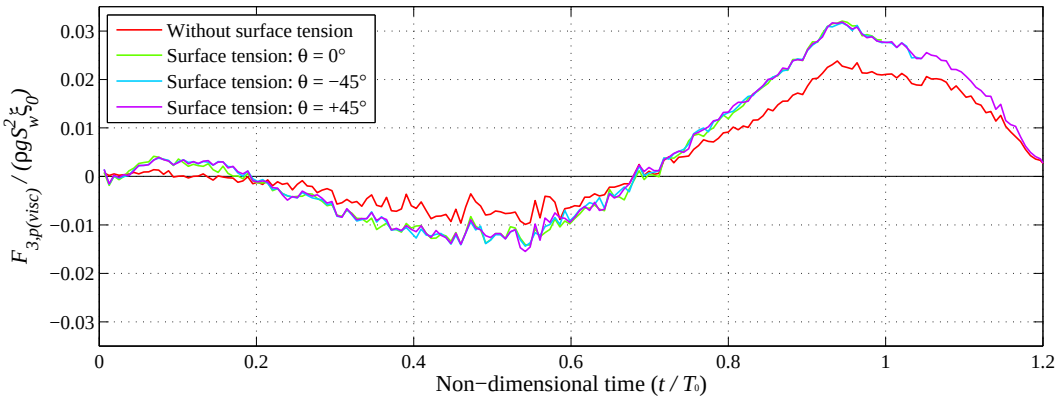

(a) Viscous pressure force component, $F_{3,p(visc)}$

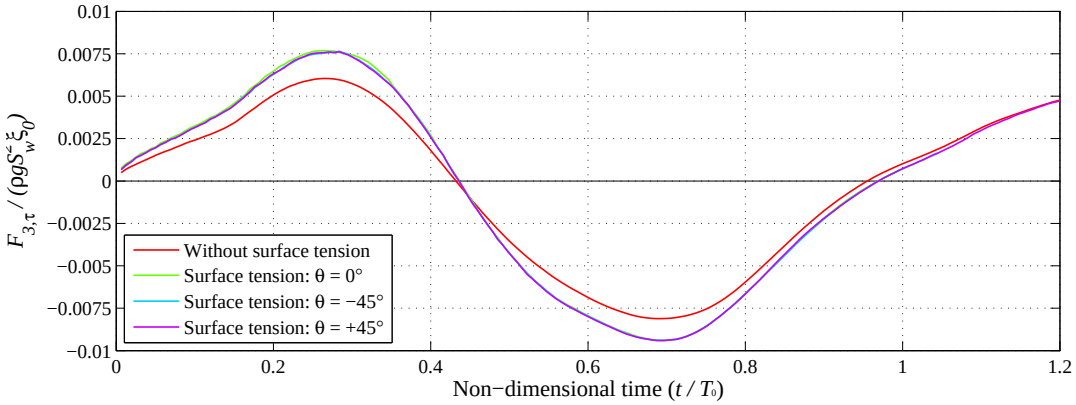

(b) Viscous shear force component, $F_{3,\tau}$

Figure C.7: Heave forces acting on the WEC, due to the effects of viscosity.

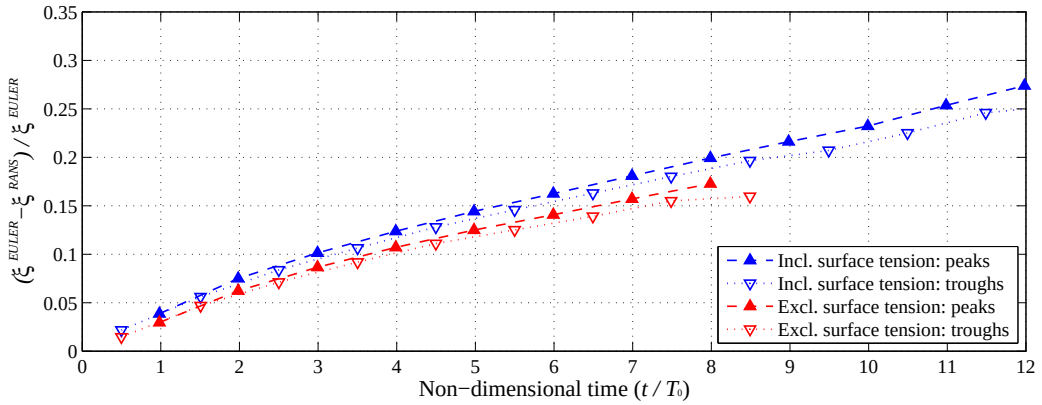

Figure C.8: Cumulative change in excursion amplitude between *FSI-EULER* and *FSI-RANS*, with and without the surface tension model (i.e the residual effects from numerical ventilation).

Bibliography

DTI/BERR: Preliminary Wave Energy Device Performance Protocol, 2007.

IEA-OES Annex II: Guidelines for the Development & Testing of Wave Energy Systems, 2010a.

IEA-OES Annex II: Development of Recommended Practices for Testing & Evaluating Ocean Energy Systems, 2010b.

Acheson, D. J. Elementary Fluid Dynamics. *Oxford Applied Mathematics and Computing Science Series*, 1990.

Agamloh, E. B., Wallace, A. K., and von Jouanne, A. Application of fluidâĂŞstructure interaction simulation of an ocean wave energy extraction device. *Renewable Energy*, 33: 748–757, apr 2008. ISSN 09601481. doi: 10.1016/j.renene.2007.04.010. URL `http://linkinghub.elsevier.com/retrieve/pii/S096014810700119X`.

Babarit, A., Hals, J., Muliawan, M. J., Kurniawan, A., Moan, T., and Krokstad, J. Numerical benchmarking study of a selection of wave energy converters. *Renewable Energy*, 41: 44–63, may 2012. ISSN 09601481. doi: 10.1016/j.renene.2011.10.002. URL `http://linkinghub.elsevier.com/retrieve/pii/S0960148111005672`.

Babarit, A., Folley, M., Charrayre, F., Peyrard, C., and Benoit, M. On the modelling of WECs in wave models using far field coefficients. *EWTEC*, (Proc. of the 10th European Wave and Tidal Energy Conf., Aalborg, Denmark), 2013.

Bearman, P. W., Graham, J. M. R., Obasaju, E. D., and Drossopoulos, G. M. The influence of corner radius on the forces experienced by cylindrical bluff bodies in oscillatory flow. *Applied Ocean Research*, 6(2):83–89, 1984.

Bearman, P. W., Downie, J., Graham, J. M. R., and Obasaju, D. Forces on cylinders in viscous oscillatory flow at low Keulegan-Carpenter numbers. *Journal of Fluid Mechanics*, 154:337–356, 1985.

Beels, C. Optimization of the Lay-Out of a Farm of Wave Energy Converters in the North Sea. Analysis of Wave Power Resources, Wake Effects, Production and Cost. *(PhD Thesis)*, 2009.

Berkhoff, J. C. W. Computation of combined refraction-diffraction. *ASCE*, 1(Proceeding of the 13th Coastal Engineering Conference, New York, USA):471–490, 1972.

Bhinder, M. A., Babarit, A., Gentaz, L., and Ferrant, P. Assessment of Viscous Damping via 3D-CFD Modelling of a Floating Wave Energy Device. *EWTEC*, (Proc. of the 9th European Wave and Tidal Energy Conf., Southampton, UK), 2011.

Bhinder, M. A., Babarit, A., Gentaz, L., and Ferrant, P. Effect of Viscous Forces on the Performance of a Surging Wave Energy Converter. *ISOPE*, (Proceedings of the 22nd International Offshore and Polar Engineering Conference, Rhodes, Greece), 2012.

Bhinder, M. A., Babarit, A., Gentaz, L., and Ferrant, P. Potential time domain model with viscous correction and CFD analysis of a generic surging floating wave energy converter. *International Journal of Marine Energy*, 10:70–96, jun 2015. ISSN 22141669. doi: 10.1016/j.ijome.2015.01.005.

Bonfiglio, L., Brizzolara, S., and Chryssostomidis, C. Added Mass and Damping of Oscillating Bodies: a fully viscous numerical approach. *Recent Advances in Fluid Mechanics, Heat & Mass Transfer and Biology*, pages 210–215, 2011.

Bonfiglio, L., Brizzolara, S., and Chryssostomidis, C. Viscous Free Surface Numerical Simulations of Oscillating SWATH Ship Sections. *Recent Researches in Mechanical Engineering*, pages 33–38, 2013.

Budal, K. Theory for absorption of wave power by a system of interacting bodies. *Journal of Ship Research*, 21(4):248–253, 1977.

Carbon Trust. UK wave energy resource. *AMEC Environmental & Infrastructure UK Limited*, 2012.

CD-Adapco. User Guide: STAR-CCM+ Version 10.02. 2015.

Chakrabarti, S. K. Hydrodynamic interaction forces on multi-moduled structures. *Ocean Engineering*, 27:1037–1063, oct 2000. ISSN 00298018. doi: 10.1016/S0029-8018(99)00034-7. URL `http://linkinghub.elsevier.com/retrieve/pii/S0029801899000347`.

Child, B. F. M. On the configuration of arrays of floating wave energy converters. *(PhD Thesis)*, 2011.

Child, B. F. M. and Venugopal, V. Optimal configurations of wave energy device arrays. *Ocean Engineering*, 37:1402–1417, nov 2010. ISSN 00298018. doi: 10.1016/j.oceaneng.2010.06.010. URL `http://linkinghub.elsevier.com/retrieve/pii/S0029801810001447`.

Clément, A. H., McCullen, P., Falcão, A. F. d. O., Fiorentino, A., Gardner, F., Hammarlund, K., Lemonis, G., Lewis, T., Nielsen, K., Petroncini, S., Pontes, M.-T., Schild, P., Sjöström, B.-O., Sørensen, H. C., and Thorpe, T. Wave energy in Europe: current status and perspectives. *Renewable and Sustainable Energy Reviews*, 6:405–431, 2002.

Cruz, J., Sykes, R., Siddorn, P., and Eatock Taylor, R. Estimating the loads and energy yield of arrays of wave energy converters under realistic seas. *IET Renewable Power Generation*, 4 (6):488–497, 2010. ISSN 17521416. doi: 10.1049/iet-rpg.2009.0174.

Cummins, W. E. The impulse response function and ship motions. *Schiffstechnik*, 9(47): 101–109, 1962.

Delft University of Technology. User Manual SWAN Cycle III version 40.85. 2011.

Dennis, J. E. J. and Schnabel, R. B. Numerical Methods for Unconstrained Optimization and Nonlinear Equations. *Englewood Cliffs, NJ: Prentice-Hall*, 1983.

Department of Energy and Climate Change. Electricity Generation Costs. (October), 2012.

Department of Energy and Climate Change. Electricity Generation Costs. (July), 2013.

Drew, B., Plummer, A. R., and Sahinkaya, M. N. A review of wave energy converter technology. *Proceedings of the Institution of Mechanical Engineers, Part A: Journal of Power and Energy*, 223(8):887–902, dec 2009. ISSN 0957-6509. doi: 10.1243/09576509JPE782. URL http://pia.sagepub.com/lookup/doi/10.1243/09576509JPE782.

EMEC. Tank Testing of Wave Energy Conversion Systems. *EMEC (European Marine Energy Centre Ltd)*, 2009.

EquiMar. D5.1: Guidance protocols on choosing of electrical connection configurations. *EquiMar (Equitable Testing and Evaluation of Marine Energy Extraction)*, 2009.

EquiMar. D3.3: Assessment of current practice for tank testing of small marine energy devices. *EquiMar (Equitable Testing and Evaluation of Marine Energy Extraction)*, 2010a.

EquiMar. D3.4: Best practice for tank testing of small marine energy devices. *EquiMar (Equitable Testing and Evaluation of Marine Energy Extraction)*, 2010b.

EquiMar. D5.2: Device classification template. *EquiMar (Equitable Testing and Evaluation of Marine Energy Extraction)*, 2011.

Evans, D. V. Some theoretical aspects of three dimensional wave-energy absorbers. (Proceedings of the 1st Symposium on Ocean Wave Energy Utilisation), 1979.

Evans, D. V. Some analytic results for two and three dimensional wave-energy absorbers. *Power from Sea Waves*, pages 213–249, 1980.

Falcão, A. F. d. O. Wave energy utilization: A review of the technologies. *Renewable and Sustainable Energy Reviews*, 14:899–918, apr 2010. ISSN 13640321. doi: 10.1016/j.rser.2009.11.003. URL http://linkinghub.elsevier.com/retrieve/pii/S1364032109002652.

Falnes, J. Radiation impedance matrix and optimum power absorption for interacting oscillators in surface waves. *Applied Ocean Research*, 2:75–80, 1980.

Falnes, J. Ocean Waves and Oscillating Systems. *Cambridge University Press*, 2002.

Falnes, J. A review of wave-energy extraction. *Marine Structures*, 20:185–201, oct 2007. ISSN 09518339. doi: 10.1016/j.marstruc.2007.09.001. URL http://linkinghub.elsevier.com/retrieve/pii/S0951833907000482.

Falnes, J. and Hals, J. Heaving buoys, point absorbers and arrays. *Philosophical Transactions of the Royal Society of London. Series A, Mathematical and Physical Sciences*, 370:246–277, jan 2012. ISSN 1364-503X. doi: 10.1098/rsta.2011.0249. URL http://www.ncbi.nlm.nih.gov/pubmed/22184661.

Field, P. L. Comparison of RANS and Potential Flow Force Computations for the ONR Tumblehome Hullform in Vertical Plane Radiation and Diffraction Problems. *(MSc Thesis)*, 2013.

Folley, M. and Whittaker, T. J. T. The effect of sub-optimal control and the spectral wave climate on the performance of wave energy converter arrays. *Applied Ocean Research*, 31 (4):260–266, oct 2009. ISSN 01411187. doi: 10.1016/j.apor.2009.10.006. URL http://linkinghub.elsevier.com/retrieve/pii/S0141118709000947.

Folley, M. and Whittaker, T. J. T. Preliminary Cross-Validation Of Wave Energy Converter Array Interactions (OMAE2013-10837). *OMAE*, (Proc. of the ASME 29th International Conf. on Ocean, Offshore and Arctic Engineering, Nantes, France), 2013.

Folley, M., Babarit, A., Child, B. F. M., Forehand, D., O'Boyle, L., Silverthorne, K. E., Spinneken, J., Stratigaki, V., and Troch, P. A Review of Numerical Modelling of Wave Energy Converter Arrays (OMAE2012-83807). *OMAE*, (Proc. of the ASME 31th International Conf. on Ocean, Offshore and Arctic Engineering, Rio de Janeiro, Brazil), 2012.

Forehand, D., Kiprakis, A. E., Nambiar, A., and Wallace, A. R. A Fully Coupled Wave-to-Wire Model of an Array of Wave Energy Converters. *IEEE Transactions on Sustainable Energy*, pages 1–11, 2015. doi: 10.1109/TSTE.2015.2476960.

Garrett, C. J. R. Wave forces on a circular dock. *Journal of Fluid Mechanics*, 46(1):129–139, 1971.

Gelci, R., Cazale, H., and Vassale, J. Prévision de la houle. La méthode des densités spectroangulaires. *Bull. Inform. Comité Central Océanogr. d'Etude Côtes*, 9:416–435, 1957.

Goda, Y. Random Seas and Design of Maritime Structures. *University of Tokyo Press*, 1985.

Goo, J. S. and Yoshida, K. A numerical method for huge semisubmersible responses in waves. *Transactions-Society of Naval Architects and Marine Engineering*, 98:365–387, 1990.

Gunn, K. and Stock-Williams, C. Quantifying the global wave power resource. *Renewable Energy*, 44:296–304, aug 2012. ISSN 09601481. doi: 10.1016/j.renene.2012.01.101. URL http://linkinghub.elsevier.com/retrieve/pii/S0960148112001310.

Hasselmann, K., Barnett, T. P., Bouws, E., Carlson, H., Cartwright, D. E., Enke, K., Ewing, J. A., Gienapp, H., Hasselmann, D. E., Kruseman, P., Meerburg, A., Müller, P., Olbers, D. J., Richter, K., Sell, W., and Walden, H. Measurement of Wind-Wave Growth and Swell Decay during the Joint North Sea Wave Project (JONSWAP). *Deutsche Hydrographische Zeitschrift*, 8(12), 1973.

Havn, J. Wave Loads on Underwater Protection Covers. *(MSc Thesis)*, 2011.

Holthuijsen, L. H., Booij, N., and Ris, R. C. A spectral wave model for the coastal zone. *ASCE*, (Proceedings of the 2nd International Symposium on Ocean Wave Measurement and Analysis):630–641, 1993.

Holthuijsen, L. H. *Waves in Oceanic and Coastal Waters*. Cambridge University Press, 2007. ISBN 9780511618536. URL http://dx.doi.org/10.1017/CBO9780511618536.

Hu, Z. Z., Causon, D. M., Mingham, C. G., and Qian, L. Numerical simulation of floating bodies in extreme free surface waves. *Natural Hazards and Earth System Science*, 11(2): 519–527, feb 2011. ISSN 1684-9981. doi: 10.5194/nhess-11-519-2011.

Hughes, S. A. Physical Models and Laboratory Techniques in Coastal Engineering. *World Scientific: Advanced Series on Ocean Engineering - Volume 7*, 1993.

ITTC. 7.5-02-01-01: Recommended Procedures and Guidelines - Testing and Extrapolation Methods, General Uncertainty Analysis in EFD Uncertainty Assessment Methodology. *International Towing Tank Conference*, 1999.

ITTC. 7.5-03-01-01: Uncertainty Analysis in CFD, Verification and Validation. *International Towing Tank Conference*, 2002.

ITTC. 7.5-02-07-03.1: Recommended Procedures and Guidelines - Testing and Extrapolation of Methods, Loads and Responses, Ocean Engineering, Floating Offshore Platform Experiments. *International Towing Tank Conference*, 2005.

ITTC. 7.5-03-02-03: Recommended Procedures and Guidelines: Practical Guidelines for Ship CFD Applications. *International Towing Tank Conference*, 2011a.

ITTC. 7.5-02-07-02.2: Recommended Procedures and Guidelines - Prediction of Power Increase in Irregular Waves from Model Test. *International Towing Tank Conference*, 2011b.

ITTC. 7.5-02-07-03.7: Recommended Guidelines - Wave Energy Converter Model Test Experiments. *International Towing Tank Conference*, 2011c.

Kagemoto, H. and Yue, D. K. P. Interactions among multiple three-dimensional bodies in water waves: an exact algebraic method. *Journal of Fluid Mechanics*, 166:189–209, 1986. ISSN 00221120. doi: 10.1017/S0022112086000101.

Kashiwagi, M. Non-linear simulations of wave-induced motions of a floating body by means of the mixed Eulerian-Lagrangian method. *IMechE, Part C: Journal of Mechanical Engineering Science*, 214:841–855, 2000. doi: 10.1243/0954406001523821.

Kleinman, R. E. On the mathematical theory of the motion of floating bodies: An update. *David W. Taylor Naval Ship Research and Development Center*, DTNSRDC-82, 1982.

Kolmogorov, A. N. The Local Structure of Turbulence in Incompressible Viscous Fluid for Very Large Reynolds Numbers. *Doklady Akademiia Nauk SSSR*, 30:301–305, 1941. ISSN 1364-5021. doi: 10.1098/rspa.1991.0075.

Komen, G. The Wave Modelling (WAM) Group, a historical perspective. *Royal Netherlands Meteorological Institute (KNMI)*, 2004.

Langhamer, O., Haikonen, K., and Sundberg, J. Wave power - Sustainable energy or environmentally costly? A review with special emphasis on linear wave energy converters. *Renewable and Sustainable Energy Reviews*, 14(4):1329–1335, may 2010. ISSN 13640321. doi: 10.1016/j.rser.2009.11.016. URL `http://linkinghub.elsevier.com/retrieve/pii/S1364032109002780`.

Le Crom, I., Brito-Melo, A., and Sarmento, A. Maritime Portuguese Pilot Zone for Wave Energy Conversion: Modelling Analysis of the Impact on Surfing Conditions. *ICOE*, (Proceedings of the 2nd International Conference on Ocean Energy, Brest, France), 2008.

Le Méhauté, B. An introduction to hydrodynamics and water waves. *Springer-Verlag, New York*, 1976. doi: 10.4319/lo.1977.22.5.0974.

Lee, C.-H. and Newman, J. N. Computation of wave effects using the panel method. *Numerical Models in Fluild-Structure Interaction*, 2004.

Levi, E. C. Complex-Curve Fitting. *IRE Trans. on Automatic Control.*, AC-4:37–44, 1959.

Li, Y. and Yu, Y.-H. A Synthesis of Numerical Methods for Modeling Wave Energy Converter-Point Absorbers. *Renewable and Sustainable Energy Reviews*, 16(6):4352–4364, aug 2012. ISSN 13640321. doi: 10.1016/j.rser.2011.11.008. URL `http://linkinghub.elsevier.com/retrieve/pii/S1364032111005351`.

Lighthill, M. J. Waves and hydrodynamic loading. *BOSS*, (Proceedings of the International Conference on Behaviour of Offshore Structures):1–40, 1979.

Lindroth, S. and Leijon, M. Offshore wave power measurements - A review. *Renewable and Sustainable Energy Reviews*, 15(9):4274–4285, dec 2011. ISSN 13640321. doi: 10.1016/j.rser.2011.07.123. URL http://linkinghub.elsevier.com/retrieve/pii/S1364032111003704.

Linton, C. M. and Evans, D. V. The interaction of waves with arrays of vertical circular cylinders. *Journal of Fluid Mechanics*, 215:549–569, apr 1990. ISSN 0022-1120. doi: 10.1017/S0022112090002750.

Longuet-Higgins, M. S. and Cokelet, E. The deformation of steep waves on water. *Philosophical Transactions of the Royal Society of London. Series A, Mathematical and Physical Sciences*, 350:1–26, 1976.

Madsen, P. A. and Sørensen, O. R. A New Form of the Boussinesq Equations with Improved Linear Dispersion Characteristics. Part 2: A Slowly-Varying Bathymetry. *Coastal Engineering*, 18:183–204, 1992.

MARINET. Best practice guidelines for marine applications of computational fluid dynamics. *Consultants and Members of the NSC, MARNET-CFD*, 2002.

Matsui, T. and Tamaki, T. Hydrodynamic interaction between groups of vertical axisymmetric bodies floating in waves. (Proceeding of the International Symposium on Hydrodynamics in Ocean Engineering, Trondheim, Norway):817–836, 1981.

Mavrakos, S. A. Hydrodynamic coefficients for groups of interacting vertical axisymmetric bodies. *Ocean Engineering*, 18:485–515, 1991.

Mavrakos, S. A. and Koumoutsakos, P. Hydrodynamic interaction among vertical axisymmetric bodies restrained in waves. *Applied Ocean Research*, 9(3):128–140, 1987.

Mavrakos, S. A. and McIver, P. Comparison of methods for computing hydrodynamic characteristics of arrays of wave power devices. *Applied Ocean Research*, 19(5-6):283–291, 1997.

McCombes, T., Iyer, A. S., Falchi, M., Elsäßer, B., Scheijgrond, P., and Lawrence, J. WP2: Marine Energy System Testing - Standardisation and Best Practice, D2.2: Collation of Tidal Test Options. *MaRINET*, 2012.

McIver, P. Wave forces on arrays of floating bodies. *Journal of Engineering Mathematics*, 18: 273–285, 1984.

McIver, P. and Evans, D. V. Approximation of wave forces on cylinder arrays. *Applied Ocean Research*, 6(2):101–107, 1984. URL http://www.sciencedirect.com/science/article/pii/0141118784900476.

Mei, C. C. *The Applied Dynamics of Ocean Surface Waves, Second Edition (1989)*. 1983.

Mendes, L., Palha, A., Fortes, C. J., Brito-Melo, A., and Sarmento, A. Analysis of the Impact of a Pilot Zone for Wave Energy Conversion Offshore Portugal. *ISOPE*, (Proceedings of the 18th International Offshore and Polar Engineering Conference, Vancouver, Canada), 2008.

Millar, D. L., Smith, H. C. M., and Reeve, D. E. Modelling analysis of the sensitivity of shoreline change to a wave farm. *Ocean Engineering*, 34:884–901, 2007. doi: 10.1016/j.oceaneng.2005.12.014.

Molin, B. Second-order diffraction loads upon three-dimensional bodies. *Applied Ocean Research*, 1(4):197–202, 1979.

Moriarty, P. and Honnery, D. What is the global potential for renewable energy? *Renewable and Sustainable Energy Reviews*, 16(1):244–252, jan 2012. ISSN 13640321. doi: 10.1016/j.rser.2011.07.151. URL http://linkinghub.elsevier.com/retrieve/pii/S1364032111003984.

Morison, J. R., O'Brien, M. P., Johnson, J. W., and Schaaf, S. A. The force exerted by surface waves on piles. *Petrolium Transactions, AIME*, 189:149–154, 1950.

Newman, J. N. Marine Hydrodynamics. *MIT Press*, 1977.

Ogilvie, T. Recent progress towards the understanding and prediction of ship motions. *Naval Hydrodynamic*, (Sixth Symposium on Naval Hydrodynamic), 1964.

Ohkusu, M. Hydrodynamic Forces on Multiple Cylinders in Waves. (Proceedings of the International Symposium on the Dynamics of Marine Vehicles and Structures in Waves, London, UK):107–112, 1974.

Palm, J., Eskilsson, C., Paredes, G. M., and Bergdahl, L. CFD Simulation of a Moored Floating Wave Energy Converter. *EWTEC*, (Proc. of the 10th European Wave and Tidal Energy Conf., Aalborg, Denmark), 2013.

Payne, G. S. Guidance for the experimental tank testing of wave energy converters. *SuperGen*, 2008.

Radder, A. C. and Dingemans, M. W. Canonical equations for almost periodic, weakly nonlinear gravity waves. *Wave Motions*, 7:473–485, 1985.

Ransley, E., Hann, M., Greaves, D. M., Raby, A., and Simmonds, D. Numerical and Physical Modelling of Extreme Wave Impacts on a Fixed Truncated Circular Cylinder. *EWTEC*, (Proc. of the 10th European Wave and Tidal Energy Conf., Aalborg, Denmark), 2013.

REN21. *Renewables 2015: Global Status Report*. 2015. ISBN 9783981593464.

RenewableUK. Marine Energy in the UK, State of the industry report. *http://www.bwea.com/pdf/publications/SOI_2012.pdf*, 2012.

Roache, P. J. Verification and Validation in Computational Science and Engineering, Hermosa Publishers, New Mexico. 1998.

Roy, C. J. Review of code and solution verification procedures for computational simulation. *Journal of Computational Physics*, 205(1):131–156, may 2005. ISSN 00219991. doi: 10.1016/j.jcp.2004.10.036. URL `http://linkinghub.elsevier.com/retrieve/pii/S0021999104004619`.

Salter, S. H. World progress in wave energy-1988. *International Journal of Ambient Energy*, 10(1):3–24, 1989.

Sarpkaya, T. Vortex shedding and resistance in harmonic flow about smooth and rough circular cylinders at high reynolds numbers. *Naval Postgraduate School, Monterey, CA,Technical Report: NPS-59SL76021*, 1976.

Sarpkaya, T. Mechanics of Wave Forces on Offshore Structures. *Van Nostrand Reinhold Company*, 1981.

Schlichting, H. Boundary-Layer Theory. *McGraw Hill*, 1979.

Siddorn, P. and Eatock Taylor, R. Diffraction and Independent Radiation by an Array of Floating Cylinders. *Ocean Engineering*, 35(13):1289–1303, 2008.

Simon, M. J. Multiple scattering in arrays of axisymmetric wave-energy devices. Part 1. A matrix method using a plane-wave approximation. *Journal of Fluid Mechanics*, 120:1–25, 1982.

Smith, H. C. M., Pearce, C., and Millar, D. L. Further analysis of change in nearshore wave climate due to an offshore wave farm: An enhanced case study for the Wave Hub site. *Renewable Energy*, 40(1):51–64, apr 2012. ISSN 09601481. doi: 10.1016/j.renene.2011.09.003. URL `http://linkinghub.elsevier.com/retrieve/pii/S0960148111005210`.

Spring, B. H. and Monkmeyer, P. L. Interaction of plane waves with vertical cylinders. *ICCE*, (Proceedings of the 14th International Conference on Coastal Engineering, Copenhagen, Denmark):1828–1845, 1974.

Stokes, S. G. G. On the effect of the internal friction of fluids on the motion of pendulums. *Transactions of the Cambridge Philosophical Society*, 9, 1851.

Stratigaki, V., Troch, P., Stallard, T. J., Forehand, D., Kofoed, J., Folley, M., Benoit, M., Babarit, A., and Kirkegaard, J. Wave basin experiments with large wave energy converter arrays to study interactions between the converters and effects on other users in the sea and the coastal area. *Energies*, 7(2):701–734, feb 2014. ISSN 1996-1073. doi: 10.3390/en7020701.

Taghipour, R., Perez, T., and Moan, T. Hybrid frequency-time domain models for dynamic response analysis of marine structures. *Ocean Engineering*, 35(7):685–705, may 2008. ISSN 00298018. doi: 10.1016/j.oceaneng.2007.11.002. URL http://linkinghub.elsevier.com/retrieve/pii/S0029801807002363.

Telste, J. G. and Belknap, W. F. Potential Flow Forces and Moments from Selected Ship Flow Codes in a Set of Numerical Experiments. No. NSWCCD-50-TR-2008-040. *Naval Surface Warfare Center Carderock Div. Bethesda MD*, 2008.

The Crown Estate. UK Wave and Tidal Key Resource Areas Project, Summary Report. 2012.

Thiruvenkatasamy, K. and Neelamani, S. On the efficiency of wave energy caissons in array. *Applied Ocean Research*, 19(1):61–72, 1997.

Thomas, G. and Evans, D. V. Arrays of three-dimensional wave-energy absorbers. *Journal of Fluid Mechanics*, 108:67–88, apr 1981. ISSN 0022-1120. doi: 10.1017/S0022112081001997.

Troch, P. A numerical model for propagation and transformation of linear water waves. *Department of Civil Engineering, Ghent University*, 1998.

Tseng, R.-S., Wu, R.-H., and Huang, C.-C. Model study of a shoreline wave-power system. *Ocean Engineering*, 27(8):801–821, aug 2000. ISSN 00298018. doi: 10.1016/S0029-8018(99)00028-1. URL http://linkinghub.elsevier.com/retrieve/pii/S0029801899000281.

Twersky, V. Multiple Scattering of Radiation by an Arbitrary Configuration of Parallel Cylinders. *Journal of the Acoustical Society of America*, 24(1):42–46, 1952.

Venugopal, V. and Smith, G. H. Wave climate investigation for an array of wave power devices. *EWTEC*, (Proc. of the 7th European Wave and Tidal Energy Conf., Porto, Portugal), 2007.

Venugopal, V., Bryden, I. G., and Wallace, A. R. On the Interaction of Waves with an Array of Open Chambered Structures: Application to Wave Energy Converters. *OMAE*, (Proc. of the ASME 29th International Conf. on Ocean, Offshore and Arctic Engineering, Shanghai, China), 2010.

Versteeg, H. K. and Malalasekera, W. An Introduction to Computational Fluid Dynamics: The Finite Volume Method. *Pearson*, 2007.

Viola, I. M., Flay, R. G. J., and Ponzini, R. CFD analysis of the hydrodynamic performance of two candidate America's Cup AC33 hulls. *Transactions of the Royal Institution of Naval Architects Part B: International Journal of Small Craft Technology*, 154(1):B1–B12, 2012. doi: 10.3940/rina.ijsct.2012.b1.113.

VIRTUE (The Virtual Tank Utility in Europe). Best Practice Guidelines for the application of Computational Fluid Dynamics in Marine Hydrodynamics. *Consultants and Members of VIRTUE*, 2009. doi: 10.13140/RG.2.1.4642.7680.

Vugts, J. H. The hydrodynamic coefficients for swaying, heaving and rolling cylinders in a free surface. *International Shipbuilding Progress*, 15:251–276, 1968.

WAMIT: Version 7. User Manual. 2012.

Wave Star A/S. Wavestar prototype at Roshage, Performance data for ForskVE project no 2009-1-10305 phase 1 & 2. 2013.

Westphalen, J., Greaves, D. M., Williams, C. K., Taylor, P. H., Causon, D. M., Mingham, C. G., Hu, Z. Z., Stansby, P. K., Rogers, B. D., and Omidvar, P. Extreme Wave Loading on Offshore Wave Energy Devices using CFD: a Hierarchical Team Approach. *EWTEC*, (Proc. of the 8th European Wave and Tidal Energy Conf., Uppsala, Sweden):500–508, 2009.

Westphalen, J., Bacelli, G., Balitsky, P., and Ringwood, J. V. Control Strategies for Arrays of Wave Energy Devices. *EWTEC*, (Proc. of the 9th European Wave and Tidal Energy Conf., Southampton, UK), 2011.

Wilcox, D. C. Reassessment of the scale-determining equation for advanced turbulence models. *AIAA Journal*, 26(11):1299–1310, 1988. ISSN 0001-1452. doi: 10.2514/3.10041.

Wu, G. X. and Eatock Taylor, R. Transient motion of a floating body in steep water waves. *IWWWFB*, (11th International Workshop for Water Waves and Floating Bodies (Hamburg, Germany)):219–223, 1996.

Yang, C., Löhner, R., and Yim, S. C. Development of a CFD Simulation Method for Extreme Wave and Structure Interactions. *OMAE*, (Proc. of the ASME 24th International Conf. on Ocean, Offshore and Arctic Engineering, Halkidiki, Greece), 2005.

Yilmaz, O. and Incecik, A. Analytical solutions of the diffraction problem of a group of truncated vertical cylinders. *Ocean Engineering*, 25(6):385–394, 1998.

Yu, Y.-H. and Li, Y. Reynolds-Averaged Navier-Stokes simulation of the heave performance of a two-body floating-point absorber wave energy system. *Computers & Fluids*, 73:104–114, mar 2013. ISSN 00457930. doi: 10.1016/j.compfluid.2012.10.007.

Yuan, Z.-d. and Huang, Z.-h. An experimental study of inertia and drag coefficients for a truncated circular cylinder in regular waves. *Journal of Hydrodynamics*, 22(5):318–323, 2010. ISSN 1001-6058. doi: 10.1016/S1001-6058(10)60258-4.

Yue, D. K. P., Chen, H. S., and Mei, C. C. A hybrid element method for diffraction of water waves by three-dimensional bodies. *International Journal for Numerical Methods in Engineering*, 12:245–266, 1978.

Zheng, W. and Dalton, C. Numerical prediction of force on rectangular cylinders in oscillating viscous flow. *Journal of Fluids and Structures*, 13:225–249, 1999.

Zhu, X. Irregular Frequency Removal from the Boundary Integral Equation for the Wave-body Problem. *(MSc Thesis)*, 1994.

Zhu, X. and Lee, C.-H. Removing the Irregular Frequencies in Wave-Body Interactions. *IWWWFB*, (9th International Workshop for Water Waves and Floating Bodies):245–249, 1994.